Dissertation

submitted to the

Combined Faculty of Mathematics, Engineering, and Natural Sciences

of Heidelberg University, Germany

and to the

Department of Physics

of the University of Trento, Italy

for the degree of

Doctor of Natural Sciences

Put forward by

Gopal Chandra Santra

born in: Tamluk, West Bengal, India

Oral examination: Oct 17, 2025

Quantum resources in quantum technologies: From quantum optimization to many-body physics

Supervisors: Prof. Dr. Philipp Hauke (Trento)

Prof. Dr. Markus Oberthaler (Heidelberg)

Referees: Prof. Dr. Richard Schmidt

apl. Prof. Dr. Jörg Evers

To Thee, the Constant through all variables,—

Whom I pursue, Who art both the Way and the Destiny;

This thesis is dedicated unto Thee.

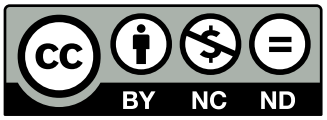

Abstract

Significant progress has been made in quantum technologies over the past decade. Despite this success, a central question remains: to what extent quantum resources are being exploited. This question is crucial not only for benchmarking quantum systems but also to unlock their full potential. This thesis analyses the role of quantum resources spanning quantum optimization algorithms to quantum many-body systems. First, we show how squeezing establishes a natural connection between the Quantum Approximate Optimization Algorithm and quantum metrology, revealing the role of quantum correlations and providing a benchmarking method for quantum-optimization devices. Further, we study multipartite entanglement in quantum optimization and demonstrate its presence on quantum hardware. However, entanglement alone is insufficient for a quantum advantage, as stabilizer states—though highly entangled—are classically simulable. We therefore study the role of nonstabilizerness in quantum optimization. Building on such resources, we further examine how they manifest in disordered systems. We show the emergence of non-Markovianity in disorder-averaged dynamics. Moreover, we examine complexity-resources across chaotic to integrable regimes in random-matrix models, highlighting the need for a multifaceted approach in quantum simulation. These investigations provide a deeper understanding of quantum technologies, from optimization to simulation, and lay the foundation for future developments toward quantum advantage.

Zusammenfassung

In den letzten zehn Jahren wurden bei den Quantentechnologien erhebliche Fortschritte erzielt. Trotz dieses Erfolges bleibt eine zentrale Frage bestehen: In welchem Umfang werden die Quantenressourcen genutzt? Diese Frage ist nicht nur für das Benchmarking von Quantensystemen von entscheidender Bedeutung, sondern auch für die Erschließung ihres vollen Potenzials. In dieser Arbeit wird die Rolle von Quantenressourcen analysiert, die von Quantenoptimierungsalgorithmen bis hin zu Quanten-Vielteilchensystemen reichen. Zunächst zeigen wir, wie Squeezing eine natürliche Verbindung zwischen dem Quantum Approximate Optimization Algorithm und der Quantenmetrologie herstellt, indem wir die Rolle von Quantenkorrelationen aufdecken und eine Benchmarking-Methode für Quantenoptimierungsgeräte bereitstellen. Darüber hinaus untersuchen wir die mehrteilige Verschränkung in der Quantenoptimierung und demonstrieren ihr Vorhandensein auf Quantenhardware. Verschränkung allein reicht jedoch nicht aus, um einen Quantenvorteil zu erzielen, da Stabilisatorzustände — obwohl sie stark verschränkt sind —klassisch simulierbar sind. Wir untersuchen daher die Rolle der Nicht-Stabilisierung in der Quantenoptimierung. Aufbauend auf diesen Ressourcen untersuchen wir, wie sie sich in ungeordneten Systemen manifestieren. Wir zeigen das Auftreten von Nicht-Markowianität in unordnungsgemittelter Dynamik. Darüber hinaus untersuchen wir Komplexitätsressourcen in chaotischen bis hin zu integrierbaren Regimen in Zufallsmatrixmodellen und unterstreichen damit die Notwendigkeit eines vielschichtigen Ansatzes in der Quantensimulation. Diese Untersuchungen ermöglichen ein tieferes Verständnis der Quantentechnologien, von der Optimierung bis zur Simulation, und legen den Grundstein für zukünftige Entwicklungen in Richtung Quantenvorteil.

Sommario

Negli ultimi dieci anni sono stati compiuti notevoli progressi nelle tecnologie quantistiche. Nonostante questi successi, rimane una domanda centrale: in che misura le risorse quantistiche vengono effettivamente sfruttate? Tale quesito è cruciale non solo per il benchmarking dei sistemi quantistici, ma anche per sbloccarne appieno il potenziale. Questa tesi analizza il ruolo delle risorse quantistiche in contesti che spaziano dagli algoritmi di ottimizzazione quantistica ai sistemi a molti corpi. In primo luogo, mostriamo come lo squeezing stabilisca una connessione naturale tra l'algoritmo di ottimizzazione approssimata quantistica (QAOA) e la metrologia quantistica, rivelando il ruolo delle correlazioni quantistiche e fornendo al contempo un metodo di benchmarking per i dispositivi di ottimizzazione quantistica. Successivamente, studiamo l'entanglement multipartito nell'ottimizzazione quantistica e ne dimostriamo la presenza nell'hardware quantistico. Tuttavia, l'entanglement da solo non è sufficiente a garantire un vantaggio quantistico: gli stati stabilizzatori, infatti, pur essendo altamente entangled, sono simulabili in modo classico. Analizziamo quindi il ruolo della non-stabilizzabilizzazione nell'ottimizzazione quantistica. Partendo da queste risorse, ci spingiamo oltre a esaminarne le manifestazioni nei sistemi disordinati. Mostriamo l'emergere della non-markovianità nelle dinamiche mediate sul disordine e analizziamo le risorse di complessità attraverso regimi caotici e integrabili in modelli a matrici aleatorie, mettendo in luce la necessità di un approccio multiforme alla simulazione quantistica. Queste indagini forniscono una comprensione più approfondita delle tecnologie quantistiche, dall'ottimizzazione alla simulazione, e pongono le basi per futuri sviluppi verso il pieno raggiungimento del vantaggio quantistico.

সারাংশ

গত দশকে কোয়ান্টাম প্রযুক্তিতে অনেক উল্লেখযোগ্য অগ্রগতি হয়েছে। এত সাফল্য সত্ত্বেও, একটি মূল প্রশ্ন রয়েই গেছে: সত্যিকারের কতটা কাজে লাগান হচ্ছে কোয়ান্টাম সম্পদকে? এই প্রশ্নটি কেবল কোয়ান্টাম সিস্টেমের বেঞ্চমার্কিংয়ের জন্যই নয়, বরং তাদের পূর্ণ সম্ভাবনা উন্মোচনের জন্যও গুরুত্বপূর্ণ। এই থিসিসটি কোয়ান্টাম অপ্টিমাইজেশন অ্যালগরিদম থেকে শুরু করে কোয়ান্টাম বহু-বস্তু-সম্বন্ধীয় পদার্থবিদ্যা পর্যন্ত বিভিন্ন ব্যপারে কোয়ান্টাম সম্পদের ভূমিকা বিশ্লেষণ করেছে। প্রথমে, আমরা দেখাই কিভাবে squeezing, কোয়ান্টাম আনুমানিক অপ্টিমাইজেশন অ্যালগরিদম এবং কোয়ান্টাম মেট্রোলজির মধ্যে একটি স্বাভাবিক সংযোগ স্থাপন করে— একদিকে কোয়ান্টাম correlation সম্পর্কে ধারণা দেয়, আবার অন্যদিকে কোয়ান্টাম-অপ্টিমাইজেশন যন্ত্রের জন্য একটি বেঞ্চমার্কিং পদ্ধতিও আমাদেরকে দেয়। এরপরে, আমরা কোয়ান্টাম অপ্টিমাইজেশনে multipartite entanglement- এর ভূমিকা অধ্যয়ন করি এবং কোয়ান্টাম হার্ডওয়্যারে এর উপস্থিতি প্রদর্শন করি। তবে, কোয়ান্টাম প্রযুক্তির শ্রেষ্ঠত্ব প্রদর্শনের জন্য কেবল entanglement থাকলেই চলে না, কারণ এক ধরনের অবস্থা আছে, স্টেবিলাইজার অবস্থা নামের, যারা অত্যন্ত entangled হওয়া সত্ত্বেও, খুবই সহজেই সিমুলেশন করা যায়। তাই আমরা কোয়ান্টাম অপ্টিমাইজেশনে non-stabilizerness-এর ভূমিকাও অধ্যয়ন করি। এই ধরনের সম্পদের উপর ভিত্তি করে, আমরা আরও পরীক্ষা করি যে তারা বিশৃঙ্খল অবস্থায় কীভাবে প্রকাশ পায়। আমরা এই বিশৃঙ্খল সিস্টেমের মধ্যে থেকে সময়ের সাথে কিভাবে non-Markovianity-এর (অতীতকে মনে রাখা) উত্থান হতে পারে সেটা দেখাই। এরপরে, আমরা বিভিন্ন random-ম্যাট্রিক্স মডেলে বিশৃঙ্খল থেকে সংহত অবস্থা পর্যন্ত জটিলতা-সম্পর্কিত সম্পদদের পরীক্ষা করি, যা থেকে বোঝা যায় যে কোয়ান্টাম সিমুলেশনে বহুমুখী পদ্ধতির প্রয়োজন আছেই। এই তদন্তগুলি অপ্টিমাইজেশন থেকে সিমুলেশন পর্যন্ত কোয়ান্টাম প্রযুক্তি সম্পর্কে গভীর ধারণা প্রদান করে এবং ভবিষ্যতে কিভাবে এই প্রযুক্তি নতুন সম্ভাবনা এনে দিতে পারে, সেই উন্নয়নের ভিত্তিপ্রস্তর স্থাপন করে।

Acknowledgements

At the end of the pandemic in October 2021, as the world was beginning to recover from a difficult period, I embarked on what is often described as a life-changing journey: my PhD. I started with little confidence, yet Prof. Philipp Hauke generously welcomed me into his team—a vibrant, diverse group of young researchers brimming with knowledge. Initially, I was uncertain about which research direction to pursue, but Philipp never discouraged me. Instead, he allowed me the freedom to explore. Over time, a series of circumstances and challenges gradually shaped the course of my PhD journey. Although it spanned four years, it never felt long, perhaps because it was dynamic, never stagnant or monotonous. There were moments when projects stretched over two years, allowing us to explore them in depth, and other moments when we worked through weekends to get results, always driven by the joy of discovery. In the process, I not only learned how research and publishing work, but also the tricks and habits of this *trade*, and how to work effectively with people. It is often said that you become like your PhD supervisor, and I feel fortunate that the person I had the opportunity to follow was Philipp. He knows precisely when and how to support us in moments of frustration and need, both academically and personally.

I am also deeply grateful to Prof. Fred Jendrzejewski for including me in the experimental cold atom group in Heidelberg. My first year in Heidelberg, surrounded by experimentalists, had a profound influence on my perspective. It sparked a curiosity to constantly ask, "How much resources are required to perform an experiment?"—a mindset cultivated by the inspiring environment of the Synthetic Quantum Systems (SynQS) group and Prof. Markus Oberthaler. I learned a great deal from observing how he poses questions and brings meaningful physics to them with amazing experimental ideas. I am also grateful to Dr. Daniel Egger, who patiently taught me the foundations of quantum optimization and guided me in thinking critically about quantum computing hardware. I would also like to acknowledge the IBM Quantum Credits Programs for allowing us to run experiments on their 156-qubit hardware.

I would like to express my sincere gratitude to Prof. Richard Schmidt and Prof. Jörg Evers for kindly agreeing to serve as referees and as members of my PhD examination committee.

I am thankful to our Heidelberg group—Lisa, Apoorva, Andy, Rohit, Jan, Lilo, Yannick, and Noah—for their patience, for making sure I never felt alone, and for graciously indulging my curiosity about the experiments, no matter how naive my thoughts may have seemed. Friday breakfasts, group hikes, and Indian takeaway dinners are cherished memories that always draw me back to Heidelberg. I owe special thanks to Mrs. Jäger and Mrs. Schmetzer; navigating the bureaucracies of two countries as a non-EU citizen would have been overwhelming without their help.

Life in Trento offered a contrasting experience, like returning to a family of theorists after an extended period of deputation in an experimental group. I soon found

myself surrounded by experts in a wide range of fields. It quickly became clear how little I know. Yet, I was never made to feel inadequate; instead, I was met with encouragement and guidance, both in group meetings and journal clubs. I would like to thank our former group members, Kevin, Ricardo, Haifeng, and Philipp U., for their support during my early days in Trento and for continuing to assist me in navigating the bureaucratic hurdles. I am equally grateful to fellow PhD students Veronica, Julius, Alberto, and Alex, who reminded me I was not alone in facing the many frustrations of this journey.

I would like to acknowledge those from whom I continue to learn and collaborate: Daniel, Sudipto, Soumik, Emanuele, Andrea, Ricardo, Julius, Matteo, Chiara, Alberto, Edoardo, and Alex. I also sincerely appreciate those who always respond to my spontaneous queries, even if we are not actively working on a project together—Ganesh, Dileep, Sebastian, and David. The afternoon fruit breaks, gelato runs, movie nights, group hikes, dinners, BBQs, BEC picnics, and Christmas celebrations made me wonder if sadness was even possible in such an environment. And most importantly, heartfelt thanks to Monica and Sara for handling our administrative matters with ease and efficiency. Special thanks to Ganesh, Alberto, Alex, Soumik, and Andrea for proofreading part of this thesis, and Sebastian, Julius, Andrea, Chiara, and Amrita for helping me translate abstracts into other languages.

When I used to read acknowledgments in other PhD theses, I often wondered why people thanked their families; what kind of support could they possibly have offered in such a technical journey? However, after going through my PhD, I understand it all too well. I now realize how many breakdowns I experienced, how often I doubted my worth, and how silently my parents carried their burdens while shielding me from them. Even as I troubled them with my worries, they never let theirs reach me. I also want to thank my grandparents, uncles, aunts, cousins, and everyone whose quiet faith kept me grounded and focused.

I am deeply grateful to Amrita, who has always believed in me, encouraged me to do my best, and stood by me through every low. If I appear efficient in data analysis or PowerPoint, much of the credit goes to her. Despite her challenges, she never turned away from mine. Without her unwavering support, I doubt I would have made it this far—certainly not with my sanity intact.

It would be incomplete if I did not acknowledge someone without whom I might never have pursued Physics and might have taken a completely different path, such as becoming a doctor or engineer. His passion for Physics and the way he spoke about it with such conviction and wonder left a lasting impression on me at a very young age. That spark was enough not only to ignite my belief in Physics, but also to reassure my parents—as if this path had always been destined. He is my guide-exemplar.

I also cannot help but acknowledge those whose infectious passion for Physics during my formative years convinced me that Physics was not only a path to curiosity, but also the coolest pursuit one could follow. I am deeply grateful to Sujit-babu, Kamal-da, Tapas-babu, Prof. Deepak Dhar, Prof. Sudarshan Ananth, Prof. Sachin Jain, Prof. Sreejith GJ, Prof. Rejish Nath, Prof. Thanu Padmanabhan, and, most importantly, the man who is surely joking.

If you are reading this and I have not already thanked you, please know that your time and attention make you a meaningful part of this work—I am truly grateful.

To everyone who contributed, in ways large and small—thank you.

Contents

List of Figures

List of Tables

Chapter 1
Introduction

In the last decades, quantum technologies have rapidly evolved, transforming quantum computation and simulation from a theoretical pursuit into an experimental reality [1–8]. This transformation has been propelled by continual progress in qubit coherence, scalable architectures, and the emergence of quantum error correction techniques across multiple hardware platforms, such as superconducting qubits [9–12], trapped ions [13–15], neutral atoms [16,17], and photonic systems [18]. This technological momentum is matched by global enthusiasm: governments and private industries alike are investing heavily in quantum research, motivated by its potential to revolutionize fields such as cryptography [19], materials discovery [20], drug design [21], and optimization [22]. At the same time, academic research is broadening the scope of quantum simulation, aiming to tackle problems that lie beyond the reach of classical computation. For example, in condensed matter physics, quantum simulators are being explored to simulate non-equilibrium dynamics and quantum phase transitions [23–26]; in high-energy physics, to study real-time dynamics and non-perturbative effects in lattice gauge theories [27–33]; in quantum chemistry, to model molecular interactions and reaction mechanisms [34, 35], or in the realms of quantum gravity and quantum chaos, to understand holographic dualities and information scrambling [36–38]. Together, these developments illustrate not only the versatility of quantum technologies but also the diverse and growing landscape of quantum applications, from fundamental physics to real-world impact.

Despite such remarkable progress, skepticism about quantum technologies persists, driven by challenges such as noisy hardware, limited coherence time, the significant overhead of error correction, or the lack of broadly applicable quantum algorithms that can outperform classical methods. At the heart of this skepticism lies a key question: *Do quantum effects truly drive the observed results, or are they merely artifacts of noise, offering no clear advantage over classical simulation?* In response, the quantum community has developed rigorous benchmarking techniques [39–41] to address this ambiguity. Identifying and isolating truly quantum signatures is critical for validating devices [42, 43] and assessing their real-world utility [44, 45]. Beyond verification, active efforts focus on developing new algorithms, error mitigation strategies [46], and resource theories [47] to better harness and understand quantum resources. This deeper understanding clarifies the realistic potential of quantum technologies, helps set achievable milestones, and inspires confidence in the field's progress toward transformative applications.

To understand which quantum resources are essential and how to harness them effectively, it helps to revisit the key milestones that have shaped the development of quantum technology and our understanding of its fundamental phenomena. Quan-

tum mechanics emerged in the early 20th century as a framework to describe microscopic phenomena that classical theories could not explain. Pioneering work by scientists such as Planck, Einstein, Heisenberg, Schrödinger, Dirac, Born, Bohr, von Neumann [48–59], and provoking key experiments such as Davisson-Germar's and later, Jönsson's double-slit interference experiments [60, 61], fundamentally reshaped physics and enabled transformative technologies like transistors, lasers, and atomic clocks. Riding on the concepts developed during this first quantum revolution, the second revolution arrived to transform the quantum theory of fundamental curiosity into practical engineering and technology. By recognizing the limitations of classical computers for simulating quantum phenomena, visionaries like Manin and Feynman proposed the idea of quantum simulators [62, 63]. As Feynman famously stated, "Nature isn't classical, dammit, and if you want to simulate it, you'd better make it quantum" [64]. Concurrently, quantum information theory introduced protocols such as the BB84 protocol for cryptography [65], and Shor's algorithm [66] for factoring large numbers. Experimental platforms have advanced steadily to realize these theoretical concepts in practice [67–70]. Later, the development of quantum error correction and fault-tolerance schemes [71, 72] shifted the focus from entanglement to magic states as the central resource for robust quantum computation. Alongside these developments, the tensor network methods [73, 74] have also advanced for the simulation of many-body quantum systems, complementing the growth of quantum technologies by enabling classical simulations that can benchmark experimental efforts in understanding complex quantum phenomena.

In the presence of such a variety of theoretical frameworks, numerical techniques, and experimental platforms, with their respective strengths and limitations, focusing on a single approach or perspective is inadequate to show quantum advantage [45, 75, 76]. For example, Google's 2019 quantum supremacy claim [11] demonstrated that their 53-qubit Sycamore processor could sample from a random quantum circuit in about 200 seconds—a task believed to take classical supercomputers thousands of years. However, the problem was artificial and specifically chosen to favor quantum devices. And yet, subsequent classical algorithms [77–80] were able to show a reduced simulation time, challenging the original supremacy claim. Another notable case is that Farhi *et al.* introduced the Quantum Approximate Optimization Algorithm (QAOA) as a promising method for problems like MaxCut [81]. Initial results suggested potential quantum advantage, but subsequent improvements in classical algorithms challenged these claims [82, 83], highlighting the evolving competition between quantum and classical approaches. These examples serve as a clear reminder that reaching quantum advantage is not straightforward; it calls for broad exploration and inventive use of quantum resources.

Throughout this thesis, we investigate the multifaceted nature of quantum resources [47] both theoretically and experimentally with a central goal to understand how they are harnessed in contexts ranging from quantum optimization to many-body physics. Quantum resources provide a rigorous framework for distinguishing between what is considered easy and what is considered hard (expensive), based on the identification of free and resourceful operations within a given resource theory. This unified perspective enables us to identify which features of a quantum state or process can be exploited to gain an advantage over classical alternatives. In this quest, the classical paradigm serves as a free resource; by identifying what is tractable within classical computation or simulation, we can define appropriate resource theories and

corresponding measures that highlight the power of quantum systems. For instance, classical systems can easily represent product states, but struggle with superposition, leading to the formulation of entanglement as a quantum resource [84]. Similarly, stabilizer states can be efficiently simulated classically, whereas non-stabilizer states cannot, thereby motivating the resource theory of nonstabilizerness [85]. Thus, quantum resources can be viewed as a unifying framework to understand quantumness that helps to assess the current capabilities of quantum systems and their potential to surpass classical approaches, which is discussed in Chapter 2.

Within quantum computation, quantum optimization [22] stands out as particularly crucial. Combinatorial optimization problems [86] are widespread across science and industry, so any quantum improvement over state-of-the-art classical algorithms can have a profound impact. This makes quantum optimization one of the most promising pathways for realizing the practical value of quantum technologies. We discuss in detail the complexity of optimization problems and how quantum algorithms may tackle such issues in Chapter 3. Given the limited capability of current quantum devices [87], and the remarkable ability of existing classical computers, hybrid algorithms are emerging as a potential test-ground for quantum advantage, for example, the Quantum Approximate Optimization Algorithm (QAOA) [81]. However, despite its successful applications, QAOA depends heavily on classical optimization routines. This raises an important question: *to what extent do such hybrid algorithms truly harness quantum resources?* Although one may think that practical performance is all that matters, understanding the role of quantum resources is crucial for achieving genuine quantum advantage, especially in predicting its capability on large-scale problems that exceed currently accessible benchmarks. Without leveraging the aspects of quantum mechanics that make the computation classically intractable, the algorithm may ultimately fail to deliver a true quantum advantage. In a more quantum information way, it is about asking a fundamental question: *when a quantum algorithm outperforms its classical counterpart, what quantum resource underpins that advantage? Is it entanglement, nonstabilizerness, or some other feature of quantumness? And more importantly, does our current quantum hardware possess the capacity to harness these resources? If not, how can such a quantum effect be introduced into the hardware?* This is some of the underlying quests of this thesis for Part II (Chapter 4-7), where we explore resources in quantum optimization.

In Chapter 4, we establish a connection between quantum optimization and quantum metrology via squeezing to understand the role of quantum correlations in QAOA. We also introduce a hardware benchmarking technique based on spin-squeezing. To probe the necessity of multipartite entanglement—known to be essential for quantum computational speed-up [88]—we examine genuine multipartite entanglement in quantum annealing and uncover its correlation with success probability in Chapter 5. We further validate the presence of such entanglement experimentally on IBM's 156-qubit quantum computer in Chapter 6. Recognizing that entanglement alone does not capture all aspects of quantum advantage, we turn our attention to nonstabilizerness in Chapter 7, studying its role in both QAOA and quantum annealing and its relationship to algorithmic fidelity.

In the realm of quantum technologies, quantum simulation [89, 90] forms another fundamental block. Its goal is to simulate highly complex physical systems, providing a powerful alternative to classical approaches. This is particularly relevant in regimes where traditional classical methods, such as tensor networks [91] or Monte

Carlo simulations [92], become inapplicable. This can also be thought of as the native and most natural application of quantum computers, where we aim to use a quantum computer to mimic the rules that describe physical microscopic quantum systems [75]. Analog quantum simulators have already yielded significant insights into many-body physics [16, 24, 93], showcasing the potential of quantum devices to explore otherwise intractable models. One of the aims of quantum simulation is to push these boundaries further, tackling increasingly complex problems. In this case, our goal is to assess the extent to which quantum resources are being utilized in quantum simulation of complex systems, particularly in the presence of disorder. In Part III (Chapter 8-9), we investigate how quantum resources manifest in disordered systems, probing whether such scenarios truly demand quantum computational power or if we are merely applying a quantum solution to problems that may not fundamentally require it.

In Chapter 8, we examine the effect of disorder in quantum dynamics, a ubiquitous feature arising from imperfections in fabrication, control, or the environment of the quantum device. We develop an analytical framework that enables the exact calculation of disorder-averaged dynamics for a broad class of quantum systems governed by periodic Hamiltonians. In Chapter 9, we explore whether different complexity markers, such as entanglement entropy, fractal dimension, and stabilizer Rényi entropy, respond uniformly when transitioning between chaotic and integrable regimes, or if there exist intermediate phases where these markers diverge, labeling the same quantum state as resourceful in one context and free in another.

The chapters in this thesis were developed as independent projects, each addressing specific questions within the field of quantum technologies. Despite this, a unifying theme emerges when viewed through the lens of quantum resources. By identifying conceptual similarities—such as the role of entanglement, nonstabilizerness, and other resource measures in optimization, as well as in disordered systems—we bring together diverse results under a common framework. These connections are visually represented in the cover illustration (Fig. 1.1), with further details provided in the caption.

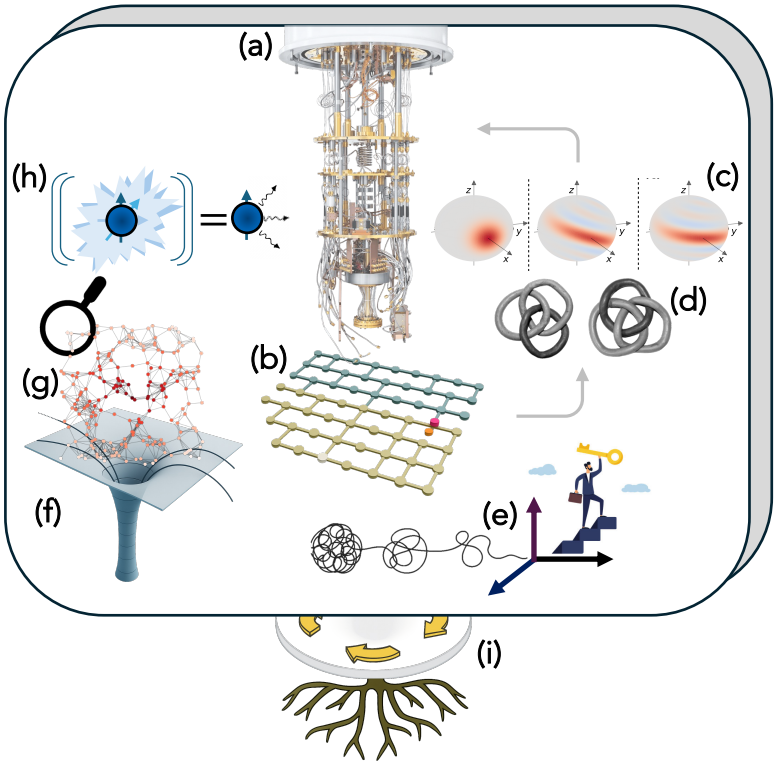

Figure 1.1. Cover illustration: Visual representation of the thesis: **(a)** A superconducting quantum computer (image taken from [94]) with **(b)** qubit layouts representing Chapter 6, where the quantum circuit is being run (motivated from Fig. 6.16, [95]), to understand the resource requirements of the hardware part of quantum optimization, either **(c)** via squeezing (see Chapter 4) or magic (see Chapter 7) generated in the process of QAOA, or **(d)** multipartite entanglement in quantum annealing (see Chapter 5) (image taken from [96]). **(e)** A recurring theme throughout the thesis is the exploration of how various quantum resources contribute to optimization success (right side) and relate to the complexity of chaotic systems (left side) [95]. **(f)** An artist's impression of the spacetime around a black hole, showing the strong curvature due to the high gravitational mass [95]. **(g)** The Sachdev-Ye-Kitaev model at low-temperature known to share similar chaotic behavior as a black hole [95, 97], is shown as a cartoon model of randomly interacting particles (Chapter 9), which can also represent the spin-glass model (Chapter 7) (image taken from [98]). **(h)** Among all these particles, consider a single particle under disorder, and in Chapter 8, we observe how a closed disorder system behaves like an open system. **(i)** All such analyses on resources, benchmarking, and complexity in quantum technology, from quantum optimization to quantum many-body physics, are rooted in the quantum informational notion of quantum resources (Chapter 2) (figure motivated from [99]).

Part I

Background

Chapter 2

Quantum resources

unification of quantumness

Quantum mechanics provides a framework to describe physical phenomena that often defy classical explanations. Concepts such as entanglement have no classical analogs and only become meaningful in the quantum regime. In this light, it becomes both natural and necessary to ask: what exactly makes quantum systems different and possibly resourceful? Identifying and characterizing the aspects of physical systems that enable such distinction leads to the notion of quantum resources. This perspective not only deepens our understanding of quantum phenomena but also guides the development of applications by framing them within the unifying structure of quantum resource theories. This process can sometimes reveal insights beyond what could have been gained by studying the phenomena individually and allows us to exploit such properties as resources in quantum technological applications.

For example, quantum entanglement was once a topic of philosophical debate during the first quantum revolution. However, once recognized as a valuable resource, it became the essential driving force behind numerous quantum information tasks, e.g., quantum simulation, quantum computation, quantum metrology, quantum communication, quantum cryptography, etc., in the second quantum revolution.

Given the success of the resource theory of entanglement, it is natural to explore other physical phenomena that can also be recognized as valuable resources. Beyond well-understood bipartite entanglement, this thesis will consider multipartite entanglement, quantum magic or nonstabilizerness (in the context of quantum computation), quantum Fisher information, and non-Markovianity, all of which will be discussed in detail in this chapter. The classic review by Chitambar and Gour [47] serves as our primary reference.

2.1 General structure of resource theory

Basic economic principles suggest that an object gains value when it is not readily accessible [47]. For instance, diamonds are deemed valuable precisely because they are rare in nature. In this way, value is inherently a relative concept. A resource theory builds on this idea by identifying which operations are considered free or restrained in a given context and then examining what can be achieved under those constraints. Any object that cannot be created using only free operations is then classified as a resource.

Each quantum resource theory is structured upon two objects: free states and free operations [47]. Free states are those quantum states that can be 'easily' created within the defined framework, and free operations represent quantum manipulations that can be effortlessly carried out. Thus, it does not encompass all quantum mechan-

ically allowed physical processes, and only certain states can be prepared freely. Any states that are not free are then called a 'resource' state. In this way, by identifying the free states and free operations, resource theory also classifies every quantum state as either free or a resource. To compare with a real-life example, see Fig. 2.1.

Quantum resource theory

Definition 1. The pair $\mathcal{R} = (\mathcal{F}, \mathcal{O}_\mathcal{F})$, consisting of free states ($\mathcal{F}$) and a set of completely positive and trace-preserving (CPTP) operations[a] ($\mathcal{O}_\mathcal{F}$), known as free operation, is called a *quantum resource theory* (QRT) if the free operations map any free state to another free state,

$$\Lambda : \rho \in \mathcal{F} \mapsto \tilde{\rho} \in \mathcal{F}, \quad \forall \Lambda \in \mathcal{O}_\mathcal{F} \,. \tag{2.1}$$

[a]See Sec. 2.8.1 for the definition of CPTP operations.

Definition 1 is considered the golden rule of QRT. However, in practice, one has to understand the details that are hidden behind such an intuitive definition. For example, the state ρ and $\tilde{\rho}$ may belong to two different systems. In general, $\mathcal{O}_\mathcal{F}$ maps two physical system A and B, with corresponding Hilbert spaces $\mathcal{H}_A$ and $\mathcal{H}_B$, i.e., $\mathcal{O}_\mathcal{F}(A \to B) \equiv \mathcal{O}_\mathcal{F}(\mathcal{H}_A \to \mathcal{H}_B) \subset \mathcal{Q}(A \to B)$, where $\mathcal{Q}$ denotes the set of all quantum channels from A to B. From the def. 1, one can ensure that (1) $\mathcal{O}_\mathcal{F}(A \to A)$ contains the identity map id^A, i.e., doing nothing is free, and (2) if $\Phi(A \to B) \in \mathcal{O}_\mathcal{F}$, and $\Lambda(B \to C) \in \mathcal{O}_\mathcal{F}$, then $\Lambda \circ \Phi(A \to C) \in \mathcal{O}_\mathcal{F}$, i.e., the free operations can be performed in composition as many times as one wants without any cost. Thus, there is no way free operations can create a resource state.

In a QRT, the set $\mathcal{F}(\mathcal{H}) \subset \mathcal{S}(\mathcal{H})$ are thus *free states*, and $\mathcal{S}(\mathcal{H}) \setminus \mathcal{F}(\mathcal{H})$ are called *resource states* or *static resources*, where $\mathcal{S}(\mathcal{H})$ are the set of valid density matrices on $\mathcal{H}$. Similarly, as $\mathcal{O}_\mathcal{F}$ is called *free operation*, and the rest of the CPTP maps are called *dynamical resources*.

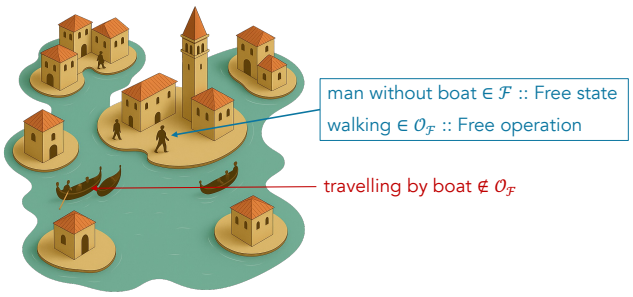

Figure 2.1. Island of Freedom, and Canal of Cost. A man can walk freely within his domain, operating without constraint. But beyond his island lies potential he cannot reach unaided. To cross the water, he must acquire a resource: a boat, and perform a resource-bound operation: rowing. Here, the resource theory $\mathcal{R}$ =(man without boat, walking).

In the experimental scenario, free operations are considered more fundamental, despite the equal footing of both free states and free operations in the definition of a QRT. Because, for an experimentalist, even the free states are not provided for granted, and hence they must be able to prepare the initial free states using free operations. Mathematically also, the free states are an induced mapping of free operations, i.e., $\mathcal{F}(\mathcal{H}) := \mathcal{O}_\mathcal{F}(\mathbb{C} \to \mathcal{H})$. However, in the theoretical sense, multiple free operations can be considered given the same free states, and thus, in a QRT, one needs the pair to define a concrete theory. Although the definition of a QRT does not include the definition of a resource state, it is indirectly implied through it. There are

several ways to have a resourceful operation. For example, a free operation together with a resource state (σ) can become a resourceful operation (dynamical resource) on a free state, i.e., given $\sigma \notin \mathcal{F}(B)$, there may exists free operation $\Phi \in \mathcal{O}_F(AB)$, such that $\Phi(\rho \otimes \sigma) = \Lambda(\rho)$, where $\Lambda \notin \mathcal{O}_\mathcal{F}(A)$, although $\rho \in \mathcal{F}$. One well-known example is quantum teleportation (Λ) with entangled state (σ) [100].

Often in quantum applications, one expects to amplify the quantum effects by considering a bigger system size. However, the isomorphism $\mathbb{C}^2 \otimes \mathbb{C}^2 \cong \mathbb{C}^4$ does not translate into the same set of free states or operations. For example, a system of 2 qubits, although it has the same Hilbert space dimension (i.e., 4) as 1 ququart, can have a different QRT compared to a 1 ququart. On the other hand, within the tensor-product structure, one can relabel the Hilbert space, i.e., the density matrices acting on $\mathcal{H}_A \otimes \mathcal{H}_B$ represent the same physical states as the density matrices acting on $\mathcal{H}_B \otimes \mathcal{H}_A$. As most operations in quantum mechanics can be represented by the tensor-product structure, it is crucial to understand when a QRT can also follow this structure.

Tensor-product structure

Definition 2. A QRT $\mathcal{R} = (\mathcal{F}, \mathcal{O}_\mathcal{F})$ admits a *tensor-product structure* if

1. $\mathcal{O}_\mathcal{F}$ is 'completely free', i.e., it remains free when acted on just one part of any joint system: $\Phi \in \mathcal{O}_\mathcal{F}(A \to B) \Rightarrow \mathrm{id}^C \otimes \Phi \in \mathcal{O}_\mathcal{F}(CA \to CB)$, where id^C is the identity map on C.
2. Appending free states is a free operation: $\Phi_\sigma(\rho) := \rho \otimes \sigma \in \mathcal{O}_\mathcal{F} \quad \forall \rho \in \mathcal{F}$.
3. Discarding a system is a free operation: $\mathcal{O}_\mathcal{F}(\mathcal{H} \to \mathbb{R})$ is not empty.

Corollary 1. The tensor-product structure has several important consequences:

- (1) $\Rightarrow$ If $\Phi, \Phi' \in \mathcal{O}_\mathcal{F}$, then $\Phi \otimes \Phi' = (\mathrm{id} \otimes \Phi') \circ (\Phi \otimes \mathrm{id}) \in \mathcal{O}_\mathcal{F}$.
- (3) $\Rightarrow$ Trace of a system is a free map.
- (1) + (3) $\Rightarrow$ Partial trace $\mathrm{Tr} \otimes \mathrm{id}$ is free.
- (2) + partial trace $\Rightarrow$ If $\rho, \sigma, \rho \otimes \sigma \in \mathcal{F}$, then ρ can be converted to σ by free operation, and vice-versa.
- Inter-convertibility + (1) $\Rightarrow$ If $\rho, \sigma \in \mathcal{F}$, then $\rho \otimes \sigma \in \mathcal{F}$. This implies $\mathcal{F}(A) \otimes \mathcal{F}(B) \subset \mathcal{F}(AB)$.
- Partial trace is free $\Rightarrow$ If $\rho^{AB} \in \mathcal{F}$, then $\rho^A, \rho^B \in \mathcal{F}$.

Most physically motivated QRTs follow a tensor-product structure, such as entanglement, coherence, etc. However, Bell non-locality may not admit such a structure, for example, even if $\rho, \sigma \in \mathcal{F}$, $\rho \otimes \sigma$ may not [101].

2.2 Types of resource theories

In addition to the definition of QRTs, these theories may also possess extra mathematical structures. Theories that share a similar structure can utilize common mathemati-

cal tools and physical insights. We briefly mention some of these here for completeness, as the thesis explores some examples of them in more detail later.

Convex resource theories. A QRT is called *convex*, if the free operation $\mathcal{O}_\mathcal{F}$ is convex, i.e.,

$$\forall \Phi, \Lambda \in \mathcal{O}_\mathcal{F} \Rightarrow p\Phi + (1-p)\Lambda \in \mathcal{O}_\mathcal{F}, \qquad p \in [0,1]\,. \tag{2.2}$$

This also implies that the set of free states is convex. Example- QRT of entanglement, coherence, asymmetry. However, sometimes convex resource theories can be defined through states, i.e., if the free states are convex.

Non-convex resource theories. An example is the QRT of non-Gaussianity in continuous variable quantum systems, where the sets of Gaussian states and Gaussian operations are not convex [102].

2.3 Quantifying through resource measures

Besides the significant effort involved in generating resource states or implementing resource operations, it is equally important to verify whether the quantum system exhibits the desired quantum features. A key challenge often lies in quantifying the available resources, which is crucial for drawing meaningful conclusions about the system. In this context, QRT offers various methods for constructing such measures. We will discuss some of these approaches in this section, as they provide the foundation for the measures used in our research analysis.

2.3.1 Axiomatic approach

We first discuss some necessary and desirable properties that the resource measures should satisfy. A true measure should be able to quantify the resource of a density operator irrespective of its Hilbert space dimension in terms of a non-negative real value, and thus, the measure $f : \mathcal{S}(\mathcal{H}) \to \mathbb{R}_{\geq 0}$. However, such system-size independence can be relaxed, and often one can work on a fixed dimension and rescale it to compare different dimensions, such as the density of some measure. The two essential requirements are:

Vanishing for free states. Free states has 'no resource':

$$\rho \in \mathcal{F} \Rightarrow f(\rho) = 0\,. \tag{2.3}$$

The converse is called *faithfulness*, i.e., $f(\rho) = 0$ implies ρ is free. Although it is appealing to be considered in the axiom, a certain resource state $\sigma \notin \mathcal{F}$ may have no operational advantage over a free state, and one would like to attribute $f(\sigma) = 0$, thus not considered as essential. For example, distillable entanglement vanishes for all bound entangled states [103].

Monotonicity. f cannot increase under free operation:

$$f(\rho) \geq f(\Phi(\rho)), \quad \forall \rho \in \mathcal{S}(\mathcal{H}), \quad \Phi \in \mathcal{O}_{\mathcal{F}}\,. \tag{2.4}$$

This is a direct implication of Def. 1. Besides the free operation, sometimes one would like to consider that quantum measurement also does not increase the measures in some QRTs. For example, in QRTs of entanglement and magic, quantum measurement in the form of quantum-classical (QC) maps $\Phi(\cdot) = \sum_i \Phi_i(\cdot) \otimes |i\rangle\langle i|$ is physically allowed. Such a function f is called

$$\text{convex linear} \Leftrightarrow f\left(\sum_i p_i\sigma_i \otimes |i\rangle\langle i|\right) = \sum_i p_i f\left(\sigma_i \otimes |i\rangle\langle i|\right), \quad \forall \sigma^{QC} = \sum_i p_i\sigma_i \otimes |i\rangle\langle i|\ . \tag{2.5}$$

The von Neumann entropy [Eq. (2.35)] has the property. Given the f is convex linear, then monotonicity [Eq.(2.4)] would further implies,

$$f(\rho) \geq \sum_i p_i f(\sigma_i \otimes |i\rangle\langle i|)\,, \tag{2.6}$$

i.e., non-increasing on average under any flagged-outcome quantum measurement (projective measurement). Now, if appending and discarding classical flags is also a free operation (e.g., tensor product structure) in the QRT, then $f(\rho_i) = f(\rho_i \otimes |i\rangle\langle i|)$, and then Eq. (2.6) would become

$$f(\rho) \geq \sum_i p_i f(\sigma_i), \quad \forall \rho \mapsto \sum_i \Phi_i(\rho) \otimes |i\rangle\langle i|\ . \tag{2.7}$$

By rewriting the same equation, one finds [104],

$$\text{Strong monotonicity}: \quad f(\rho) \geq \sum_i \mathrm{Tr}[\Phi_i(\rho)] f\left(\frac{\Phi_i(\rho)}{p_i}\right)\,. \tag{2.8}$$

Such *strong monotonicity* conditions imply f is non-increasing even after post-selection or multiple flagged outcomes.

Convexity. f is convex under mixing states,

$$f(\sum_i p_i\rho_i) \leq \sum_i p_i f(\rho_i)\,, \tag{2.9}$$

i.e., by mixing states, one cannot increase the amount of resource. Note, this makes sense, as mixing in this sense means losing information. However, such property is not essential, but rather convenient when computing some functions within QRTs.

Sub-additivity. f is sub-additive

$$f(\rho \otimes \sigma) \leq f(\rho) + f(\sigma) \quad \forall \rho, \sigma\,, \tag{2.10}$$

i.e., two states together cannot have more resources than the sum of their resources. Although this feels intuitive to include as an essential condition, some measures may not follow this, for example, non-locality [101]. When the equality holds, f is called

additive. Such a property simplifies calculation and provides reasoning, for example, having N states has the same resources as having 1 state. In Chapter 7, it helps us to infer results as stabilizer Rényi entropy has this property (sec. 7.5.1). Although most measures do not have additivity, by regularization, one can construct functions that are additive on multiple copies of the same state,

$$f^{\infty}(\rho) = \lim_{n\to\infty} \frac{1}{n} f(\rho^{\otimes n}) \,, \tag{2.11}$$

provided the limit exists. One sufficient condition for a limit's existence is a weaker form of sub-additivity: $f(\rho^{\otimes(m+n)}) \leq f(\rho^{\otimes m}) + f(\rho^{\otimes n}), \quad \forall \rho, m, n$ [105]. If f is resource monotone, f^{∞} is also.

Asymptotic continuity. f is asymptotically continuous if [106]

$$|f(\rho) - f(\sigma)| \leq K\epsilon \log\left[\dim(\mathcal{H})\right] + c(\epsilon), \quad \epsilon = \frac{1}{2}||\rho - \sigma||_1; \ \forall \rho, \sigma \in \mathcal{S}(\mathcal{H}) \,, \tag{2.12}$$

where K is some constant, and $c(\epsilon) \to 0$ as $\epsilon \to 0$. The trace norm is defined as $||M||_1 = \mathrm{Tr}\sqrt{M^\dagger M}$. Physically, it implies that if one state is perturbatively close to another state, then one would naturally anticipate their resource content to be similarly close to each other. Of course, the difference will increase as the system size increases, hence $\log\left[\dim(\mathcal{H})\right]$. For example, von Neumann entropy S_{vN} is an asymptotically continuous function, as ensured by the Fannes-Audenaert inequality [107, 108],

$$|S_{\mathrm{vN}}(\rho) - S_{\mathrm{vN}}(\sigma)| \leq \epsilon \log\left[\dim(\mathcal{H}) - 1\right] + h(\epsilon) \,, \tag{2.13}$$

where $h(x) = -x\log x - (1-x)\log(1-x)$, also known as binary entropy function. Such a property is often useful when proving bounds on the measures using perturbation theory.

2.3.2 General distance-based constructions

One can define resource measures by quantifying 'how far' the state is from the set of free states. Here, instead of using standard metric measures for distance, one may use monotonicity as a defining quality. A distance function $d : \mathcal{S}(\mathcal{H} \otimes \mathcal{H}) \to \mathbb{R}_{\geq 0}$ is called

$$\textit{contractive} \text{ under all CPTP maps } \Phi \Leftrightarrow d(\rho,\sigma) \geq d(\Phi(\rho), \Phi(\sigma)), \quad \forall \rho, \sigma \in \mathcal{S}(\mathcal{H}) \,. \tag{2.14}$$

Then, one has to minimize the distance from all free states to get a reliable measure [1],

$$\mathcal{R}_d(\rho) = \inf_{\sigma \in \mathcal{F}(\mathcal{H})} d(\rho, \sigma) \,. \tag{2.15}$$

It is obvious, that $\mathcal{R}_d = 0, \forall \rho \in \mathcal{F}$, and monotonicity is also satisfied as

$$\mathcal{R}_d(\Phi(\rho)) = \inf_{\tau \in \mathcal{F}} d(\Phi(\rho), \tau) \leq \inf_{\sigma \in \mathcal{F}} d(\Phi(\rho), \Phi(\sigma)) \leq \inf_{\sigma \in \mathcal{F}} d(\rho, \sigma) = \mathcal{R}_d(\rho) \,. \tag{2.16}$$

[1] Note that we do not use min, rather we use inf, because it is possible that the minimum may not be found within the set. However, when the set $\mathcal{F}(\mathcal{H})$ is closed, each infimum is attained by some free state σ.

The first inequality implies that measuring the distance from a state $\Phi(\sigma)$ cannot yield a smaller value than measuring the distance from a free state $\tau \in \mathcal{F}$, and the second inequality uses d as contractive under Φ [Eq.(2.14)]. Thus, it becomes clear how one can use a contractive distance function to define the resource measure. Quantum Fisher Information (QFI) is an example of such a contractive measure (sec. 2.6.3).

2.3.3 Entropic measures

Most entropic measures are some generalization of the relative Rényi entropies from classical information theory [109]. The *quantum relative Rényi entropy* is defined by [110]

$$D_\alpha(\rho||\sigma) = \frac{1}{1-\alpha}\log\left[\mathrm{Tr}(\rho^\alpha\sigma^{1-\alpha})\right], \quad 0<\alpha<1\,. \tag{2.17}$$

Often, we deal with only the limiting case,

$$D_0(\rho||\sigma) = -\log\left[\mathrm{Tr}(\Pi_\rho\sigma)\right], \text{ where } \Pi_\rho \text{ projects onto supp}(\rho), \tag{2.18}$$

$$\lim_{\alpha\to 1} D_\alpha(\rho||\sigma) \to S_{\mathrm{rel}}(\rho||\sigma) := -\mathrm{Tr}[\rho(\log\sigma - \log\rho)], \tag{2.19}$$

where $S_{\mathrm{rel}}(\rho||\sigma)$ is the quantum relative entropy [111]. The well-known Rényi entropy can be obtained by taking $\sigma = \mathbb{I}_{\mathcal{H}}$:

$$S_\alpha(\rho) := -D_\alpha(\rho||\mathbb{I}_{\mathcal{H}}) = \frac{1}{1-\alpha}\log\left[\mathrm{Tr}(\rho^\alpha)\right]. \tag{2.20}$$

At $\alpha = 1$, we can recover von Neumann entanglement entropy,

$$S_{\mathrm{vN}}(\rho) = -D_1(\rho||\mathbb{I}_{\mathcal{H}}) = -\mathrm{Tr}[\rho\log\rho]\,. \tag{2.21}$$

One crucial property of $D_\alpha(\rho||\sigma)$ is that they are contractive under CPTP maps, i.e.,

$$D_\alpha(\rho||\sigma) \geq D_\alpha(\Phi(\rho),\Phi(\sigma)), \quad \alpha\in[0,1]\,. \tag{2.22}$$

This is also known as a data processing inequality [110]. Now, using this contractive property, we can define resource measures for any QRT,

$$\mathcal{R}_\alpha(\rho) := \inf_{\sigma\in\mathcal{F}} D_\alpha(\rho||\sigma), \quad \text{for } \alpha\in[0,1]\,. \tag{2.23}$$

Similarly, the *relative entropy of a resource* is defined as

$$\mathcal{R}_{\mathrm{rel}}(\rho) = \inf_{\sigma\in\mathcal{F}} S_{\mathrm{rel}}(\rho||\sigma)\,. \tag{2.24}$$

Interestingly, $\mathcal{R}_{\mathrm{rel}}$ is asymptotically continuous [Eq. (2.12)] when the maximally mixed state is free in the QRT [112].

2.3.4 Geometric measures

Relative entropy measures, while useful as resource monotones, are not proper metrics since they do not satisfy the triangle inequality. In some cases, one may be interested in using a measure with geometric interpretation, i.e., far from free states means more resources. It is indeed a special scenario under general distance-based constructions

(Sec. 2.3.2), which are contractive under CPTP. One such example is *trace distance of resource*,

$$\mathcal{R}_{\mathrm{Tr}}(\rho) = \inf_{\sigma\in\mathcal{F}} D_{\mathrm{Tr}}(\rho,\sigma) = \inf_{\sigma\in\mathcal{F}} \frac{1}{2}||\rho-\sigma||_1 \,. \tag{2.25}$$

Operationally, the trace distance quantifies how distinguishable two states are: for a system prepared in either state ρ_0 or ρ_1 with probabilities p_0 and p_1, the minimum error in identifying the correct state decreases as the distinguishability between the states increases, and the probability is given by $\frac{1}{2}(1-||p_0\rho_0-p_1\rho_1||_1)$ (*Holevo-Helström theorem*) [113, 114].

Similarly, using the Bures metric, $D_B(\rho,\sigma) = \sqrt{2}\sqrt{1-F(\rho,\sigma)}$, one can also define the Bures distance of resource measure as its infimum,

$$\mathcal{R}_B(\rho) = \inf_{\sigma\in\mathcal{F}} D_B(\rho,\sigma) \,. \tag{2.26}$$

Here, $F(\rho,\sigma)$ is the Uhlmann fidelity between two states, defined as $(\mathrm{Tr}\sqrt{\sqrt{\rho}\sigma\sqrt{\rho}})^2$, and for the pure states $F(|\psi\rangle, |\phi\rangle) = |\langle\psi|\phi\rangle|^2$.

As both the trace-distance and Bures metric are true metrics, these are called geometric measures. However, one can directly minimize the fidelity $F(\rho,\sigma)^2$ as a geometric measure, which historically happened in entanglement [115, 116], and then generalized as the geometric measure. In an arbitrary QRT,

$$\mathcal{R}_{\mathrm{G}} = \inf_{\sigma\in\mathcal{F}} \left(1-F(|\psi\rangle\langle\psi|,\sigma)^2\right) = \frac{1}{4}\mathcal{R}_B(|\psi\rangle)^4 \,. \tag{2.27}$$

If $\mathcal{F}(\mathcal{H})$ is a convex set with pure states being extreme points, then the infimum is always attained by a pure state, $\sigma = |\phi\rangle\langle\phi|$. In the entanglement theory, it is also the case that minimization over product states is enough (see Sec. 2.6.4). In Sec 2.6.4, we use such a geometric measure [Eq. (2.66)] to measure multipartite entanglement. Although $\mathcal{R}_{\mathrm{G}}$ does not have an operational meaning like trace distance, it is still valuable for deriving bounds, such as

$$1-\sqrt{1-\mathcal{R}_{\mathrm{G}}(\rho)} \le \mathcal{R}_{\mathrm{Tr}}(\rho) \le \sqrt{\mathcal{R}_{\mathrm{G}}(\rho)} \,, \tag{2.28}$$

using the following inequality: $1-F(\rho,\sigma) \le D_{\mathrm{Tr}}(\rho,\sigma) \le \sqrt{1-F(\rho,\sigma)^2}$ [117].

2.4 Entanglement as a resource

In classical physics, it is easy to correlate distant systems by sharing information and acting on it locally. For example, Alice flips a coin and sends the result to Bob. If it is a head, he turns on a red light; if tails, a blue one. Repeating this many times creates a shared pattern based on a probability distribution. This approach is called Local Classical Systems, Operations, and Classical Communication (LCSOCC).

Quantum mechanics allows for more powerful correlations. One key framework is Local Operations and Classical Communication (LOCC), where local systems are quantum rather than classical. So, every LOCC involves a local measurement operation, followed by a broadcast of the measurement outcome, which can be written as Kraus-operator notation (see Sec. 2.8.1):

$$\Lambda(\cdot) = \sum_k \left(\otimes_{i=1}^N M_{k,i}^{A_i}\right)(\cdot)\left(\otimes_{i=1}^N M_{k,i}^{A_i}\right)^\dagger , \tag{2.29}$$

where $M_{k,i}^{A_i}$ acts on A_i for a N-partite state space $\mathcal{H} = \otimes_{k=1}^N \mathcal{H}^{A_k}$. The QRT of entanglement can be defined using such LOCC as free operation [84, 118]. Any states obtained by LOCC would impose a tensor product structure (LO) and probabilistic mixture (CC) of the following form

$$\rho = \sum_{k=1}^{n} p_k \rho_{1,k}^{A_1} \otimes \rho_{2,k}^{A_2} \otimes \cdots \otimes \rho_{N,k}^{A_N} , \tag{2.30}$$

where $\rho_{i,k}^{A_i}$ is an arbitrary state for party A_i. Any state having such a form is called a *separable* state, which forms the set of free states called SEP, and LOCC keeps SEP invariant. As every convex combination of separable states is also separable, the QRT is convex. Any state not belonging to SEP is called *entangled*. Thus, operationally, entanglement can be defined as a resource in this QRT (see Fig. 2.2).

Quantum Entanglement

Definition 3. Entanglement is a characteristic of a composite physical system that cannot be created or enhanced through local (quantum) operations and classical communication (LOCC).

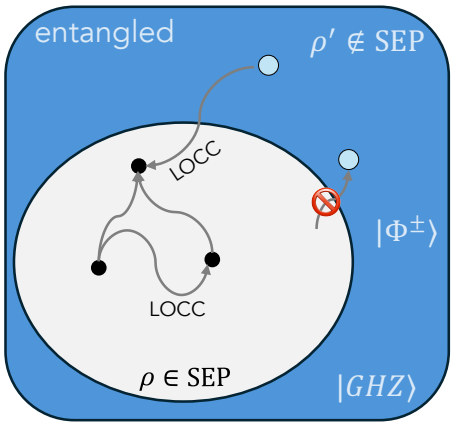

Figure 2.2. The set of quantum states contains the subset of separable states SEP. The LOCC operations map states within the set of separable states (SEP) to other states that also remain within SEP. Entangled states lie outside this set, for example, the Bell state, the GHZ state, etc. LOCC can bring an entangled state (outside) to a separable state (inside). However, it cannot generate entanglement.

Deciding whether a state is in SEP or not is difficult; in fact, the problem is **NP-hard** [119] (see sec. 3.2.1 for complexity classes). Instead, traditionally, research has been pushed along identifying separability criteria, which are necessary but not sufficient conditions for a state to be separable [120]. It might seem that fully understanding the set of free operations would resolve the problem. However, determining whether a given map Λ belongs to the class of LOCC operations remains an open question. Note that the structure described by Eq. (2.29) for LOCC is not the only structure for the separability condition. For example, there exist separable maps that cannot be realized via LOCC, and such maps were initially introduced to illustrate the phenomenon known as *nonlocality without entanglement* [121]. Hence, to obtain interesting QRTs, one needs to consider free operations more powerful than LOCC.

2.5 Bipartite entanglement

Bipartite systems serve as a fundamental framework for studying entanglement. Historically, the EPR paradox [122] and the subsequent discovery of Bell inequalities [123] are also primarily concerned with such systems. Moreover, quantum technological applications such as dense coding [124], quantum key distribution [125], and quantum teleportation [100] rely heavily on bipartite entanglement as a key resource for enabling secure and efficient quantum communication.

Consider a bipartite system AB, admitting a tensor product structure

$$\mathcal{H}_{AB} = \mathcal{H}_A \otimes \mathcal{H}_B \,, \tag{2.31}$$

where each subsystem is a qudit. For a pure state,

$$|\psi\rangle = \sum_{i,j} c_{ij} \, |i\rangle_A \otimes |j\rangle_B \,, \quad |i\rangle_A \in \mathcal{S}(\mathcal{H}_A), |j\rangle_B \in \mathcal{S}(\mathcal{H}_B) \,. \tag{2.32}$$

The coefficient matrix c_{ij} can be simplified with a singular value decomposition (SVD), yielding a common Schmidt basis,

$$|\psi\rangle = \sum_k \lambda_k \, |k\rangle_A \otimes |k\rangle_B \,, \tag{2.33}$$

where λ_k are singular values, also known as Schmidt values in the context of quantum information, where SVD is also called the Schmidt decomposition of a state. Moreover, as the Schmidt values are the probability amplitude of the state, they fulfill the normalization condition, i.e., $\sum_k \lambda_k^2 = 1$.

Separable states have only one non-zero Schmidt value, hence $\lambda_0 = 1$, i.e., $|\psi\rangle = |\psi\rangle_A \otimes |\psi\rangle_B$. Such states can be obtained using LOCC, and belong to the set of free states $\mathrm{SEP}(\mathcal{H})$. Moreover, they do not contain any local correlation, and hence, one can claim that there is no loss of information when a separable state is restricted to one of the subsystems.

For an arbitrary state, one may not have the full information by looking at a subsystem. Thus, we can differentiate between a separable state and a non-separable state by quantifying the information content of the restricted subsystem state. For example, consider measuring $\hat{O}_A$ only on subsystem A: $\hat{O}_A \otimes \hat{\mathbb{I}}_B$ on $|\psi\rangle$,

$$\langle\psi| \, \hat{O}_A \otimes \hat{\mathbb{I}}_B \, |\psi\rangle = \sum_k \lambda_k \, \langle k|_A \, \hat{O}_A \, |k\rangle_A = \mathrm{Tr}\Big(\underbrace{\sum_k \lambda_k \, |k\rangle_A \, \langle k|_A}_{:=\rho_A} \, \hat{O}_A \Big) \,. \tag{2.34}$$

Thus, the restriction to a subsystem makes the pure state $|\psi\rangle$ a mixed state ρ_A. The *mixedness* of ρ_A, can be measured by its entropy, known as von Neumann entanglement entropy,

$$S_{\mathrm{vN}}(\rho_A) = -\sum_k p_k \log p_k \,. \tag{2.35}$$

Interestingly, one can see that the entanglement entropy depends on λ_k — probability amplitude shared between two subsystems, and thus indeed it contains the information of the indissociability of two subsystems, i.e., how correlated two systems are, and how

one can lose information if dissociated. Note that the operation $\rho \to \rho_A$, i.e., acting only on one part of the joint system, and then discarding the subsystem, is still a free operation (see Definition. 2.1), thus it does not change the resource contents. For a product state, as $\lambda_k = 1$, $S_{\text{vN}} = 0$ for any bipartitions.

The Bell states are the four maximally entangled two-qubit states and form an orthonormal basis for the two-qubit Hilbert space:

$$|\Phi^{\pm}\rangle = \frac{1}{\sqrt{2}}(|00\rangle \pm |11\rangle), \quad |\Psi^{\pm}\rangle = \frac{1}{\sqrt{2}}(|01\rangle \pm |10\rangle). \tag{2.36}$$

Each Bell state has equal absolute value of Schmidt coefficients $\left(\frac{1}{\sqrt{2}}, \frac{1}{\sqrt{2}}\right)$, indicating maximal entanglement.

Von Neumann entanglement entropy follows some of the additional properties mentioned in Sec. 2.3.1. For example, subadditivity. For a system with two subsystems A and B,

$$S_{\text{vN}}(\rho_{AB}) \leq S_{\text{vN}}(\rho_A) + S_{\text{vN}}(\rho_B) \tag{2.37}$$

We utilize the fact that the quantum relative entropy [Eq. (2.19)] is non-negative for states. Consider $\sigma_{AB} = \rho_A \otimes \rho_B$, then:

$$\begin{aligned} S_{\text{rel}}(\rho_{AB} \| \rho_A \otimes \rho_B) &= \text{Tr}\left[\rho_{AB}\left(\log \rho_{AB} - \log(\rho_A \otimes \rho_B)\right)\right] \\ &= \text{Tr}[\rho_{AB} \log \rho_{AB}] - \text{Tr}[\rho_{AB}(\log \rho_A \otimes I_B + I_A \otimes \log \rho_B)] \\ &= -S_{\text{vN}}(\rho_{AB}) + S_{\text{vN}}(\rho_A) + S_{\text{vN}}(\rho_B)\,. \end{aligned}$$

Now, using $S_{\text{rel}} \geq 0$, we can obtain Eq. (2.37).

2.6 Multipartite entanglement

The concept of bipartite entanglement extends naturally to multipartite systems. For instance, in a system composed of three subsystems, $\mathcal{H}_{ABC} = \mathcal{H}_A \otimes \mathcal{H}_B \otimes \mathcal{H}_C$, a state is said to be (fully) separable if it can be written as a product of individual states: $|\psi_A\rangle \otimes |\psi_B\rangle \otimes |\psi_C\rangle$. Any state that does not take this form is considered entangled. At first glance, this might appear to be a straightforward generalization. However, it raises an important question: *Is there a fundamental difference between entanglement in multipartite systems and the well-understood bipartite case*? The answer is yes that multipartite entanglement exhibits qualitatively richer and more complex behavior than bipartite entanglement [96]. Even three qubits show fundamentally new types of entanglement beyond Bell states [126].

2.6.1 Example of multipartite entangled states: GHZ, W, Dicke

To understand the possible entangled states with multiple qubits, we will follow a diagrammatic approach for the sake of visualization. Let's consider the 2^N computational basis states as the corners of the hypercube (see Fig. 2.3). In this way, every

edge is traversed by a Hamming distance[2] of 1. For the 2-qubit case (square), any superposition of two states forming an edge of the square is separable, but equal-weight superpositions of states represented by two corners on a diagonal give maximally entangled Bell states [Eq. (2.36)]. A Similar picture is easily generalized to the case of three qubits. Here we can see that superpositions of two states at Hamming distance one, belonging to the same edge of the cube are separable, and superpositions of states at a Hamming distance of two display bipartite entanglement.

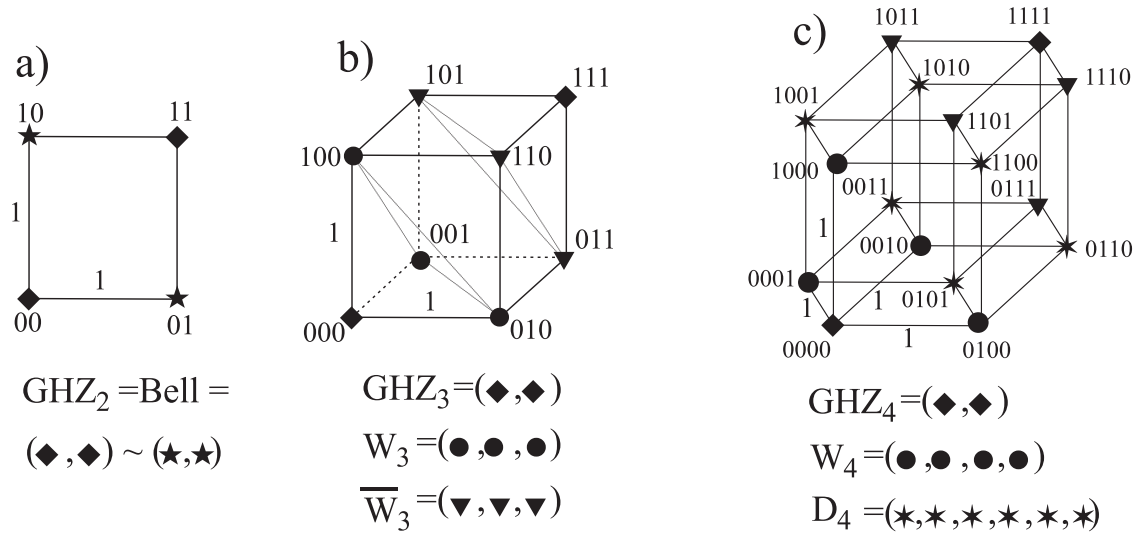

Figure 2.3. Distinguished pure states for systems of (a) two, (b) three, and (c) four qubits can be represented geometrically. In the case of two qubits, the Bell states correspond to pairs of opposite corners along a diagonal of a square. For three qubits, the Greenberger–Horne–Zeilinger (GHZ) state, $|GHZ_3\rangle = |000\rangle + |111\rangle$, is represented by two opposite corners along a main diagonal of a cube. Similarly, for four qubits, the GHZ state $|GHZ_4\rangle = |0000\rangle + |1111\rangle$ corresponds to two opposite corners of a hypercube. The states W_3 and $\bar{W}_3$, which are locally equivalent, are represented by two parallel triangles in the three-qubit case (b), while in the four-qubit case (c), the locally equivalent W_4 and $\bar{W}_4$ states correspond to two parallel tetrahedra. Additionally, the state labeled D_4 represents a four-qubit Dicke state (Taken from [96]).

Now consider the following state, which can be decomposed into an entangled state and a product state.

$$|\psi_{AB|C}\rangle = \frac{1}{\sqrt{2}}(|000\rangle + |110\rangle) = |\Phi^+_{AB}\rangle \otimes |0_C\rangle \ . \tag{2.38}$$

States that cannot be decomposed in this manner are said to possess genuine multipartite entanglement. One can rightfully guess that a superposition of two states corresponding to maximally distant corners (Hamming distance equals the number of qubits) may be highly entangled. This is indeed the case, and they are called Greenberger–Horne–Zeilinger (GHZ) states [127]:

$$|GHZ\rangle_N = \frac{1}{\sqrt{2}}\left(|0\rangle^{\otimes N} + |1\rangle^{\otimes N}\right). \tag{2.39}$$

[2]The Hamming distance between two binary strings of equal length is the number of positions at which the corresponding bits differ. It measures how many substitutions are needed to change one string into the other.

The three-qubit GHZ state was created in 1999 [128].

Another genuinely multipartite entangled state is the W state, formed by triangles for the 3-qubit case, or tetrahedra for the 4-qubit case (see Fig. 2.3), where each basis state has only one qubit in state 1 :

$$|W_3\rangle = \frac{1}{\sqrt{3}}\big(|001\rangle + |010\rangle + |100\rangle\big)\,, \tag{2.40}$$

$$|W_4\rangle = \frac{1}{2}(|0001\rangle + |0010\rangle + |0100\rangle + |1000\rangle)\,. \tag{2.41}$$

One can also observe that the superposition of permutationally invariant states can form entangled states, which are known as Dicke states. For example,

$$|D_4\rangle = \frac{1}{\sqrt{6}}(|1001\rangle + |1010\rangle + |1100\rangle + |0101\rangle + |0110\rangle + |0011\rangle). \tag{2.42}$$

More generically,

$$D_k^n = \binom{n}{k}^{-1/2} \sum_i P_i \left(|1\rangle^{\otimes k} \otimes |0\rangle^{\otimes (n-k)}\right). \tag{2.43}$$

Perseverance (fragility) of the entangled states

Given a different kind of multipartite entangled states, one may wonder if there is something different between them. One can perform a perseverance (fragility) analysis in the sense that, by tracing out any subsystem, we can determine whether it remains entangled (not fragile) or becomes a separable state (fragile) [See Fig. 2.4]. GHZ states are fragile, as they become separable after tracing out, which also means that all the entanglement is of a global nature. Interestingly, this property holds if and only if the state is already in Schmidt decomposable form [129]. On the other hand, the W state is more robust than the GHZ state, because after tracing out, an entangled mixed state remains, and it cannot be written as a superposition of less than three separable states [130]. Such fragility does not say if one state is more entangled than the other; instead, it shows that they are entangled in different ways. For instance, W and GHZ states cannot be transformed into each other by LOCC [130].

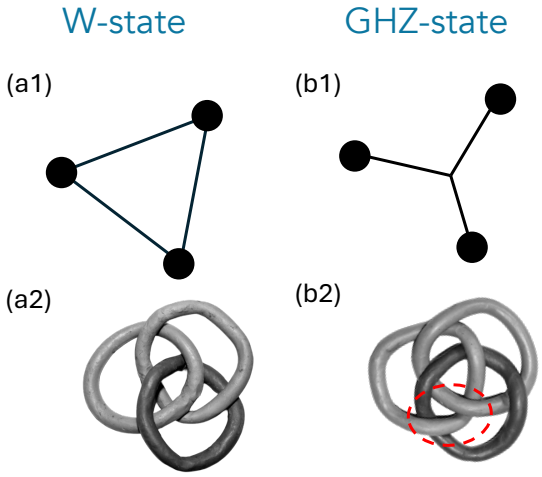

Figure 2.4. A schematic comparison of W and GHZ states is illustrated using strings and knots, where you can envision the fragility of the state. For the W state (a1, a2), tracing out one subsystem leaves the remaining two subsystems still entangled. In contrast, for the GHZ state, which can be represented by three objects connected by a single thread or by three rings, removing any one ring unlinks the others (b1, b2) [Adapted from [96]].

As more qubits are added, classification becomes increasingly difficult and relies on detailed knowledge of the states, making it hard to link to observable features. Instead, here we use a hierarchy of separability criteria that offers less structural detail but is more practical and scalable.

2.6.2 Partitions of many-body systems

Consider a quantum system composed of N-parties,

$$|\psi\rangle = \sum_{i_k} c_{i_1,\ldots,i_N} |i\rangle_1 \otimes \cdots \otimes |i\rangle_N \,, \tag{2.44}$$

where the state belongs to the Hilbert space $\mathcal{H} = \otimes_{k=1}^{N} \mathcal{H}_k$. Such a multipartite system is quite different from the bipartite case. As there are multiple subsystem choices, and entanglement explicitly relies on the subsystem, we require a systematic formalism to treat all possible partitions on equal footing. To understand the multipartite entanglement [131], the main question we ask is whether it is possible to cluster the N parties into n groups, for $n \leq N$, such that $|\psi\rangle$ is a product state with respect to the partition,

$$n\textbf{-separable:} \quad |\psi\rangle = |\phi_1\rangle \otimes |\phi_2\rangle \otimes \ldots |\phi_n\rangle \,. \tag{2.45}$$

If this is possible, then we can call $|\psi\rangle$ as *n-separable*. If it is N-separable, then it is a product state with respect to all subsystems, and hence we call such a state *fully separable*. On the other extreme, if the state is not even biseparable, then it is *genuine N-partite entangled*. However, some states are in neither of the above classes; instead, they are expressed as some superposition of various classes of entangled or separable states. In that case, we ask if a state $|\psi\rangle$ is producible by k-party entangled states, which let us define k-producible states. For instance, if we can write

$$k\textbf{-producible:} \quad |\psi\rangle = |\phi_1\rangle \otimes |\phi_2\rangle \otimes \cdots \otimes |\phi_m\rangle \,, \quad \forall\ |\phi_i\rangle \text{ containing maximally } k\text{-parties}, \tag{2.46}$$

we can call it k-producible, and it has to fulfill that $k \cdot m \geq N$[3]. In this way, k-producible implies it is enough to generate specific k-party entanglement to prepare $|\psi\rangle$. In the same way, we can say the converse statement that a state has *k-party entanglement*, if it is not producible by $(k-1)$-party entanglement, as it requires at least k-party entanglement. Formally, we can define,

$$k\textbf{-party entangled:} \ k\text{-producible, but not } (k-1)\text{-producible.} \tag{2.47}$$

For example, if a 6-qudit system can be written like

$$\underbrace{|\psi\rangle}_{\{1,2,3,4,5,6\}} = \underbrace{|\psi\rangle_{R_1}}_{\{1,2,3\}} \otimes \underbrace{|\psi\rangle_{R_2}}_{\{4\}} \otimes \underbrace{|\psi\rangle_{R_3}}_{\{5,6\}}, \tag{2.48}$$

it is called 3-producible, where the partition $P = \{R_1, R_2, R_3\}$ is with $R_1 = \{1,2,3\}$, $R_2 = \{4\}$, $R_3 = \{5,6\}$. If the $|\psi\rangle_{R_1}$ cannot be represented by further partition, then we can say $|\psi\rangle$ is 3-party entangled. Thus, the notion of multipartite entanglement stands on the idea of k-producible states.

[3]Note, this provides a way to relate m-separability and k-producibility.

Note that defining n-separability does not reveal some structures of the entanglement. For example, for large N, n-separability cannot distinguish whether the two partitions are of equal size or just one partition has one qubit and the other partition has a large, genuinely multipartite entangled state. Moreover, to tell about n-separability, one needs to know what N is. On the other hand, the notion of k-producibility, by design, can say 'how many parties are entangled'. Moreover, deciding whether a state is k-producible does not require knowledge of N, for example, if $k \ll N$ subsystems, one can still conclude if the system has k-party entanglement.

2.6.3 Multipartite entanglement through Fisher information

Entanglement plays a vital role in phase estimation, and hence in quantum metrology [132], where the task is to estimate a parameter shift θ as precisely as possible. If one uses a probe state of N classically correlated particles, it is possible to obtain a parameter uncertainty of $\Delta\theta \sim 1/\sqrt{N}$, whereas if an N-particle entangled state is used, the uncertainty can be further reduced to $1/N$. Thus, parameter uncertainty can be related to the number of particles being genuinely entangled.

Phase estimation. In a general phase estimation scenario, a probe state ρ is perturbed under O,

$$\rho \xrightarrow{O} \rho_\theta = e^{-i\theta O}\rho e^{i\theta O}, \tag{2.49}$$

where the operator O is known, and θ is unknown, and the goal is to estimate θ by studying the relation between ρ_θ and O. An estimator $\theta_{\text{est}}(\{\mu_i\}_m)$ is used depending on the results obtained from m-independent repeated measurements: $\{\mu_i\}_m = \{\mu_1, \ldots, \mu_m\}$, with mean $\langle\theta_{\text{est}}\rangle$, and variance $\Delta^2\theta_{\text{est}} = \langle\theta^2_{\text{est}}\rangle - \langle\theta_{\text{est}}\rangle^2$. This variance quantifies the precision of the estimator and provides a figure of merit for its quality. In case of an unbiased estimator, one can recover the true phase, $\langle\theta_{\text{est}}\rangle = \theta$, and in this case, the minimal standard deviation is bounded by something called Fisher information, according to the Cramér–Rao inequality [133, 134]

$$\textbf{Cramér–Rao inequality: } \Delta^2 \geq 1/F(\theta)\,, \tag{2.50}$$

where $F(\theta)$ is called Fisher information as we defined below.

Fisher information (classical). The expectation value $\langle\theta_{\text{est}}\rangle$ is dependent on the probability distribution obtained after repeated measurement,

$$\langle\theta_{\text{est}}\rangle = \sum_\mu p(\mu|\theta)\theta_{\text{est}}(\mu)\,. \tag{2.51}$$

Assuming an unbiased estimator, the quality of the estimation depends on the quality of the measurement scheme itself, which is related to the probability distribution $p(\mu|\theta)$. The Fisher information [135, 136] precisely defines a function that measures the sensitivity of $p(\mu|\theta)$ to changes of the parameter:

$$F(\theta) = \Delta^2[\underbrace{\partial_\theta \ln p(\mu|\theta)}_{=-s(\mu|\theta)}] = \sum_\mu p(\mu|\theta)\Big(\partial_\theta \ln p(\mu|\theta)\Big)^2\,. \tag{2.52}$$

Here $s(\mu|\theta)$ is the score of the distribution and measures the change in the likelihood function with respect to θ. As its mean is zero, the variance defines the simplest non-trivial measure of the properties of the score.

Quantum Fisher information. In the quantum case, the probability distribution is made of outcomes of positive operator-valued measurements (POVM), denoted as $\{\Pi_i\}$, such that

$$\sum_\mu \Pi_\mu = \mathbb{I}, \quad p(\mu|\theta) = \mathrm{Tr}(\rho(\theta)\Pi_\mu)\,. \tag{2.53}$$

By removing the explicit dependence on POVM, i.e., by optimizing over all possible POVMs, one obtains quantum Fisher information (QFI) as

$$F_Q(\rho_\theta) = \max_{\{\Pi_\mu\}} F(\theta)\,. \tag{2.54}$$

In this case, we can obtain [137, 138]

$$\textbf{quantum Cramér–Rao bound: } \Delta^2 \geq 1/F(\theta) \geq 1/mF_Q(\rho_\theta)\,. \tag{2.55}$$

where m is the number of independent repetitions. However, this way of defining QFI associates the classical outcomes of quantum experiments with precision. One can see the explicit connection to ρ_θ through the original definition of QFI, defined as a geometrical measure of statistical distinguishability in the space of states [137, 138].

We first define the symmetric logarithmic derivative (SLD) $L(\theta)$ implicitly through

$$\partial_\theta \rho(\theta) = \frac{1}{2}\{\rho(\theta), L(\theta)\} = \frac{1}{2}(\rho(\theta)L(\theta) + L(\theta)\rho(\theta)), \tag{2.56}$$

which is connected to the probability distribution as

$$\partial_\theta p(\mu|\theta) = \mathrm{ReTr}(\rho(\theta)\Pi_\mu L(\theta))\,. \tag{2.57}$$

Now we can use the definition of classical Fisher information [Eq. (2.52)],

$$\begin{aligned} F(\theta) &= \sum_\mu \frac{(\partial_\theta p(\mu|\theta))^2}{p(\mu|\theta)} = \sum_\mu \frac{(\mathrm{ReTr}(\rho(\theta)\Pi_\mu L(\theta)))^2}{\mathrm{Tr}(\rho(\theta)\Pi_\mu)} \\ &\leq \sum_\mu \frac{\left|\mathrm{Tr}\left(\sqrt{\rho}\sqrt{\Pi_\mu}\sqrt{\Pi_\mu}L(\theta)\sqrt{\rho}\right)\right|^2}{\mathrm{Tr}(\rho(\theta)\Pi_\mu)} \end{aligned} \tag{2.58}$$

$$(\text{Schwartz inequality}) \leq \mathrm{Tr}(\rho(\theta)L(\theta)^2)\,. \tag{2.59}$$

One can show that there is a POVM for which the above bound is attained,

$$F_Q[\rho(\theta)] = \mathrm{Tr}(\rho(\theta)L(\theta)^2)\,. \tag{2.60}$$

By inserting the particular form of $\rho(\theta)$ of Eq. (2.49), we obtain,

$$\textbf{QFI}: F_Q[\rho, O] = 2\sum_{\mu,\nu} \frac{\rho_\mu - \rho_\nu}{\rho_\mu + \rho_\nu}(\rho_\mu - \rho_\nu)|\langle\mu|O|\nu\rangle|^2, \tag{2.61}$$

where $\{|\mu\rangle\}$ basis diagonalizes ρ. For a pure state, it simplifies to the variance,

$$F_Q[|\psi\rangle\langle\psi|, O] = 4\sum_{\mu,\psi}|\langle\mu|O|\psi\rangle|^2 = 4(\langle\psi|O^2|\psi\rangle - \langle\psi|O|\psi\rangle^2)\,. \tag{2.62}$$

Relation between k-party entanglement and F_Q. The relation between QFI and k-partite entanglement can be understood by computing the maximum QFI of a k-producible state, where one can consider the operator $\hat{O}$ as some linear operator of Pauli matrices, for example,

$$\hat{O}_{\text{lin}} = \frac{1}{2}\sum_{l=1}^{N}\vec{n_l}\cdot\vec{\sigma_l} = \frac{1}{2}\sum_{l}\alpha_l\sigma_x^{(l)} + \beta_l\sigma_y^{(l)} + \gamma_l\sigma_z^{(l)}\,. \tag{2.63}$$

For k-producible states and an arbitrary linear operator $\hat{O}_{\text{lin}}$, the QFI is bounded by [139, 140]

$$F_Q^{k+1}\textbf{ criterion: }\; F_Q[\rho_{k-\text{prod}}, O_{\text{lin}}] \leq sk^2 + r^2, \tag{2.64}$$

where $s = \lfloor\frac{N}{k}\rfloor$ and residue $r = N - sk$. Hence, a violation of the bound implies $(k+1)$-partite entanglement. Thus, utilizing the inequality, one can estimate that at least k-partite entanglement is present in the state (see Fig. 2.5).

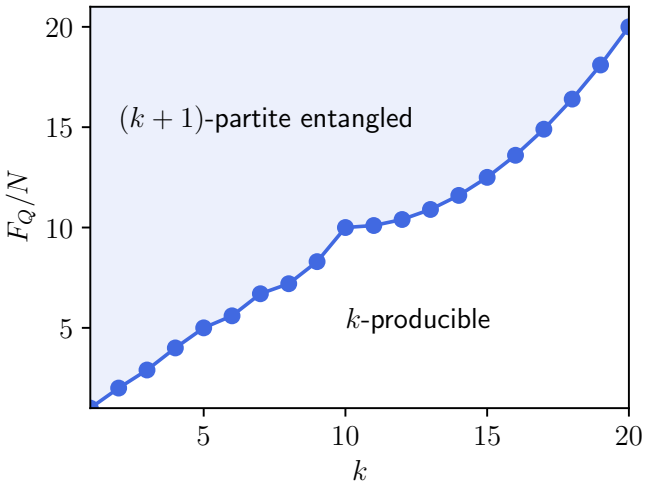

Figure 2.5. F_Q^{k+1} criterion. The solid line denotes the bound, which provides the bound for $k+1$-partite entanglement. Larger k-party entanglement requires higher QFI density. Note that to obtain the same k-partite entanglement, a larger N would require a higher F_Q.

2.6.4 Generalized geometric measure of entanglement

The Generalized Geometric Measure of entanglement (GGM) of entanglement generalizes the notion of geometric measure of entanglement and quantifies genuine multipartite entanglement [115, 116, 141–143]. Intuitively, the GGM measures the shortest distance between a quantum state and the set of product states [see Fig. 2.6(a)]. Formally, we can define a hierarchy of geometric measures G_k with $2 \leq k \leq N$ of a N-party pure quantum state $|\psi\rangle$ as the minimum distance between $|\psi\rangle$ and the set $\mathcal{S}_k$ of k-separable states $|\pi\rangle = |\psi_1\rangle\otimes|\psi_2\rangle\otimes\cdots\otimes|\psi_k\rangle$, given by

$$G_k(|\psi\rangle) = \min_{|\pi\rangle\in\mathcal{S}_k}(1 - |\langle\pi|\psi\rangle|^2) = 1 - \max_{|\pi\rangle\in\mathcal{S}_k}|\langle\pi|\psi\rangle|^2. \tag{2.65}$$

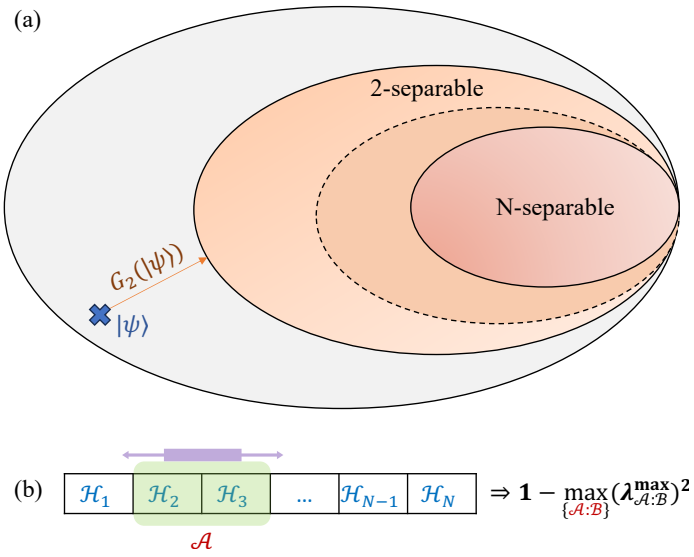

Figure 2.6. (a) Pictorial representation of the GGM: The GGM of a state is the minimum distance from all separable states, which coincides with the minimum distance from the 2-partite product states. (b) For pure states, instead of needing to minimize the distance of a given pure state to all 2-separable states, a much more efficient way exists to compute the GGM. Namely, it can be obtained from the maximum Schmidt coefficient across all possible bipartitions of the system. Sketched is a system described as a tensor product of local Hilbert spaces $\mathcal{H}_j$, bi-partitioned into sets $\mathcal{A}$ and $\mathcal{B}$.

This distance measure resembles the Fubini–Study [144] and the Bures metrics [145]. The original geometric measure of entanglement $G_{k=N}$ measures the distance between $|\psi\rangle$ and fully separable states. At the other extreme, $G_{k=2}$ is zero if $|\psi\rangle$ can be written as a product state across any *single* bipartition of the Hilbert space. Even if that is the case, bipartite entanglement can still be found in other bipartitions. Since $\mathcal{S}_k \subset \mathcal{S}_2$ for all k [Fig. 2.6(a)], the GGM measures the distance between $|\psi\rangle$ and the union of all forms of k-separable states ranging from fully separable to biseparable states. The G_2 thus captures the amount of genuine multipartite entanglement present in the system.

One may think that the inclusion of all kinds of biseparable states makes the measure hard to compute. However, one can show that for pure states the GGM takes the simple form [see Fig. 2.6(b)]

$$G_2(|\psi\rangle) = 1 - \max_{|\pi\rangle_{\mathcal{A}:\mathcal{B}} \in \mathcal{S}_2} |_{\mathcal{A}:\mathcal{B}}\langle \pi|\psi\rangle|^2 = 1 - \max_{\mathcal{A}:\mathcal{B}} (\lambda^{\max}_{\mathcal{A}:\mathcal{B}})^2. \tag{2.66}$$

Here, $|\psi\rangle$ belongs to the Hilbert space $\mathcal{H}_{A_1} \otimes \mathcal{H}_{A_2} \otimes \cdots \otimes \mathcal{H}_{A_N}$. The bipartition $\mathcal{A} : \mathcal{B}$ satisfies $\mathcal{A} \cup \mathcal{B} = \{1, 2, \cdots, N\}$, and $\mathcal{A} \cap \mathcal{B} = \emptyset$ [142, 143]. In other words, maximizing $|_{\mathcal{A}:\mathcal{B}}\langle \pi|\psi\rangle|$ across the biparition $\mathcal{A} : \mathcal{B}$ is equivalent to finding the maximum Schmidt coefficient, $\lambda^{\max}_{\mathcal{A}:\mathcal{B}}$, for that bipartition. Finally, to compute the GGM, one has to find the global maximum of the Schmidt coefficient over all bipartitions $\mathcal{A} : \mathcal{B}$ of the system[4]. Although in general the number of partitions grows exponentially with the system size, one can often use symmetry or bounds to estimate the GGM effectively. Moreover, in the context of analyzing the ground state of local many-body Hamiltonians, it is often observed that the main contribution to GGM comes from

[4]In the absence of simplifications such as symmetries, we need to calculate over the following number of bipartitions— $\binom{N}{1} + \cdots + \binom{N}{\frac{N-1}{2}} = 2^{N-1} - 1$ for odd N and $\binom{N}{1} + \cdots + \binom{N}{\frac{N}{2}-1} + \binom{N}{\frac{N}{2}} = 2^{N-1} - 1 + \frac{1}{2}\binom{N}{\frac{N}{2}}$ for even N.

the bipartitions of the system into contiguous blocks. Hence, focusing on a smaller number of blocks would be sufficient to obtain the exact value of GGM in these cases, and one can expect a similar approach to work in some cases of quantum optimization as well. One can show that the theoretical maximum value of GGM is obtained when, for a given bipartition, all the Schmidt coefficients become equal $\frac{1}{\sqrt{d}}$, and thus we have $G_2^{\max}(|\psi\rangle) = 1 - 1/d$, where d is the local Hilbert space dimension, also known as qudit dimension. We can understand this intuitively as follows. Consider an arbitrary bipartition $\mathcal{A} : \mathcal{B}$ where $|\mathcal{A}| = m$ and $|\mathcal{B}| = N - m$. For this bipartition, there can be at most d^m non-zero Schmidt coefficients, denoted as $\{\lambda^1_{\mathcal{A}:\mathcal{B}}, \lambda^2_{\mathcal{A}:\mathcal{B}}, \ldots, \lambda^{k=d^m}_{\mathcal{A}:\mathcal{B}}\}$. To maximize the GGM, we need to arrange these Schmidt coefficients so that $1 - (\lambda^1_{\mathcal{A}:\mathcal{B}})^2$ is as large as possible. This is achieved when all $\lambda^k_{\mathcal{A}:\mathcal{B}}$ are equal, i.e., $\lambda^k_{\mathcal{A}:\mathcal{B}} = \frac{1}{\sqrt{d^m}}$ for all k. Therefore, among all possible bipartitions, the maximum of $1 - (\lambda^1_{\mathcal{A}:\mathcal{B}})^2$ is obtained in the case where $m = 1$, and the maximally possible GGM value is $G_2 = 1 - \frac{1}{d}$. Extending the GGM to mixed states is non-trivial, though it can still be calculated by exploiting symmetries [141, 146, 147].

2.7 Nonstabilizerness

One of the main questions in quantum information theory is to understand to what extent quantum computers can offer advantages over classical computers. Entanglement is considered one of the underlying resources that can provide such advantages, as an entangled state of N qudits typically requires storing on the order of $\mathcal{O}(d^N)$ complex amplitudes for its classical representation. Thus, one expects a quantum algorithm utilizing entanglement to be complex enough not to have a fast counterpart in the classical algorithm. However, this is not always the case. Stabilizer states can exhibit large entanglement yet remain efficiently simulable classically via Clifford circuits, as guaranteed by the Gottesman–Knill theorem [148–151]. The existence of such states calls for a different resource-theoretic formalism where free operations are quantum-computational processes that can be efficiently simulated using a classical computer. In other words, although entanglement is considered one of the primary necessities for quantum advantages, it is certainly not enough to acquire something beyond classical simulation.

2.7.1 Classical simulation of quantum computation

In order to distinguish the power of quantum computation from classical computation, the notion of classical simulation of quantum computation provides a good handle. An efficient classical simulation of quantum computation can be precisely defined [88, 152].

Consider a uniform family of quantum circuits $\mathcal{U}_N$ acting on the N-qubit input state $|\mathbf{0}\rangle \equiv |0\rangle^{\otimes N}$, and then followed by a measurement of one qubit in the computational basis. This has two possible outcome $\alpha \in \{0, 1\}$, and the probability of its outcome being α is

$$\pi(\alpha) = \langle \mathbf{0} | \mathcal{U}_N^\dagger [|\alpha\rangle \langle \alpha| \otimes I] \mathcal{U}_N |\mathbf{0}\rangle . \tag{2.67}$$

Strong simulation. If it is possible to evaluate $\pi(0)$ up to M digits in $\text{poly}(N, M)$ time on a classical computer, we say that the above quantum computation can be efficiently simulated classically in the strong sense.

Weak simulation. If it is possible to *sample once* from a probability distribution which is not necessarily exactly $\{\pi(\alpha)\}$, but sufficiently close to it, in poly(N) time on a classical computer, it is called weak simulation.

Most of the understanding on simulation of quantum computations is related to *strong* classical simulation, e.g., the Gottesman-Knill theorem [149, 150], matchgate circuits [152], etc. Also, most of the quantum circuits become hard when asked for strong simulation, more precisely **#P**-hard[5] problem, a set much bigger than the class of decision problems solvable by a quantum computer in polynomial time (**BQP**). On the other hand, weak simulation provides a more appropriate way to understand the difference between classical and quantum computation.

2.7.2 Stabilizer formalism and Clifford group

Some circuits do not provide any speedups, and such systems are studied in literature [153, 154], mainly via the help of stabilizer formalism. In fact, one of the ways to understand the Gottesman-Knill theorem is indeed through this formalism.

Stabilizer formalism

The basic idea is to fix a state $|\psi\rangle$ with the set of operators $O_1, O_2, \ldots, O_k$ such that

- $|\psi\rangle$ is $+1$ eigenvector for all O_i, i.e., $O_i |\psi\rangle = +1 |\psi\rangle\,,\ \forall O_i$,
- $|\psi\rangle$ is unique up to a complex phase.

These conditions allow for a full characterization of the state by only specifying the list of operators. Such operators O_i forms a set $\mathcal{A}_N \subset U_N(d)$, called *stabilizing set*, and any such state $|\psi\rangle$ is a *stabilizer state*. Here, we consider the state as an N-qudit state with local dimension d.

From here, one can introduce *generalized Clifford group* as the normalizer of the set of operators, $O_i \in \mathcal{A}_N$[6] as follows [155]

$$\textbf{generalized Clifford group: } \mathcal{C}_N(\mathcal{A}_N) = \{U \mid UOU^\dagger \in \mathcal{A}_N,\ \forall O \in \mathcal{A}_N\}. \quad (2.68)$$

Such a structure ensures that a stabilizer state $|\psi\rangle$ remains a stabilizer state after the action of any Clifford unitary, $O|\psi\rangle$, $O \in \mathcal{C}_N$.

A classic example of such stabilization is given by the Pauli group (see Fig. 2.7 for single-qubit Clifford gates), i.e., $\mathcal{A}_N = \mathcal{P}_N$. The generalized Pauli matrices generate

[5] A function $f : \{0,1\}^* \to \mathbb{N}$ is called **#P**-hard if, for every function $g \in$ **#P**, there exists a polynomial-time Turing reduction from g to f. That is, f is at least as hard as any problem in **#P**.

[6] The **centralizer** of a subset $A \subseteq G$, denoted $C_G(A)$, is the set of all elements in G that commute with every element of A.

$$C_G(A) = \{g \in G \mid ga = ag \text{ for all } a \in A\}$$

The **normalizer** of a subset $A \subseteq G$, denoted $N_G(A)$, is the set of all elements in G that conjugate A to itself.

$$N_G(A) = \{g \in G \mid gAg^{-1} = A\}$$

Whereas centralizer assures commutativity, normalizer assures stability under conjugation, and they follow a subset structure as:

$$C_G(A) \subseteq N_G(A) \subseteq G$$

.

the Pauli group, also known as the Heisenberg-Weyl group, which defines quantum kinematics and the states of the quantum register, and it is a subgroup of the unitary group $U(N)$. The generalized Pauli (Heisenberg-Weyl) operators are defined as products of X and Z [85, 156],

$$T_{\vec{v}} = \omega^{v_1} X^{v_2} Z^{v_3}; \quad v_j \in \{0, 1, 2..., d-1\}, \tag{2.69}$$

where Z and X are defined as the phase and shift operators,

$$Z = \sum_{j=0}^{d-1} \omega^j |j\rangle\langle j|, \quad X = \sum_{j=0}^{d-1} |j+1\rangle\langle j|\,; \quad \omega = e^{2\pi i/d}\,. \tag{2.70}$$

Note that there are d^3 Paulis, which can be labelled by (v_1, v_2, v_3), where $v_j \in \mathbb{Z}$ has a physical interpretation as the position of the basis states $|j\rangle$.

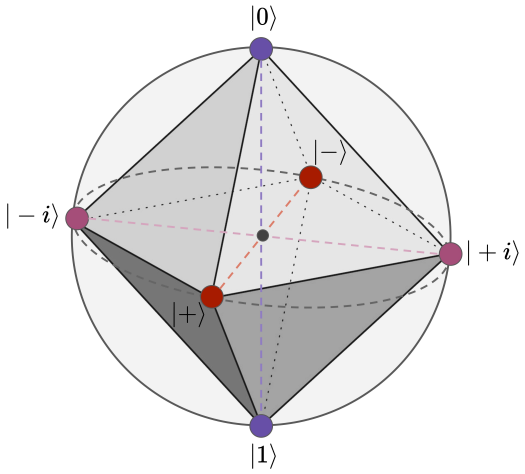

Figure 2.7. The octahedron in the Bloch sphere defines the states accessible via single-qubit Clifford gates (Taken from Pennylane demonstration [157]).

We consider a system of N qudits with Hilbert space $\mathcal{H} = \otimes_{j=1}^{N} \mathcal{H}_i$, where $\mathcal{H}_i$ correspond to local Hilbert space for each qudits. The N-qudit Pauli group $\mathcal{P}_N$ encompasses all the possible Pauli strings with overall phases ± 1 or $\pm i$. The N-qudit Pauli group $\mathcal{P}_N$ is defined as the set of $\{T_{\vec{V}}\}$

$$T_{\vec{V}} := T_{\vec{v}^{(1)}} \otimes \cdots T_{\vec{v}^{(N)}};\ \theta \in [0, 2\pi]. \tag{2.71}$$

The well-known *Clifford group* is the largest subgroup of the unitary group that acts on the Pauli/Heisenberg-Weyl group by conjugation and normalizes it; thus, the Clifford group ($\mathcal{C}_N$) is also called the normalizer of the Heisenberg-Weyl group ($\mathcal{P}_N$):

$$\mathcal{C}_N(\mathcal{P}_N) = \left\{U \text{ such that } UPU^\dagger \in \mathcal{P}_N \text{ for all } P \in \mathcal{P}_N\right\}. \tag{2.72}$$

The Clifford group can be generated by

- Hadamard gate $\frac{1}{\sqrt{2}} \begin{pmatrix} 1 & 1 \\ 1 & -1 \end{pmatrix}$,
- $\pi/2$ phase gate $\begin{pmatrix} 1 & 0 \\ 0 & i \end{pmatrix}$,

- CNOT gate $\begin{pmatrix} 1 & 0 & 0 & 0 \\ 0 & 1 & 0 & 0 \\ 0 & 0 & 0 & 1 \\ 0 & 0 & 1 & 0 \end{pmatrix}$.

The pure stabilizer states are defined as the states formed by the action of Clifford unitaries on $|0\rangle$,

$$\textbf{Pure stabilizer states: } \{S_i\} = \{U\,|0\rangle \text{ such that } U \in \mathcal{C}_N\}, \tag{2.73}$$

and the convex hull of this set defined the full set of stabilizer states:

$$\textbf{Stabilizer states: } \mathrm{STAB}(\mathcal{H}) = \left\{ \sigma \in L(\mathcal{H}) \text{ such that } \sigma = \sum_i p_i S_i \right\}, \ \sum_i p_i = 1\,. \tag{2.74}$$

A circuit made of only Clifford unitaries is called a Clifford circuit, and is efficiently classically simulable via the Gottesman–Knill theorem [149].

Gottesman–Knill theorem

Theorem 1. *Every uniform family of Clifford circuits, applied to the input state $|0\rangle$ and followed by measurement on one qubit in the computational basis, can be efficiently simulated classically in the strong sense.*

We define *stabilizer operations* to be any combination of computational basis preparation, Clifford rotations, and computational basis measurements. Using stabilizer formalism, one can prove the above theorem. However, it is not necessary to go through the formalism in order to understand why the Clifford group is easier to simulate [158].

The Gottesman-Knill theorem is $\oplus\mathbf{L}$ complete[7]. Only a few classical computing structures allow for the simulation of arbitrary Clifford circuits. For example, a classical circuit model comprising only NOT and CNOT gates should be enough. The strong simulation then asks if the state of the first qubit can be learned with certainty. Interestingly, such a problem can be mapped, under a logarithmic-space reduction, to a problem of simulating a classical poly-size CNOT-NOT circuit [151], which has complexity class of $\oplus\mathbf{L}$ (parity-L) (see more in Sec. 3.2).

2.7.3 Discrete Wigner functions

The discrete Wigner representation for odd dimensions enjoys a special property that all stabilizer operations can be represented non-negatively, i.e., it provides a classical probability model for the stabilizer theory [85]. Such a connection motivates one to study Wigner functions, which offer an alternative way to understand stabilizer states.

The Wigner function [159] provides a representation of the wavefunction in terms of a probability distribution in phase space. The discrete Wigner function is a direct

[7]The complexity class $\oplus\mathbf{L}$ consists of decision problems that can be solved by a nondeterministic log-space Turing machine, where the correct answer is "yes" if and only if the number of accepting computation paths is odd. A problem is $\oplus\mathbf{L}$-*complete* if it belongs to $\oplus\mathbf{L}$ and every problem in $\oplus\mathbf{L}$ can be reduced to it via a log-space reduction. Such problems are the hardest in $\oplus\mathbf{L}$ under log-space reductions.

analog of it, but is only defined for quantum systems with finite, odd Hilbert space dimension [160]. Given a phase-space point $\vec{V} = (v_1^{(1)}, v_2^{(1)}) \oplus \cdots \oplus (v_1^{(N)}, v_2^{(N)})$ of N-qudits, we define the corresponding phase space operators using Pauli operators,

$$A_0 = \frac{1}{d^N} \sum_{\vec{V}} T_{\vec{V}}, \quad A_{\vec{V}} = T_{\vec{V}} A_0 T_{\vec{V}}^\dagger . \tag{2.75}$$

From here we arrive at the definition of the discrete Wigner function of a state ρ as

$$\textbf{Wigner function: } W_\rho(\vec{V}) = \frac{1}{d^N} \mathrm{Tr}[A_{\vec{V}} \rho]. \tag{2.76}$$

The main connection between Wigner representation and stabilizer formalism is through discrete Hudson's theorem [160].

Discrete Hudson's theorem

Theorem 2. *A pure state $|S\rangle$ has a positive representation if and only if it is a stabilizer state,*

$$\forall \vec{V},\ W_{|S\rangle\langle S|}(\vec{V}) \geq 0 \quad \Leftrightarrow \quad \exists U \in \mathcal{C}_N, \text{such that } |S\rangle = U|0\rangle , \tag{2.77}$$

Moreover, Clifford unitaries act as permutations of phase space,

$$W_{U\rho U^\dagger}(\vec{V}) = W_\rho(\vec{V'}), \quad \forall \vec{V}. \tag{2.78}$$

2.7.4 Non-Clifford resources

Given that we know stabilizer states are easy to simulate, one may expect that a state that is not a stabilizer state will be interesting and necessary for quantum computing. Indeed, one needs some non-Clifford gates, for example, a T-gate $\begin{pmatrix} 1 & 0 \\ 0 & e^{i\pi/4} \end{pmatrix}$ to make a universal quantum computation.

Why are T-gates (non-Clifford) required for fault-tolerant universal quantum computing?

In fault-tolerant quantum computation, transversal gates[8] are commonly employed [161]. However, the set of gates that can be implemented transversally may differ between stabilizer codes. For instance, the 7-qubit Steane code [162] does not allow for transversal implementation of the T gate. Notably, no non-trivial quantum error-correcting code permits the transversal implementation of a *universal* gate set, which is a limitation formalized by the Eastin-Knill Theorem [163].

[8] A transversal gate is a fault-tolerant quantum gate implemented by applying independent gates to corresponding physical qubits across different code blocks. It is called *transversal* because the operation acts across these blocks rather than within a single block, thereby preventing errors from spreading between qubits in the same code block.

Eastin-Knill Theorem

Theorem 3. *For any quantum error correcting code with distance at least 2, the set of logical gates that can be implemented transversally generates a set of operations that (up to a global phase) is discrete, and is therefore not universal.*

In other words, no quantum error-correcting code can have a continuous symmetry that acts transversely on physical qubits, and we can see that the T-gate implements the smaller rotational gates.

Moreover, as stabilizer states are efficiently simulable classically, and as Clifford operations keep the stabilizer states stabilizer, one can construct a resource theory of nonstabilizerness by considering stabilizer states as free states, and Clifford operations as free operations [85]. A resource state is thus easily defined as a state that is not a stabilizer state, which we call a nonstabilizer state or a *magic state*[9]. One can show that T-gate is indeed optimal for generating magic resources among the class of diagonal unitary operators, both for the qubit and qutrit cases [165].

To define a resource measure of magic (let's say $\mathcal{M}$), we need to fulfill the two conditions we discussed in Sec. 2.3.1:

- $|\psi\rangle \in \mathrm{STAB} \Leftrightarrow \mathcal{M}(|\psi\rangle) = 0$,
- $\mathcal{M}(|\psi\rangle) \geq \mathcal{M}(U|\psi\rangle), \quad \forall\, |\psi\rangle \in \mathcal{H}, \quad U \in \mathcal{C}_N$.

2.7.5 Stabilizer Rényi entropy

The Stabilizer Rényi entropy (SRE) captures how a state is distributed when expressed in the basis of Pauli operators $P \in \mathcal{P}_N$, where $\mathcal{P}_N$ represents the Pauli group for n-qudits. The squared (normalized) expectation value $|\langle\psi|P|\psi\rangle|^2/d^N$ forms a probability distribution[10] over all $P \in \mathcal{P}_N$, as they are positive and sum to 1:

$$\sum_{P\in\mathcal{P}_\mathcal{N}} \frac{|\langle\psi|P|\psi\rangle|^2}{d^N} = \mathrm{Tr}[(|\psi\rangle\langle\psi|)^2] = 1. \tag{2.79}$$

Note that the second equality comes from the fact that any state can be represented in the Pauli basis,

$$\begin{aligned}
\rho &= \frac{1}{d^N}\sum_P \underbrace{c_P}_{\mathrm{Tr}(\rho P)} P \\
\Rightarrow \rho^2 &= \frac{1}{d^{2N}}\sum_{P,Q} c_P c_Q PQ \\
\Rightarrow \mathrm{Tr}(\rho^2) &= \frac{1}{d^N}\sum_P c_P^2 = \frac{1}{d^N}\sum_P |\langle\psi|P|\psi\rangle|^2 .
\end{aligned}$$

Stabilizer states, which are common eigenstates of a maximal set of mutually commuting Pauli operators (d^N-many), have $\langle\psi|P|\psi\rangle = \pm 1$ for d^N Paulis, out of a total of d^{2N} many Paulis. That means stabilizer state is a highly concentrated

[9] The term *magic* probably came from magic-state distillation, a purification protocol which allows a qubit to increase the polarization only along certain 'magic' directions [164].

[10] probability of finding P in the representation of the state $|\psi\rangle$ in Pauli basis.

probability distribution, and thus is easily simulable [148, 149, 151, 158, 166, 167]. In contrast, a Haar-random state has approximately equal weight on all P's [168]. Thus, a natural way to quantify the nonstabilizerness of a state $|\psi\rangle$ is by assessing the spread of this distribution.

Stabilizer Rényi entropy

Definition 4. The q-th order stabilizer Rényi entropy of a state $|\psi\rangle$ is defined as the Rényi entropy on the probability distribution formed by the Pauli expectation value [169]:

$$M_q(\psi) = \frac{1}{1-q} \log_2 \sum_{P \in \mathcal{P}_N} \frac{|\langle\psi|P|\psi\rangle|^{2q}}{d^N} \,. \tag{2.80}$$

The SRE is zero for the stabilizer state, as exactly d^N expectation values are ± 1. As the Clifford group stabilizes the Pauli group, any action of unitary $U \in \mathcal{C}_N$ keeps the Pauli group intact, $U^\dagger P U = \pm Q$, where $Q \in \mathcal{P}_N$. Thus, SRE is conserved under Clifford operations. Moreover, it is additive,

$$M_q(|\psi\rangle \otimes |\phi\rangle) = \frac{1}{1-q} \log_2 \sum_{P_1 \in \mathcal{P}_N^1, P_2 \in \mathcal{P}_N^2} \frac{|\langle\psi|P_1|\psi\rangle|^{2q} |\langle\phi|P_2|\phi\rangle|^{2q}}{d_1^N d_2^N} = M_q(|\psi\rangle) + M_q(|\phi\rangle) \,.$$

Monotonicity holds only for $q \geq 2$ [170], while it can be violated when $q < 2$ [171]. Importantly, values of $q > 1$ and $q < 1$ highlight different properties of stabilizer Rényi entropies (SREs) and correspond to distinct quantum computational applications. Specifically, $q < 1$ SREs are connected to the number of stabilizer state superpositions required to represent a given quantum state, which determines the resource cost for Clifford-based simulation algorithms and fault-tolerant state preparation. In contrast, $q > 1$ SREs quantify the distance to the nearest stabilizer state, serving as a measure of the cost in Pauli-based fidelity certification [172].

SRE is related to many quantum information protocols, for example, it relates to phases of error-corrected circuits [173], quantifies the entanglement spectrum [174], bounds fidelity estimation [175–177], characterizes the robustness of shadow tomography [178], and characterizes pseudorandom states [179, 180]. It also provides a lower bound on T-gates [169], and experimentally computable [173].

2.7.6 Sum negativity and mana

The discrete Wigner function offers a robust resource measure. Early work on bound magic states [181] used this framework to show that negativity in a state's Wigner representation is a necessary condition for magic state distillation. However, this negativity was not initially explored as a quantitative measure of resource.

Intuitively, one expects that a state exhibiting only slight negativity should possess less magic than a state with large negative values in its Wigner function. This intuition is formalized in later work [85], which demonstrates that the sum of the negative entries in the Wigner function defines a valid magic monotone, capturing the degree of non-classicality relevant for quantum computation.

Sum negativity

Definition 5. The sum negativity of a state ρ is the sum of the negative elements of its Wigner function:

$$\mathrm{sn}(\rho) = \sum_{\vec{V}|W_\rho(\vec{V})<0} |W_\rho(\vec{V})| = \frac{1}{2}(\sum_{\vec{V}} |W_\rho(\vec{V})| - 1). \tag{2.81}$$

Due to the discrete Hudson's theorem, free states have a magic zero, and, as Clifford unitaries keep the Wigner function unchanged (Eq. (2.78), monotonicity is also satisfied. However, the composition law of sum-negativity follows,

$$\mathrm{sn}(\rho^{\otimes n}) = \frac{1}{2}[(2 \cdot \mathrm{sn}(\rho) + 1)^n + 1], \tag{2.82}$$

i.e., a linear increase in the number of resource states implies an exponential increase in the amount of resource according to the measure. One can make such dependence linear, essentially putting a log in front of similar quantities, which defines another measure called mana:

Mana

Definition 6. The mana of a quantum state ρ is

$$\mathrm{Mana}(\rho) = \log\left(\sum_{\vec{V}} |W_\rho(\vec{V})|\right) = \log(2 \cdot \mathrm{sn}(\rho) + 1)\,. \tag{2.83}$$

As log is a monotonic function, Mana also follows the necessary properties of a magic monotone. It is also additive, i.e., $\mathrm{Mana}(\rho \otimes \sigma) = \mathrm{Mana}(\rho) + \mathrm{Mana}(\sigma)$.

2.8 Non-Markovianity

In the classical setting, a Markovian process is a type of stochastic (random) process that satisfies the Markov property, i.e., the future state of the process depends only on the present state, and not on the sequence of past states. More mathematically, three random variables XYZ with joint probability distribution p_{XYZ} form a Markov chain $(X - Y - Z)$, if the conditional mutual information between X and Z is independent of Y,

$$\textbf{Markov chain: } I(X : Z|Y) = I(X : Y|Z) - I(X : Y) = 0\,. \tag{2.84}$$

Here, $I(A : B) = H(A) - H(A|B)$, where $H(A)$ is the Shannon entropy. Equivalently, the conditional probability distribution $p_{Z|X=x}(z) := p_{ZX}(z, x)/p_X(x)$ satisfy

$$p_{Z|X=x}(z) = \sum_y p_{Z|Y=y}(z)\; p_{Y|X=x}(y)\,. \tag{2.85}$$

When such past-future independence fails, i.e., some history is retained, the process is referred to as non-Markovian. The relevance of quantum non-Markovianity, or the characterization of memory effects, becomes particularly important in open quantum

systems. A quantum system is called *open* when it has interaction with its environment [182]. As time evolves, it builds up correlations, such as entanglement, and destroys them through decoherence and dissipation, which are detrimental to quantum devices. Thus, it is essential to determine whether any past information is lost over time or not, as quantified by witnesses of non-Markovianity. However, a universal definition of non-Markovianity has remained elusive; hence, we will discuss some different witnesses, which, together, can provide a hint about non-Markovianity.

2.8.1 Quantum channels

Open system dynamics is represented by quantum dynamical maps, also known as quantum channels, which we discuss in this section before exploring non-Markovianity witnesses. Linear maps, e.g.,- Φ, Λ, represent a physical evolution map from density matrices to density matrices. A linear map $\Phi; \mathcal{H}(A) \to \mathcal{H}(B)$ is called:

$$\text{positive}: \quad \Phi(\rho) \geq 0, \quad \forall \rho\,; \tag{2.86}$$

$$k-\text{positive}: \quad \Phi \otimes \mathrm{id}^C \geq 0, \quad \dim \mathcal{H}_C = k\,; \tag{2.87}$$

$$\text{completely}-\text{positive}: \quad k-\text{positive}\ \forall k\,. \tag{2.88}$$

Additionally, a physical evolution must preserve the trace, and such completely-positive trace-preserving (CPTP) maps are called *quantum channels*, denoted as $\mathcal{Q}$.

There are three well-known representations of quantum channels, which we use to express quantum processes throughout the thesis on several occasions..

1. System-Environment representation. The evolution of an open quantum system A with environment E, is modeled by the unitary evolution of the joint system U^{AE}. Given an uncorrelated initial state of environment $|0\rangle\langle 0|^E$, the dynamics of the system are represented by the reduced density matrix:

$$\rho^A \mapsto \Phi(\rho^A) = \mathrm{Tr}_{E'}\left[U^{AE}\left(\rho^A \otimes |0\rangle\langle 0|^E\right) U^{\dagger AE}\right], \tag{2.89}$$

where E' does not need to be the same system as E. Every completely positive trace-preserving (CPTP) map admits a unitary representation; that is, any physical evolution can be viewed as a unitary process acting on a larger system that includes the environment. CPTP maps effectively describe this evolution by tracing out the environment, whose degrees of freedom are not directly accessible.

2. Kraus operator. Φ can be represented by set of matrices $\{K_j\}$ satisfying $\sum_j K_j^\dagger K_j = \mathbb{I}^A$ in the following form-

$$\rho^A \mapsto \Phi(\rho^A) = \sum_j K_j \rho^A K_j^\dagger\,. \tag{2.90}$$

3. Choi matrix. For any CP map, Φ maps half of a maximally entangled vector $|\phi^+\rangle^{AA'} = \sum_{j=1}^{d_A} |j\rangle^A |j\rangle^{A'}$ of $\mathcal{H}^A \otimes \mathcal{H}^{A'}$ to another system B, and it can produce the bipartite operator known as Choi matrix of Φ,

$$J_\Phi^{AB} := \mathrm{id}^A \otimes \Phi(\phi^+). \tag{2.91}$$

Conversely, any bipartite positive semi-definite operator J^{AB} corresponds to a CP map Φ given by

$$\Phi_J(\rho) = \mathrm{Tr}_A \left[J^{AB} (\rho^T \otimes I^B) \right], \tag{2.92}$$

where ρ^T denotes the matrix transpose with respect to some basis of A. If this basis can be chosen as same as used for $|\phi^+\rangle^{AA'}$, then $\Phi_{J_\Phi} = \Phi$, and thus defines Choi-Jamiołkowski Isomorphism between the CP maps (Φ) $(A \to B)$ and Choi matrices J_Φ^{AB}.

Unital map. A special class of CP maps that act invariantly on the identity, i.e., $\Phi(\mathbb{I}) = \mathbb{I}$, are called *unital* maps, which will be helpful to understand as it has a close connection to the CPTP map. For every map Φ, its dual is the adjoint map fixed by the Hilbert-Schmidt inner product,

$$\mathrm{Tr}\left(X \Phi^\dagger(Y)\right) = \mathrm{Tr}(\Phi(X)Y), \quad \forall X \in \mathcal{B}(A), Y \in \mathcal{B}(B). \tag{2.93}$$

Thus, one can verify that

$$\Phi \text{ is trace preserving} \Leftrightarrow \Phi^\dagger \text{ is unital}. \tag{2.94}$$

Proof. It is worth understanding how two-way implication works.

- Φ is trace preserving $\Rightarrow \mathrm{Tr}(\Phi(\rho)) = \mathrm{Tr}(\rho)$. Now, substituting $X = \rho, Y = \mathbb{I}$ at Eq. (2.93), $\mathrm{Tr}(\rho \Phi^\dagger(\mathbb{I})) = \mathrm{Tr}(\Phi(\rho)\mathbb{I}) = \mathrm{Tr}(\rho) \Rightarrow \Phi^\dagger(\mathbb{I}) = \mathbb{I}$.
- $\Phi^\dagger$ is unital $\Rightarrow \mathrm{Tr}(X \underbrace{\Phi^\dagger(\mathbb{I})}_{\mathbb{I}}) = \mathrm{Tr}(\Phi(X))$:: Trace-preserving.

Note that we do not use any particular representation of the Φ, yet we can prove the above statement.

2.8.2 Witnesses of non-Markovianity

The memory effect of a non-Markovian process is sometimes characterized by the backflow of information from the environment to the system, leading to revivals of information [183,184][see Fig. 2.8(b)], although the precise relation between such revivals and backflow is a matter of ongoing investigations [185]. Alternatively, non-Markovianity can be described in terms of the divisibility property, positive or completely-positive, of the associated dynamical maps, where non-divisibility is linked to non-Markovian behavior [186–190]. Non-Markovian behavior is also sometimes related to nonexponential decays and dissipationless oscillations [191]. Non-Markovianity can also serve as a tool to probe quantum complexity [192]. To characterize the non-Markovianity, we use the following witnesses.

Trace distance (BLP criterion). As an open system evolves, it typically develops correlations with its environment and undergoes an irreversible loss of information, particularly when the system is weakly coupled to the environment. Under the strong coupling limit, the information might periodically be revived from the environment, which is known as the backflow of information. As the trace-norm is CP-contractive under a CPTP map, we can consider the trace distance as a measure to define the

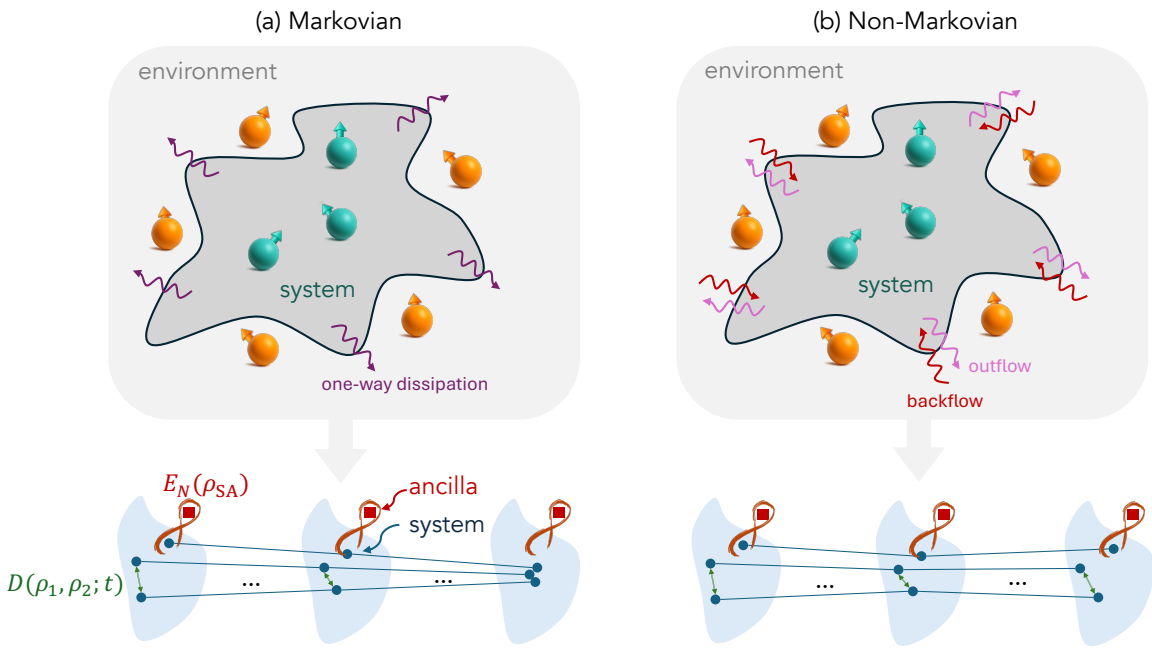

Figure 2.8. Temporal flow of information in open Quantum Systems: (a) In the Markovian regime, the system experiences one-way dissipation, i.e., information flows irreversibly from the system to the environment. (b) In contrast, the non-Markovian regime exhibits backflow, where the environment can return information to the system, impacting its evolution. The trace distance $D(\rho_1, \rho_2; t)$ (BLP criterion), which captures changes in distinguishability over time, reduces monotonically in Markovian dynamics, whereas it can increase again in non-Markovian dynamics. Similarly, the entanglement between system and ancilla $E_N(\rho_{SA})$ (RHP criterion) only decreases in Markovian, but it can be revived in non-Markovian dynamics, showing the signature of memory effects arising from the backflow of information.

distance between the density of matrices, which can define the distinguishability. The trace distance between two different initial states $\rho_1(0)$ and $\rho_2(0)$, defined as

$$D(\rho_1, \rho_2; t) = \frac{1}{2}||\rho_1 - \rho_2||_1 \,. \tag{2.95}$$

Here, $||M||_1$ is the trace norm $\mathrm{Tr}[\sqrt{M^\dagger M}]$. A map Φ is said to be Markovian if it follows the data-processing inequality [Eq. (2.22)] for trace distance, i.e., tends to reduce the distinguishability between any two states continuously.

$$D(\rho_1, \rho_2) \geq D(\Phi(\rho_1), \Phi(\rho_2)), \quad \forall t \,. \tag{2.96}$$

Thus, according to the Breuer–Laine–Piilo (BLP) criterion, breakdown of the monotonicity of trace distance between any two orthogonal initial states implying a temporal growth of distinguishability can be considered a hallmark of non-Markovianity [183]. Note that this criterion is only sufficient, but not necessary, since it might fail to witness non-Markovianity for some non-unital channels [193, 194] and unital channels [190].

Logarithmic negativity (RHP criterion). Entanglement is considered one of the pivotal resources in quantum computing [195]. One of the entanglement measures, known as logarithmic negativity [196,197], can also be used to identify non-Markovian

evolutions following the Rivas–Huelga–Plenio (RHP) criterion [188]. Consider an initial maximally entangled state between the system and an ancilla. For the example of a system given by a qubit, this state can be written as

$$|\Phi\rangle = \frac{1}{\sqrt{2}}(|\uparrow\uparrow\rangle + |\downarrow\downarrow\rangle) \Rightarrow \rho_{\mathrm{SA}}(0) = |\Phi\rangle\langle\Phi| \ . \tag{2.97}$$

Evolving the system in time with a quantum evolution operator, $\rho_{\mathrm{SA}}(t) = (\mathcal{E}_t \otimes \mathbb{I})\rho_{\mathrm{SA}}(0)$, and partially transposing the joint density matrix, one can calculate the logarithmic negativity as

$$E_N(\rho_{\mathrm{SA}}) = \log_2 ||\rho_{\mathrm{SA}}^{T_{\mathrm{S}}}||_1 \, . \tag{2.98}$$

Here, $(\ )^{T_{\mathrm{S}}}$ denotes the partial transposition with respect to the system S. As Markovian dynamics will always destroy quantum correlations between ancilla and system, a temporal increase in logarithmic negativity witnesses non-Markovianity [188, 197]. Note that nonmarkovianity witnessed by the BLP criterion (which checks P-indivisibility) also implies it will be detected in the RHP criterion (related to CP-indivisibility), but not the other way around.

Purity. The purity of a state is defined as $\mathrm{Tr}[\rho^2(t)]$. For finite-dimensional Hilbert spaces, the purity is monotonically decreasing during dynamics generated by a Lindbladian if and only if the Lindbladian is unital, i.e., $\mathcal{L}_t[\mathbb{I}] = 0$ [198]. Note that a Lindbladian form (where decay rates are absorbed in jump operators, thus requiring positive decay rates) guarantees a completely-positive-trace-preserving map (CPTP) [183, 190]. If the dynamics induced by any unital Lindblad-like generator[11] leads to an increasing purity, then the associated map is non-CPTP in the time interval. Thus, the increase in purity can witness non-Markovianity for unital maps [199].

We want to highlight that although purity-increasing maps can be unital, they cannot be represented in the exact Lindbladian form, as the CPTP conditions need to be conserved there. Thus, such non-Markovian features do not contradict the 'if and only if' conditions for unital Lindbladians mentioned above. For example, such a scenario can appear in the presence of a negative decay rate in a Lindblad-like master equation.

To summarize, if the map is unital, an increasing purity is a good non-Markovianity witness, but if the map is non-unital, one has to employ different measures [194] to reveal the non-Markovianity originating from the non-unital aspect of the dynamics. Regardless of the purity's ability to reveal non-Markovianity, it remains an important figure of merit, e.g., in optimal control: a control pulse can be identified as robust against imperfections when the purity of a disorder-averaged state revives near the completion of the pulse [200, 201].

Non-Markovian states have been identified as valuable resources for various quantum information tasks such as quantum state redistribution [202], secure communication [203], and state deconstruction [204]. These applications motivate the treatment of non-Markovianity as a quantum resource [205, 206].

[11] By Lindblad-like, we mean the form where the decay rate is not absorbed in the jump operators.

2.9 Summary

This chapter introduces the concept of quantum resources, which serves as the central theme of this thesis. We begin by outlining the desirable properties of resource measures, including axiomatic approaches, as well as practical formulations such as entropic and geometric measures. We then explore the resource theory of entanglement, with a particular emphasis on multipartite entanglement and its quantification using tools like quantum Fisher information and the geometric measure of entanglement—topics that play a key role in Chapters 4, 5, and 6. The chapter also covers the notion of nonstabilizerness and its quantifiers, including Stabilizer Rényi entropy and mana, which are relevant for Chapters 7 and 9. Finally, we discuss non-Markovianity as a crucial resource in open quantum systems and review non-Markovianity witnesses, providing supporting background for Chapter 8.

Chapter 3

Quantum optimization

quantum solutions for optimization problems

Quantum computing is increasingly regarded as a transformative technology for both scientific research and industrial applications. This view is supported by sustained efforts within the scientific community and by substantial investments from governments and industry stakeholders. Among the most promising applications of quantum computing is quantum optimization, a new computational paradigm that has drawn significant attention due to its potential impact across a wide range of fields.

Optimization problems arise naturally in many areas, including logistics, finance, energy systems, drug discovery, etc. These problems often become extremely difficult to solve as their size and complexity grow. While classical algorithms have advanced considerably, they continue to face limitations when dealing with large-scale or highly constrained problems. Therefore, any improvement, whether from classical heuristics, machine learning techniques, or quantum approaches, can be highly valuable.

The key motivation behind quantum optimization lies in the fundamentally different way quantum computers process information. Quantum algorithms can make use of quantum phenomena such as superposition and entanglement, allowing them to explore solution spaces in ways that are not possible for classical systems. This has led to the belief that quantum devices could offer new routes to solving problems that are currently intractable, or at least deliver improvements in speed or accuracy.

Although large-scale, fault-tolerant quantum computers are still under development, significant attention is being directed toward identifying near-term advantages. Both academic researchers and industry practitioners are actively evaluating whether quantum optimization methods can show benefits across several important metrics: the quality of the solutions, the time required to reach them, the overall cost of computation, and the general applicability of the approach to different problem types. These questions are central to understanding when and where quantum computing can provide a meaningful advantage over classical methods.

In this chapter, we begin by introducing the computational complexity associated with optimization problems to understand where the challenging problems lie (Sec. 3.2). We then present quantum optimization algorithms that are employed later in this thesis, including Quantum Annealing (QA) and the Quantum Approximate Optimization Algorithm (QAOA) in Sec. 3.3. In Sec. 3.6, we provide an overview of how quantum algorithms can be implemented on actual quantum computing hardware. The review by Abbas *et al.* [22] is our primary reference for this chapter.

3.1 Classical optimization

Optimization problems involve identifying the optimal solution from a potentially vast set of candidates, often under complex constraints. Mathematically, these problems are framed as the minimization or maximization of an objective function $f(\vec{x})$,

$$\min_{\{\vec{x}\}} f(\vec{x}) \quad \text{or,} \quad \max_{\{\vec{x}\}} f(\vec{x})\,, \tag{3.1}$$

where the search domain $\{\vec{x}\}$ can be discrete or continuous, constrained or unconstrained.

Here are some examples to understand how it is often structured.

- In portfolio optimization, the goal is to determine the optimal allocation of capital across a set of assets to maximize expected return while minimizing risk.
- Job scheduling problem in Operations Research aims to minimize total completion time given multiple jobs are scheduled across machines.
- In drug discovery, determining the lowest-energy 3D structure of a molecule is the goal.
- In power-grid optimization, the goal is to balance supply and demand to minimize loss and maintain stability.
- In many-body physics, finding the ground state can also be considered an optimization problem, for example, when using the variational principle to obtain the best solution.

The main challenge of such problems is to find a solution or a set of solutions efficiently. However, for some combinatorial optimization problems, the required effort (one can think of it as resources, but in a classical sense) using a known classical algorithm may scale exponentially with problem size, in a worst-case scenario. One may expect that a quantum computer can provide some quadratic speedup, though it may remain an exponential runtime. However, in classical optimization, one is not always worried about the worst-case scenario, and when considering a concrete problem instance, the story can be different. Many classical algorithms and heuristics can obtain almost optimal solutions in a reasonable time, even for large problems, for example, the travelling salesperson problem (TSP) [207–209]. The problem does not necessarily lie in the number of variables to optimize, as one may sometimes claim, because there are hard problems with fewer than 100 variables as well [210, 211]. The key mantra one should keep in mind is that although quantum optimization algorithms will not necessarily improve performance for all instances of a problem, they can exploit some *quantumness* that can potentially improve performance for some problem instances, if used wisely, and thus improve overall capabilities in optimization.

3.2 Computational complexity classes

The difficulty of quantum optimization largely depends on the nature of the optimization problems it addresses. Therefore, it is helpful to categorize problems into different complexity classes based on the computational resources they require, such as

time and memory. In theoretical computer science, these complexity classes serve as a framework for analyzing problem difficulty and provide a systematic way to approach and compare different problem types. While complexity theory primarily evaluates classical computational difficulty, it also offers insights into areas where quantum algorithms might outperform classical ones in terms of resource efficiency.

However, demonstrating a clear advantage of quantum computing over classical methods is not straightforward. Complexity theory focuses on worst-case scenarios, which do not always reflect the practical performance of algorithms. Real-world instances are often much easier than the hardest theoretical cases [212, 213]. Consequently, even if quantum algorithms do not outperform classical ones in worst-case scenarios, they may still offer significant benefits on average-case instances.

This distinction between worst-case and average-case performance suggests that the notion of quantum advantage should extend beyond traditional complexity-theoretic comparisons. In this context, we will explore various complexity classes, examine the types of problems they encompass, and highlight corresponding quantum algorithms. This overview will help identify problem domains where quantum approaches hold the potential for meaningful advantages.

3.2.1 Exact solutions

A decision problem involves deciding whether there exists a particular solution to the problem or not.

Decision problem

Definition 7. A decision problem is a binary function $f_n : \{0,1\}^n \to \{0,1\}$ where $f_n(x) = 1$ if and only if $x \in L$, which is a set of "yes" instances.

Note that a decision problem only cares about the existence of a particular solution, and not the actual solution itself. In a practical scenario, finding an actual solution is often necessary, which leads to relational problems.

Relational problem

Definition 8. Given a relation $R \subseteq \{0,1\}^n \times \{0,1\}^n$ between input x and output y, the relational problem is about finding a y, that satisfies the relation, i.e., $(x, y) \in R$.

For example, consider the MaxCut problem, where the goal is to bipartition the nodes of the graph in such a way that the maximum number of edges is traversed between the two sets (see Fig. 4.1). In such problems, the *decision problem* asks whether there exists a cut of size greater than a given threshold d, while the *relational problem* seeks the exact configuration, that is, which nodes belong to each partition, assuming the cut size is d. In this context, we can represent the input as $x = d$, and the output as y, denoting the corresponding partition configuration. It is important to note that the decision problem already encapsulates the computational complexity of the relational problem. This is because one can, in principle, solve the relational version by iteratively applying the decision problem; for instance, by successively removing edges and checking whether the maximum cut size remains unchanged.

Given such problem classes of decision and relational problems, one can define several complexity classes in terms of solvability.

Easy problems when asked for *exact* solution

Definition 9. Concerns about whether it needs *polynomial* resources to obtain the exact solution.

Under deterministic computation

- Efficiently solvable by a deterministic machine in polynomial *time* –
  1. **P**: for decision problem,
  2. **FP**: for relational/functional problem,
  3. **PO**: for the set of optimization problems, **PO** $\subset$ **FP**.
- Efficiently solvable by a deterministic machine in polynomial *space* –**PSPACE**, but no restriction on time. Thus, **PSPACE** is larger than **P**-time.

Under probabilistic computation

Efficiently solvable in polynomial time, with an error probability $\leq 1/3$

- **BPP**: when solved in a classical probabilistic machine (**b**ounded-error **p**robabilistic **p**olynomial time), thus **P** $\subset$ **BPP**.
- **BQP**: when solved in a quantum computer. **BPP** $\subset$ **BQP**, i.e., there exists problem in **BQP**, which are not in **BPP**, example: Recursive Fourier Sampling [214].

BQP class already provides a set of problems where quantum advantage can be achieved, as it contains problems outside **BPP**. However, there are more useful problems for optimization, which are outside **P**, and hence hard to solve due to the

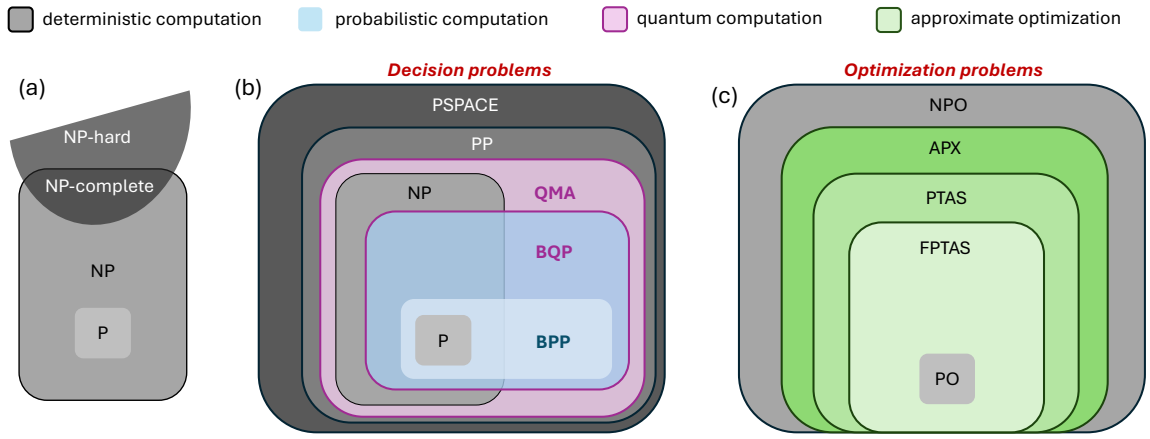

Figure 3.1. The inclusions of various complexity classes concerned with decision problems (b) and optimization problems (c). The well-known complexity classes concerning only deterministic computation are shown in (a).

unavailability of polynomial-time algorithms. These problems are also a test bed for quantum algorithms to be successful, such as Shor's algorithm [66].

Hard problems when asked for *exact* solution

Definition 10. **In classical machines.**

- Although finding a solution is difficult, *checking* if it is a solution can be done in polynomial time in classical machines
  1. **NP:** for decision problem (*nondeterministic polynomial* time),
  2. **FNP:** for relational/ functional problem,
  3. **NPO:** for optimizational problem, **NPO** $\subset$ **FNP**.
- **NP-complete:** If all other problems in **NP** can be efficiently reduced to it with a polynomial overhead in time. E.g.,- Travelling salesperson problem, graph coloring [215].
- **NP-hard:** If it is at least as hard as the hardest problems in **NP**, but not necessarily inside **NP** (see Fig. 3.1a).

Thus, **NP-complete** $\subset$ **NP** and **NP-complete** $\subset$ **NP-hard**.

In quantum machines.

- **QMA**: (*quantum Merlin-Arthur*) where the 'yes' instance can be verified efficiently and with high probability in a quantum computer (see Fig. 3.1b for its inclusion).

Average-case scenarios. Although one does not expect the quantum computer to solve **NP-hard** problems in the worst case, in the average-case settings, it can gain some advantage over a classical solver. In this context, two important concepts should be mentioned.

(a) Overlap Gap Property (OGP): Every two solutions that are *close* (within an additive error) to optimality are either close to each other or far from each other, thus exhibiting a fundamental topological discontinuity of the set of distances of near-optimal solutions [216]. Such behavior introduces average-case hardness in classical algorithms, though it is still possible to gain superpolynomial speedups in quantum computers.

(b) Computational statistical gaps: The underlying statistical problem is information-theoretically possible, although no efficient algorithm exists, rendering the problem essentially unsolvable for large instances [217].

Another interesting complexity class is **#P**[1], which emerges in the context of Gaussian Boson Sampling, and is interestingly related to stabilizer theory. It is con-

[1]The complexity class **#P** consists of functions $f : \{0,1\}^* \to \mathbb{N}$ for which there exists a non-deterministic polynomial-time Turing machine M such that for all inputs $x \in \{0,1\}^*$, the value $f(x)$ equals the number of accepting computation paths of M on input x. Formally,$f(x)$ = #accepting paths of $M(x)$ Equivalently, **#P** captures the complexity of counting the number of solutions to decision problems in **NP**.

cerned with counting the number of acceptable computation paths of an NP machine on input x. Its decision analogue is **PP**, and it is known that **QMA** $\subseteq$ **PP** [218].

3.2.2 Approximate solutions

If finding exact solutions efficiently were considered the marker of success, the field of computing would not have been motivating enough. In reality, finding an approximate solution close to the optimal one is often sufficient. Such consideration leads to the study of approximability, i.e., how hard it is to approximate solutions to various problems. Although it may seem that allowing approximate solutions would reduce the complexity of a problem, it is not that straightforward. Hence, it is essential to understand the hardness of approximation.

A longstanding result called the **PCP–theorem** informally says that, for many problems, computing an approximate solution with arbitrary precision is as hard as computing the exact solution. The approximate ratio, a ratio between the approximate solution and the optimal solution, quantifies the success of such an approximate solution. For many **NP-hard** problems, there exist some known inapproximability bounds. A famous example is the MaxCut problem by the Goemans and Williamson algorithm, which achieves ≈ 0.87856 [219], and there cannot exist a polynomial-time algorithm that can achieve better than this [220] under the assumption of the Unique Games Conjecture[2]. In such cases, if quantum computers can go beyond it, that would imply that quantum computers can solve **NP-hard** problems or that the Unique Games Conjecture is false.

when asked for *approximate* solution

Definition 11. Depending on the approximability in terms of the approximation ratio,

- **APX:** *approximable* if there are polynomial-time approximation algorithms with approximation ratios bounded by some constant c. Example.- MaxCut, MAX-3-SAT.
- **PTAS:** *polynomial-time approximation scheme* if it is guaranteed to find a solution in polynomial-time within an arbitrary $1 \pm \varepsilon$ factor of the optimum, $\varepsilon > 0$, thus the runtime is in polynomial time in system size. Example.- Euclidean Travelling Salesperson problem.
- **FPTAS:** *fully-polynomial time approximation scheme* if runtime is polynomial is both the problem size and $1/\varepsilon$. Example.- Knapsack problem.

Thus, **PO** $\subseteq$ **FPTAS** $\subseteq$ **PTAS** $\subseteq$ **APX** $\subseteq$ **NPO** [see Fig. 3.1(c)].

Understanding the complexity of approximability has consequences in many-body physics as well. For example, quantum **PCP**–conjecture [222–224] states that determining the ground state of a k-local hamiltonian is **QMA-complete** [225]. Even if one allows approximability, it can be **QMA-hard**.

[2]The conjecture postulates that problem of determining the approximate value of a certain type of game, known as a unique game, has **NP-hard** computational complexity [221].

The hardness of approximation suggests that quantum algorithms may outperform classical methods when there is a gap between known inapproximability bounds on classical algorithms and provable approximation factors.

3.3 Quantum optimization algorithms

Optimization problems are of different kinds, depending on the types of variables, objective functions, constraints, and allowed approximations. The choice of problem formulations also defines the solution strategy. Hence, some algorithms may only work on specific problem formulation classes. Quantum optimization algorithms are designed to solve optimization problems using a quantum hardware device, e.g.,- an analog or digital quantum computer. Thus, in such algorithms, it is crucial to encode the problem in quantum bits (or dits), such that it is possible to exploit quantum mechanical phenomena to obtain (possibly) better solution than its classical counterparts. Grover search [226] and the Quantum Adiabatic Algorithm (QAA) [227] are the prominent examples of exact quantum optimization algorithms, which are expected to require Fault-Tolerant Quantum Computing (FTQC) [150] due to the resulting circuit sizes. In the era of noisy quantum computers [87], one may expect to exploit quantum subroutines to accelerate known classical approximation algorithms. For instance, Semi-Definite Programming (SDP) relaxations [228], or more general variants of binary optimization problems, may profit from Quantum SDP solvers [229, 230]. Similarly, the so-called Variational Quantum Algorithms (VQAs) [231] work well in the noisy hardware, though there is no provable advantage.

In this thesis, we consider a particular type of problem known as unconstrained discrete optimization problems. There also exists a large class of other optimization problems, for example, constrained discrete optimization, continuous optimization (includes convex and non-convex optimization), mixed-integer programming, and dynamic programming (see [22] for a review).

3.3.1 Quadratic Unconstrained Binary Optimization (QUBO)

Quadratic unconstrained binary optimization (QUBO) is a foundational example of unconstrained discrete optimization [232–234], where the cost function is expressed as

$$\min_{x\in\{0,1\}^n} x^T Q x, \tag{3.2}$$

where x denotes the discrete decision variables, $Q \in \mathbb{R}^{n\times n}$ is the cost matrix, and $n \in \mathbb{N}$ is the number of decision variables. One can also consider higher-order polynomial objective functions known as PUBO (polynomial unconstrained binary optimization). Some ubiquitous problems, such as the maximum-cut (MaxCut) problem [see Fig. 4.1], are naturally formulated in this QUBO.

Complexity of QUBO problem

QUBO problems are **NP-hard**. Also **APX-hard**, i.e., there cannot exist a **PTAS** for QUBO unless **P=NP** [235].

A QUBO problem can be translated to an Ising-type Hamiltonian [232], where

finding an optimal solution is the same as finding the ground state of the Hamiltonian. Such a connection is fundamental to many quantum optimization algorithms. The variables $x \in \{0, 1\}$ is substituted with spin variables $z = 1-2x$, where $z \in \{-1, +1\}$. By replacing the spin-variables z by the operator, Pauli-Z matrices, resulting in a diagonal Hamiltonian $H \in \mathbb{R}^{2^n \times 2^n}$ and the problem looks similar to the Ising model [232]. Now, we will discuss two algorithms in detail: quantum annealing [227,236] and quantum approximate optimization algorithm [81,237].

3.3.2 Quantum annealing

Probably the first quantum computing approach introduced for solving QUBO-type problems was quantum annealing [227,238,239]. It is a quantum adiabatic algorithm method that specializes in finding the ground state of an Ising model by continuously evolving (*annealing*) from the known ground state of an *easy* Hamiltonian to the problem Hamiltonian. It is an exact optimization algorithm, reminiscent of homotopy methods of numerical mathematics[3].

The known solution is chosen as the eigenstate of the so-called mixing Hamiltonian, $\hat{H}_M$, which should have an easy-to-prepare ground state $|\psi_0\rangle$, and also has a non-zero overlap with the ground state of the problem Hamiltonian $\hat{H}_C$. Moreover, it should be non-commuting with the problem Hamiltonian, such that they do not have common eigenstates, and allow exploration of several eigenstates (hence, it is called *mixing* Hamiltonian). A common choice is

$$\hat{H}_M = \sum_{i=1}^{n} X_i, \text{ where } X_i = \cdots \otimes \underbrace{\begin{pmatrix} 0 & 1 \\ 1 & 0 \end{pmatrix}}_{i^{\text{th}}} \otimes \ldots, \tag{3.4}$$

having ground state $|+\rangle^{\otimes n} = \frac{1}{\sqrt{2^n}} \sum_{x \in \{0,1\}^n} |x\rangle$, i.e., n-qubit equal superposition state that has non-zero overlap with every computational basis state. Starting from $|\psi_0\rangle = |+\rangle^{\otimes n}$, quantum annealing slowly evolves the state according to the instantaneous Hamiltonian:

$$\hat{H}(t) = A(t)\hat{H}_C + B(t)\hat{H}_M. \tag{3.5}$$

This Hamiltonian $\hat{H}(t)$ is slowly evolved from $\hat{H}_M$ at $t = 0$ to the cost Hamiltonian H_C at $t = T$, whose ground state encodes the solution to the target problem (see Fig. 3.2), following the time-dependent Schrödinger equation:

$$i\frac{d\,|\psi_t\rangle}{dt} = H(t)\,|\psi_t\rangle\,. \tag{3.6}$$

I.e., $B(t)$ is slowly reduced from $B(0) = 1$ to $B(T) = 0$, and $A(t)$ is slowly increased from $A(0) = 0$ to $A(T) = 1$ (for simplicity, we choose $A(t) = t/T$ and $B(t) =$

[3] If one wishes to solve $f(\mathbf{x}) = \mathbf{0}$, then construct a system $g(\mathbf{x}) = \mathbf{0}$, whose solutions are known. For example, consider the *homotopy*:

$$H(\mathbf{x}, t) := (1-t)g(\mathbf{x}) + tf(\mathbf{x}) = \mathbf{0}. \tag{3.3}$$

By continuation, trace the paths starting from the known solutions of $g(\mathbf{x}) = 0$ to the desired solutions of $f(\mathbf{x})$. Such homotopy continuation methods are symbolic-numeric, where homotopy methods treat polynomials as algebraic objects and continuation methods use polynomials as functions [240].

$(1-t/T)$ throughout). According to the adiabatic theorem, if the time evolution is slow enough, the quantum state always remains in the ground state of the instantaneous Hamiltonian and reaches the solution state at the end of the sweep [236, 241].

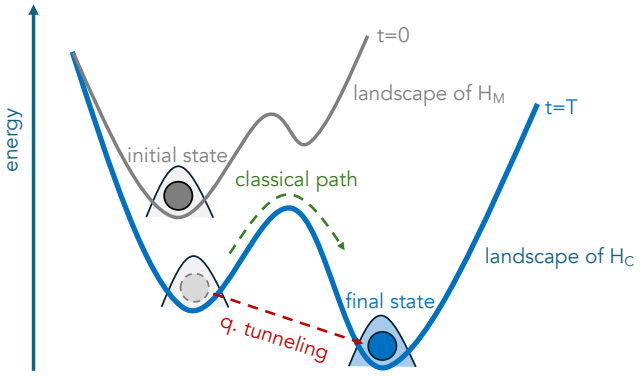

Figure 3.2. Scheme of quantum annealing: starting from the ground state of the mixer Hamiltonian at $t = 0$, and with evolution, the cost landscape approaches H_C, and then through quantum tunneling it can cross the energy barrier to reach the final state in the absolute minima, which is otherwise harder to obtain through a classical path.

In practice, quantum annealing requires a very long sweep to successfully reach the solution state, i.e., the corresponding circuits are deep and error-prone. To execute quantum annealing on noisy digital devices with limited coherence time, one can discretize the continuous evolution as a sequence of gates, resulting in a Trotterized quantum annealing (TQA). A first-order Trotter–Suzuki decomposition transforms the continuous sweep, up to $\mathcal{O}(\Delta t^2)$, into

$$e^{-i\Delta t\hat{H}(t)} \simeq e^{-i\beta\hat{H}_M} e^{-i\gamma\hat{H}_C}\,, \tag{3.7}$$

where $\beta = (1 - t/T)\Delta t$, and $\gamma = (t/T)\Delta t$. Discretizing the entire quantum annealing schedule into p time steps requires $\Delta t = T/p$. The resulting discretized annealing schedule is

$$\gamma_s = \frac{s}{p}\Delta t, \quad \beta_s = (1 - \frac{s}{p})\Delta t\,, \tag{3.8}$$

where the time-factor of t/T is replaced by the layer-number s/p. Crucially, unlike in quantum annealing, here Δt and the total time T can be modified independently by changing p, which hands us an additional control knob for TQA.

The performance of annealing depends on the total sweep time T, and if T is large enough, with a suitable annealing schedule, the Adiabatic Theorem guarantees that the state $|\psi_t\rangle$ always remains in the ground state of $H(t)$. To understand this in more detail, we estimate how close the time-evolved state is to the instantaneous ground state of $H(t)$. Let's denote the kth eigenstate of $H(t)$ as $|k(t)\rangle$ with eigenvalue $\varepsilon_k(t)$,

$$\hat{H}(t)|k(t)\rangle = \varepsilon_k(t)|k(t)\rangle. \tag{3.9}$$

Here, denote $|0(t)\rangle$ as the ground state, and other eigenstates are orthogonal to it. The above equation already gives us,

$$\langle j(t)|\frac{d}{dt}|k(t)\rangle = \frac{-1}{\varepsilon_j(t) - \varepsilon_k(t)}\langle j(t)|\frac{d\hat{H}(t)}{dt}|k(t)\rangle\,,\ j \neq k. \tag{3.10}$$

Now, when the instantaneous state is written as a superposition of energy eigenstates,

$$|\psi(t)\rangle = \sum_j c_j(t) e^{i\Delta t \phi_j(t)} |j(t)\rangle\,, \qquad \Delta t = T/p\,. \tag{3.11}$$

Then one can show that [242], the probability amplitude of being in the ground state is

$$c_0(t) \simeq 1 + \mathcal{O}(1/T^2), \tag{3.12}$$

and the error (i.e., contamination from higher excited states) is

$$c_{j\neq 0}(t) \simeq \frac{i}{T}[A_j(0) - e^{iT[\phi_j(t)-\phi_0(t)]} A_j(t)] + \mathcal{O}(1/T^2), \tag{3.13}$$

where $\phi_j(t) \equiv \int_0^t ds\ \varepsilon_j(s)$, and

$$A_j(t) \equiv \frac{1}{\Delta_j(t)^2} \langle j(t)| \frac{d\hat{H}}{dt} |0(t)\rangle\,, \tag{3.14}$$

where $\Delta_j(t) \equiv \varepsilon_j(t) - \varepsilon_0(t)$. Thus, the adiabaticity condition is written as

$$\frac{1}{\Delta_j(t)^2} \left| \langle j(t)| \frac{d\hat{H}}{dt} |0(t)\rangle \right| = \delta \ll 1 \Rightarrow T \sim \mathcal{O}(1/\Delta^2). \tag{3.15}$$

During annealing, the system can undergo phase transitions. In the spin-glass phases, the energy gap closes exponentially with system size, demanding an exponentially long runtime [243–245], which is often not possible, and hence we are limited to at most polynomial speedups.

In practical scenarios, quantum annealing is repeatedly run for a finite time [246], or potentially, diabatic annealing [247]. Thus, in its practical implementation, it often becomes a heuristic algorithm. In gate-based quantum computing, typical long annealing times imply notably long quantum circuits, which become challenging for NISQ devices.

3.3.3 Variational quantum algorithms

Due to the intrinsic noise and errors present in Noisy Intermediate-Scale Quantum (NISQ) devices, the behavior of the system often deviates from the idealized theoretical model. As a result, the parameter tuning that we aim to perform in an ideal setting does not translate directly to what is actually achieved on the hardware. In such cases, the so-called Variational Quantum Algorithms (VQAs) [231] have attracted a lot of attention. Such algorithms exploit the quantum hardware for the resource-intensive job of evaluating expectation values. Specifically, as Fig. 3.3 depicts, provided some problem data $\mathcal{D}$, a parametrized circuit $U(\vartheta)$ is empirically evolved in the quantum computer, and then from measurement in some basis $\{\mathcal{O}_k\}$ corresponding function $C(\vartheta)$ is evaluated. Thereafter, classical optimization of the variational parameters is executed over the experimentally-measured cost function to obtain updated parameters, which are used as feedback for the circuit.

As finding the optimal parameters in VQA is considered **NP**-hard [249], the classical optimization becomes the main bottleneck in VQA. Yet, it can still be useful in the path of finding good solutions, even potentially offering speedups [250].

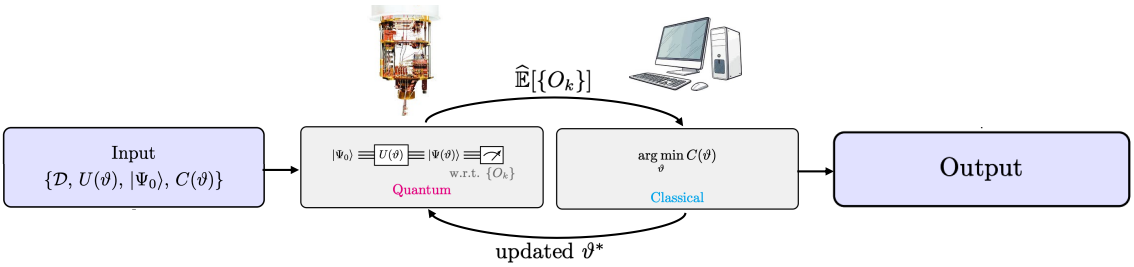

Figure 3.3. Variational algorithms iterate between the evaluation of experimental estimates of the expectations and classical optimization with updated parameters. (adapted from Ref. [248])

Barren plateaus [251]. The training of a parametrized circuit, i.e., finding the optimal parameters, is a major challenge, especially if the cost landscape becomes flat, the gradients concerning the parameters are exponentially small, and the optimization process cannot proceed. Formally, a cost function $C(\vartheta)$ exhibits a *probabilistic* barren plateau if, for some variational parameters $\theta_i \in \vartheta$, the variance of the partial derivative of the cost function vanishes exponentially in the number of qubits:

$$\mathrm{Var}_{\vartheta}[\partial_i C(\vartheta)] \in \mathcal{O}(b^{-n}), \quad b > 1. \tag{3.16}$$

This inequality immediately implies (due to Chebyshev's inequality) that the probability that it will find a gradient different than a given constant c is upper bounded,

$$\Pr\big[|\partial_i C(\vartheta)| \geq c\big] \leq \frac{1}{c^2}\mathrm{Var}_{\vartheta}[\partial_i C(\vartheta)]. \tag{3.17}$$

A type of VQA is the Variational Quantum Eigensolver (VQE) [252], which approximates the ground states of Hamiltonians and was initially proposed for quantum chemistry problems. Here, the job of a quantum computer is to evaluate $\langle\Psi(\vartheta)|\hat{H}|\Psi(\vartheta)\rangle$ for a given parameter value of ϑ. The variational principle guarantees that this expectation value is lower bounded by the ground state energy of H, and the equality is reached if and only if the ground state is reached:

$$\begin{aligned}\langle\Psi|\hat{H}|\Psi\rangle &= \sum_{\varepsilon_1,\varepsilon_2\in\mathrm{spec}(\hat{H})} \langle\Psi|\psi_{\varepsilon_1}\rangle\langle\psi_{\varepsilon_1}|\hat{H}|\psi_{\varepsilon_2}\rangle\langle\psi_{\varepsilon_2}|\psi\rangle \\ &= \sum_{\varepsilon\in\mathrm{spec}(\hat{H})} \varepsilon|\langle\psi_\varepsilon|\Psi\rangle|^2 \geq \sum_{\varepsilon\in\mathrm{spec}(\hat{H})} E_0|\langle\psi_\varepsilon|\Psi\rangle|^2 = E_0. \end{aligned} \tag{3.18}$$

3.3.4 Quantum Approximate Optimization Algorithm (QAOA)

A special class of VQE is the Quantum Approximate Optimization Algorithm (QAOA) [81], which has been successfully applied to several types of optimization problems in the last decade. QAOA is motivated by both quantum annealing and VQE. The standard QAOA applies p layers of unitaries

$$\hat{U}_k(\boldsymbol{\beta},\boldsymbol{\gamma}) = \exp\Big(-i\beta_k\hat{H}_M\Big)\exp\Big(-i\gamma_k\hat{H}_C\Big), \text{where} \quad k = 1,...,p\,, \tag{3.19}$$

to the ground state of a mixer Hamiltonian $\hat{H}_M$, e.g., $-\sum_i \hat{X}_i$ with $\hat{X}_i$ being a Pauli operator) to create the trial state $|\psi(\boldsymbol{\beta}, \boldsymbol{\gamma})\rangle$ (see Fig. 3.4). To obtain the optimal values of $\boldsymbol{\beta} = (\beta_1, \ldots, \beta_p)$ and $\boldsymbol{\gamma} = (\gamma_1, \ldots, \gamma_p)$, which minimize the energy $\langle\psi(\boldsymbol{\beta}, \boldsymbol{\gamma})|\hat{H}_C|\psi(\boldsymbol{\beta}, \boldsymbol{\gamma})\rangle$, a classical optimizer is employed. The energy is measured on the quantum processor to find the best solution.

Performance guarantee. QAOA appears as a promising candidate despite being a heuristic algorithm, because it comes with worst-case performance bounds for certain problems and algorithmic settings. For example, the MaxCut problem on a 3-regular graph, there is a lower-bound on the approximation ratio of 0.692 for $p = 1$ [81], 0.7559 for $p = 2$, and 0.7924 for $p = 3$ [253]. Moreover, for d-regular graphs, numerically QAOA outperforms many known Semi-Definite Programming (SDP)-based relaxations when $p \geq 11$ [254, 255].

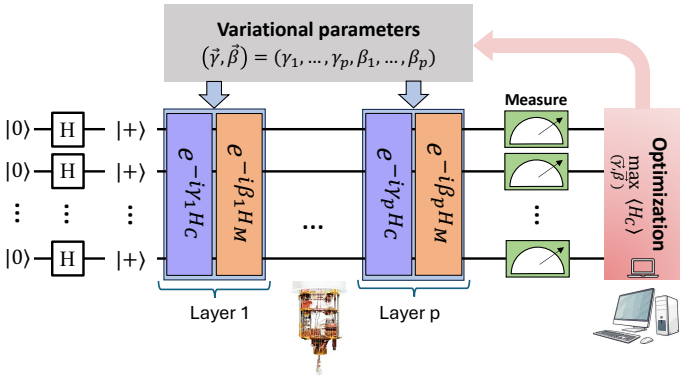

Figure 3.4. Structure of QAOA ansatz. Every layer consists of the cost Hamiltonian ($\hat{H}_C$) and the mixer Hamiltonian ($\hat{H}_M$) with corresponding variational parameters $\{\beta_k, \gamma_k\}$ for $k = 1, \ldots, p$.

Similar to any hybrid optimization algorithm, QAOA is also bottlenecked by the training of variational parameters. Hence, considerable research has been done on different training strategies for QAOA, e.g.,-

1. initialize with random parameters and optimize them by evaluating the cost function multiple times (conventional approach).

2. bound-search the parameter space of $(\vec{\beta}, \vec{\gamma})$ to certain regimes, depending on the symmetry of $\hat{H}_C$ and $\hat{H}_M$ (e.g., time-reversal symmetry, $\mathbb{Z}_2$ symmetry) [237].

3. using Physics-inspired initialization, e.g.,-

   (a) Trotterized quantum annealing inspired parameters [256].

   (b) linearly interpolate the curve formed by optimized parameters at depth p to extract a set of initial parameters for level $p + 1$ [237, 257].

   (c) machine learning based approaches [258, 259].

4. evaluating the cost-function classically using tensor networks or Clifford perturbation theory from empirically sampled solutions obtained in hardware, which is computationally easier than sampling the expectation value from the complete quantum state [260, 261].

5. using the concentration of parameters, where the optimal parameters become problem-instance independent, and reuse the parameters for multiple different

problem-instances by training on one of them [262–264]. Such a transfer of parameters can work for the problem of the same size and sometimes also for larger sizes. It is often helpful because one can train a small system classically and then apply it to a larger system where classical optimization is not possible. It also enables reasonable solutions to a problem quickly.

Recently, the Qiskit community has released a repository called *qaoa training pipeline* [265], which is a set of tools designed to generate optimal parameters for QAOA Ansatz circuits using classical means. In Chapter 6, we use the package to obtain optimal parameters for QAOA up to 76 qubits efficiently.

Variants of QAOA. Several variants of QAOA, depending on different mixers and initial states, have been proposed to achieve certain goals, see [266] for a review.

1. The Quantum Alternating Operator Ansatz encodes constraints into the mixer to preserve the constraints and to restrict the algorithm to feasible states [267].

2. Using a classical algorithm to obtain an approximate solution, and then using it to warm-start QAOA to further improve upon the obtained solution [268, 269].

3. Recursive QAOA uses the quantum computer to produce a sequence of reduced problems by fixing the strongest one, and at each step, QAOA estimates the correlation between variables. The process is iterated until the reduced problem becomes small enough for classical solvers [270].

4. ADAPT-QAOA [271] starts with a pool of candidate mixers. At each iteration, it selects the mixers from the pool that give the greatest gradient improvement to the cost function, instead of fixing the mixers beforehand.

Motivated by QAOA, the Mean Field Approximate Optimization Algorithm [272] is developed, where the QAOA circuit is approximated through mean-field approximations without any quantum effects.

3.4 Basics of quantum computation

In the upcoming sections, we will explore how to work with real quantum computers. To prepare for that, it is important to first introduce some fundamental concepts, terminology, and standard gate sets. Quantum computers aim to exploit the uniquely quantum mechanical properties of matter to process information in ways that classical computers cannot. Superposition enables quantum bits (qubits) to represent multiple states simultaneously, while entanglement allows for non-classical correlations that can be harnessed for computational advantages. A variety of physical platforms, including trapped ions [273], superconducting circuits [274], Rydberg atoms [275], and photonic systems [276], have been developed to realize quantum processors.

3.4.1 Quantum bits and gates

In classical computing, the fundamental bits of information are 0 and 1. Similarly, in quantum computation, the unit of information is encoded in two objects[4] They reside in the Hilbert space, where superposition is allowed. The two logical states, also known as qubits, defined in the two-dimensional Hilbert space $\mathcal{H}$ can be written as basis matrices of a 2-dimensional system. One popular choice is considering the eigenstates of the Pauli-Z matrix as a qubit basis, which are also known as the computational basis:

$$|0\rangle = \begin{pmatrix} 1 \\ 0 \end{pmatrix}, \quad |1\rangle = \begin{pmatrix} 0 \\ 1 \end{pmatrix}. \tag{3.20}$$

This allows us to write a generic state of a single qubit in the continuous space of its superposition,

$$|\psi\rangle = \alpha\,|0\rangle + \beta\,|1\rangle\,, \quad \alpha, \beta \in \mathbb{C},\ |\alpha|^2 + |\beta|^2 = 1. \tag{3.21}$$

Such superposition principle implies that the probability amplitude defines the state, not the probability, which means $(|0\rangle + |1\rangle)/\sqrt{2}$ and $(|0\rangle - |1\rangle)/\sqrt{2}$ are different state, despite them having same probability of occurring $|0\rangle$ and $|1\rangle$. In matrix notation, it is easy to see that they are orthogonal to each other, which is quite different from the classical world. Thus, the superposition of states allows us to define three sets of operators, whose eigenstates form one of the possible bases in the Hilbert space of a single qubit, with eigenvalues ± 1. Pauli matrices define the operators-

$$Z = \begin{pmatrix} 1 & 0 \\ 0 & -1 \end{pmatrix}, \ X = \begin{pmatrix} 0 & 1 \\ 1 & 0 \end{pmatrix}, \ Y = \begin{pmatrix} 0 & -i \\ i & 0 \end{pmatrix}. \tag{3.22}$$

We can represent a single-qubit state on the sphere, known as the Bloch sphere, where the coordinates denote the expectation value of $\sigma = X, Y, Z$, (see Fig. 3.5)–

$$|\psi\rangle = \cos\frac{\theta}{2}\,|0\rangle + e^{i\phi}\sin\frac{\theta}{2}\,|1\rangle\,, \quad \theta \in [0, \pi],\ \phi \in [0, 2\pi). \tag{3.23}$$

$$(x, y, z) = (\sin\theta\cos\phi, \sin\theta\sin\phi, \cos\theta). \tag{3.24}$$

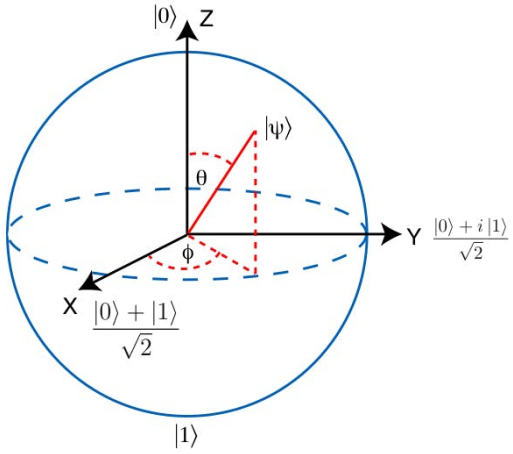

Figure 3.5. Bloch sphere: representation of the qubit state on sphere. At the opposite poles of the sphere along the axes, we find the eigenstates of the corresponding Pauli operator. Note that the orthogonal states $|0\rangle$ and $|1\rangle$ are $\theta = \pi$ away from other, contrary to the geometrical understanding of $\pi/2$. This is an artifact of SU(2) symmetry of spins instead of SO(2), and hence in Eq. (3.23), there is $\theta/2$ instead of θ.

Points lying on the surface of the sphere represent pure states, while mixed states

[4]It is not limited to two units only. A qudit generalizes the concept of a qubit ($d = 2$) to a quantum unit of information that exists in a d-dimensional Hilbert space.

lie inside the sphere. Computational basis states (corresponding to the eigenvectors of Pauli-Z) lie at the poles: $|0\rangle \leftrightarrow (0,0,1)$ and $|1\rangle \leftrightarrow (0,0,-1)$. The eigenstates of X are denoted by

$$|+\rangle = \frac{1}{\sqrt{2}}(|0\rangle + |1\rangle), \quad |-\rangle = \frac{1}{\sqrt{2}}(|0\rangle - |1\rangle)\,. \tag{3.25}$$

Similar to the logic-gates (OR, AND, etc) in classical computations, one can construct quantum gates in quantum computations that manipulate the state of qubits through mathematically defined, reversible transformations. These gates are represented by unitary matrices, which preserve the total probability (or norm) of the quantum system, a key feature of quantum mechanics. Quantum gates act on one or more qubits and are the building blocks of quantum circuits. The Pauli matrices, specifically Pauli-X, Y, and Z, are examples of single-qubit quantum gates.

Beyond the Pauli matrices, there are also other unitaries that are used as gate-sets for digital quantum computing, which allow the manipulation of qubits to modify their state. Any quantum algorithm can be reduced to a sequence of gates, called a quantum circuit, applied to a register of qubits.

Together with the identity operator, Pauli matrices form the basis of two-dimensional Hermitian matrices. Moreover, the Pauli matrices can also be used to generate a rotation of an arbitrary angle around the axes of the Bloch sphere:

$$\text{Rotation gates: } R_\sigma(\vartheta) = e^{-i\frac{\vartheta}{2}\sigma}, \quad \sigma \in \{X, Y, Z\} \tag{3.26}$$

Other single-qubit gates often used in quantum algorithms are :

$$\text{Hadamard } \hat{H} = \frac{1}{\sqrt{2}}\begin{pmatrix} 1 & 1 \\ 1 & -1 \end{pmatrix}, \quad \text{Phase } \hat{S} = \begin{pmatrix} 1 & 0 \\ 0 & i \end{pmatrix}, \quad \hat{T} = \begin{pmatrix} 1 & 0 \\ 0 & e^{i\pi/4} \end{pmatrix}. \tag{3.27}$$

They correspond to different quantum operations: the Hadamard-gate ($\hat{H}$) creates a superposition state, the phase-gate ($\hat{S}$) creates a phase in one of the superpositions, and the $\hat{T}(\pi/8)$-gates are used as non-Clifford resources.

If we expand this framework to a system composed of n-qubits, the Hilbert space of the system can be defined by the tensor product of the individual Hilbert spaces of each qubit:

$$\mathcal{H}_n = \bigotimes_{i=1}^{n} \mathcal{H}_i\,.$$

In such scenarios, there could be gates that act on more than one qubit simultaneously. In fact, two-qubit gates are necessary to create quantum correlation, for example, a CNOT gate. This gate conditionally inverts the state of the second (target) qubit depending on the state of the first (control). For example, if the control qubit is set to 0, the state of the target qubit is left unchanged; if the control qubit is set to 1, then the target qubit is flipped. Depending on the physical system used for their construction, it can be achieved by various types of gates, such as the controlled-Z (CZ) or the iSWAP gate.

$$\text{CNOT} = \begin{pmatrix} 1 & 0 & 0 & 0 \\ 0 & 1 & 0 & 0 \\ 0 & 0 & 0 & 1 \\ 0 & 0 & 1 & 0 \end{pmatrix}, \text{CZ} = \begin{pmatrix} 1 & 0 & 0 & 0 \\ 0 & 1 & 0 & 0 \\ 0 & 0 & 1 & 0 \\ 0 & 0 & 0 & -1 \end{pmatrix}, \text{iSWAP} = \begin{pmatrix} 1 & 0 & 0 & 0 \\ 0 & 0 & i & 0 \\ 0 & i & 0 & 0 \\ 0 & 0 & 0 & 1 \end{pmatrix}. \quad (3.28)$$

Notably, the CNOT gate is considered a fully entangling gate as it can transform a separable state into a maximally entangled one, resulting in the generation of one of the Bell states. For example, by acting on the Hadamard gate on the left qubit and then using the CNOT gate, we can obtain one of the Bell states,

$$|00\rangle \xrightarrow{H_0} \frac{1}{\sqrt{2}}(|00\rangle + |10\rangle) \xrightarrow{\text{CNOT}_{01}} \frac{1}{\sqrt{2}}(|00\rangle + |11\rangle)\,. \quad (3.29)$$

A circuit is defined through a set of gates applied in a given sequence:

$$|\psi\rangle = \left(\prod_k \hat{U}_{i_k j_k}(\vec{\theta}_k)\right)|\psi_0\rangle\ , \quad (3.30)$$

where $|\psi_0\rangle$ is an initial states (often it is $|0\rangle^{\otimes n}$), and $\hat{U}_{i_k j_k}(\vec{\theta}_k)$ denotes the unitary gate acting on qubits i_k and j_k with parameters $\vec{\theta}_k$, where k is the index of the gate.

3.4.2 Quantum measurements

Quantum measurement differs fundamentally from classical measurement in that it collapses a superposition of states into a single outcome, with probabilities governed by the system's wavefunction. Despite the probabilistic nature of quantum measurements, deterministic algorithms can still be implemented on a quantum computer. By executing the same algorithm multiple times and analyzing the resulting outcome distribution, one can extract reliable, deterministic results. Consequently, quantum computing often requires repeated execution of identical circuits to capture the full range of possible measurement outcomes. The accuracy and confidence in the results improve with the number of measurements performed.

Quantum measurement plays a central role in numerous quantum algorithms, such as quantum teleportation, error correction, and measurement-based quantum computation. In these protocols, measurement outcomes guide the choice of subsequent operations, allowing for the manipulation and transfer of quantum information. However, since measurements can introduce decoherence, reducing measurement-related errors is essential in designing reliable quantum algorithms. Additionally, post-processing methods are often required to interpret measurement results and correct for noise or inaccuracies.

To show the measurement process in quantum computing, we define a set of measurement operators $\{\hat{M}_m\}$, which act on the states being measured. The index m refers to the possible measurement outcomes. If $|\psi\rangle$ is the state of the quantum system immediately before the measurement, the probability of obtaining the result m is:

$$p(m) = \langle\psi|\hat{M}_m^\dagger \hat{M}_m|\psi\rangle\,, \quad (3.31)$$

and since the operator M_m is not unitary, the state after the measurement needs to be normalized:

$$|\psi'\rangle = \frac{\hat{M}_m|\psi\rangle}{\sqrt{\langle\psi|\hat{M}_m^\dagger\hat{M}_m|\psi\rangle}} \tag{3.32}$$

The measurement operators satisfy the completeness relation:

$$\sum_m \hat{M}_m^\dagger\hat{M}_m = \mathbb{I} \quad \Rightarrow \quad \sum_m p(m) = 1\,. \tag{3.33}$$

Let us now examine a straightforward example: the measurement of a qubit in the computational basis. This scenario involves two possible outcomes, represented by the measurement operators:

$$\hat{M}_0 = |0\rangle\langle 0|, \quad \hat{M}_1 = |1\rangle\langle 1|. \tag{3.34}$$

Assuming the qubit is in a general state $|\psi\rangle = \alpha|0\rangle + \beta|1\rangle$, the probability of obtaining outcome 0 is:

$$p(0) = \langle\psi|\hat{M}_0^\dagger\hat{M}_0|\psi\rangle = \langle\psi|\hat{M}_0|\psi\rangle = |\alpha|^2. \tag{3.35}$$

Similarly, the probability of measuring outcome 1 is given by:

$$p(1) = |\beta|^2. \tag{3.36}$$

Measuring observables

In quantum computing, information about a circuit is extracted by measuring observables, i.e., quantities associated with Hermitian operators, often constructed from Pauli matrices. Theoretically, the expectation value of an observable $\hat{O}$ is obtained as:

$$\langle\hat{O}\rangle = \langle\psi|\hat{O}|\psi\rangle\,. \tag{3.37}$$

In an experiment, the first measurement is executed by evaluating the probability of 0 or 1 along the z-basis (projection to the Z), and then it can be used to obtain the expectation value. For instance, the expectation value of the Pauli-Z operator for a single-qubit state is:

$$\langle\hat{Z}\rangle = \langle\psi|\hat{Z}|\psi\rangle = p(0) - p(1)\,. \tag{3.38}$$

Similarly, one can determine the expectation values of $\hat{X}$ and $\hat{Y}$ by first rotating the state into the respective bases and then measuring the computational basis. Hence, to measure the observable $\mathcal{O}$, one needs to find a unitary U such that $\mathcal{O} = U^\dagger ZU$. Then, projective measurement of the state is the same as measuring the expectation value $\langle Z\rangle$ as the states are represented in the computational basis.

$$\langle\psi|\,\mathcal{O}\,|\psi\rangle = \langle\psi|\,U^\dagger ZU\,|\psi\rangle = \langle\psi'|\,Z\,|\psi'\rangle \simeq p(0) - p(1)\,. \tag{3.39}$$

For example, in Tab. 3.1, we show how to measure different $\mathcal{O}$, using corresponding unitary rotations U.

This methodology naturally extends to multi-qubit systems. For example, to compute the expectation value of a product operator such as $\hat{Z}_i\hat{Z}_j$ on a two-qubit state, one multiplies the outcomes of the individual measurements on qubits i and j. For

Measurement operator ($\mathcal{O}$)	Unitary transformation (U)
Z	I
X	H
Y	$HS^\dagger$
$Z \otimes I$	$I \otimes I$
$1 \otimes Z$	SWAP

Table 3.1. Unitary transformation (U) for measuring observables ($\mathcal{O}$).

example,

$$\langle\psi|Z_1Z_2|\psi\rangle = p_1(0)p_2(0) - p_1(1)p_2(0) - p_1(0)p_2(1) + p_1(1)p_2(1), \tag{3.40}$$

where p_i denotes the probability corresponding to site i.

Tomography

As previously discussed, one can measure specific operators to infer about the features of the quantum state. One can similarly reconstruct the full state. Another hurdles come in noisy or mixed settings that are described by a density matrix (or density operator), which generalizes the concept of a wavefunction. Given a statistical ensemble of n pure states $|\psi_i\rangle \in \mathcal{H}$ with associated probabilities p_i, the density matrix is defined as:

$$\rho = \sum_{i=1}^{n} p_i |\psi_i\rangle\langle\psi_i| \tag{3.41}$$

The density operator is a Hermitian, positive semi-definite matrix with unit trace. When $n = 1$, the system is in a pure state. Otherwise, the state is mixed. One can distinguish between the two by evaluating:

$$\mathrm{Tr}(\rho^2) = \begin{cases} 1 & \text{for pure states}\,, \\ < 1 & \text{for mixed states}\,. \end{cases} \tag{3.42}$$

A general mixed state of a single qubit can be decomposed in terms of the Pauli matrices:

$$\rho = \frac{1}{2}\left(\mathbb{I} + \sum_{i=1}^{3} r_i \hat{\sigma}_i\right), \quad \hat{\sigma} = (\hat{X}, \hat{Y}, \hat{Z}). \tag{3.43}$$

Here, the vector $r = (\langle\hat{X}\rangle, \langle\hat{Y}\rangle, \langle\hat{Z}\rangle)$ represent the Bloch vector. If $|r| = 1$, the state lies on the surface of the Bloch sphere and is pure. If $|r| < 1$, it corresponds to a mixed state residing inside the sphere. By estimating the expectation values of the Pauli operators, one can reconstruct the full density matrix of a qubit. This process is known as *quantum state tomography* [277].

3.5 Superconducting quantum computer

The fundamental ingredients for quantum computers are qubits, two-level quantum systems, robust control of gates, and the ability to measure the final output. However, to retain the quantum properties, it is also important to isolate the system while

allowing accessibility to manipulate qubits in terms of gates as well as measurements. Regardless of the physical system used for the physical realization of a qubit, a qubit Hamiltonian is generally given by the following form:

$$H = c_z(t)\, Z + c_x(t)\, X + c_y(t)\, Y, \tag{3.44}$$

where X, Y, Z are Pauli matrices, and c_x, c_y, c_z are their respective tunable coefficients. For example, when considered a Harmonic oscillator kind of Hamiltonian, the first two levels can form the computational basis states, i.e., $|0\rangle$ and $|1\rangle$, and are separated by an energy difference $\hbar\omega_q$, where ω_q is the oscillator frequency. In this case, $c_z = \hbar\omega_q$. This term produces rotations around the z-axis of the Bloch sphere, representing phase gates. On the other hand, by manipulating the coefficients $c_x(t), c_y(t)$, a qubit can oscillate between the two states, performing arbitrary single-qubit rotations. Different physical systems can be used to implement a qubit, such as photons, electrons, ions, or neutral atoms. Rather than exploring all quantum platforms in detail, we focus on superconducting qubits, utilized in IBM's quantum devices, where our experiments are conducted. In this section, we provide a brief introduction to the topic, primarily following Krantz et al. [274] as the primary reference.

The superconducting qubits are implemented using electrical circuits, typically arranged in two-dimensional layouts, while the third dimension is reserved for interfacing with control and readout hardware. To understand how a superconducting qubit circuit works, it is useful to first understand how a linear LC resonant circuit works [Fig. 3.6(a)]. Due to the presence of both the capacitor (C) and inductor (L), the energy oscillates between the electric energy of C (think of it as kinetic energy of electrons) and the magnetic energy of L (potential energy of the oscillator). From here, one can see that the instantaneous energy is defined from the current and voltage of the capacitor or inductor,

$$E(t) = \int_{-\infty}^{t} V(t')I(t')dt'. \tag{3.45}$$

Similarly, we can define the flux as the time integral of the voltage

$$\Phi(t) = \int_{-\infty}^{t} V(t')dt'. \tag{3.46}$$

Now using the relations, $V = L\frac{dI}{dt}$ and $I = C\frac{dV}{dt}$, we can write the energy terms for the capacitor and inductor in terms of the node flux:

$$T_C = \frac{1}{2}C\dot{\Phi}^2, \quad U_L = \frac{1}{2L}\Phi^2. \tag{3.47}$$

From here, we can define the Lagrangian as $T_C - U_L$, and can derive the Hamiltonian using Legendre transformation as [274],

$$H = \frac{1}{2}CV^2 + \frac{1}{2}LI^2, \text{ with } \omega = \frac{1}{\sqrt{LC}}. \tag{3.48}$$

We can further introduce the reduced charge $n = Q/2e$ and reduced flux $\phi = 2\pi\Phi/\Phi_0$ to obtain the Hamiltonian in terms of $E_C = e^2/(2C)$ and $E_L = (\Phi_0/2\pi)^2/L$, in the

quantized form as

$$\hat{H} = 4E_C\hat{n}^2 + \frac{1}{2}E_L\hat{\phi}^2\,. \tag{3.49}$$

Here, $\Phi_0 = h/(2e)$ is the superconducting magnetic flux quantum, and the number operator $\hat{n}$ is the excess number of Cooper pairs. In this quantum scenario, $[\hat{\phi}, \hat{n}] = i$, and one can get Harmonic oscillator [Fig. 3.6(b)],

$$\hat{H} = \hbar\omega_r(\hat{a}^\dagger\hat{a} + \frac{1}{2}), \quad \omega_r = \sqrt{8E_LE_C}/\hbar\,, \tag{3.50}$$

where $\hat{a}^\dagger(\hat{a})$ are the usual creation (annihilation) operator.

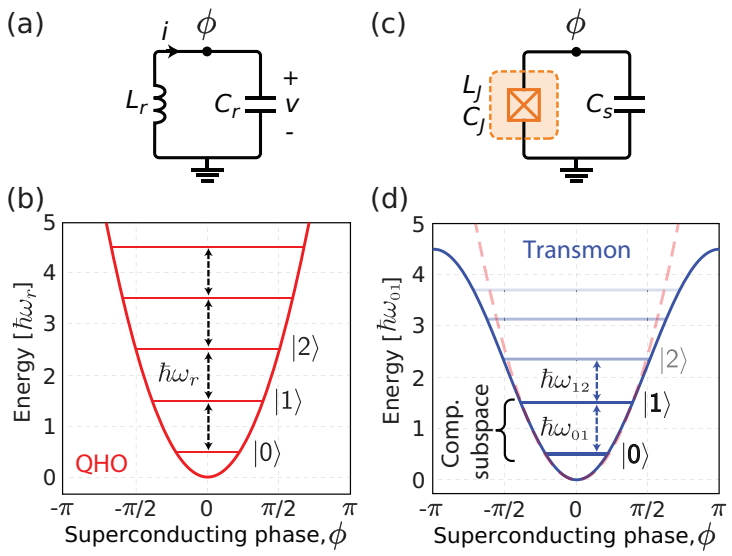

Figure 3.6. (a) Circuit for a parallel LC-oscillator. The superconducting phase on the island is denoted as ϕ, referencing the ground as zero. (b) Energy potential for the quantum harmonic oscillator, where energy levels are equidistantly spaced $\hbar\omega_r$ apart. (c) Josephson qubit circuit, where the nonlinear inductance L_J is shunted by a capacitance, C_s. (d) The Josephson inductance makes the potential anharmonic, forming a computational subspace of $|0\rangle$ and $|1\rangle$ (Taken from Ref. [274]).

However, in this case, the level spacing of all the energy levels is equal, and hence there could be transitions to other higher levels by using the same frequency of ω_r. To mitigate this problem of unwanted dynamics involving non-computational states, we need to introduce non-linearity (anharmonicity) into the system, which can be achieved by using a Josephson junction that serves as a nonlinear inductor. The energy corresponding to it can be derived using two relations,

$$I = I_c \sin\phi, \quad V = \frac{\hbar}{2e}\frac{d\phi}{dt}, \tag{3.51}$$

resulting in a modified Hamiltonian, making the energy spectrum non-degenerate [Fig. 3.6(d)]–

$$\hat{H} = 4E_C\hat{n}^2 - E_J\cos\hat{\phi}. \tag{3.52}$$

Here, $E_C = e^2/(2(C_s+C_J))$ is the total capacitance, including both shunt capacitance C_s and the self-capacitance of the junction C_J, and $E_J = I_c\Phi_0/2\pi$ is the Josephson energy, I_c being the critical current of the junction. The system dynamics is governed by the E_J/E_C ratio. As the community has realized that charge noise is more challenging to mitigate than flux noise, it is often chosen as $E_J \gg E_C$. Additionally, current experimental technology enables greater flexibility in engineering the E_J component. To achieve this limit, one approach is to make E_C small by shunting the junction with

a large capacitor $C_s \gg C_J$ [see Fig. 3.6(c)], which is known as the *transmon qubit*[5]. In this limit, one can express the state in terms of the superconducting phase ϕ, and the ϕ does not fluctuate much. In such scenario, we can expand the $\cos\phi$ in power series,

$$E_J \cos\phi = \frac{1}{2}E_J\phi^2 - \frac{1}{24}E_J\phi^4 + \mathcal{O}(\phi^6). \tag{3.53}$$

Now, the qubit frequency becomes $\omega_q = (\sqrt{8E_JE_C} - E_C)/\hbar$. The excitation to higher states can be suppressed either by a large enough anharmonicity or by using robust control techniques, and thus, one can achieve a two-level system

$$\hat{H} = \frac{\omega_q}{2}\hat{Z}. \tag{3.54}$$

In practice, several architectures for superconducting quantum computers exist, such as frequency-tunable qubits [279], fixed-frequency qubits with static couplings [280], and fixed-frequency qubits with tunable coupling elements [281, 282].

3.6 Quantum stack for running on a quantum computer

Executing quantum optimization on noisy devices requires specialized tools and best practices to achieve good results from the hardware. We focus on gate-based cloud computing platforms, where quantum algorithms theorists can directly test their algorithms on hardware. In abstract design, Fig. 3.7 describes the common stages of the quantum stack, which also helps us to understand where scalability and performance bottlenecks arise.

At the highest level of the quantum computing stack lies a conceptual representation of the algorithm, such as abstract, hardware-agnostic, and built from mathematical formulations and logical structures tailored to solving a specific problem. As this algorithm progresses through the stack, a transpilation process transforms it into a hardware-compatible circuit by translating abstract operations into executable instructions for the chosen quantum platform. During this phase, additional circuit elements may be added or adjusted to support error mitigation. Next, a pulse-level compiler further refines these instructions into precise electromagnetic pulses designed to manipulate quantum states and carry out the intended computation. This transformation from abstract logic to physical execution highlights how the algorithm evolves across layers of the stack, with each stage providing opportunities to optimize performance on noisy quantum hardware.

3.6.1 Adjusting quantum problems and algorithms

From a pen-and-paper abstract circuit to hardware-aware quantum problems or problem-dependent circuit structures— these are crucial in mitigating the effects of noise at the lower level of the quantum stack. For example, a problem with more qubits and low connectivity could have a lower noise effect compared to a model with densely

[5]The name transmon comes from 'transmission-line shunted plasma oscillation qubit' [278]. The suffix *-mon* refers to its similarity to the Cooper pair box (often called a quantronium) and its oscillatory behavior, reminiscent of other artificial atoms like the fluxmon or phasemon. The *trans-* prefix highlights the addition of a large shunting capacitance that suppresses charge noise, transforming the charge qubit into a more stable, weakly anharmonic oscillator.

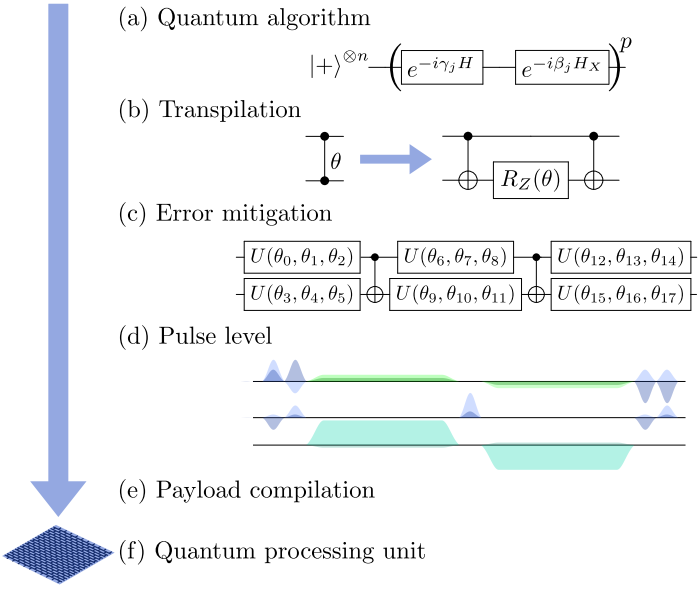

Figure 3.7. Abstract levels of quantum stack from quantum algorithm to quantum processing unit (QPU). (a) Quantum algorithm in high-level quantum circuit, (b) Circuit transpiled to native-gate sets of the QPU, (c) Error mitigation methods, (d) QPU is instructed with physical pulses corresponding to the native-gate instructions, (e) finally, the circuit is compiled into QPU-executable waveforms, (f) which are run on the QPU (taken from Fig.4 of [248]).

connected variables. Alternatively, one can project a fully-connected QUBO problem onto the sparse connectivity of a quantum computer [283].

To efficiently utilize the quantum resources in the hardware, it is often helpful to select the algorithms wisely. For example,

- Warm-start can reduce the number of QAOA layers [268, 269].
- Including the constraints of the optimization problem in the mixer instead of the cost function [267].
- Counter-diabatic terms can improve the quality of the solution [284].
- Using circuit-cutting to reduce the depth and fight against coherence time [285].

Nevertheless, it is crucial from a hardware perspective to choose the methods that limit the final circuit depth and gate counts, without reducing the solution quality.

3.6.2 Transpilation

A transpiler plays a crucial role in quantum computing by converting a quantum circuit into another version that adheres to the constraints and capabilities of the target quantum hardware. This transformation typically results in a lower-level circuit expressed in domain-specific languages for continuous-variable platforms. Because every quantum device has unique physical and architectural characteristics, transpilers must be adapted to each hardware platform to ensure optimal performance.

To generate circuits that can be executed effectively on a given device, the transpilation process must consider several constraints, including the hardware's native gate set and the qubit connectivity. For the NISQ devices, additional factors, such as gate error rates, qubit decoherence times (e.g., T_1 and T_2)[6], and cross-talk play a significant role. Thus, the effectiveness of the transpiler has a substantial impact

[6] T_1, or relaxation time, is the average time it takes for a qubit to decay from the excited state $|1\rangle$ to the ground state $|0\rangle$. T_2, or dephasing time, measures how long a qubit maintains phase coherence between the states $|0\rangle$ and $|1\rangle$. T_2 is always less than or equal to T_1, and both are critical for determining how long quantum information can be stored and manipulated reliably.

on both the total gate count and the overall execution fidelity of the algorithm on hardware.

```
# Tips: Check your gate counts and circuit depth after transpilation
print("Gate Counts:", qc.count_ops())
print("Circuit Depth:", qc.depth())
```

Generally, the transpilation process involves three main steps:

1. Qubit selection

This step is influenced by both the hardware's characteristics and the specific requirements of the algorithm. When not all qubits on the chip are needed, it is advantageous to select the most reliable ones based on a suitable performance metric. Metrics might include gate fidelity [286], cross-talk levels [287], or layer fidelity [288], depending on the circuit's structure. For circuits dominated by two-qubit operations, choosing qubits with high two-qubit gate fidelity is appropriate [286]. Conversely, if the algorithm requires many mid-circuit measurements, measurement fidelity should influence the selection [289]. In some quantum optimization problems, individual decision variables are mapped to specific qubits, and the mapping itself can affect the circuit depth [290].

```
## Qubit selection
import networkx as nx
import numpy as np
from typing import Tuple, Dict, List, Any
from networkx.algorithms.isomorphism import GraphMatcher

def make_subgraph(num_qubits: int) -> nx.Graph:
    """Example: Constructs linear structure."""
    edges = [(i, i + 1) for i in range(2 * num_qubits - 1)]
    return nx.from_edgelist(edges)

def evaluate_mapping(graph: nx.Graph, mapping: Dict[int, int], backend:
↪  Any) -> Tuple[float, List[int]]:
    """
    Computes circuit fidelity based on gate errors and returns the list of
    ↪  measured physical qubits.
    """
    reverse_map = {v: k for k, v in mapping.items()}
    fidelity = 1.0
    for edge in graph.edges():
        physical_edge = (reverse_map[edge[0]], reverse_map[edge[1]])
        try:
            gate_error = backend.properties().gate_error("ecr",
            ↪  physical_edge)
        except:
            gate_error = backend.properties().gate_error("ecr",
            ↪  physical_edge[::-1])
        fidelity *= (1 - gate_error)
    # All logical qubits are measured now
```

```
    measured_qubits = list(mapping.values())
    return fidelity, measured_qubits

def find_best_qubits(
    num_qubits: int,
    backend: Any,
    minimum_fidelity: float,
    readout_threshold: float = 0.99
) -> Tuple[int]:
    """
    Returns the best mapping tuple that satisfies fidelity and readout
    ↪ threshold.
    If no mapping meets criteria, returns an empty tuple and prints a
    ↪ message.
    """
    logical_graph = make_subgraph_for_two_copies(num_qubits)
    hardware_graph = nx.from_edgelist(backend.coupling_map.get_edges())
    matcher = GraphMatcher(hardware_graph, logical_graph)

    used_qubits = set()

    for mapping in sorted(matcher.subgraph_isomorphisms_iter(), key=lambda
    ↪ m: hash(frozenset(m.items()))):
        ordered_mapping = tuple(mapping[i] for i in range(2 * num_qubits))
        if set(ordered_mapping) & used_qubits:
            continue

        fidelity, measured_qubits = evaluate_mapping(logical_graph,
        ↪ mapping, backend)

        readout_fidelities = [
            1 - backend.properties().readout_error(q) for q in
            ↪ measured_qubits
        ]
        avg_readout = np.mean(readout_fidelities)

        if fidelity >= minimum_fidelity and avg_readout >=
        ↪ readout_threshold:
            print("map_used:", ordered_mapping)
            return ordered_mapping

        used_qubits.update(ordered_mapping)

    print("No valid mapping found above fidelity and readout thresholds.")
    return ()

```

2. Gate decomposition

In this phase, high-level operations are broken down into sequences of native gates supported by the hardware [291–293]. Achieving this requires a universal gate set [294], and the choice of decomposition strategy depends on the desired trade-off between circuit accuracy and depth. Some techniques are exact, while others allow for approximations that reduce gate count and depth at the cost of some fidelity. For instance, exponentials of Pauli operators can be implemented using Pauli-Z rotations along with local two-qubit gates and single-qubit Clifford gates [295]. In noisy environments, approximate compilation methods may be preferred to keep the circuit shallower [296, 297].

```
# transpile from the qc to backend using basis_gates
transpile(qc,
          basis_gates= backend.basis_gates,
          initial_layout=[idx for idx in range(0,n_qc,1)]),
          [idx for idx in range(0,n_qc,1)],
          inplace=True)
```

3. Qubit routing

Limited connectivity between qubits requires routing strategies to enable interactions between non-adjacent qubits. This typically involves inserting SWAP gates to bring qubits into proximity. General-purpose routing algorithms exist for arbitrary circuits [298–300]. However, some quantum algorithms, such as QAOA, produce structured circuits with blocks of commuting two-qubit gates. Leveraging this structure allows for more efficient routing and shallower circuits [290, 301–303]. Still, when the problem graph is denser than the hardware's coupling map, a larger number of SWAP gates may be needed, increasing depth [301]. Consequently, quantum algorithms that map to sparse graphs tend to perform better on devices with limited connectivity [286, 304], highlighting the importance of identifying classically complex problems that remain sparse.

Some modern hardware platforms support dynamic circuits, which include mid-circuit measurements and conditional logic executed within the coherence time of the qubits [305]. These capabilities can be leveraged to address connectivity issues more efficiently [306]. For example, a QAOA circuit that would traditionally require SWAP operations to respect the layout of a grid-like coupling map can be replaced with a constant-depth implementation that uses auxiliary qubits at a quadratic overhead [307]. This area is still under active research, with the intention of reducing both circuit depth and width.

It is also important to note that hardware limitations vary across quantum technologies. For example, trapped-ion systems often feature all-to-all qubit connectivity, which allows them to execute dense circuits without increasing depth [308]. However, these systems currently scale to fewer qubits than superconducting platforms, limiting the size of problems they can handle.

3.6.3 Error suppression and mitigation

Once a quantum circuit has been transpiled, it may be further modified to incorporate instructions aimed at suppressing or mitigating errors.

Error suppression reduces the effects of noise in quantum circuits without requiring additional measurement shots. A well-known method in this category is Dynamical Decoupling (DD), which mitigates non-Markovian noise by inserting additional pulses during idle times in a circuit [309–311]. This can improve circuit performance with minimal resource overhead. However, when the transpiled circuit is dense, such as in QAOA circuits employing SWAP networks [286], the limited idle time may restrict the use of DD. In contrast, circuits with longer idle periods, such as those native to hardware with heavy-hex connectivity, can benefit substantially from DD [312].

> Dynamical decoupling (DD) is a family of open-loop quantum control techniques used to suppress dephasing in quantum systems by averaging out environmental noise through time-dependent control pulses. It originates from refocusing techniques in NMR (like spin-echoes) and involves applying a carefully timed sequence of unitary control pulses to reverse or cancel out the effect of unwanted system-environment interactions.

```
# using dynamical decoupling
from qiskit.circuit.library import XGate
from qiskit.transpiler import PassManager, InstructionDurations
from qiskit_ibm_runtime.transpiler.passes.scheduling import
 ↪  ALAPScheduleAnalysis, PadDynamicalDecoupling

durations = InstructionDurations.from_backend(backend)
dd_sequence = [XGate(), XGate()]
pm = PassManager([ALAPScheduleAnalysis(durations),
                  PadDynamicalDecoupling(durations, dd_sequence)])
circ_dd = pm.run(tqc)
```

Error mitigation methods aim to reduce the impact of noise by applying classical pre- and post-processing around the quantum circuit execution. These approaches do not require full-scale quantum error correction, which involves encoding logical qubits into large arrays of physical ones [313]. While error mitigation does not eliminate errors, it can enhance computational results at a lower classical cost [314–316]. Common techniques in this category include Probabilistic Error Cancellation (PEC) [317] and Zero-Noise Extrapolation (ZNE) [44, 315, 318, 319], both of which are designed to yield more accurate expectation values.

- PEC involves characterizing the noise channel Λ associated with layers of Pauli-twirled gates [317]. Although the inverse channel Λ^{-1} is non-physical, it can be approximated using quasi-probability decompositions to yield an unbiased estimate of a noiseless observable O. The trade-off is a variance increase by a factor of γ^2, where $\gamma \geq 1$ reflects the strength of the noise in the learned model and serves as a proxy for the circuit's execution fidelity. The value of γ is closely

related to metrics like Layer Fidelity (LF) and Error Per Layered Gate (EPLG), which characterize hardware noise in large-scale systems [288]. If the average noise factor per qubit is $\bar{\gamma}$, then a circuit with n qubits and d layers will incur a mitigation cost scaling as $\bar{\gamma}^{2\times n\times d}$. PEC becomes impractical for large-scale circuits due to its exponential variance overhead; for instance, applying PEC to 60 CNOT layers on 127 qubits yielded a γ^2 value of 10^{128} in Kim *et al.* [44]. To address this, Probabilistic Error Amplification (PEA) was introduced [44], which instead amplifies the learned noise to enable extrapolation, potentially reducing bias in the final estimate. PEA and PEC are particularly efficient when circuits consist of a small number of repeating gate layers, as is the case with SWAP-network-based designs [301].

- ZNE, on the other hand, estimates the zero-noise expectation value by executing equivalent circuits at different noise levels and extrapolating the results. Early implementations involved pulse stretching [315], which introduced significant calibration overhead, or gate folding, which increased circuit depth. Newer strategies, such as partial gate folding [320] and pulse-level techniques like cross-resonance stretching [321], help reduce these drawbacks. Unlike PEC, ZNE's resource requirements do not scale with the problem size, although deep circuits limit the stretch factors that can be used effectively (see sec. 6.3.1 for an example).

Zero Noise Extrapolation (ZNE) works by deliberately increasing the noise in a quantum circuit, typically through methods like gate folding, then executing the circuit at multiple noise levels and mathematically extrapolating the results back to the zero-noise limit using polynomial or exponential fits. This allows us to approximate the expected value of observables as if they were measured on a perfect quantum computer. ZNE was first formally introduced by Temme et al. [314], and has since become a widely adopted approach in the NISQ era. As an example, see Fig. 3.6.3.

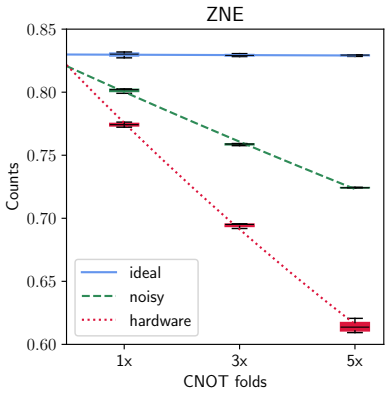

Figure 3.8. Example of ZNE. 1x CNOT folds represent the actual data, and then 3x and 5x imply that the number of CNOTs is increased without changing the unitary to incorporate the effect of noise coming from the CNOT gates. Then by extrapolation, we can look at 0x noise, or the *noiseless* case, where it approaches close to the ideal (noiseless) data.

- Conditional Value at Risk (CVaR). Due to noisy hardware, the estimation of energy can be biased by the bad samples, and then minimizing it would not provide a good solution. Instead, if one cares about sampling good solutions, then one can use alternative cost functions to increase the robustness against noise or relax the requirements on an ansatz. In CVaR, good samples are sorted by taking the best α-fraction of samples, where $\alpha = 1$ corresponds to the full expectation value and $\alpha = 0$ corresponds to the single best observed sample. By

choosing α based on the noise of the device, CVaR can provably bound noise-free expectation values [322].

Expectation-value-based mitigation methods like PEC and ZNE are especially valuable during variational parameter optimization [286, 315]. However, for quantum optimization tasks that require generating high-quality samples, e.g., finding a bit-string x that minimizes a cost function $f(x)$. It is essential to mitigate noise not just in expectation values but in actual circuit outputs. Therefore, advancing techniques that can produce noise-resilient samples will be critical to the success of QAOA.

3.7 Hardware benchmarks

Quantum hardware performance is commonly characterized by three primary aspects: scale, quality, and speed [323].

Scale refers to the total number of available qubits.

Quality encompasses both low-level device metrics, such as qubit coherence times and gate fidelities, and more comprehensive indicators like Layer Fidelity (LF), Error per Layered Gate (EPLG) [288], Quantum Volume (QV) [324], and the γ and average $\bar{\gamma}$ parameters from Probabilistic Error Cancellation (PEC) [317]. For instance, a QPU with a QV of 2^n can reliably execute an n-qubit circuit with n layers of random SU(4) gates [324] [see Fig. 4.6], effectively capturing performance contributions from gate fidelities, qubit connectivity, and the effectiveness of noise suppression and mitigation techniques.

However, these quality-focused metrics do not reflect the *speed* at which quantum computations are performed. Speed is a critical factor for optimization tasks, especially when a quantum device is expected to outperform classical systems by delivering high-quality solutions more quickly. Moreover, faster execution allows for more accurate observable estimates within time constraints and helps pay off the cost of error mitigation techniques, which typically require additional sampling. To address this, the Circuit Layer Operations Per Second (CLOPS) metric was introduced as a quantum analog to classical FLOPS. CLOPS quantifies a device's throughput by measuring how many layers of gates can be executed per unit time, including the classical overhead involved in updating circuit parameters. This makes CLOPS especially relevant for variational workloads where runtime is dominated by repeated circuit executions with parameter updates.

Metrics like QV, EPLG, and CLOPS are designed to provide general-purpose benchmarks that allow comparisons across different quantum hardware platforms and to monitor progress over time. For example, on *ibm_kingston*, EPLG and CLOPS are reported as 0.113% and 250000, respectively (see Fig. 3.9). While these figures offer useful insight, they are ultimately only proxies and may fall short in predicting real-world performance on specific tasks.

The most informative benchmark for a quantum processor is its performance on application-relevant tasks, evaluated using the appropriate performance criterion, be it solution quality, execution time, or sample efficiency. In this context, our research in Chapter. 4 shows that the ability to generate spin-squeezed states is directly related to solving fully connected MaxCut instances with QAOA [325]. As many quantum algorithms are heuristic in nature, we anticipate the growing importance of problem-specific benchmarking frameworks that more accurately reflect their practical utility.

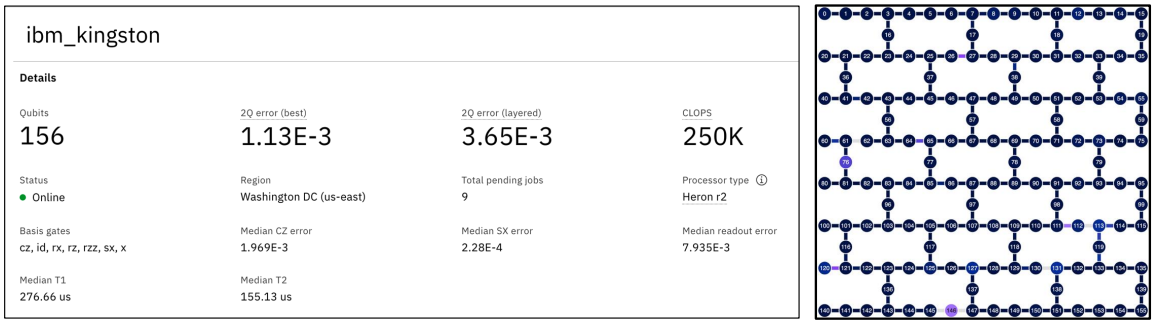

Figure 3.9. Benchmarking properties of *ibm_kingston*: 2Q error (EPLG), CLOPS, and readout error are among the most important metrics. Right: One can also decide which qubits to choose by looking at the quality of the connectivity (CZ error) and readout error.

3.8 Summary

This chapter provides an overview of quantum optimization, a major focus of this thesis. To identify where quantum advantage may emerge, we begin by reviewing quantum computational complexity classes. We then introduce key quantum optimization algorithms, including quantum annealing, relevant to Chapter 5, and the quantum approximate optimization algorithm (QAOA), which plays a central role in Chapters 4, 6, and 7. In the final section, we discuss tools and techniques for implementing quantum algorithms on noisy quantum devices, which are employed in Chapter 6.

Part II

Resources in Quantum Optimization

Chapter 4

Squeezing and quantum approximate optimization

where quantum metrology meets quantum optimization

4.1 Introduction

The Quantum Approximate Optimization Algorithm (QAOA) [326] is a promising approach for solving combinatorial optimization problems using digital quantum computers [327, 328] as discussed in Chapter 3. It uses constructive interference to find solution states [329], and it has better performance than finite-time adiabatic evolution [330]. However, such a hybrid algorithm heavily uses classical optimization techniques to obtain suitable parameters, and one may wonder if quantum effects, such as entanglement, play a role in QAOA.

Here, we show how concepts from quantum metrology shed light on this question through squeezing and how it connects to the performance of QAOA. Illustratively, the connection is established through the insight that (a) the aim of QAOA is to obtain the ground state as precisely as possible, while (b) quantum metrology leverages entanglement between particles to generate states that permit precision beyond the capacities of any comparable classical sensor [331–333]. For example, squeezed states can increase sensitivity for detecting phases [334], magnetic fields [335], and gravitational waves [336]. The most sensitive states for phase estimation are Dicke states [332, 337], where all qubits are equally entangled. We substantiate this connection through numerically exact calculations and data gathered on IBM Quantum hardware with up to eight qubits. Our analysis shows how the search for an optimal solution to the MaxCut problem on a complete graph through QAOA generates Dicke states, with squeezing [338, 339] and multipartite entanglement [139, 140]. Based on this, we propose the amount of squeezing generated as an application-tailored performance benchmark of QAOA, which is able to capture the depth dependency of QAOA better than quantum volume [324, 340, 341], and can be used to detect errors. Our work thus further strengthens the intimate links between quantum metrology and quantum information processing [132, 342–344]. Moreover, we show that warm-starting the optimization of a weighted MaxCut problem with a squeezed state can provide enhanced performance. We also discuss the parameter regimes, compared for different platforms, where a metrological task using a multi-party-entangled squeezed state generated through QAOA could become advantageous over fast repetitions with simple unsqueezed states.

In the rest of this chapter, we first provide some background on the MaxCut problem and spin-squeezing. Then, QAOA is formally connected to the generation of en-

tangled squeezed states (Sec. 4.4), which was subsequently demonstrated numerically. Based on squeezing, then, we develop a benchmark tailored for QAOA (Sec. 4.5), and assess the ability of superconducting qubits to run QAOA on fully connected problems while simultaneously creating Dicke states and estimating the number of entangled particles (Sec. 4.6). Finally, we extend this connection for application in metrology and quantum optimization (Sec. 4.7).

4.2 MaxCut problem in QAOA

Recall from sec. 3.3.1 that universal quantum computers can address hard classical problems such as quadratic unconstrained binary optimization (QUBO), which is defined through

$$\min_{x\in\{0,1\}^n} x^T\Sigma x \quad \text{with } \Sigma \in \mathbb{R}^{n\times n}. \tag{4.1}$$

Then, the binary variables x_i are mapped to qubits through $x_i = (1-z_i)/2 \rightarrow (1-\hat{Z}_i)/2$, where $\hat{Z}_i$ is a Pauli spin operator with eigenstates $|0\rangle$ and $|1\rangle$. The result is an Ising Hamiltonian $\hat{H}_C$ whose ground state is the solution to Eq. (4.1) [345]. The standard QAOA then applies p layers of the unitaries $\exp\left(-i\beta_k\hat{H}_M\right)\exp\left(-i\gamma_k\hat{H}_C\right)$, with $k = 1, ..., p$, to the ground state of a mixer Hamiltonian $\hat{H}_M$, such as $-\sum_i \hat{X}_i$ where $\hat{X}_i$ is a Pauli operator, to create the trial state $|\psi(\boldsymbol{\beta},\boldsymbol{\gamma})\rangle$. A classical optimizer seeks the $\boldsymbol{\beta} = (\beta_1,\ldots,\beta_p)$ and $\boldsymbol{\gamma} = (\gamma_1,\ldots,\gamma_p)$ that minimize the energy $\langle\psi(\boldsymbol{\beta},\boldsymbol{\gamma})|\,\hat{H}_C\,|\psi(\boldsymbol{\beta},\boldsymbol{\gamma})\rangle$, which is measured in the quantum processor (see Fig. 3.4).

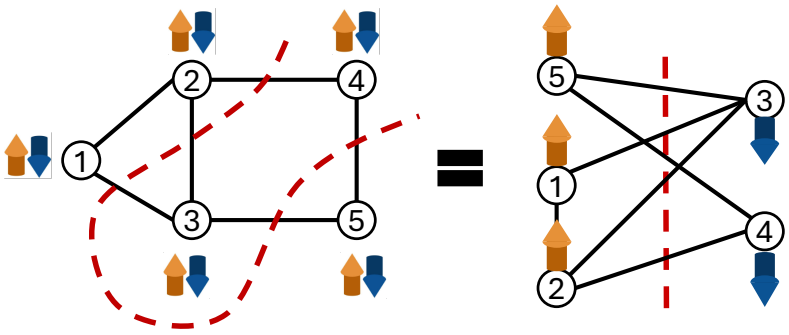

Figure 4.1. Example of a MaxCut Problem. Left: A five-node graph with the maximum cut indicated by the red dashed line, which partitions the graph into two disjoint subsets. Right: The corresponding bipartition, where nodes in each subset represent opposite spin orientations, up or down, in the qubit encoding. In the QUBO formulation of MaxCut [Eq. (4.2)], this corresponds to finding an antiferromagnetic ground state of the associated Ising Hamiltonian, where graph edges represent spin-spin interactions.

MaxCut aims at bipartitioning the set of nodes V in a graph $G(V,E)$ such that the sum of the weights $\omega_{i,j}$ of the edges $(i,j) \in E$ traversed by the cut is maximum, i.e.

$$\max_{z\in\{-1,1\}^n} \frac{1}{2}\sum_{(i,j)\in E} \omega_{i,j}(1-z_iz_j). \tag{4.2}$$

Note that $z_i = \pm 1$ and that means the above equation is maximum only when $z_i z_j = -1$, which occurs when edges become anti-ferromagnetic, see Fig. 4.1 for an example.

Another extreme problem instance is when $\omega_{i,j} = 1, \forall(i,j)$, i.e., an unweighted fully connected graph labelled $\mathcal{G}_n$, see Fig. 4.4(a). Dividing V into two sets of size as equal as possible creates a maximum cut.

Optimization method. In this chapter, the Qiskit QAOA Runtime program [301] is used to simulate QAOA. To optimize the $\{\boldsymbol{\gamma}, \boldsymbol{\beta}\}$, we use the simultaneous perturbation stochastic approximation (SPSA) algorithm [346], which simultaneously optimizes multiple parameters and can handle noisy environments. We do not initialize the optimizer with values for the learning rate and a perturbation. Instead, we let SPSA calibrate itself in the first 25 iterations. To obtain good solutions, we allow SPSA a maximum of 500 iterations and gather a total of 2^{15} shots per iteration.

4.3 Squeezing

Squeezed states are entangled states with a reduced variance of one observable at the cost of an increased variance in non-commuting observables. A large body of experimental work exists addressing the generation of squeezing in various platforms [343, 347–351]. Squeezing can also detect multipartite entanglement among qubits [352–356].

4.3.1 Squeezing in qubit ensemble

In our setting, we are interested in squeezing within an ensemble of n qubits (whose symmetric subspace can be seen as a qudit with length $\ell = \frac{n}{2}$). Consider a coherent state, such as the collective superposition $|+\rangle^{\otimes n}$, where $|+\rangle = (|0\rangle + |1\rangle)/\sqrt{2}$. This state has a variance of $\sigma^2_{\text{css}} = \frac{n}{4}$, commonly called the shot-noise, in the collective observable $\hat{L}_z = \frac{1}{2}\sum_{i=1}^{n} \hat{Z}_i$. By evolving $|+\rangle^{\otimes n}$, e.g., under the non-linear one-axis-twisting (OAT) operator [338]

$$\hat{L}_z^2 = \frac{1}{4}(n + \sum_{i \neq j} \hat{Z}_i \hat{Z}_j), \tag{4.3}$$

the state is stretched over the collective Bloch sphere[1]. The direction with reduced variance can be transferred to the z coordinate by rotating the state around the x-axis with [338, 349, 357] (see Fig. 4.2)

$$\hat{L}_x = \frac{1}{2}\sum_{i=1}^{n} \hat{X}_i \,. \tag{4.4}$$

[1]The collective Bloch sphere is a generalization of the standard Bloch sphere used to represent the quantum states of multiple qubits, typically in a system with n two-level systems. It provides a way to visualize the evolution and properties of these multi-qubit states. One can also think of it as a qudit Bloch sphere, where instead of 2 poles, one would also have multiple rings on the sphere to denote the d levels. Given the collective spin observable, $L_z = \frac{1}{2}\sum_{i=1}^{n} Z_i$, its eigenvalues $\{-\frac{n}{2}, \ldots, 0, \ldots, \frac{n}{2}\}$ would define $n+1$ level qudits. For example, the north (south) pole would be $|0\rangle^{\otimes N}$ ($|1\rangle^{\otimes N}$), and the equator would be superposition of equal number of 0 and 1: $D^n_{n/2}$ for even n (see Eq. (4.9)).

The resulting n particle state is called number squeezed along z when the observed variance is below $\sigma^2_{\rm css}$, i.e., if the squeezing parameter

$$\mathcal{S}\ [\mathrm{dB}] = 10\log_{10}\left(\frac{\mathrm{Var}(\hat{L}_{\rm z})}{\sigma^2_{\rm css}}\right) \tag{4.5}$$

is negative [338, 339].

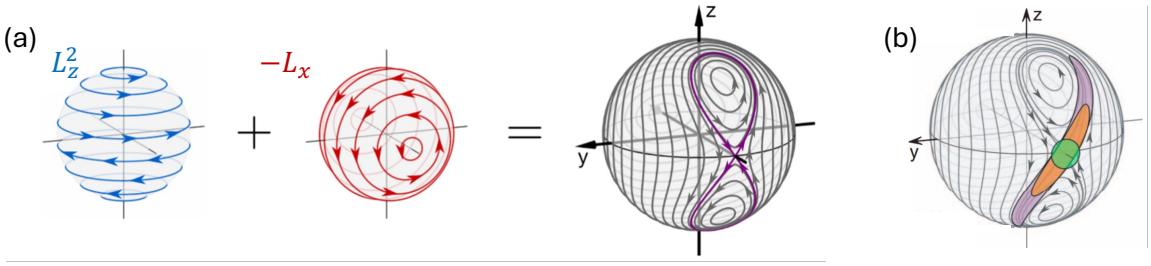

Figure 4.2. Spin-squeezing via one-axis twisting Hamiltonian. (a) Pictorial mean-field representation of the two contributions on the collective Bloch sphere, coming from the nonlinear term $\hat{L}_z^2$ and rotation term $\hat{L}_x$, which leads in combination to the bifurcated phase space, where the arrow indicates the existence of an unstable point. (b) If a state is initiated in that unstable fixed point, under the dynamics (will follow the arrow), its quasi-probability distribution will stretch along the lines, and in the orthogonal direction, it will be squeezed. Adapted from Ref. [358].

4.3.2 Entanglement from squeezing

Measurements of collective spin observables can reveal entanglement. In particular, separable states satisfy [356]

$$(E1): \qquad \langle\hat{L}_x^2\rangle + \langle\hat{L}_y^2\rangle \leq \frac{n}{2}\left(\frac{n}{2}+\frac{1}{2}\right) \Longleftrightarrow \frac{n}{4} \leq \langle\hat{L}_{\rm z}^2\rangle = \mathrm{Var}(\hat{L}_{\rm z})\,. \tag{4.6}$$

The second implication is reached using the identity $\langle\hat{L}^2\rangle = \langle\hat{L}_x^2\rangle + \langle\hat{L}_y^2\rangle + \langle\hat{L}_z^2\rangle = \frac{n}{2}(\frac{n}{2}+1)$, and $\langle\hat{L}_{\rm z}\rangle = 0$ for our target states. Any squeezed state defined through Eq. (4.5) violates the relation above and is thus entangled. Moreover, $\langle\hat{L}_x^2\rangle + \langle\hat{L}_y^2\rangle$ reaches the maximum $\frac{n}{2}(\frac{n}{2}+1)$ in the Dicke state [356], which is the same as having $\mathrm{Var}(\hat{L}_{\rm z}) = 0$.

4.3.3 Multipartite entanglement: quantum Fisher information and squeezing

Here, we recall some concepts for multipartite entanglement from Sec. 2.6. A pure state of n-qubits, written as a product $|\psi\rangle = \otimes_{j=1}^{M}|\psi_j\rangle$, is k-partite entangled when at least one state $|\psi_j\rangle$ contains non-factorizable k-qubits (k-producible) [139, 359]. This definition is the same as the entanglement depth [360], see Fig. 4.3(c). A sufficient condition for $(k+1)$-partite entanglement stems from the quantum Fisher information F_Q (see Sec. 2.6.3): a state reaching

$$(E2): \qquad F_Q[\rho_n, \mathcal{O}] > (sk^2 + r^2)\,, \tag{4.7}$$

where $s = \lfloor n/k \rfloor$ denotes the integer division of n by k, and r is the remainder—is at least $(k+1)$-partite entangled [139, 140] (see Fig. 4.3(a) for a concrete example).

While F_Q is becoming a useful witness for entanglement in quantum many-body systems [361–366], its origin is as a key figure of merit in quantum metrology, where F_Q quantifies the distinguishability of a state ρ from $\rho' = e^{-i\theta\mathcal{O}}\rho e^{i\theta\mathcal{O}}$, generated by the Hermitian operator $\mathcal{O}$ with infinitesimal θ. Thus, a large F_Q implies a high measurement precision for estimating the value of θ [137, 367]. For pure states ψ, the quantum Fisher information becomes simply $F_Q[\psi, \mathcal{O}] = 4\mathrm{Var}(\mathcal{O})_\psi$ [368], whereas for mixed states it provides a lower bound on the variance.

The target state of the QAOA for MaxCut on $\mathcal{G}_n$, the Dicke state, is invariant under a unitary evolution generated by $\hat{L}_z$ but is highly sensitive to rotations around the x- or y-axes of the collective Bloch sphere [349]. Thus, to obtain a large F_Q, it is advantageous to choose $\mathcal{O} = \hat{L}_x$ or—even more so—$\mathcal{O} = \hat{L}_y$, as can be observed in Fig. 4.3(b).

(a)

$F_Q(\rho, \mathcal{O})/n$

	n=4	n=6	n=8	n=12
k=2	1	1	1	1
k=3	2	2	2	2
k=4	2.5	3	2.75	3
k=5	4	3.33	4	4
k=6	—	4.33	4.25	4.5
k=7	—	6	5	6
k=8	—	—	6.25	6.17
k=9	—	—	8	6.67
k=10	—	—	—	7.5
k=11	—	—	—	8.67
	—	—	—	10.17

(b)

Simulation

#qubits (p)	F/n (Lx)	k	F/n (Ly)	k	$\sigma^2_{css}/\mathrm{Var}(\hat{L}_z)$	k
n=4 (1)	1.21	2	2.83	4	3.26	4
n=6 (1)	1.03	2	3.27	4	3.89	5
n=8 (1)	1.33	2	4.12	5	4.51	6
n=4 (2)	3	4	3	4	10^6	4
n=12(3)	6.66	8	7.04	9	9.37	11

(c)

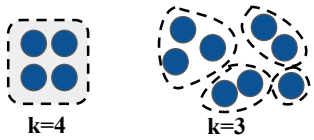

Figure 4.3. Multipartite entanglement from quantum Fisher information and number squeezing. (a) F_Q witnessing k-partite entanglement for different n, (b) In the simulations, F_Q obtained with $\hat{L}_y$ is larger than $\hat{L}_x$. The numbers of entangled particles (k) estimated from squeezing ($\sigma^2_{\mathrm{css}}/\mathrm{Var}(\hat{L}_z) = 10^{-\mathcal{S}/10}$) are close to the numbers obtained from $F_Q[\hat{L}_y]$ for most cases. In a proper Dicke state as obtained with $n = 4(p = 2)$, the $\mathrm{Var}(\hat{L}_z)$ becomes extremely small, leading to the very large value of $\sigma^2_{\mathrm{css}}/\mathrm{Var}(\hat{L}_z)$ seen in the fourth row. (c) Illustrative examples of k-partite entanglement as entanglement depth.

In the hardware, where the system is no longer in a pure state, it is considerably more challenging to directly access F_Q [361, 369]. However, for Gaussian states, one can nevertheless use the empirical relation [349]

$$(E3): \qquad F_Q/n[\hat{L}_y] \simeq \sigma^2_{\mathrm{css}}/\mathrm{Var}(\hat{L}_z) = 10^{-\mathcal{S}/10} \tag{4.8}$$

between F_Q and squeezing. For the simulation, the estimated k using this relation is close to the exact estimation from F_Q in most of cases, see Fig. 4.3(b), except for the depth-three QAOA, where the states are no longer Gaussian [370]. Assuming that the above relation holds for depth-one QAOA, where the states are expected to be Gaussian, we obtain the estimates for k-partite entanglement in the hardware implementation reported in Fig. 4.12(b).

4.4 Connecting QAOA to Squeezing

In a quantum circuit representation, the steps described above for the generation of squeezed states coincide with a single-layer QAOA sequence, see Fig. 4.4(c): (i) The application of Hadamard gates to $|0\rangle^{\otimes n}$ initialize the system in $|+\rangle^{\otimes n}$, the ground state of the mixer Hamiltonian $\hat{H}_M$. (ii) The evolution under the OAT operator corresponds to applying the unitary $\exp\left(-i\gamma_1\hat{H}_C\right)$ with the cost function $\hat{H}_C \propto \hat{L}_z^2$. On the qubit level, this corresponds to controlled-Z gates generated by $\hat{Z}_i\hat{Z}_j$ between all qubits i and j. (iii) The rotation around the x-axis to reveal the squeezing corresponds to the unitary $\exp\left(-i\beta_1\hat{H}_M\right)$, i.e., an application of the mixer.

Interestingly, the cost function $\hat{H}_C \propto \hat{L}_z^2$ is a special instance of the MaxCut problem (Eq. 4.2). For even n, the set of all maximum cuts corresponds to the symmetric Dicke state [337] (see Section. 2.6.1 for more details about Dicke state):

$$D_k^n = \binom{n}{k}^{-1/2} \sum_i P_i \left(|1\rangle^{\otimes k} \otimes |0\rangle^{\otimes(n-k)}\right), \tag{4.9}$$

with $k = \frac{n}{2}$. Here, $P_i(\cdot)$ denotes a permutation of all states with k particles in $|1\rangle$ and $n-k$ particles in $|0\rangle$. For odd n, the set of all maximum cuts corresponds to $(D^n_{\lfloor n/2\rfloor} + D^n_{\lceil n/2\rceil})/\sqrt{2}$. These states are maximally squeezed along z and are useful for metrological applications [332]. The QAOA cost function Hamiltonian to minimize in this problem is $\hat{H}_C = \frac{1}{2}\sum_{i<j}(\hat{Z}_i\hat{Z}_j - 1) = \hat{L}_z^2 - \frac{n^2}{4}\mathbb{I}$. Therefore, QAOA is tasked to find the maximum cut of a fully connected unweighted graph that maximizes the squeezing. This relation thus translates analog metrological protocols [349] to a digital quantum processor. In addition, by formulating the constraints that an arbitrary Dicke state D_k^n imposes on the spins as a QUBO, we can generate D_k^n for arbitrary k (see Sec. 4.7.1).

4.4.1 QAOA as generator of squeezing

To illustrate the connection between QAOA and squeezing, we numerically simulate a system with $n = 12$ qubits and follow the usual QAOA protocol, using $\hat{H}_C = \hat{L}_z^2 - \frac{n^2}{4}\mathbb{I}$, $\hat{H}_M = -2\hat{L}_x$, and $p = 3$. We depict the generated collective-spin/ qudit state using the Wigner quasi-probability distribution as well as the probability distribution over the spin eigenvalues $\{m = \langle\hat{L}_z\rangle + \frac{n}{2}\}$ at each step, see Fig. 4.4(d)-(j). Each application of $\hat{H}_C$ stretches the Wigner distribution, making it resemble an ellipse with the major axis tilted with respect to the equatorial plane of the qudit Bloch sphere. As $[\hat{H}_C, \hat{L}_z] = 0$, this operation does not alter the distribution of $\langle\hat{L}_z\rangle$. Next, the mixer operator rotates the Wigner distribution back towards the equator, thereby transferring the squeezing to the operator $\hat{L}_z$. After three layers, the final state has an overlap with the symmetric Dicke state of 96% and the squeezing number reaches $\mathcal{S} = -9.71$ dB. Crucially, noiseless QAOA with fewer layers produces less squeezing, e.g., see depth-one QAOA in Sec. 4.4.2.

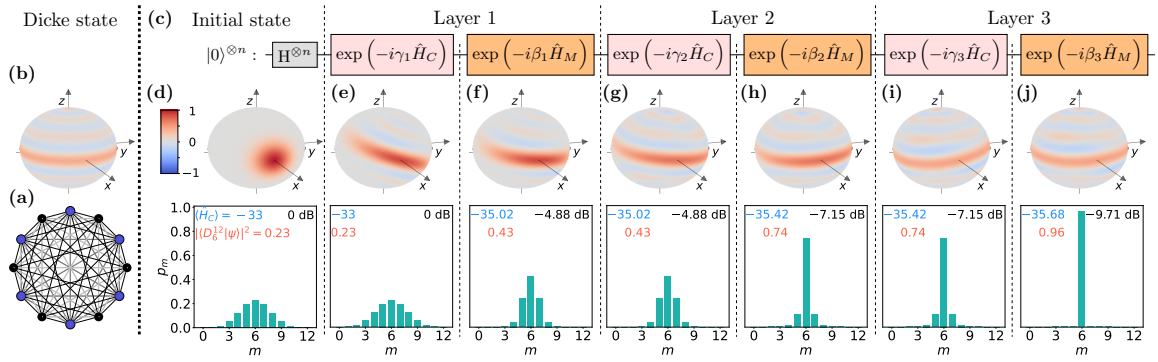

Figure 4.4. Metrologically useful squeezing generated by a depth-three QAOA for the MaxCut problem in a complete graph of 12 nodes. (a) Fully connected unweighted graph with the nodes and edges colored according to one of the 924 possible maximum cut configurations. (b) Wigner quasi-probability distribution of the symmetric Dicke state D_6^{12}, an idealized example of a squeezed state, and the target for our QAOA.(c) Circuit representation of QAOA with alternating application of cost-function and mixer Hamiltonian. The Bloch spheres and histograms from (d) to (j) show the state after the corresponding gate in the optimized QAOA circuit with (γ_i, β_i) given by $(0.199, 0.127)$, $(0.306, 0.087)$, and $(4.592, 1.518)$ for $i = 1$, 2, and 3, respectively. Negativity in the Wigner distribution indicates that the states are non-Gaussian [370]. The squeezing (in black), energy expectation $\langle \hat{H}_C \rangle$ (in blue), and overlap probability density $|\langle D_6^{12}|\psi\rangle|^2$ with the target Dicke state (in orange) are shown inside each histogram.

4.4.2 Advantage of using QAOA to generate squeezing

Merely increasing the duration of $\hat{H}_C$ does not increase squeezing. Squeezing is generated by $\hat{L}_z^2$ [349], which suggests that simply applying $\hat{H}_C \propto \hat{L}_z^2$ for a longer duration, corresponding to a larger coefficient γ in the QAOA, may transform the coherent state to a squeezed state, after which we can use the mixer $\hat{H}_M$ to reveal the squeezing along $\hat{L}_z$. In this way, one layer of QAOA would suffice to create any squeezing, which would also require fewer CNOT gates than when $p > 1$. To test this hypothesis, we run depth-one QAOA using $\gamma = \gamma_1 + \gamma_2 + \gamma_3$ where the γ_i are taken from Fig. 4.4, as they contain the source of "total" squeezing. The result is a fragmented Wigner distribution on the Bloch sphere without observable squeezing in any direction, see Fig. 4.5(a). Furthermore, no squeezing is detected along z for any value of the tomography angle β, see Fig. 4.5(b). This finding is in agreement with the known observation that over-squeezing can be detrimental for precision [358], however, the states here do not wrap around points near poles because $\hat{L}_z^2$ and $\hat{L}_x$ are not applied simultaneously as in Ref. [358].

Advantages of multi-layer QAOA. One may object to the arguments in the preceding paragraph that the γ we chose is sub-optimal. To address that, in Fig. 4.5(c), we numerically map the energy landscape of depth-one QAOA in the $\{\gamma, \beta\}$ plane. The results reveal a minimum energy of $\langle \hat{H}_C \rangle_{\min} = -35.47$ which corresponds to $|\langle D_6^{12}|\psi\rangle|^2 = 98.53\%$. These results are inferior to those we obtain from the depth-three QAOA, i.e., $\langle \hat{H}_C \rangle_{\min} = -35.68$ and $|\langle D_6^{12}|\psi\rangle|^2 = 99.08\%$. Alternating multiple layers of $\hat{H}_C$ and $\hat{H}_M$ is therefore advantageous over a single application of the one-axis-twisting operator.

To quantify the obtainable improvement as a function of the number of layers used, we can define a new performance metric $\Delta_p^n(\%)$, which compares the energy reduction over the initial ansatz obtained by p-layers of QAOA with the one achieved

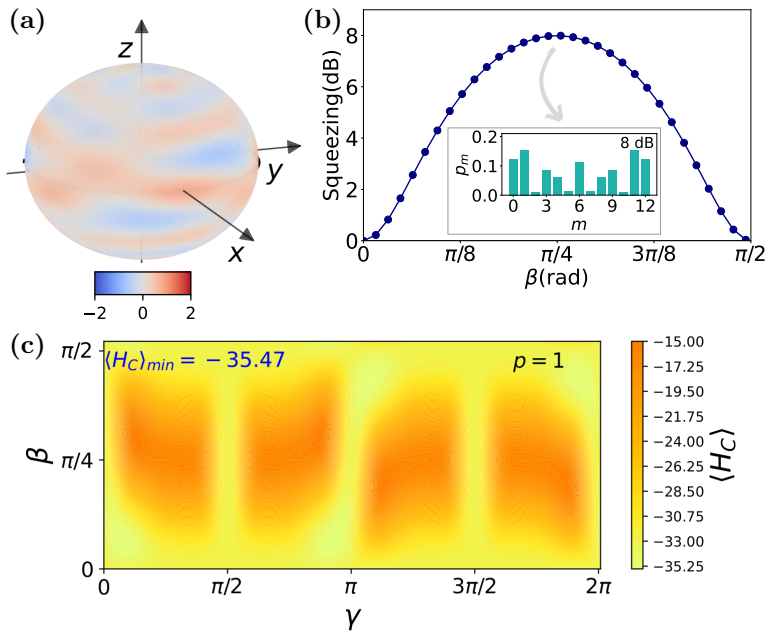

Figure 4.5. Illustration of the importance of alternating the cost-function and the mixer operator. (a) A fragmented Wigner distribution on the Bloch sphere is obtained when $\hat{H}_C$ is applied with $\gamma = \gamma_1 + \gamma_2 + \gamma_3$ from Fig. 4.4. (b) For the state in (a) no squeezing is observed at any β. The inset shows the probability distribution at $\beta = \pi/4$, corresponding to $\mathcal{S} = 8$ dB, i.e. over-squeezing. (c) The energy landscape of the depth-one QAOA reveals that the lowest energy it can reach is -35.47, which is inferior to -35.68 obtained in depth-three QAOA.

by the ideal target state. In the $n = 12$ case, the initial coherent state and the target Dicke state have $\langle \hat{H}_C \rangle = -33$, and -36, respectively. Thus, a depth-one QAOA (corresponding to the usual squeezing protocol) can reach a maximum $\Delta_1^{12} = 2.47/3$. In contrast, the depth-three QAOA can reach $\Delta_3^{12} = 2.68/3$, as shown in Fig. 4.4. Thus, according to this metric, a depth-three QAOA is $0.21/3 = 7\%$ better than a depth-one QAOA.

4.4.3 Multipartite entanglement in QAOA

The squeezing in collective spin observables can further be related to entanglement, using the notions introduced in Sec. 4.3.3. We employ three different criteria:

(E1) If $\frac{n}{4} > \langle \hat{L}_z^2 \rangle$, the state violates a bound on separable states [356]. Any squeezed state ($\mathrm{Var}(\hat{L}_z) < \frac{n}{4}$) at the equator ($\langle \hat{L}_z \rangle = 0$) is witnessed as entangled by this criterion (Sec. 4.3.2). Here, $\langle \hat{L}_z^2 \rangle = 0.32 < \frac{n}{4} = 3$, which is close to the minimal value of 0 achieved by the Dicke state.

(E2) If the quantum Fisher information for a pure state ψ, $F_Q[\psi, \mathcal{O}] = 4\mathrm{Var}(\mathcal{O})$, is larger than $(sk^2 + r^2)$, where $s = \lfloor n/k \rfloor$ denotes the integer division of n by k, and r is the remainder, at least $(k+1)$ particles are entangled [139, 140]. Here, $F_Q[\psi, \hat{L}_y] = 84.48$ and the final state has multipartite entanglement between at least 9 out of 12 particles (see Fig. 4.12(b) to compare with Fig. 4.3(b)). In Fig. 4.3(b), we also report F_Q for both $\mathcal{O} = \hat{L}_x, \hat{L}_y$ and the resulting k-partite entanglement witnessed by it for the ideal simulations. In this ideal scenario of noiseless numerical simulations, the large values of $F_Q[\psi, \hat{L}_{x,y}]$ are directly

related to the anti-squeezing of the final state along the equator of the Bloch sphere.

(E3) Specifically for Gaussian states, one can approximately estimate the number of entangled particles k assuming the identity $F_Q/n \simeq \sigma^2_{\text{css}}/\text{Var}(\hat{L}_z)$ [349](see Sec. 4.3.3 for more discussion), which here yields $k = 11$. We have to use this estimate for the hardware results where direct access to F_Q is not possible (Sec. 4.6).

4.4.4 Comparative metrological gain via QAOA in quantum platforms

The law of large numbers suggests that increasing the number of measurements leads to more accurate phase estimation by reducing statistical variance. It is thus important to analyze when QAOA-prepared sequeezed states can be convenient for a metrological task, as compared to simply repeating various shots with an unsqueezed coherent time. With that motivation, we study the time taken to measure a phase θ with the coherent spin state (CSS) versus QAOA-generated Dicke states within different hardware architectures (but without an attempt at comparing the different architectures to each other, which often have different aims and boundary conditions that are difficult to compare on an even footing). The coherent state is easily prepared by a single rotation around the y-axis. It has no entanglement, and m measurements of the phase θ have a variance bound by $\Delta^2\theta \geq 1/(mN)$. By contrast, a QAOA-prepared state with F_Q above the $k+1$-partite entangled limit takes more time to prepare than the CSS, but it requires a smaller number of measurements to reach the same variance since $\Delta^2\theta \geq 1/(mkN)$ is lowered by a factor of $1/k$ [140].

One may then wonder whether, in a practical application, the improved precision can offset the larger preparation time. Crucially, the optimization cost of QAOA can be ignored in these considerations since the optimal $\boldsymbol{\gamma}$ and $\boldsymbol{\beta}$ parameters are reusable across different measurements and experiments. We therefore compute the duration of a single measurement repetition $t_{\text{repet.}}$, which is the sum of the duration of the gates in the circuit to prepare the state t_{gates} and the readout time including the reset of the measurement apparatus t_{rr}, i.e., $t_{\text{repet.}} = t_{\text{gates}} + t_{\text{rr}}$. The gate duration for the coherent spin state $t^{\text{CSS}}_{\text{gate}}$ is the duration of a single-qubit gate, while the QAOA protocol requires two-qubit gates, whose number can depend on the available universal gate set and the hardware connectivity.

The QAOA-generated states are advantageous when the time $t^{\text{QAOA}} = t^{\text{QAOA}}_{\text{repet.}} \times m_{\text{QAOA}}$ to achieve a certain precision is smaller than the time $t^{\text{CSS}} = t^{\text{CSS}}_{\text{repet.}} \times m_{\text{CSS}}$ to achieve the same precision with coherent states. If the QAOA-prepared state achieves $F_Q = kN$, we have for equal precision $m_{\text{QAOA}} \times k = m_{\text{CSS}}$, i.e., the QAOA-prepared states are advantageous if

$$t^{\text{QAOA}}_{\text{gates}} + t_{\text{rr}} < k\left(t^{\text{CSS}}_{\text{gates}} + t_{\text{rr}}\right). \tag{4.10}$$

Superconducting qubits: The duration of a QAOA layer is impacted by the qubit connectivity. Each QAOA layer on N linearly connected superconducting qubits requires $3(N-2)$ layers of simultaneously executable CNOT gates, which include SWAP gates [301]. Under the assumption that QAOA can create $k+1$-partite entanglement in $p = \log_2(k)$ layers [371], the duration $t^{\text{QAOA}}_{\text{gates}} = 3(N-2)\log_2(k)t_{\text{cx}}$ with t_{cx} the duration of a CNOT gate. Here, we neglected the duration of single-qubit gates. With

$k = N$, Eq. (4.10) yields

$$3(N-2)\log_2(N)t_{\rm cx} + t_{\rm rr} \lesssim N t_{\rm rr}\,, \tag{4.11}$$

which, for large N and the durations in Tab. 4.1, amounts to

$$N \lesssim 2^{t_{\rm rr}/(3t_{\rm cx})} = 2^{1000/3}. \tag{4.12}$$

Although the linear layout of the hardware poses a limit on when QAOA-generated states remain useful, this limit is extremely high. Assuming noisy hardware achieves only a finite k, one has

$$(N-2)\log_2 N < (k-1)t_{\rm rr}/(3t_{\rm cx})\,. \tag{4.13}$$

For $k = 2$, e.g., the QAOA-generated states would remain advantageous up to about 60 qubits arranged in a linear chain, which lies at the size limit of the current hardware. These numbers are conservative estimates that can be significantly increased by improved noise resilience and higher hardware connectivity.

Trapped-ion qubits: Large multipartite entangled states of trapped-ions can be generated by a single application of the Mølmer–Sørensen gate (MS) [372,373] where interaction strength among all qubit pairs is equal [374]. Therefore, if we neglect the duration of single-qubit gates, $t^{\rm QAOA}_{\rm gates}$ only depends on the number of QAOA layers $p = \log_2(k)$, and $t^{\rm QAOA}_{\rm gates} = \log_2(k)t_{ms}$ with t_{ms} being the duration of a MS gate. Following Tab. 4.1, QAOA-generated $k+1$-partite entangled states are therefore advantageous when

$$\log_2(k)t_{\rm ms} \lesssim (k-1)t_{\rm rr} \Rightarrow k^{\frac{1}{k-1}} \lesssim 2^{t_{\rm rr}/t_{\rm rm}} = 2^{25}. \tag{4.14}$$

Since $k^{1/(k-1)}$ is a decreasing function, QAOA-generated states are always advantageous in trapped-ion setups.

Cold-atoms: We now consider cold-atoms in Bose-Einstein condensates, which can, e.g., manipulate states with a number of the order of 400 atoms [349]. Following QAOA, we assume that $\log_2(k)$ layers of the one-axis-twisting Hamiltonian interleaved with x-rotations can generate $k+1$-partite entanglement. The squeezed state is thus created in a time $t^{\rm QAOA}_{\rm gates} = \log_2(k)t_{\rm OAT}$. We neglect the duration of x and y-rotations. Equation (4.10) implies $\log_2(k)t_{\rm OAT} < (k-1)t_{\rm rr}$, showing that given a Bose-condensed atom cloud of fixed size it is always favorable to create spin squeezed states for metrology since $t_{\rm OAT} \ll t_{\rm rr}$, see Tab. 4.1.

Platform	Single-qubit	Entanglement	Readout & Reset $t_{\rm rr}$
Transmons	10 ns [375]	100 ns [340]	100 μs [376]
Trapped ions [377]	15 μs	200 μs	300 μs +5 ms [378]
Cold atoms (BEC)		10 ms [349]	1 s

Table 4.1. Duration of key operations presented as orders of magnitude only. The entangling operation for the transmons, trapped-ions, and cold atoms is the two-qubit CNOT gate, the Mølmer–Sørensen gate, and the one-axis twisting Hamiltonian, respectively.

4.5 QAOA-tailored hardware benchmarks

The performance of quantum computing hardware is often measured by metrics such as randomized benchmarking [379–381] and quantum process tomograph [382, 383], which focus on gates acting on typically one to two qubits, while Quantum Volume (QV) (Sec. 4.5.1) is designed to measure the performance of a quantum computer as a whole [324, 340, 341]. For certain applications, these are complemented by specifically designed benchmarks, e.g., for quantum chemistry [384], generative modelling [385, 386], variational quantum factoring [387], Fermi-Hubbard models [388], and spin Hamiltonians [389]. It is of particular interest to identify such application-tailored benchmarks also for variational algorithms, as these employ highly structured circuits. This necessity is well illustrated by considering the QV: the circuit complexity of a 2^n QV system is equivalent to a $p = 2$ QAOA running on n linearly connected qubits.

4.5.1 Quantum Volume

A processor with a Quantum Volume of $QV = 2^n$ can reliably, as defined by the generation of heavy output bit-strings, execute circuits that apply n layers of SU(4) gates on random permutations of n qubits [324]. When transpiled to a line of n qubits, QV circuits result in n layers of SU(4) gates that have at most $\lfloor \frac{n}{2} \rfloor$ individual SU(4) gates simultaneously executed on the qubits [340]. In between these SU(4) layers, there are at most $\lfloor \frac{n}{2} \rfloor$ SWAP gates, see Fig. 4.6. Furthermore, each SU(4) and SWAP gate require at most and exactly three CNOT gates, respectively [390]. Under these conditions, the total number of CNOT gates is at most

$$3n \left\lfloor \frac{n}{2} \right\rfloor + 3(n-1) \left\lfloor \frac{n}{2} \right\rfloor , \tag{4.15}$$

which approaches $3n^2$ as n becomes large. By comparison, the cost operator of QAOA circuits of complete graphs transpiled to a line requires exactly $\frac{3}{2}n(n-1)-n+1$ CNOT gates, approaching $3n^2/2$ for large n. This suggests that a 2^n Quantum Volume is a good performance indicator for a depth $p = 2$ QAOA on n qubits. Importantly, this comparison is only possible as long as the QAOA circuit is executed using the same error mitigation and transpilation methods as those employed to measure QV [341]. However, QV fails to capture the depth dependency p of QAOA. The benchmark that we develop overcomes this limitation as the QAOA depth should be chosen such that the measured squeezing is maximum. This also provides the maximum p for which it makes sense to run QAOA on the benchmarked noisy hardware.

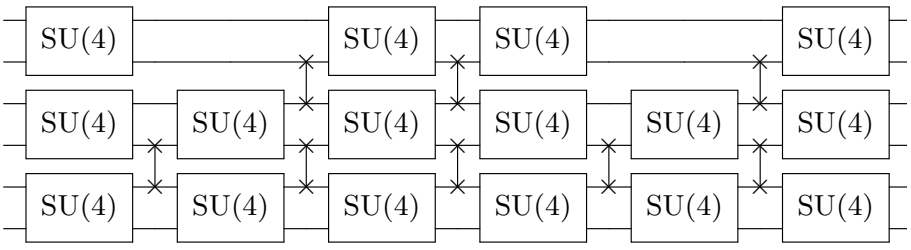

Figure 4.6. Example of a six-qubit quantum volume circuit as presented in Ref. [340], which shows the layers of SU(4) and SWAP gates.

4.5.2 Proposed benchmark

As the above section shows, QV fails to properly capture the dependency on p as QAOA circuits on complete graphs are deeper than their width. Ref. [391] shows using entropic inequalities, if the circuit is too deep, a classical computer can sample in polynomial time from a Gibbs state while achieving the same energy as the noisy quantum computer. That bound is based on the fidelity of layers of gates, which is, however, often overestimated when built from fidelities of gates benchmarked in isolation, e.g., due to cross-talk [301].

Since the solution to the MaxCut problem on the fully connected unweighted graph $\mathcal{G}_n$ is known, we propose squeezing as a good hardware benchmark for QAOA to complement other performance metrics. For our proposed benchmark, we first label the quantum numbers of $\hat{L}_z + \frac{n}{2}$ by $m \in \{0, 1, ..., 2\ell\}$, which correspond to cuts of size $c(m) = m(n-m)$ on $\mathcal{G}_n$. We relate squeezing to a QAOA performance metric through the question:

> *Given the squeezing $\mathcal{S}$ in the trial state, what is the probability $P_\alpha(n, \mathcal{S})$ of sampling a cut with size $c(m)$ greater than a given α-fraction of the maximum cut size $c_{max} = n^2/4$?*

Here, α can be seen as an approximation ratio. By definition, cuts with $c(m) > \alpha c_{\max}$ must satisfy $m_-(\alpha) < m < m_+(\alpha)$ for even n, where $m_\pm(\alpha) = \frac{n}{2}(1 \pm \sqrt{1-\alpha})$. Under a QAOA trial state $|\psi(\boldsymbol{\beta}, \boldsymbol{\gamma})\rangle$ with a distribution p_m over m, see Fig. 4.7(a), the probability to sample cuts larger than $\alpha c_{\max}$ is thus

$$P_\alpha(n) = \sum_{m=\lceil m_-(\alpha)\rceil}^{\lfloor m_+(\alpha)\rfloor} p_m. \tag{4.16}$$

We now make the simplifying assumption that the distribution p_m is a Gaussian

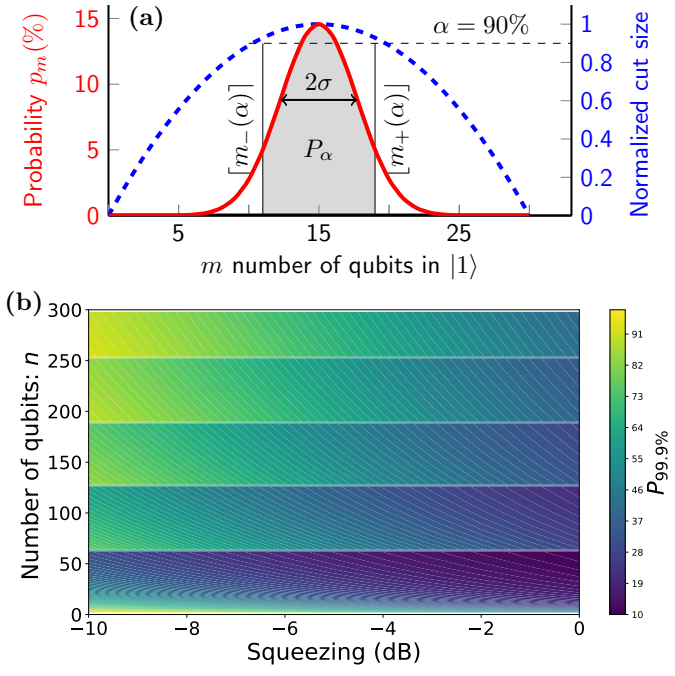

Figure 4.7. Benchmarking QAOA with squeezing. (a) Probability distribution (p_m, red solid line) and normalized cut size ($c_m/c_{\max}$, blue dashed line) simultaneously plotted against $m = \langle \hat{L}_z \rangle + \frac{n}{2}$ for $n = 30$. States with normalized cut-size more than α lie in $m \in [\lceil m_-(\alpha)\rceil, \lfloor m_+(\alpha)\rfloor]$. These yield the shaded area under the probability p_m, which is the figure of merit P_α defined in Eq. (4.16). (b) P_α shows how the probability of sampling high-value cuts changes with squeezing $\mathcal{S}$ and qubit count n, based on trial Gaussian distributions.

$\mathcal{N}(\frac{n}{2}, \sigma)$, where the standard deviation σ—the only free variable for fixed n—is, by definition, in one-to-one correspondence to the squeezing $\mathcal{S} = 10\log_{10}(4\sigma^2/n)$. In summary, the benchmark (i) relates squeezing to the probability of sampling good solutions, a QAOA performance metric, (ii) captures the ability of QAOA to create entangled states (Sec. 4.4.3), and (iii) is as susceptible to hardware noise as other fully connected QAOA circuits (Sec. 4.5.3).

We illustrate the benchmark by numerically computing $P_\alpha(n, \mathcal{S})$ as a function of n and the squeezing $\mathcal{S}$ in the Gaussian distribution $p_m(\mathcal{S})$. Since the ground state of $\mathcal{G}_n$ is highly degenerate, we select a high value of α, e.g., 99.9%. At fixed n, an increased squeezing (more negative) increases P_α, see Fig. 4.7(b), as cuts with a larger size receive more weight. In addition, P_α has discontinuous jumps at $n_{\text{dis.}}$, where $z = \lfloor \frac{n_{\text{dis.}}}{2}\sqrt{1-\alpha} \rfloor \in \mathbb{Z}^+$. In between discontinuities, P_α diminishes with increasing n because σ increases $\propto \sqrt{n}$ for fixed $\mathcal{S}$, which reduces the weight attributed to high value cuts.

Explaining the discontinuity. According to Eq. (4.16), the states in the domain $(\lceil m_- \rceil, \lfloor m_+ \rfloor)$ are included in P_α, where $m_\pm(n, \alpha) = \frac{n}{2} \pm \frac{n}{2}\sqrt{1-\alpha}$. Since $\lfloor m_+ \rfloor$ and $\lceil m_- \rceil$ must both be integers, the span of the domain $\lfloor m_+ \rfloor - \lceil m_- \rceil$ remains constant over a large n range and changes abruptly when $\lfloor \frac{n}{2}\sqrt{1-\alpha} \rfloor \in \mathbb{Z}$ changes value. We denote the values of n at which such changes occur as $n_{\text{dis.}}$, which correspond to the discrete jumps along the n-axis in Fig. 4.7(b). For $\alpha = 99.9\%$ and n even, we obtain discontinuities in $P_{99.9\%}$ at $n_{\text{dis.}} = 64, 128, 190, 254$.

4.5.3 Error detection by spin-squeezing

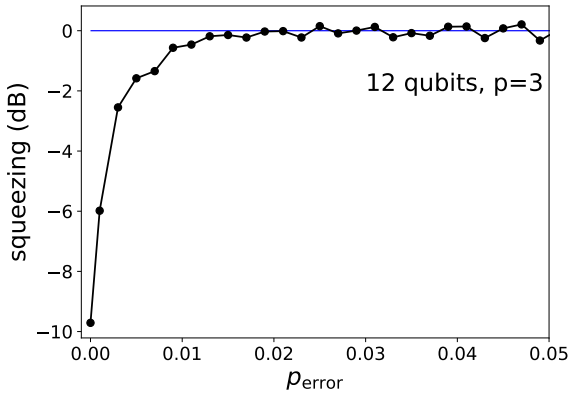

Figure 4.8. Squeezing as a function of the strength of gate noise modeled as bit-flip errors. A bit-flip error is added to every CNOT gate by 2-qubit Pauli channels, $\mathcal{P}_2 = \mathcal{P}_1 \otimes \mathcal{P}_1$, where $\mathcal{P}_1 = \sqrt{p_{\text{error}}}X + \sqrt{1-p_{\text{error}}}I$. The squeezing approaches zero as gate errors increase, showing the validity of squeezing as an application-tailored hardware benchmark.

As undesired processes destroy fragile quantum superpositions, the degree of squeezing is sensitive to the noise levels of the quantum device. To illustrate this, we run our depth-three QAOA example of Fig. 4.4 on a noisy simulator. After each CNOT gate, we include a Pauli bit-flip error with strength p_{error}. We observe that the squeezing rapidly decays towards zero as p_{error} increases, resulting in a non-squeezed state, see Fig. 4.8. This simple simulation demonstrates that gate errors destroy the fragile correlations needed to create a squeezed state. Conversely, the ability (or inability) to realize squeezing through QAOA can be used as a tool to estimate the errors in a circuit experiment.

4.5.4 Squeezing as a good benchmark for arbitrary QUBO problem

From a hardware perspective, although $\mathcal{G}_n$ is a specific problem, its QAOA circuit is representative of the noise of an arbitrary fully-connected QUBO problem since the gates constituting a generic cost function $\exp\left(-i\gamma_k \hat{H}_C\right)$ can be implemented with virtual Z-rotations and CNOT gates [392]. Indeed, the difference between the pulse schedules only amounts to phase changes, indicated by circular arrows in Fig. 4.9(c). The duration of the QAOA pulse schedule and the absolute amplitude of the pulses are thus independent of the variables Σ in the QUBO, see Eq. (4.1), and the variational parameters $\boldsymbol{\gamma}$ and $\boldsymbol{\beta}$ (compare Fig. 4.9(b) and (c)). Therefore, much like Quantum Volume, the hardware benchmark based on squeezing captures effects such as limited qubit connectivity, unitary gate errors, decoherence, and cross-talk. Furthermore, from a hardware perspective, the squeezing circuit is also the hardest to implement since QUBOs that are not fully connected, i.e., $\exists\ (i,j) \mid \Sigma_{i,j} = 0$, require fewer pulses.

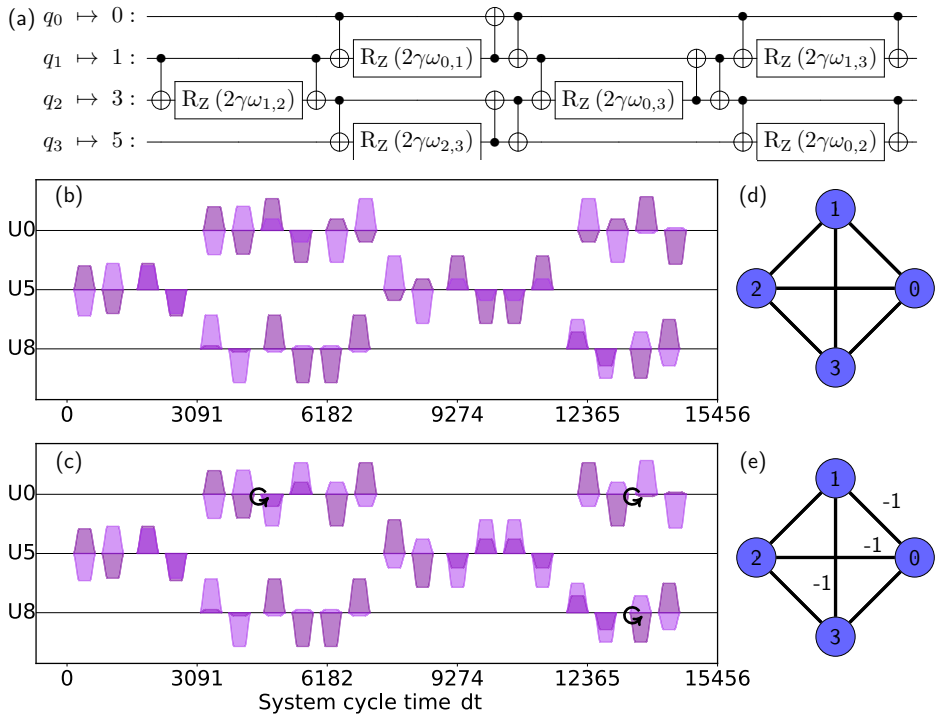

Figure 4.9. Cross-resonance pulse schedules of the squeezing circuit and an arbitrary QUBO. (a) Quantum circuit of a general four-qubit fully connected cost operator $e^{-i\gamma\hat{H}_C}$ transpiled to qubits 0, 1, 3, and 5 of *ibm_lagos*. (b) Pulse schedule of the cost operator used to generate the symmetric Dicke state, i.e., $\omega_{i,j} = 1\ \forall i,j$. (c) Pulse schedule of a MaxCut instance with edge weights $\omega_{0,1} = \omega_{0,2} = \omega_{1,3} = -1$ and $\omega_{0,3} = \omega_{1,2} = \omega_{2,3} = 1$. The circular arrows show where the phase shifts differ from the pulse schedule in (b). (d) and (e) MaxCut graph corresponding to the pulse schedule in (b) and (c), respectively. The duration of a single sample of the arbitrary waveform generators is $\mathrm{d}t = 0.222$ ns. The light and dark pulses show the in-phase and quadrature of each complex amplitude pulse applied to control channels U0, U5, and U8 of *ibm_lagos*.

4.6 Squeezing in superconducting qubits

We now evaluate the benchmark on gate-based superconducting transmon qubits [393] with the following characteristics.

4.6.1 Hardware details

The superconducting qubit data is gathered on the *ibmq_mumbai* system, which has 27 fixed-frequency qubits connected through resonators; its coupling map is shown in Fig. 4.10. We chose a set of qubits that form a line with the smallest possible CNOT gate error. Each circuit is measured with 4000 shots. The properties of the device, such as T_1 times and CNOT gate error, are shown in Tab. 4.2.

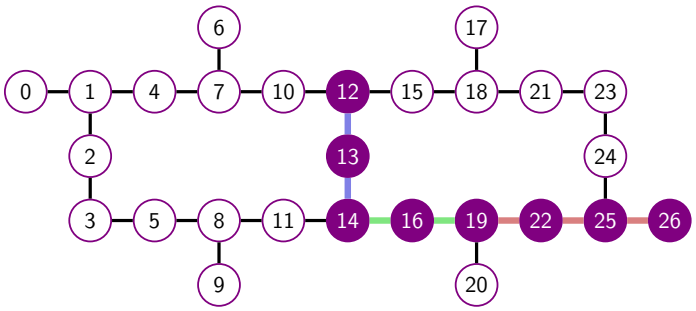

Figure 4.10. Coupling map of *ibmq_mumbai* with the qubits used shown in violet. The four, six, and eight-qubit data were measured on the linearly connected qubits $\{19, 22, 25, 26\}$, $\{14, 16, 19, 22, 25, 26\}$, and $\{12, 13, 14, 16, 19, 22, 25, 26\}$, respectively, chosen based on the CNOT gate fidelity.

Qubit pair	CNOT gate error (%)	duration (ns)	Qubit	T_1 (μs)
(12, 13)	0.77	548	12	166
(13, 14)	1.26	320	13	137
(14, 16)	1.04	348	14	174
(16, 19)	0.77	747	16	118
(19, 22)	0.66	363	19	227
(22, 25)	0.58	484	22	122
(25, 26)	0.50	348	25	194
	0.80±0.27	451±155	26	103

Table 4.2. Properties of the relevant CNOT gates as reported by *ibmq_mumbai* on the date of the circuit execution. The average T_1 of the selected qubits is 155 ± 43 μs.

4.6.2 Measurement of squeezing on IBMq hardware

We measure the squeezing on the IBM Quantum system *ibmq_mumbai* using Qiskit [394] for four, six, and eight qubits. Since the chosen qubits have a linear connectivity, we use a line swap strategy [301,395] to create the all-to-all qubit connectivity required by the squeezing circuit, shown in Fig. 4.11(a) for $p = 1$. This circuit is then transpiled to the cross-resonance-based hardware [396, 397] employing a pulse-efficient strategy instead of a CNOT decomposition [398] using Qiskit Pulse [399]. The optimal value of the variational parameter γ is found with a noiseless simulation for each n. We use readout error mitigation [400, 401], which on average improves the best measured squeezing by -0.7 ± 0.1 dB averaged over all three $n \in \{4, 6, 8\}$. At depth one, a sweep of the tomography angle β_1 reveals a squeezing of -4.80, -4.18, and -4.02 dB whereas noiseless simulations reach -5.14, -5.90, and -6.56 dB for $n = 4, 6$, and 8, respectively. These metrological gains are comparable to prior works in trapped ions [373, 402–406] (see at the end of this section). Given the measured squeezing, we compute a $P_{99.9\%}(n, \mathcal{S})$ of 61.5%, 49.1%, and 42.6%, respectively. Furthermore, we

run a depth-two QAOA on the fully connected four-qubit graph to create a state with a -5.96 dB squeezing, see Fig. 4.11(c), which results in $P_{99.9\%}(4, -5.96) = 68.2\%$. These results indicate that the potential to generate squeezing in a four-qubit system is limited by the variational form at depth one. By contrast, in systems with six and eight qubits, the squeezing generated in practice is limited by the large number of CNOT gates at depth one (40 and 77, respectively).

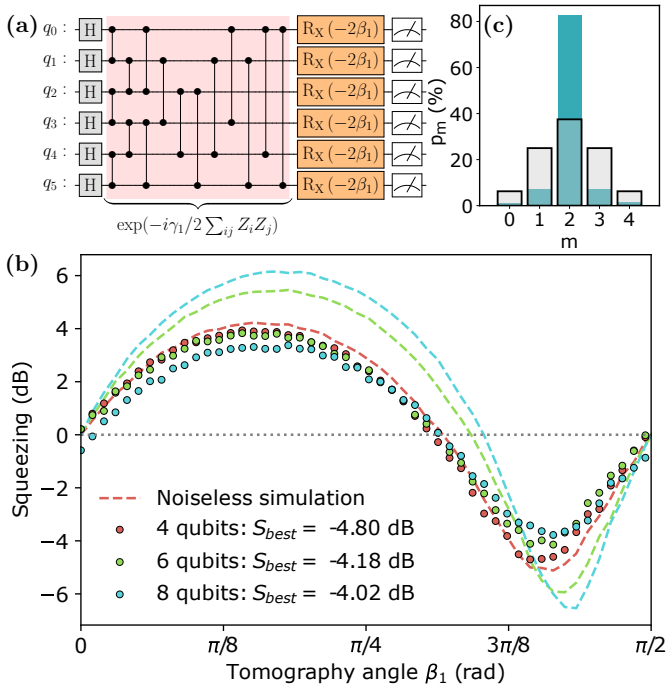

Figure 4.11. Squeezed states generated on superconducting qubits. (a) A quantum circuit implementing a single QAOA-layer for the MaxCut problem on a six-qubit system, producing a state with a reduced variance along the z-axis. (b) Squeezing measured with the quantum circuit in (a). The dashed lines show a noiseless QASM simulation. (c) The p_m distribution of the four-qubit state with -5.96 dB squeezing generated by a depth-two QAOA with optimal parameters $\gamma_1 = 0.918$, $\gamma_2 = -0.257$, $\beta_1 = -0.711$, and $\beta_2 = -2.175$. The gray histogram shows the state $(H|0\rangle)^{\otimes n}$.

4.6.3 Entanglement in hardware

Here we use the entanglement criteria from Sec. 4.3.3. The criterion (E1) witnesses the generated states in both simulation and hardware as entangled, see Fig. 4.12(a). In a noiseless simulation of a depth-one QAOA of system sizes $n = 4, 6, 8$, criterion (E2) witnesses at least $4, 4, 5$ qubit entanglement, respectively. In the noisy hardware implementation, estimate (E3) suggests these numbers to still reach $4, 3, 3$, respectively, see Fig. 4.12(b).

(a)

#qubits (p)	$\langle \hat{L}_z^2 \rangle$ *Simulation*	$\langle \hat{L}_z^2 \rangle$ *Hardware*	$n/4$ Upper bound
n=4 (1)	*0.31*	*0.33*	1
n=6 (1)	*0.38*	*0.57*	1.5
n=8 (1)	*0.44*	*0.79*	2
n=4 (2)	*0*	*0.25*	1
n=12(3)	*0.32*	—	3

(b)

	Simulation (E2)		Hardware (E3)	
qubits (p)	*F/n(Ly)*	*k*	*S(dB)*	*k*
n=4 (1)	2.83	*4*	-4.80	*4*
n=6 (1)	3.27	*4*	-4.18	*3*
n=8 (1)	4.12	*5*	-4.02	*3*
n=4 (2)	3	*4*	-5.96	*4*
n=12 (3)	7.04	*9*	—	*-*

Figure 4.12. Entanglement from squeezing and quantum Fisher information. (a) The values of $\langle \hat{L}_z^2 \rangle$ (E1) obtained in simulation and hardware are close to 0, indicating that the states are in the vicinity of entangled Dicke states. (b) Number of entangled particles k calculated from $F_Q[\hat{L}_y]$ (E2) in simulation, and estimated for hardware using (E3).

4.6.4 Comparison of metrological gain

The squeezing generated by QAOA in the superconducting hardware (see Fig. 4.12) is comparable to prior trapped ion works whose aim was to generate highly entangled states (see Fig.2 of Reference [332]). Even more, our depth-three QAOA simulations with 12 qubits indicate that with lower CNOT error rates, superconducting qubit hardware may reach -9.7 dB of squeezing. The same method could also be applied in trapped ions, where the QAOA circuit—thanks to the trapped-ion all-to-all connectivity—is particularly compact (Sec. 4.4.4). In addition, our method has a number of advantages over variational ansätze developed explicitly for a metrological phase-estimation scenario [343, 407–409]. For example, Marciniak et al. [343], (i) use a cost function particularly tailored for sensing tasks that optimize the phase sensitivity of their quantum sensor, (ii) use a very general variational ansatz consisting of entangling and decoding unitaries containing rotation once and one-axis twisting operations twice in different directions, following the established knowledge in quantum metrology, and (iii) use a linear phase estimator with an unknown parameter a to estimate the phase from spin-measurement, where a also has to be optimized.

By contrast to (i), our cost function is the energy that also creates an entangled state. By contrast to (ii), our variational ansatz is grounded in QAOA, i.e., a Trotterized version of adiabatic computing with a classical optimization that inherits the performance guarantee in the limit $p \to \infty$. By contrast to (iii), our results can be applied to enhance phase-sensitivity but are not limited to it. Indeed, the optimization does not include any phase estimator, potentially making the approach useful for other problems while also reducing the number of parameters to optimize. These three points result in a variational form with fewer parameters to optimize than a general variational form and thus are, in principle, easier to optimize. Furthermore, the approach chosen here allows us to benefit from the vast literature on optimizing QAOA parameters, of which the TQA initialization is just one example.

4.7 Extension

In this section, we extend the connection between QAOA and metrology to create arbitrary Dicke states and warm-starting QAOA with partially squeezed states for random MaxCut problems.

4.7.1 Creating arbitrary Dicke states

We can create arbitrary Dicke states (Eq. 4.9) by minimizing a QUBO cost function with QAOA. Let $|x_{n-1}...x_0\rangle$ be a basis state in which qubit i is in state $x_i \in \{0, 1\}$. Each basis state in D_k^n satisfies the equation $\sum_{i=0}^{n-1} x_i = k$, which is a constraint on the binary variables x_i. We express this constraint as the QUBO problem

$$\min_{x\in\{0,1\}^n} \left(k - \sum_{i=0}^{n-1} x_i \right)^2 . \tag{4.17}$$

The solution to this optimization problem is a superposition of all basis states with k qubits in the excited state, i.e., D_k^n. We apply the change of variables $x_i = (z_i + 1)/2$

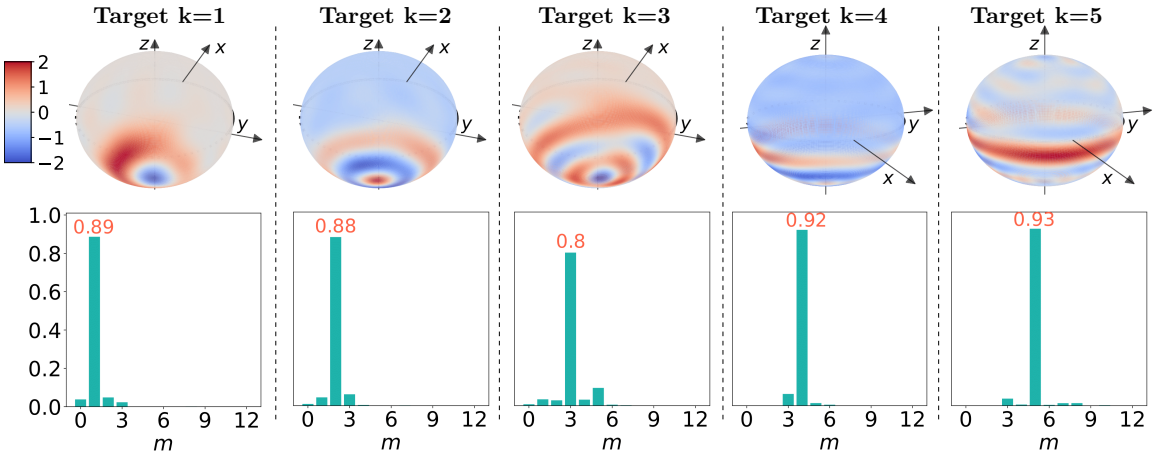

Figure 4.13. Metrologically useful arbitrary Dicke states generated by a depth-three QAOA by minimizing the cost Hamiltonian Eq. (4.19). The top panels show the Wigner quasi-probability distribution on the Bloch spheres. The bottom panels show the corresponding histograms of the total spin operator $\langle \hat{Z} \rangle = m$. The orange numbers in each histogram show the overlap probability density $|\langle D_k^{12} | \psi \rangle|^2$ with the target Dicke states.

to rewrite $(k - \sum_i x_i)^2$ as

$$k^2 - kn + \frac{n}{4}(n+1) + \left(\frac{n}{2} - k\right) \sum_{i=0}^{n-1} z_i + \frac{1}{2} \sum_{i<j} z_i z_j. \tag{4.18}$$

After promoting each z_i variable to a Pauli spin operator $\hat{Z}_i$, Eq. (4.18) yields a cost Hamiltonian to minimize

$$\hat{H}_C = \left(\frac{n}{2} - k\right) \sum_{i=0}^{n-1} \hat{Z}_i + \frac{1}{2} \sum_{i<j} \hat{Z}_i \hat{Z}_j. \tag{4.19}$$

When $k = n/2$, we recover the MaxCut problem on the symmetric graph. For $k \neq n/2$, we have an extra term $(n/2 - k) \sum \hat{Z}_i$ that biases the total spin towards $\langle \hat{Z} \rangle = k$. The Hamiltonian in Eq. (4.19) can therefore be used to generate the Dicke state D_k^n with QAOA.

For n=12 qubits, we use the cost Hamiltonian in Eq. (4.19) to simulate the generation of Dicke states with $k = 1, 2, 3, 4, 5$. With three QAOA layers, we obtain fidelities $> 80\%$, see Fig. 4.13. The corresponding QAOA parameters $\boldsymbol{\gamma}$ and $\boldsymbol{\beta}$ are shown in Tab. 4.3.

Num. spin up k	γ_1	β_1	γ_2	β_2	γ_3	β_3
1	0.101	0.903	0.317	1.324	1.506	-0.155
2	0.093	1.106	0.427	1.409	1.457	-0.068
3	0.149	1.205	1.645	1.576	0.472	-0.076
4	0.111	1.220	0.441	1.690	1.028	0.062
5	0.231	1.340	1.643	1.500	1.774	0.004

Table 4.3. The parameters (γ_i, β_i) of an optimized depth-three QAOA circuit to create $k = 1, 2, 3, 4, 5$ Dicke states that are shown in Fig. 4.13.

4.7.2 Warm-starting QAOA with squeezed states

In this section, we explore how far the symmetric MaxCut problem that has a Dicke state as a ground state can help solve non-trivial MaxCut problems with asymmetric edge-weights. We show how such squeezed states increase the likelihood of sampling good cuts on graphs with random edge weights. Each edge $\omega_{i,j}$ of a graph is sampled from a Gaussian distribution $\mathcal{N}(\mu, \epsilon)$ and then rounded to one decimal place to increase the separation in the cut-values of the graph. We compare standard QAOA with p layers to a QAOA with $p_\mathrm{s} + p$ layers in which the first p_s layers have fixed parameters to produce a squeezed state. Both methods, therefore, have $2p$ parameters that require optimization for each graph instance. For the second approach, in addition, $2p_\mathrm{s}$ parameters are optimized once with the symmetric MaxCut problem as a target and are reused for different problem instances. For each $n \in \{4, 6, 8, 10, 12\}$, we sample 100 graph instances from $\mathcal{N}(\mu, \epsilon)$ for which we chose $\mu = 4$ and $\epsilon = 0.5$ and optimize the cut-value for varying p. The resulting energy, normalized to the minimum energy and averaged over the 100 graph realizations, is used to compare both methods. To ensure that p layers always produce a result that is at least as good as the one for $p-1$ layers, we bootstrap the optimization parameters. The initial guess of the parameters for layer p are based on the optimized parameters of layer $p-1$, i.e., $(\beta_1, \beta_2, ..., \beta_p, \gamma_1, \gamma_2, ..., \gamma_p)_\mathrm{initial} = (\beta_1^\mathrm{opt}, \beta_2^\mathrm{opt}, ..., \beta_{p-1}^\mathrm{opt}, 0, \gamma_1^\mathrm{opt}, \gamma_2^\mathrm{opt}, ..., \gamma_{p-1}^\mathrm{opt}, 0)$.

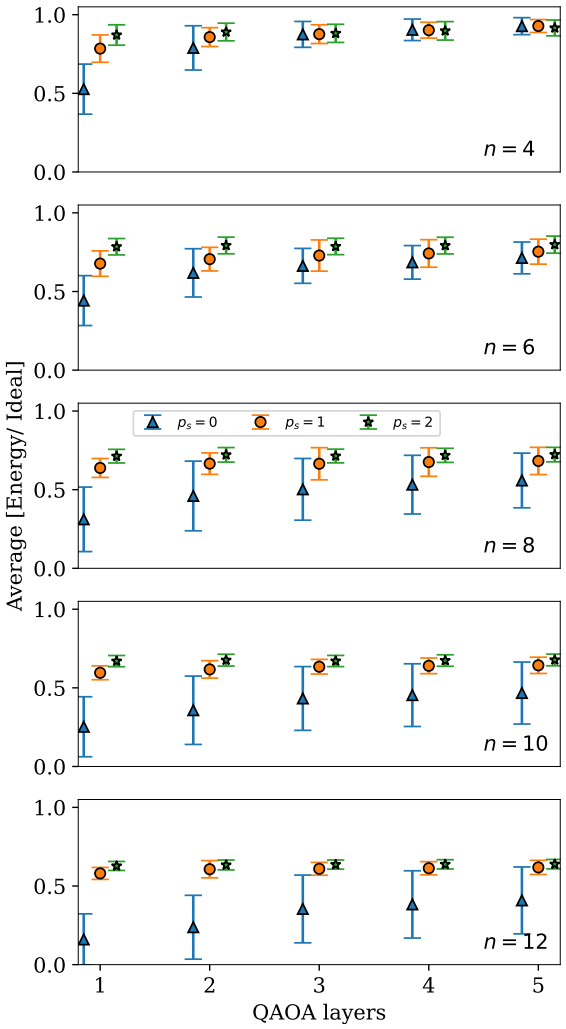

Figure 4.14. Advantages of QAOA initialized with squeezed states. The blue triangles show standard QAOA initialized from a coherent spin state. The orange circles and green stars show QAOA initialized with a spin-squeezed state created with $p_s = 1$ and 2 QAOA layers, respectively. The x-axis is the QAOA depth after the initial state, and the y-axis is the energy normalized to the ideal value. The markers and error bars indicate the average and variance of 100 graph instances drawn from $\mathcal{N}(4, 0.5)$ with different sizes $n = 4$ (top) to $n = 12$ (bottom). Squeezed initial states boost the average energy of the QAOA optimized state, as shown by the orange and green markers having an energy that is closer to the ideal energy than the blue markers. The energy increases only modestly as p increases due to the complexity of the optimization landscape.

QAOA initialized with squeezed states, shown as orange circles and green stars in Fig. 4.14, significantly improves the average energy when compared to QAOA initialized from an equal superposition, shown as blue triangles in Fig. 4.14. We observe a slight improvement in solution quality with increasing p. We attribute this to the complexity of the optimization landscape, which has many local minima, even at depth-one, due to the interference of the frequencies generated by the different edge weights, see Fig. 4.15. In the four-qubit case, the energy for $p \geq 3$ layers of both methods is comparable. As the system size is increased, we observe a greater advantage for QAOA initialized with a squeezed state. These results indicate that, when solving a family of problems, it may be advantageous to initialize QAOA with a state that corresponds to the average problem even when such a problem is trivial to solve.

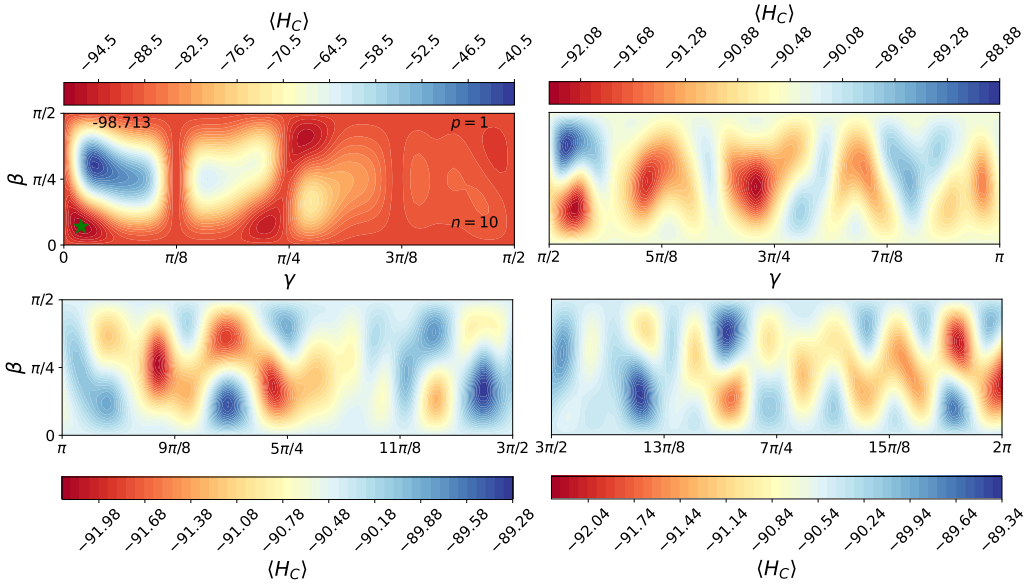

Figure 4.15. Complexity of the optimization landscape for a $n = 10$ vertices graph with edge weights [3.1, 3.5, 3.9, 3.6, 4.6, 4.2, 4.8, 3.8, 4.1, 4.8, 5.0, 4.8, 4.0, 3.8, 3.2, 4.1, 4.2, 4.6, 4.3, 3.5, 3.9, 3.8, 3.2, 3.2, 4.7, 3.7, 4.1, 3.5, 4.1, 4.0, 4.2, 3.6, 4.4, 4.1, 3.5, 4.2, 3.7, 3.4, 4.4, 4.4, 3.6, 4.0, 4.3, 4.9, 4.1] and QAOA depth $p = 1$. Out of the full landscape, we show the first 0 to 2π portion of the γ landscape in four subplots $\gamma \in [0, \pi/2], [\pi/2, \pi], [\pi, 3\pi/2], [3\pi/2, 2\pi]$ with different color scales to increase the contrast between the local minima and maxima. This reveals a large number of local minima. The small improvement in solution quality with increasing p can therefore be attributed to the many local minima, created from the interference of the frequencies generated by the different edge weights.

4.8 Summary

In summary, the generation of squeezed states that are useful for metrology can be cast as a MaxCut problem, which in turn can be addressed with variational algorithms. Such squeezing also unveils the multipartite entanglement structure, as we discussed in detail. The procedure that we illustrated in the creation of a 12-qubit Dicke state can be implemented on universal quantum computing platforms, such as superconducting qubits or trapped ions, as well as on special-purpose machines such as BECs trapped in optical tweezers [349]. Interestingly, an enhancement of squeez-

ing within the multilayer QAOA protocol is not equivalent to simply applying the $\hat{L}_z^2$ operator for a longer period, as the mixer Hamiltonian periodically intervenes. Our results show how variational algorithms may generalize existing protocols and provide systematic guidance for the creation of highly squeezed states for metrology. By contrast to, e.g., Ref [343, 407–409], which uses variational quantum algorithms with a hardware native ansatz to enhance phase sensitivity, the QAOA approach to create squeezing encapsulates the structure of the target state in the variational form, which may reduce the number of parameters to optimize. In a similar vein, we show that custom states beyond Dicke states can be generated by QAOA by casting them as solutions of a combinatorial optimization problem. In addition, we suggested squeezing as a QAOA-specific hardware benchmark. This benchmark is both portable across hardware platforms and captures hardware-specific properties such as limited qubit connectivity and cross-talk. On the other hand, warm-started QAOA using squeezed states seems to have an advantage as well.

Chapter 5

Genuine multipartite entanglement in quantum optimization

entanglement barrier and relation to success probability

5.1 Introduction

Quantum effects are expected to play a central role in quantum algorithms designed to address specific computational tasks [195]. However, understanding their precise contribution to the algorithm's performance is a subtle question. For instance, a key question is whether entanglement is necessary or sufficient in pure-state quantum computing [88,410,411]. Among the various applications of quantum computers, quantum combinatorial optimization stands out as particularly promising [22]. Here, the algorithm is tasked to find an optimal solution x^*, or a near-optimal one, of a classical optimization problem $\min f(x)$ [412]. Interestingly, in quantum optimization approaches, such as quantum annealing (QA) [236,413], the quantum approximate optimization algorithm (QAOA) [326], and variational quantum algorithms (VQA) [231], the initial state is typically a product state, while the solution state should encode a classical problem and thus (barring superpositions of degenerate solutions) may not contain any entanglement. Having both the initial and solution state with little to no entanglement raises the question of how much entanglement is genuinely required to make a quantum-optimization algorithm successful [414].

In previous years, most analyses focused exclusively on bipartite entanglement [414–418], where the entanglement between two non-overlapping partitions of the quantum state is computed. However, the behavior of bipartite entanglement can vary significantly depending on the chosen partitions [419, 420]. Additionally, a state may be entangled across all possible bipartitions or may exhibit global or multipartite entanglement, making it impossible to describe the total entanglement through contributions from individual bipartitions [421]. Since quantum optimization is, in essence, concerned with navigating a many-body system through a quantum spin-glass transition [422, 423], one may expect entanglement shared between multiple parties to play an important role. In the context of pure-state quantum computing, it is known that merely increasing bipartite entanglement with system size is insufficient for an exponential speed-up [88]. In contrast, multipartite entanglement shared among many parties can be a valuable resource for quantum information processing, such as in quantum secret sharing [424], multi-party quantum teleportation [425], quantum key distribution [426], quantum metrology [427], and measurement-based quantum computation [428]. However, its precise role in ensuring successful performance remains unclear for quantum optimization algorithms [325, 414, 429].

Here, we analyze the role of genuine multipartite entanglement in quantum optimization using the generalized geometric measure (GGM) of entanglement [115, 116, 141–143]. The GGM is an attractive measure for multipartite entanglement as it is experimentally accessible [430]. From detailed numerical benchmarks, we find—similar to the bipartite entanglement barrier [414, 418]—a multipartite entanglement barrier in quantum annealing. Initially, the circuit builds up multipartite entanglement as it approaches the minimal gap, where the system enters approximately a GHZ state between the two lowest-energy states. Subsequently, in successful optimization schedules, this multipartite entanglement is removed as the system approaches the solution state. We further analytically derive how the GGM in the optimization schedule is upper-bounded by the distances between the instantaneous eigenstate and both the initial and final product states, which can also be used as a proxy for bounding multipartite entanglement in experiments. Through our work, we shed light on the role and existence of multipartite entanglement in quantum optimization, and its relation to the success probability of the algorithm.

Our studies are complementary to a vigorous ongoing effort to understand the role of quantum resources in quantum optimization. E.g., there are works that study whether quantum optimization still performs well with a cap on entanglement [417, 431–436] or if the success of the algorithm requires other quantum resources [47].

The rest of this chapter is structured as follows. First, we provide a general overview of how entanglement manifests in quantum optimization, along with a definition of the GGM. From Sec. 5.2.3 onwards, we introduce quantum annealing and the MaxCut problem used in our simulation. Section 5.3 details the results from Trotterized quantum annealing, focusing on success probability, bipartite entanglement, and the GGM. In Sec. 5.4, we explore the emergence of the entanglement barrier and its connection to success probability. Finally, we conclude in Sec. 5.5.

5.2 Background

Here, we briefly summarize earlier works that relate bipartite entanglement and the performance of certain classes of quantum algorithms. Thereafter, we motivate the necessity of analyzing multipartite entanglement properties in quantum algorithms and define a computable measure for it, the GGM of multipartite entanglement. Finally, we describe the quantum optimization algorithm and the problem we investigate.

5.2.1 Entanglement in quantum optimization

Various efforts have already demonstrated how bipartite entanglement manifests in quantum optimization algorithms. The presence of von Neumann entanglement entropy has been observed numerically during quantum annealing sweeps in the exact cover problem [415]. Furthermore, entanglement witnesses in experiments have detected non-zero entanglement during quantum annealing [437]. Reference [414] explores a potential connection between bipartite entanglement and the success probability of adiabatic quantum optimization. It shows that high entanglement during the optimization does not necessarily mean a high success probability. On the contrary, in clean systems, significant final entanglement after slow sweeps suggests a superposition state rather than a separable ground state and thus implies a reduced probability of successfully finding the classical ground state. Therefore, measuring bi-

partite entanglement alone is insufficient to gauge the efficiency of adiabatic quantum optimization.

The subtle role of bipartite entanglement is also observed in the variational quantum eigensolver (VQE), where distributing the entangling gates according to the problem's topology increases success rates and reduces runtime [438]. Moreover, the ADAPT variant of QAOA uses a non-standard mixer, which allows a larger amount of entanglement in the earlier part of the circuit and accelerates convergence in the later stages [439]. To further understand the role of bipartite entanglement, one can simulate a quantum algorithm with matrix-product states with finite bond dimension (χ), since χ bounds the maximum bipartite entanglement. Using this approach, reference [417] shows that the state fidelity in QAOA can be limited by χ. In particular, QAOA needs a bond dimension that scales exponentially with the system size N to create high-fidelity states [418]. However, increasing the bond dimension beyond a certain threshold does not appear to improve the fidelity [435]. Also, reference [325] demonstrates numerically, as well as on IBM Quantum hardware, how QAOA can generate high entangled states with multipartite entanglement witnessed through squeezing inequalities and the quantum Fisher information.

5.2.2 Generalized geometric measure of entanglement

Recall from sec. 2.6.4 that the GGM of entanglement generalizes the notion of geometric measure of entanglement and quantifies genuine multipartite entanglement. Here we recapitulate the definition for the sake of convenience. For pure states, the GGM takes the simple form

$$G_2(|\psi\rangle) = 1 - \max_{|\pi\rangle_{\mathcal{A}:\mathcal{B}} \in \mathcal{S}_2} |_{\mathcal{A}:\mathcal{B}}\langle\pi|\psi\rangle|^2 = 1 - \max_{\mathcal{A}:\mathcal{B}} (\lambda^{\max}_{\mathcal{A}:\mathcal{B}})^2. \tag{5.1}$$

Here, $|\psi\rangle$ belongs to the Hilbert space $\mathcal{H}_{A_1} \otimes \mathcal{H}_{A_2} \otimes \cdots \otimes \mathcal{H}_{A_N}$. The bipartition $\mathcal{A} : \mathcal{B}$ satisfies $\mathcal{A} \cup \mathcal{B} = \{1, 2, \cdots, N\}$, and $\mathcal{A} \cap \mathcal{B} = \emptyset$ [142, 143]. In other words, maximizing $|_{\mathcal{A}:\mathcal{B}}\langle\pi|\psi\rangle|$ across the biparition $\mathcal{A} : \mathcal{B}$ is equivalent to finding the maximum Schmidt coefficient, $\lambda^{\max}_{\mathcal{A}:\mathcal{B}}$, for that bipartition. For qubits, the theoretical maximum value of GGM is 1/2.

Reference [440] investigates the GGM in Grover's algorithm. Here, the GGM initially increases and reaches a maximum in the first half of the optimal number of iterations and then decreases towards the end of the algorithm. In the Bernstein–Vazirani algorithm, the presence of geometric entanglement in the initial state prevents it from reaching an optimal performance (the key resource for the Bernstein–Vazirani algorithm is coherence rather than entanglement, and maximally entangled states cannot be maximally coherent) [436]. One can thus expect that the presence of an exaggerated amount of multipartite entanglement can have a detrimental effect, and understanding the nature of such entanglement may help us design more efficient quantum algorithms.

5.2.3 Trotterized quantum annealing

We have already discussed quantum annealing in detail in Sec. 3.3.2. Here, we use first-order Trotter–Suzuki decomposition of the continuous sweep, up to $\mathcal{O}(\Delta t^2)$, into

$$e^{-i\Delta t H(t)} \simeq e^{-i\beta H_{\mathrm{M}}} e^{-i\gamma H_{\mathrm{C}}}, \tag{5.2}$$

where $\beta = (1 - t/T)\Delta t$, and $\gamma = (t/T)\Delta t$. Discretizing the entire quantum annealing schedule into p time steps requires $\Delta t = T/p$. The resulting discretized annealing schedule is

$$\gamma_s = \frac{s}{p}\Delta t, \quad \beta_s = (1 - \frac{s}{p})\Delta t\,, \tag{5.3}$$

where the time-factor of t/T is replaced by the layer-number s/p. Crucially, unlike in quantum annealing, here Δt and the total time T can be modified independently by changing p, which hands us an additional control knob for Trotterized annealing.

5.2.4 Maximum-Cut problem

As a paradigmatic example, we focus on the Maximum Cut problem (MaxCut). MaxCut aims at partitioning the set of N nodes V in a graph $\mathcal{G}(V, E)$, such that the sum of the weights $\omega_{i,j}$ of the edges $(i, j) \in E$ traversed by the cut is maximum. By introducing Ising variables $z_i \in \{-1, 1\}$ to describe which side of the cut node i falls on, this task is mathematically equivalent to maximizing the cost function (see Fig. 4.1 as an example)

$$\max_{z\in\{-1,1\}^N} \frac{1}{2} \sum_{(i,j)\in E} \omega_{i,j}(1 - z_i z_j). \tag{5.4}$$

Since z_i can also be seen as the eigenvalues of the Pauli Z_i operator acting on a qubit i, the maximization is equivalent to finding the ground state of the Ising model [345,441]

$$\tilde{H}_\mathrm{C} = \frac{1}{\sqrt{N}} \sum_{i<j} J_{ij} Z_i Z_j. \tag{5.5}$$

Here, J_{ij} encode the edge weights of $\mathcal{G}$ with $J_{ij} = 0$ if $(i, j) \notin E$.

Due to the $\mathbb{Z}_2$ symmetry of $\tilde{H}_\mathrm{C}$, there are two equivalent degenerate solutions. A ground-state search may thus result in varying superpositions of the two solutions, whose entanglement content can depend significantly on the details of the annealing sweep. To ensure that the entanglement we observe is solely a signature of the performance of the quantum algorithm, we remove this degeneracy by adding a small perturbation $f Z_0$ to $\tilde{H}_\mathrm{C}$ to break the symmetry. We choose $f = 0.05$ for all problems. The modified Hamiltonian is thus

$$H_\mathrm{C} = f Z_0 + \frac{1}{\sqrt{N}} \sum_{i<j} J_{ij} Z_i Z_j\,, \tag{5.6}$$

which will be the problem on which we study genuine multipartite entanglement.

5.2.5 Degeneracy breaking and pairing of states

To break the $\mathbb{Z}_2$ symmetry in MaxCut, we add an offset term as described in Eq. (5.6). Here, we show how the degeneracy in the spectrum of H_C is lifted with increasing offset. We choose 0.05 as an offset to lift the degeneracy while preserving the eigenlevel structure.

At this level of bias, although the $\mathbb{Z}_2$-symmetric states are no longer degenerate, they are still energetically close and thus have a pairing effect during the annealing

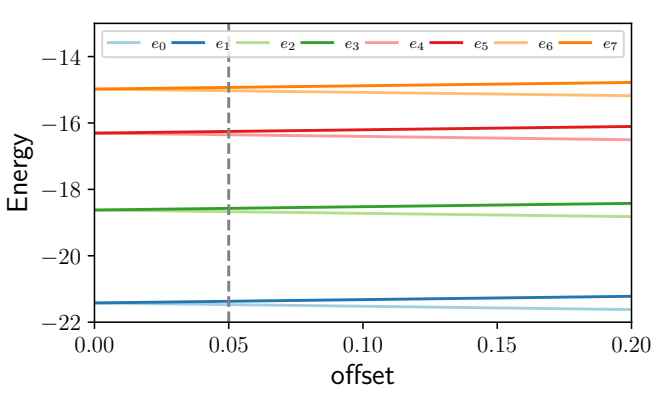

Figure 5.1. Effect of offset f on degeneracy of H_C. A non-zero magnitude f of the offset fZ_0 lifts the degeneracy in the eigenvalue of H_C, as illustrated for the instance described in Fig. 5.3. As f increases, the paired states become increasingly distinguishable. For the data shown, we choose an offset of $f = 0.05$ (grey vertical line) at which the states are non-degenerate but still form pairs close to each other in energy.

sweep. For example, let us consider the graph instance (Fig. 5.3) which we study in detail later. We study the overlap probability of the instantaneous state with the four lowest energy states $|e_i\rangle$, $i \in \{0, 1, 2, 3\}$ of H_C during the sweep. Until the sweep reaches the GGM peak, as we will see in Fig. 5.5(a), the population of the ground and the first excited states is almost equal, see Fig. 5.2. The same holds for the third and fourth excited states. This hints at a pairing of $|e_0\rangle$ with $|e_1\rangle$ and of $|e_2\rangle$ with $|e_3\rangle$. Moreover, again due to the $\mathbb{Z}_2$ symmetry, $|e_0\rangle$ and $|e_1\rangle$ are bit-wise orthogonal basis states (and the same for $|e_2\rangle$ and $|e_3\rangle$). An equal superposition of such states creates a GHZ-like state with a high GGM. For example, with the graph considered here $|e_0\rangle = |10101001\rangle$ and $|e_1\rangle = |01010110\rangle$ form the state $|\mathrm{GHZ}_8\rangle = \frac{1}{\sqrt{2}}(|e_0\rangle + |e_1\rangle)$ state.

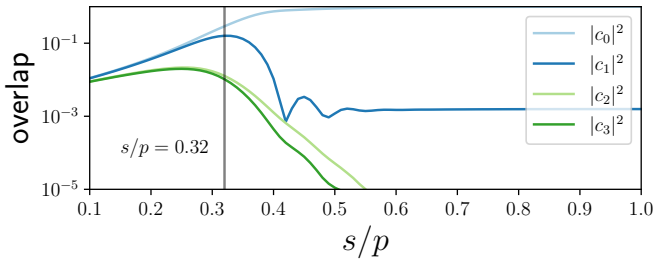

Figure 5.2. Population of the four lowest-energy instantaneous eigenstates, for the MaxCut problem from Fig. 5.3 and with $p = 5000$. Pairing is observed until the barrier, after which the pairs break, and $|c_0(s)|^2$ approaches 1.

5.3 Genuine multipartite entanglement for a fixed instance of MaxCut

In this section, we illustrate how, for an instance of the MaxCut problem, the success probability, the von Neumann entanglement entropy, and the generalized geometric measure of multipartite entanglement behave during an optimization schedule. Unless stated otherwise, we choose the MaxCut problem on six-regular graphs on eight vertices, with edge weights J_{ij} randomly chosen from a Gaussian distribution with mean $\mu = 6$ and standard deviation $\sigma = 3$. Figure 5.3 shows the resulting six-regular eight-node graph instance used. The solution of this MaxCut instance is defined by the separation into vertex sets $(1, 3, 5, 6)$ and $(0, 2, 4, 7)$.

For illustration purposes, in this section, we choose the above graph instance, and in the next section, we choose from many instances to study the average behavior. We solve the problem with Trotterized quantum annealing and an increasing number

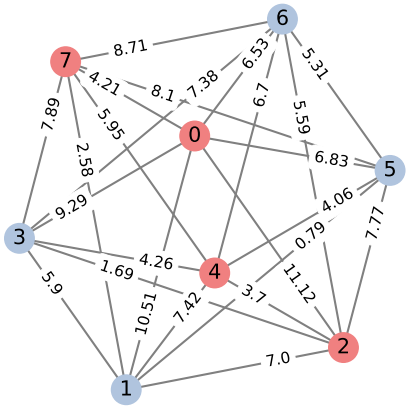

Figure 5.3. Details of the MaxCut problem for the fixed graph instance used in Sec . 5.3. Weights J_{ij} are indicated on the edges. The MaxCut solution is denoted by red and blue node colors.

of Trotter steps, or circuit layers, ranging from $p = 100$ to $p = 10000$. We select $\Delta t = 0.19$, which allows us to achieve a good minimum energy across all layer counts (see Fig. 5.4). The total time is $p\Delta t$, which amounts to, e.g., $T = 950$ for $p = 5000$.

Δt for TQA. In Trotterized quantum annealing (TQA), the quality of the annealing, which is related to the success probability, depends on the total number of Trotter layers p and the chosen time step Δt, see Eq. (5.3). In principle, Δt should be chosen to maximize the success probability. However, to study the impact of the sweep time (i.e., the number of layers multiplied by the step size Δt) on the behavior of the GGM, we choose a value of Δt that keeps the energy of the final state small for all considered numbers of layers ($p = 100, 1000, 5000$). Our simulations show that there is no Δt value that simultaneously minimizes the energy of all layers p, see Fig. 5.4. As a compromise, we choose $\Delta t = 0.19$ for Fig. 5.5, for which the final energy is close to the absolute ground state for all p considered. In Fig. 5.9, when we average over 100 instances, we will use $\Delta t = 0.2$ for all instances instead of optimizing Δt for each instance.

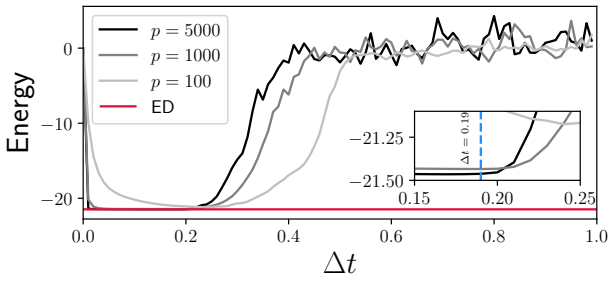

Figure 5.4. Energy of the final state of Trotterized quantum annealing as a function of Δt for different Trotter layers p for the MaxCut problem of Fig. 5.3, compared to the ground-state energy obtained from exact diagonalization (ED).

5.3.1 Success probability for different sweep speeds

As the number of Trotter steps increases, the evolution becomes more adiabatic, and thus the success probability is expected to improve with larger p. We define the success probability as the degree of overlap between the final state $|\psi(p)\rangle_{\mathrm{TQA}}$ and the true ground state $|e_0\rangle$ of H_C. To understand the evolution of the state at each Trotter step, we evaluate the instantaneous probability of finding the ground state $|e_0\rangle$ and first excited state $|e_1\rangle$ of the final cost Hamiltonian at each layer s. Expressing the

instantaneous state in the eigenbasis of H_C,

$$|\psi(s)\rangle_{\mathrm{TQA}} = \sum_i c_i(s)\,|e_i\rangle\ , \tag{5.7}$$

the instantaneous probability of being in the ground and first excited states are $|c_0(s)|^2$ and $|c_1(s)|^2$, respectively. Here, the basis states $\{|e_i\rangle\}$ are ordered by increasing energy. The probability of reaching the final ground state, $|c_0(s=p)|^2$, defines the success probability of the algorithm.

For all $p \in [1000, 10000]$, the instantaneous ground-state probability $|c_0|^2$ increases with layer index s and reaches the highest value at the end of the sweep $s = p$, see solid lines in Fig. 5.5(b). As the number of layers p increases, so does the success probability, i.e., slower sweeps are more successful. The first excited state probability $|c_1|^2$ (dashed lines) increases until $s/p \approx 0.32$, after which it decreases if p is sufficiently large. This results in a peak, whose location is around the minimal energy gap between the first excited and the ground state of the instantaneous Hamiltonian [see Fig. 5.5(d)]. The peak becomes sharper as the sweep speed is reduced, i.e., as p increases.

For the smallest considered number of layers ($p = 100$, i.e., $T = 19$), an oscillation appears after crossing the minimum energy gap between the instantaneous ground and the first excited states. In such fast sweeps, the adiabatic conditions break down, causing the instantaneous state to become a superposition of multiple eigenstates. The dynamical phases between these lead to oscillations. One can also see these as the formation of defects, as described by the Kibble-Zurek mechanism (KZM) [442–444]. As the adiabatic condition becomes valid for slower sweep speeds, the defects and oscillations disappear.

5.3.2 von Neumann entanglement entropy for bipartite entanglement

Our modified MaxCut problem, given by Eq. (5.6), has by design a non-degenerate solution state. Therefore, we expect the ideal quantum anneal to reach this desired product state solution with vanishing entanglement. However, any realistic sweep within finite time has some degree of non-adiabaticity, thereby populating higher energy states, which generates undesired final-state entanglement [414]. For comparison purposes to the GGM, we quantify the bipartite entanglement across the half–half bipartition of the system, i.e., $(0,1,2,3) : (4,5,6,7)$, using the von Neumann entanglement entropy $S_{vN} = -\mathrm{Tr}\left[\rho_{\mathcal{A}} \log_2(\rho_{\mathcal{A}})\right]$. Note that S_{vN} depends on the chosen bipartition, whereas the GGM is optimized over all bipartitions.

As shown in Fig. 5.5(c), we observe a maximum in S_{vN} around the gap closing, reaching almost half of its theoretical maximum of $4\log_2(2)$ for the given subsystem size at $s/p \simeq 0.3$. Similar to reference [414], slow sweeps (large p) reduce the entropy after this point as the quantum fluctuations produced by H_M become weaker, while fast sweeps (small p) are unable to remove the entropy, resulting in a loss of success probability.

5.3.3 Generalized geometric measure for multipartite entanglement

For the fastest sweep considered, $p = 100$, the GGM oscillates in accord with the oscillations of the overlaps with the ground and excited states, see Fig. 5.5(a,b). The

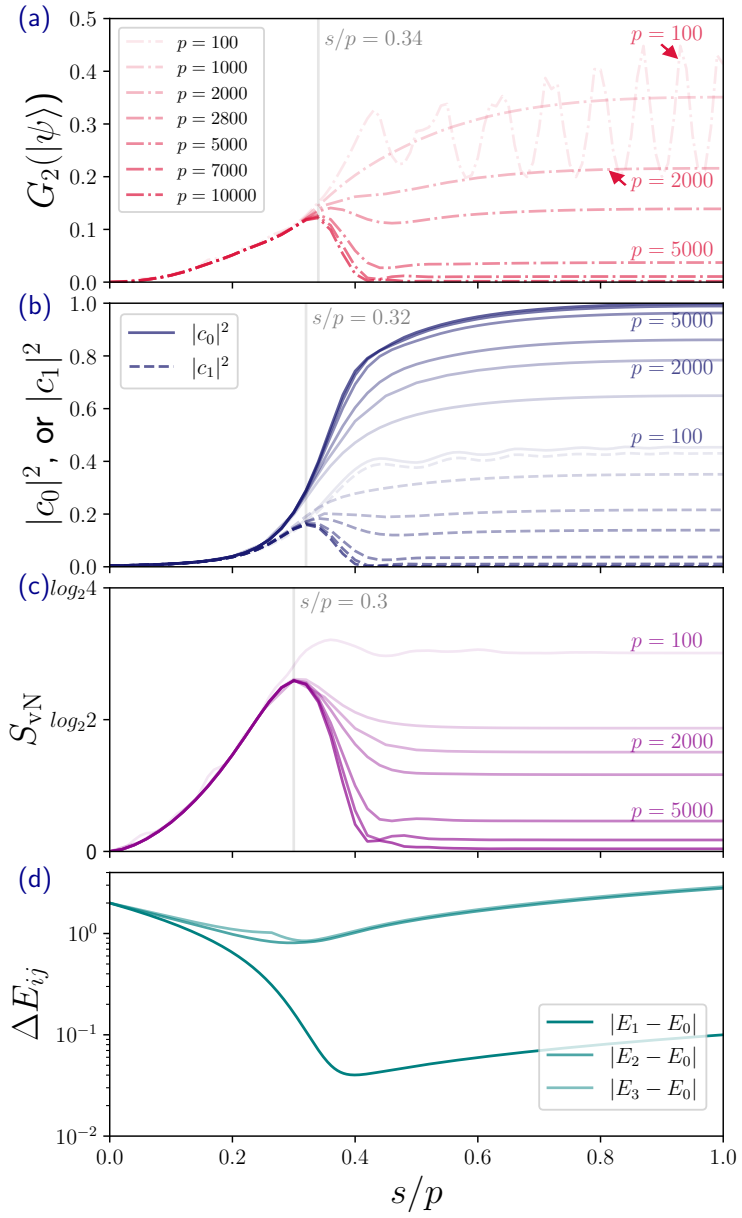

Figure 5.5. Results shown as a function of normalized layer number s/p for a single MaxCut instance, for various total TQA layers p. (a) For low p, the GGM saturates at high s/p, while for high p, a peak appears near $s/p = 0.34$ followed by a dip. Fast sweeps ($p = 100$) show oscillations due to non-adiabatic transitions. (b) Overlap of $|\psi(s)\rangle$ with the ground and first excited state of H_C, with $|c_1|^2$ peaking near max GGM. (c) The mid-graph von Neumann entropy peaks for all p but saturates lower as p increases. (d) Instantaneous energy gaps; key features in (a)–(c) align with low-lying gap closings.

GGM peak near $s/p = 0.34$ becomes more visible with slower sweeps, which resembles the observed peak in $|c_1|^2$. As the GGM follows qualitatively the same structure as the von Neumann entropy on the fixed bipartition, one may wonder if the optimal bipartition for the GGM is static or if the half–half bipartition captures the GGM on average. For the particular problem instance we considered, we found that the optimal bipartition remains constant for $0.3 \leq s/p \leq 0.8$ and is $\mathcal{A} = (2), \mathcal{B} = (0, 1, 3, 4, 5, 6, 7)$, which differs from the half–half bipartition (see Fig. 5.6).

Optimal bipartitions corresponding to the GGM

To find the value of the GGM, we need to look for the bipartition that yields the maximum Schmidt coefficient. A question that may naturally arise is whether such a bipartition is unique or changes with the annealing sweep. At the start of the anneal, at $s/p = 0$, we have $\lambda^2_{max} = 1$ in all bipartitions. This implies a vanishing GGM, see Fig. 5.6. As the annealing schedule proceeds, λ^2_{max} of different partitions starts

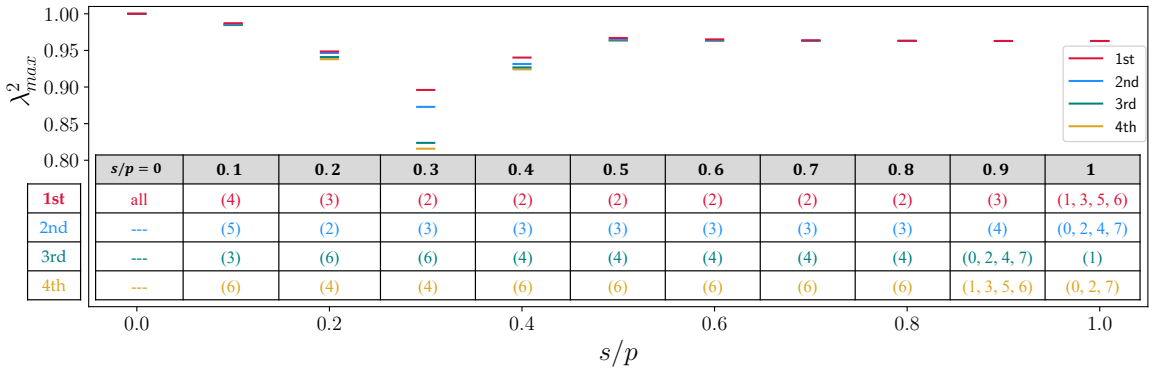

$s/p = 0$	0.1	0.2	0.3	0.4	0.5	0.6	0.7	0.8	0.9	1
1st	all	(4)	(3)	(2)	(2)	(2)	(2)	(2)	(2)	(3)	(1, 3, 5, 6)
2nd	---	(5)	(2)	(3)	(3)	(3)	(3)	(3)	(3)	(4)	(0, 2, 4, 7)
3rd	---	(3)	(6)	(6)	(4)	(4)	(4)	(4)	(4)	(0, 2, 4, 7)	(1)
4th	---	(6)	(4)	(4)	(6)	(6)	(6)	(6)	(6)	(1, 3, 5, 6)	(0, 2, 7)

Figure 5.6. Largest Schmidt coefficients along the annealing sweep, at selected times for the partitions $(\mathcal{A}) : (\mathcal{B})$ yielding the four largest values, for the MaxCut problem of Fig. 5.3. The table gives the corresponding sets of qubits in $\mathcal{A}$. The maximum Schmidt values decrease from the initial states until $s/p = 0.3$, implying an increasing GGM. Later, the Schmidt values increase while the optimal bipartitions remain unchanged until $s/p = 0.8$. Subsequently, the GGM remains constant while the optimal bipartition changes to finally reach $\mathcal{A} = (1, 3, 5, 6)$.

to differ; for example, at $s/p = 0.2$, partition $\mathcal{A} = (3), \mathcal{B} = (0, 1, 2, 4, 5, 6, 7)$ and partition $\mathcal{A} = (2), \mathcal{B} = (0, 1, 3, 4, 5, 6, 7)$ have different values of λ^2_{max}. The individual Schmidt values decrease during the sweep until they reach the lowest λ^2_{max} corresponding to the GGM barrier at around $s/p = 0.3$. After this point, the GGM decreases, and the partition producing the λ^2_{max} — $\mathcal{A} = (2), \mathcal{B} = (0, 1, 3, 4, 5, 6, 7)$ — does not change until $s/p = 0.8$. Towards the end of the anneal, in the range $s/p > 0.8$, the maximum Schmidt values and the GGM do not change considerably. However, the optimal bipartition varies until it finally reaches $\mathcal{A} : \mathcal{B} = (1, 3, 5, 6) : (0, 2, 4, 7)$. This bipartition has the maximum Schmidt values (maximal bipartite entanglement). In summary, it is interesting to see that from $s/p = 0.1$ to 0.3, the GGM changes, but the corresponding partition does not. Thereafter, and until the end of the anneal, the GGM remains constant, but the underlying partition changes.

Effect of graph's connectivity

One might naturally question whether a graph's connectivity affects the value of the GGM, for instance, if a more connected graph would display greater entanglement. Perhaps surprisingly, even a two-regular graph, with just two edges per node, can exhibit nearly the same amount of GGM as a six-regular graph, see Fig. 5.7. The same is true for the von Neumann entanglement entropy. Thus, it is crucial to understand in what sense bipartite and multipartite entanglement differ.

In general, bipartite entanglement for fixed bipartitions does not need to follow the behavior of the GGM, as we now show through some counterexamples. As discussed in Sec. 5.2.2, multipartite entanglement exists only when there is a non-zero bipartite entanglement for *all* possible bipartitions. This implies that a state can have a large bipartite entanglement for a particular bipartition and yet can have a significantly smaller GGM, even zero. To exemplify the strong dependence of the von Neumann entropy on the bipartition, we consider $S^{\max}_{vN}$ as S_{vN} maximized over $\binom{N}{\lfloor N/2 \rfloor}$ equal-sized (half–half) bipartitions,

$$S^{\max}_{vN} = \max_{|\mathcal{A}|=N/2:|\mathcal{B}|=N/2} S_{vN}[\mathcal{A}]\,. \tag{5.8}$$

For the 6-regular graph studied above, we observe that the GGM peaks later than $S_{vN}^{\max}$, and the same happens in the example of a connected two-regular graph, see Fig. 5.7. This implies that in both cases, the bipartition corresponding to the GGM is not the same as the maximal bipartition of $S_{vN}^{\max}$. An even more substantial difference between half–half von Neumann entanglement entropy and GGM can be found in the example of a disconnected two-regular graph, see the "2-reg, two ring" in Fig. 5.7. In this extreme example, while the maximum bipartite entanglement entropy is large throughout the entire annealing schedule, the optimal bipartition of the GGM corresponds to the disconnected subgraphs, resulting in an identically vanishing GGM.

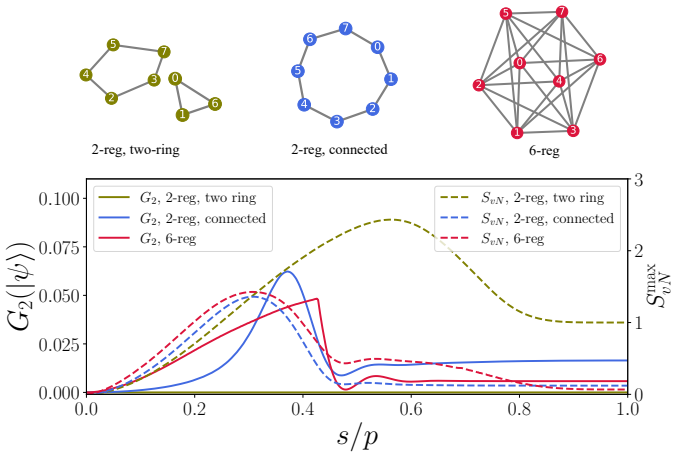

Figure 5.7. The von Neumann entanglement entropy of a half–half bipartition and the GGM can peak at different times during an annealing sweep. A two-regular graph may exhibit similar entanglement strength as a six-regular graph. In disconnected graphs, a fixed bipartition may show large bipartite entanglement while the multipartite entanglement (GGM) can vanish.

5.3.4 Relation between state occupation probability and GGM

In Fig. 5.5(a,b), the GGM and the occupation probability of the first excited state $|c_1|^2$ are quite comparable throughout the sweep, especially for larger p. This similarity becomes even more apparent by plotting G_2 and $|c_1|^2$ together in Fig. 5.8. This quantitative comparison shows that the GGM and $|c_1|^2$ do neither strictly coincide with each other nor do one strictly bound the other. Instead, G_2 is strictly bounded from above by the overlap probability with the initial state and the exact solution state, as we now prove.

Calculating the GGM of a given state $|\psi\rangle$ is equivalent to finding the two-party product state $|\pi\rangle_{\mathcal{A}:\mathcal{B}}$ with minimal distance from $|\psi\rangle$, see Eq. (5.1). As the annealing sweep terminates with the cost Hamiltonian, whose eigenstates $|e_i\rangle$, defined in Eq. (5.7) are product states, it seems reasonable to estimate the GGM by using these as a basis. The true GGM has to be smaller than the distance to any of these, i.e.,

$$G_2\left(|\psi(s)\rangle\right) \leq 1 - \underbrace{|\langle e_i|\psi(s)\rangle|^2}_{|c_i(s)|^2}, \quad \forall i\,. \tag{5.9}$$

Towards the end of a slow sweep, the expansion of Eq. (5.7) will have the largest weight in the ground-state of the cost Hamiltonian $|e_0\rangle$. We thus estimate the GGM by the upper bound

$$G_2\left(|\psi(s)\rangle\right) \leq 1 - |c_0(s)|^2. \tag{5.10}$$

Similarly, during the early stages of the sweep, the wave function will have a considerable weight in the initial product state $|+\rangle^{\otimes N}$. It is thus reasonable to expect

the distance to this state to provide a good upper bound in the initial part of the anneal,

$$G_2\left(|\psi(s)\rangle\right) \leq 1 - |(\langle +|^{\otimes N})|\psi(s)\rangle|^2 \equiv 1 - |d_+(s)|^2\,. \tag{5.11}$$

Moreover, the GGM for qubits has a theoretical maximum of 1/2. Putting all three bounds together, the GGM is upper bounded by

$$G_2\left(|\psi(s)\rangle\right) \leq \min\left\{1 - |c_0(s)|^2, 1 - |d_+(s)|^2, \frac{1}{2}\right\}. \tag{5.12}$$

Numerical experiments exemplify this bound, see Fig. 5.8. Considering the simplicity of the bound, the qualitative agreement is very satisfactory. In particular, the bound is saturated by $1-|c_0|^2$ towards the end of a successful anneal, as $|c_0|^2$ becomes the most significant probability among all $|c_i|^2$s. Later, in Sec. 5.4.3, we further use Eq. (5.10), to relate the success probability, i.e., the final $|c_0|^2$, to the final GGM. Importantly, the values entering Eq. (5.12) are easily obtained experimentally by projecting the state onto the computational basis or a locally rotated basis. It can thus be used as a physically-informed proxy for bounding multipartite entanglement.

As remarked above, in addition, there seems to be a qualitative similarity between the first excited state overlap probability $|c_1(s)|^2$ and the GGM $G_2(\psi)$, see Fig. 5.8. Towards the very end of the sweep for $p = 1000, 10000$, this similarity can be explained as only the states $|e_0\rangle$ and $|e_1\rangle$ remain prominent, i.e., $|c_0|^2 + |c_1|^2 \simeq 1$, and the upper bound of the GGM saturates, thus giving $G_2 = 1 - |c_0|^2 \simeq |c_1|^2$. However, their similarity in the middle of the sweep cannot be explained solely by this reasoning. Nonetheless, we speculate that such a non-zero $|c_1|^2$ has a role in keeping the instantaneous state entangled, as—assuming $|c_1|^2 < |c_0|^2$—it heralds the presence of an entangled superposition state.

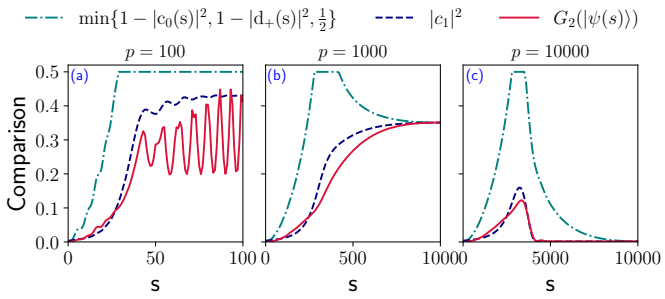

Figure 5.8. The GGM G_2 (solid red) is upper bounded by $\min\left\{1 - |c_0(s)|^2, 1 - |d_+(s)|^2, \frac{1}{2}\right\}$ (dash-dotted teal). For slow sweeps ($p = 1000, 10000$), the final state becomes a superposition of a few eigenstates, leading to $G_2 \approx |c_1|^2$ (blue dashed), as seen in panels (b) and (c).

5.4 Genuine multipartite entanglement barrier in Random Max-Cut ensemble

In Sec. 5.3, we have observed that the GGM assumes a peak during a slow quantum-annealing sweep, see Fig. 5.5(d). We call this a multipartite entanglement barrier since the inability to build up and then reduce the GGM prevents the algorithm from preparing the non-entangled solution state. We now investigate whether the observed barrier is (i) a universal feature not specific to the MaxCut problem instance used above and (ii) whether it is related to the instantaneous energy gap.

5.4.1 For random instances

We analyze 100 random MaxCut instances for eight vertices of 6-regular graphs with edge weights sampled from a Gaussian distribution $\mathcal{N}(\mu = 6, \sigma = 3)$. We run TQA with annealing sweep speeds $p = 100, 2000, 5000$. For $p = 100$, many instances display a peak or an oscillation in the GGM. However, there is no peak on average since the peaks occur at different times for different instances, see Fig. 5.9(a). Notably, the spread in the GGM at the beginning of the protocol is small. This trend is also observed for $p = 2000$ and $p = 5000$.

For $p = 2000$, we observe a small hump also in the instance-averaged GGM around $s/p = 1/3$, see Fig. 5.9(b). The final state's GGM is lower as compared to $p = 100$. The entanglement peak, or barrier, becomes more strongly apparent at $p = 5000$, see Fig. 5.9(c). In this case, the multipartite entanglement remains relatively low throughout the sweep, and the final GGM is minimal, indicating that the protocol has reached the solution state with high probability. Nevertheless, there are problem instances for which the GGM increases until $s/p = 1$, e.g., see the two red lines in Fig. 5.9(c), which do not exhibit a multipartite entanglement barrier.

For comparison, we also investigate the GGM in a QAOA protocol with few layers but classically optimized angles β and γ in Eq. (5.2), see Sec. 5.4.4 for details. Here, we do not observe a peak in the GGM but rather a build-up of the GGM with each additional QAOA layer. This behavior is similar to a short-depth quantum anneal, as in Fig. 5.9(a), which is reasonable considering the few layers used in QAOA.

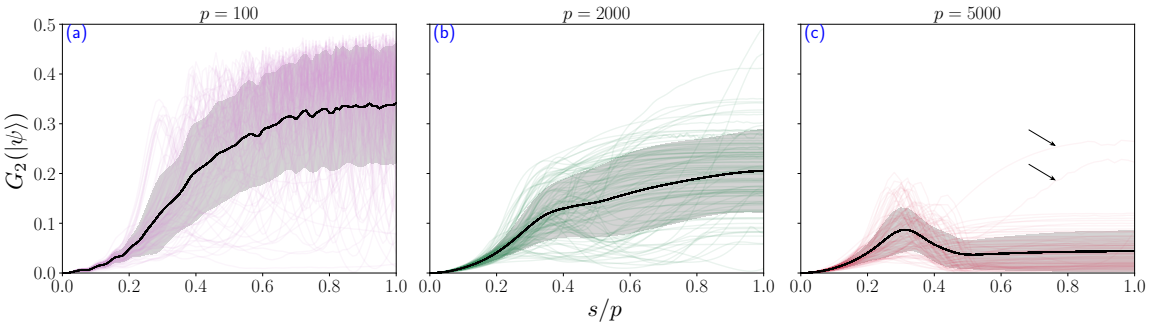

Figure 5.9. GGM from numerical benchmarks of 100 MaxCut instances. Panels (a) to (c), correspond to TQA with $p = 100, 2000, 5000$ layers, respectively, i.e., increasing annealing time. For $p = 100, 2000$, although some individual instances have peaks in the GGM (refer to Fig. 5.5 for an example), the average GGM does not show any peak (panel a) or only a small hump (b). In contrast, for $p = 5000$ (c), a peak in the GGM is also visible on average. With increasing p, the fluctuations in GGM between different instances decrease. Problem instances with no barrier are indicated by arrows. Again, strong oscillations typical for the defects generated by fast sweeps appear in $p = 100$.

5.4.2 Relation between GGM barrier and energy gap

In equilibrium, high entanglement can appear at quantum critical points with small energy gaps [361, 415]. However, this connection between low-lying spectrum and entanglement may not necessarily be expected in the out-of-equilibrium context of quantum optimization. Here, we investigate (a) whether the point where the energy gap closes correlates with the position of the GGM peak and (b) whether the size of the energy gap relates to the amount of GGM generated.

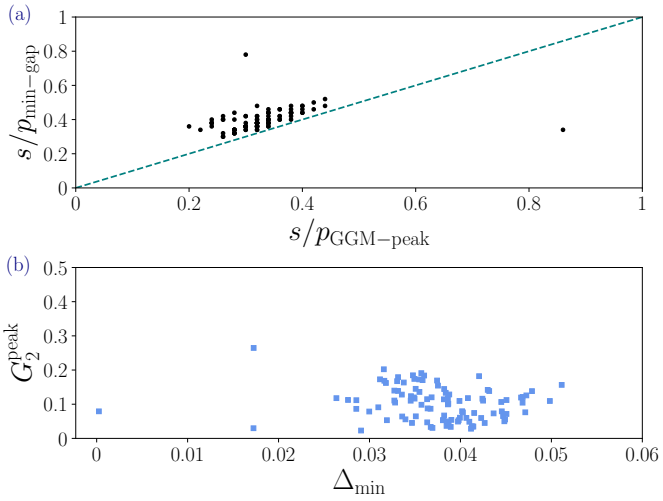

Figure 5.10. Relation between the multipartite entanglement barrier and the energy gap for 100 instances solved with TQA with $p = 5000$ layers and $\mathrm{d}t = 0.2$. (a) The time of minimum energy gap and the time of peak GGM are strongly correlated (99% confidence level). (b) The peak magnitude of GGM and the minimum energy gap show only weak anti-correlation (80% confidence level).

In Fig. 5.10(a), we plot the time s/p at which the energy gap and the GGM are minimum and maximum, respectively, for the same 100 problem instances as in Fig. 5.9. We report the first peak in the GGM to avoid ambiguities in case the GGM oscillates. The position of the minimum gap has a linear correlation with the position of the first GGM peak. Quantitatively, Pearson's correlation coefficient is $r = 0.28$ for the whole dataset, including the two extreme points. The corresponding t-score is $t = |r|\sqrt{(n-2)/(1-r^2)} = 2.89$, with $n = 100$ problem instances. This implies a statistically significant correlation at the 99% confidence level. Excluding the two outliers increases Pearson's correlation coefficient to $r = 0.525$. By contrast, we do not observe such a strong correlation between the magnitude of the energy gap and the size of the GGM peak, see Fig. 5.10(b). Indeed, the associated correlation coefficient of $r = -0.16$ is only significant at the 80% confidence level. As in this out-of-equilibrium situation, the near-degeneracy between ground and first excited state is not the sole reason for entanglement, the absence of a strong correlation between the amount of entanglement and the energy gap is not unexpected.

5.4.3 Relation to success probability

Generating and removing entanglement in quantum circuits are complex operations. For our MaxCut problems with a non-degenerate solution, quantum annealing must eliminate any existing entanglement to achieve the final product state. This raises an interesting question: Does the non-zero entanglement generated during quantum annealing hinder the optimization algorithm's ability to find the optimal solution? Specifically, does a higher GGM in the final state limit the probability of success? If so, given the presence of an entanglement barrier, could a drop in the GGM from its peak enhance the chances of achieving a better success probability?

Final GGM and success probability

As a corollary to the Sec. 5.3.4, the success probability, i.e., the probability corresponding to the ground-state of the cost Hamiltonian, $|c_0|^2$, is bounded above by $1 - G_2^{\mathrm{final}}$. In Fig. 5.11(a), we see that with an increasing number of layers (slower sweep), the success probability saturates the bound. In contrast, with fewer layers, the success probability does not saturate the bound, as the final state has support on multiple

eigenstates, making the bound of Eq. (5.10) using a single amplitude too loose. These results are similar to the observed relation between *bipartite* entanglement for a fixed bipartition and the success probability in Ref. [414].

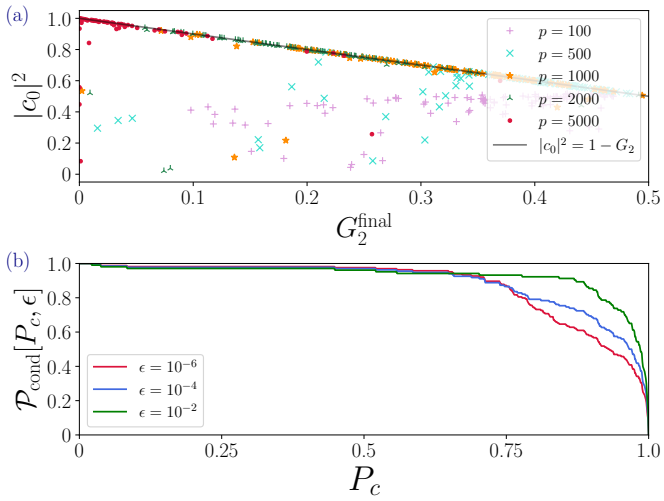

Figure 5.11. Relation of entanglement and success probability, over 100 instances of 6-regular graphs with 8 vertices (a) Final success probability $|c_0|^2$ is upper bounded by $1 - G_2^{\text{final}}$, and large p values approach this bound. (b) The conditional probability of achieving a success probability $> P_c$ increases with greater disentanglement ΔG, shown for $\epsilon > \{10^{-6}, 10^{-4}, 10^{-2}\}$ across 100 instances with $p = 2000$ and $p = 5000$.

Disentanglement and success probability

As a complementary analysis, we also study how the amount of dis-entanglement, i.e., the reduction of GGM after its peak, $\Delta G = G_2^{\max} - G_2^{\text{final}}$, is related to the success probability. To this end, we calculate the conditional probability ($\mathcal{P}_{\text{cond}}[P_c, \epsilon]$) of obtaining a success probability greater than some P_c, given that the sweep has shown some minimum amount of disentanglement, $\Delta G > \epsilon$

$$\mathcal{P}_{\text{cond}}\Big[|c_0|^2 > P_c \big| \Delta G > \epsilon\Big] = \frac{\mathcal{P}\Big[(|c_0|^2 > P_c) \cap (\Delta G > \epsilon)\Big]}{\mathcal{P}\Big[\Delta G > \epsilon\Big]}. \tag{5.13}$$

We study only the cases where a GGM barrier is observed, i.e., $G_2^{\max} > G_2^{\text{final}}$. We choose $p = 2000, 5000$, computing the TQA of 100 instances for both numbers of layers. To show reasonable comparison, we need to choose small values of $\epsilon = (10^{-6}, 10^{-4}, 10^{-2})$, as the final GGM is itself small in terms of absolute values. We find a larger ΔG (increasing ϵ) to result in a larger success probability, see Fig. 5.11(b). In particular, large values of P_c are capped by the given fixed minimum disentanglement, leading to a downward bend in the curves [Fig. 5.11(b)] and suggesting the necessity of a large amount of disentanglement for a good success probability.

5.4.4 GGM in Quantum Approximate Optimization Algorithm

In this chapter, we are primarily interested in Trotterized quantum annealing. Nonetheless, it is interesting to compare the results with those obtained with a QAOA protocol. The standard QAOA applies p layers of the unitaries $\exp(-i\beta_k H_{\text{M}}) \exp(-i\gamma_k H_{\text{C}})$, with $k = 1, ..., p$ on the initial state $|+\rangle^{\otimes N}$ to create a trial state $|\psi(\boldsymbol{\gamma}, \boldsymbol{\beta})\rangle$. Then, a classical optimizer seeks the optimal parameters $\boldsymbol{\beta} = (\beta_1, \ldots, \beta_p)$ and $\boldsymbol{\gamma} = (\gamma_1, \ldots, \gamma_p)$ that minimize the energy $\langle\psi(\boldsymbol{\beta}, \boldsymbol{\gamma})| \hat{H}_C |\psi(\boldsymbol{\beta}, \boldsymbol{\gamma})\rangle$, which is measured by the quantum

processor. As optimizing over $2p$ parameters in the classical optimizer is a bottleneck, we limit our simulation to small depths p.

In its spirit, QAOA is an approximate algorithm. It is designed to provide samples of a good set of solutions using only short-depth circuits (in contrast to quantum annealing, where one is typically more interested in slow but near-optimal runs). Therefore, as a figure of merit to quantify the performance of QAOA, we use the approximate ratio $\alpha = \langle E \rangle / E_{\text{exact}}$ instead of success probability. We run QAOA with different depths p for the same MaxCut instance we consider in Sec. 5.3.

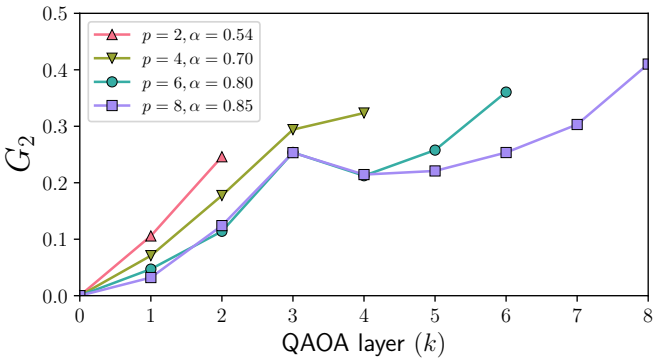

Figure 5.12. The GGM (G_2) of the state obtained after layer $k = 0, \ldots, p$ of a depth-p QAOA. The approximation ratio (see legend) and final GGM both increase with p.

For fixed depth p, the GGM increases with each QAOA layer k; however, for larger p, there is a kink at $k = 3$. Nonetheless, the approximation ratio α and the final GGM increase with QAOA depth p without a clear presence of an entanglement barrier. This is akin to the observed feature in the GGM when the number of TQA layers is small, see $p = 100$ in Fig. 5.9(a). Recall that the multipartite entanglement barrier appears when the instantaneous overlap probability of the ground state $|c_0|^2$ and the first excited state $|c_1|^2$ starts to become distinguishable, see Fig. 5.5(b) and Fig. 5.2. Thus, a large GGM may not necessarily hinder its performance as long as it stems from the superposition of the actual ground state $|e_0\rangle$ with a few excited states $|e_{i>0}\rangle$. In that case, there is a high probability that a manageable number of repetitions of the algorithm will then permit us to measure the optimal state on the computational basis at least once.

5.5 Summary and outlook

To summarize, multipartite entanglement arises in Trotterized quantum annealing even when the solution of the classical optimization problem is non-degenerate. While fewer layers—or a faster sweep—generate more entanglement, increasing the number of layers causes the GGM to grow, reach a peak, and then decline to zero during the sweep—a phenomenon one can call a multipartite entanglement barrier. We prove that the success probability is upper-bounded by $1 - G_2^{\text{final}}$, which is saturated when the final state is close to a product state (such as the desired solution state), as illustrated by numerical results from MaxCut instances. Thus, achieving a higher success probability typically requires lower final-state entanglement. Such a relation can be leveraged to benchmark quantum hardware [325, 443, 445, 446]. From the phenomena of the entanglement barrier, we quantify the relation between disentanglement and success probability through a conditional probability and find that a stronger drop in multipartite entanglement after the GGM peak improves the success probability.

Moreover, as the GGM corresponds to an optimal bipartition with minimal bipartite entanglement [447], insights about GGM can be used in circuit-cutting protocols to find an optimal cut such that the multipartite entanglement loss is minimal [448].

Our work has consequences for short-depth protocols such as QAOA and its variants. The classical parameter optimization loop is time-consuming [301], and navigating the optimization landscape in variational quantum algorithms is NP-hard [449]. Therefore, recent research investigates methods to obtain QAOA parameters by classical means. In particular, tensor networks may help to obtain good parameters [260]. Here, it is sufficient to approximate the loss landscape to produce good QAOA parameters qualitatively. Our work shows that multipartite entanglement can build up in QAOA. An interesting research question is thus whether tensor-network methods can provide a qualitative approximation of the loss landscape that is good enough to produce good QAOA parameters at a classically tractable bond dimension.

Further research could explore how the multipartite entanglement barrier manifests if the Hamiltonian is engineered using the tools from shortcuts to adiabaticity [450]. By exploring possible links to the graph's spectral properties, one may hope to understand better why GGM barriers cluster in specific regions [451]. Moreover, understanding the source of such entanglement in terms of physical phenomena, e.g., the Landau–Zener transition [444] or multiqubit quantum tunneling [452], one may hope to better predict the possibility or impossibility of reaching the solution state [243]. Our work focuses on pure states. However, some quantum algorithms may leverage mixed states [453–456], and it will be interesting to use the GGM to study the role of multipartite entanglement in such cases [141, 146, 147].

Chapter 6

Validating quantum effects in quantum algorithm

Do quantum processing units generate entanglement in QAOA?

6.1 Introduction

In recent years, quantum computation has seen sustained and accelerating progress in both algorithmic development [457–459] and experimental platforms [288, 460–462]. Among the many potential applications, quantum optimization stands out as a particularly promising area, where even modest improvements over the best-known classical methods could lead to significant advancements across scientific and industrial domains. Hybrid quantum-classical algorithms, such as the Quantum Approximate Optimization Algorithm (QAOA) [81,237], have emerged as viable approaches for harnessing the capabilities of noisy intermediate-scale quantum (NISQ) devices. These algorithms combine quantum circuits with classical optimization routines, leveraging the strengths of both computational paradigms. Despite notable improvements in quantum hardware, including increased qubit counts and extended coherence times, the performance of QAOA is often limited by the efficiency and effectiveness of the classical optimization component. This raises a critical question: to what extent does the quantum processing unit (QPU) contribute to the overall performance of the algorithm? In other words, if classical routines primarily perform the heavy lifting, are there genuinely quantum effects at play that are essential to the algorithm's success? Empirically investigating such "quantumness" within QAOA is crucial, as any claims of quantum advantage hinge upon it. Without meaningful quantum contributions, the potential for QAOA to surpass classical methods would be fundamentally undermined.

We address this question by measuring entanglement on IBMQ hardware for classically optimized QAOA. We find that the optimized QAOA on hardware exhibits entanglement, which is qualitatively comparable to that in a noiseless simulation up to a certain circuit depth. To detect entanglement, we employ an entanglement measure inspired by the geometric measure of entanglement of Chapter. 5.

In this chapter, first, in Section 6.2, we describe our measurement protocol in detail, including how we estimate entanglement from a fixed bipartition using a hardware-efficient SWAP test, and how Schmidt coefficients can be extracted from Rényi entropy. Section 6.3 presents benchmarks of our method against exact simulations on small systems, analyzing its robustness under realistic noise models. We then move to implementation in Section 6.4, where we discuss the practical challenges of executing the protocol on IBM quantum devices. Finally, in Section 6.5, we apply our protocol to QAOA circuits across various system sizes up to 76 qubits and analyze

how entanglement evolves in QAOA. This progression allows us to assess the presence of entanglement in QAOA circuits experimentally.

6.2 Methods: Obtaining GGM in experiment

Measuring entanglement can offer profound insights into quantum correlations, extending beyond the conventional benchmarking of individual qubit performance in noisy intermediate-scale quantum (NISQ) devices [463–466]. Yet, its role in quantum optimization remains largely unexplored. As hybrid quantum algorithms gain attention, understanding entanglement becomes essential for two reasons: (1) to quantify how much genuine quantum resource the algorithm is using, and (2) to assess whether any observed advantage truly stems from quantum effects beyond classical optimization capabilities.

One established method for probing entanglement is the SWAP test [467–470], which compares copies of a quantum state to measure the purity of the subsystem. From this, one can compute quantities such as the Rényi entropy or, in ideal scenarios, the von Neumann entropy, provided that multiple Schmidt coefficients can be resolved. However, creating multiple identical copies is challenging on current small-scale hardware.

6.2.1 SWAP test to Rényi entropy

Consider a system composed of two subsystem $\mathcal{A}$ and $\mathcal{B}$, which can be written as

$$|\psi\rangle = \sum_{ij} c_{ij} |a_i\rangle \otimes |b_j\rangle , \tag{6.1}$$

where the states $|a_i\rangle$ and $|b_j\rangle$ form orthonormal bases of $\mathcal{A}$ and $\mathcal{B}$. The reduced density matrix for subsystem $\mathcal{A}$ is defined by tracing over $\mathcal{B}$,

$$\rho_A = \mathrm{Tr}_B(|\psi\rangle \langle\psi|), \tag{6.2}$$

which contains the information about entanglement between $\mathcal{A}$ and $\mathcal{B}$. For example, one can define the nth Rényi entropy,

$$S_n = \frac{1}{1-n} \log(R_n), \;\; R_n = \mathrm{Tr}(\rho_A^n). \tag{6.3}$$

Similarly, one can also calculate von Neumann entanglement entropy,

$$S_{\mathrm{vN}} = -\mathrm{Tr}[\rho_A \log \rho_A]. \tag{6.4}$$

Now, the main challenge in the experiment is to obtain R_n without estimating the state ρ_A, which is costly in terms of tomography. On the other hand, it is clear that to find the trace of the power of a matrix, knowing the entire matrix is overkill. In this scenario, the SWAP test provides a way.

SWAP test. In quantum computation, the SWAP test is a well-known method to check how much two states differ [471,472]. To demonstrate the method, let's consider two states $|\phi\rangle$ and $|\psi\rangle$. Now, if we follow the circuit in Fig. 6.1, we can see that after Hadamard and C-SWAP, the state becomes

$$\frac{1}{\sqrt{2}}(|0,\phi,\psi\rangle + |1,\psi,\phi\rangle), \tag{6.5}$$

and then the second Hadamard results in

$$\frac{1}{2}|0\rangle(|\phi,\psi\rangle + |\psi,\phi\rangle) + \frac{1}{2}|1\rangle(|\phi,\psi\rangle - |\psi,\phi\rangle). \tag{6.6}$$

Thus, the probability of ancilla being 0 captures their overlap,

$$\text{Prob(ancilla} = 0) = \frac{1}{2} + \frac{1}{2}|\langle\psi|\phi\rangle|^2. \tag{6.7}$$

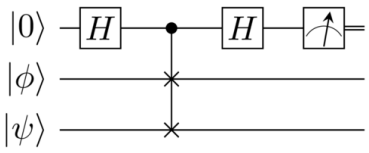

Figure 6.1. Circuit for the quantum SWAP test: used to estimate the overlap between two quantum states. An ancilla qubit controls a SWAP operation between the two input states, and the probability of measuring $|0\rangle$ on the ancilla is related to the fidelity between the states (from Wikipedia).

The SWAP test, originally used to assess similarity between states, can also estimate subsystem purity—e.g., applying it to subsystem $\mathcal{A}$ yields $\text{Tr}(\rho_A^2)$, and with n copies, one can access $\text{Tr}(\rho_A^n)$. We elaborate on this below.

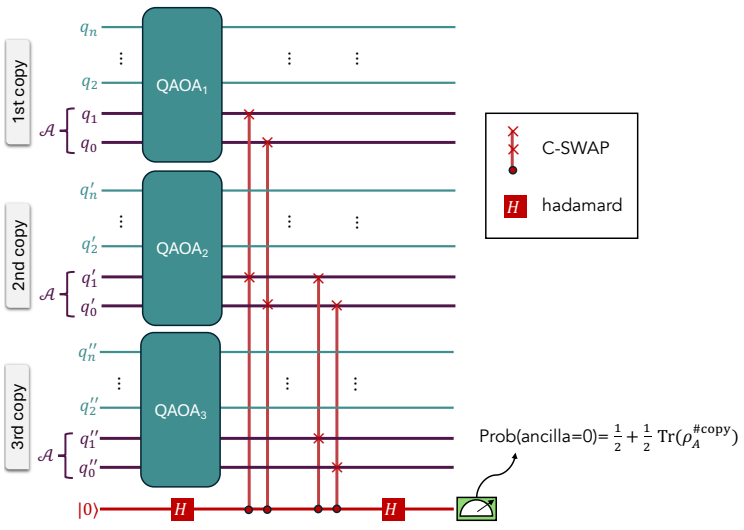

Figure 6.2. Multi-copy SWAP test: By preparing multiple copies of a quantum state and applying the SWAP test on a subset of qubits ($\mathcal{A}$), one can estimate the Rényi entropy of order n, which is proportional to $\text{Tr}(\rho_A^n)$. This procedure requires n copies of the state. The estimation is obtained from the probability of measuring the ancilla qubit in the $|0\rangle$ state. The SWAP test involves a controlled-swap (or controlled-permutation) operation between corresponding qubits in the copies, with the ancilla (control) qubit encoding the interference information.

Let's consider two copies of the state: $|\psi\rangle = \sum_{ij} c_{ij}|a_i\rangle|b_j\rangle$ and $|\psi'\rangle = \sum_{i'j'} c_{i'j'}|a_{i'}\rangle|b_{j'}\rangle$. The full circuit for measuring R_n involves applying a Hadamard gate to an ancilla qubit, followed by a controlled-SWAP (C-SWAP), and then another Hadamard gate,

as shown in Fig. 6.2. Let's consider the simplest case with just two copies:

$$\begin{aligned}
|\psi\rangle|\psi'\rangle|0\rangle &\xrightarrow[\mathbb{I}\otimes\mathbb{I}\otimes H]{} |\psi\rangle|\psi'\rangle|+\rangle \\
&\xrightarrow[C-\mathrm{SWAP_A}]{} \frac{1}{\sqrt{2}}(|\psi\rangle|\psi'\rangle|0\rangle + \sum_{ij}\sum_{i'j'} c_{ij}c_{i''j'}|a_{i'}\rangle|b_j\rangle|a_i\rangle|b_{j'}\rangle|1\rangle) \\
&\xrightarrow[\mathbb{I}\otimes\mathbb{I}\otimes H]{} \frac{1}{2}\Big[\Big(|\psi\rangle|\psi'\rangle + \sum_{ij}\sum_{i'j'} c_{ij}c_{i''j'}|a_{i'}\rangle|b_j\rangle|a_i\rangle|b_{j'}\rangle\Big)|0\rangle \\
&\qquad + \Big(|\psi\rangle|\psi'\rangle - \sum_{ij}\sum_{i'j'} c_{ij}c_{i''j'}|a_{i'}\rangle|b_j\rangle|a_i\rangle|b_{j'}\rangle\Big)|1\rangle\Big] .
\end{aligned} \tag{6.8}$$

From here we can see the probability of ancilla being 0 is given by

$$\begin{aligned}
\mathrm{Prob}(\text{ancilla} = |0\rangle) &= \frac{1}{4}\left|\left|\Big(|\psi\rangle|\psi'\rangle + \sum_{ij}\sum_{i'j'} c_{ij}c_{i''j'}|a_{i'}\rangle|b_j\rangle|a_i\rangle|b_{j'}\rangle\Big)\right|\right|^2 \\
&= \frac{1}{2} + \frac{1}{2}\sum_{ij}\sum_{i'j'} c_{ij}c_{i'j'}\langle\psi|\langle\psi'|a_{i'}\rangle|b_j\rangle|a_i\rangle|b_{j'}\rangle \\
&= \frac{1}{2} + \frac{1}{2}\sum_{kl}\sum_{k'l'}\sum_{ij}\sum_{i'j'} c^*_{kl}c^*_{k'l'}c_{ij}c_{i'j'}\underbrace{\langle a_k|a_{i'}\rangle}_{\delta_{ki'}}\underbrace{\langle b_l|b_j\rangle}_{\delta_{lj}}\underbrace{\langle a_{k'}|a_i\rangle}_{\delta_{k'i}}\underbrace{\langle b_{l'}|b_{j'}\rangle}_{\delta_{l'j'}} \\
&= \frac{1}{2} + \frac{1}{2}\sum_{ii'jj'} c^*_{i'j}c^*_{ij'}c_{ij}c_{i'j'} .
\end{aligned} \tag{6.9}$$

We can identify the last term as $\mathrm{Tr}(\rho_A^2)$,

$$\begin{aligned}
\rho_A = \sum_{ii'j} c^*_{i'j}c_{ij}|a_{i'}\rangle\langle a_i| \Rightarrow \rho_A^2 &= \sum_{kk'l}\sum_{ii'j} c^*_{k'l}c_{kl}c^*_{i'j}c_{ij}|a_{k'}\rangle\langle a_k|a_{i'}\rangle\langle a_i| \\
\Rightarrow \mathrm{Tr}(\rho_A^2) &= \sum_{ii'jl} c^*_{il}c_{i'l}c^*_{i'j}c_{ij} = \sum_{ii'jj'} c^*_{ij'}c_{i'j'}c^*_{i'j}c_{ij} .
\end{aligned} \tag{6.10}$$

Thus, by measuring the probability of the ancilla being in $|0\rangle$, one can obtain the information about $\mathrm{Tr}(\rho_A^2)$ in the experiment.

6.2.2 R_n to Schmidt values

To obtain von Neumann entropy, one needs to have the eigenvalues of ρ_A instead of only the trace of it. Or, one can extract the Schmidt eigenvalues from there. We know that for a state $|\psi\rangle \in \mathbb{C}^{ab} = \mathbb{C}^a \otimes \mathbb{C}^b$, we can do Schmidt decomposition to obtain

$$|\psi\rangle = \sum_{k=1}^{D} \lambda_k |u_k\rangle \otimes |v_k\rangle , \quad \{|u_k\rangle\} \in \mathbb{C}^a, \{|v_k\rangle\} \in \mathbb{C}^b. \tag{6.11}$$

Now, we need to obtain the Schmidt values, i.e., eigenvalues of ρ_A from the information of $R_n = \mathrm{Tr}(\rho_A^n)$. We can use the Newton–Girard formula to obtain the roots of a polynomial made of R_n [469, 473].

Newton-Girard formula. It connects power sums $\sum_i x_i^k$ to the elementary symmetric polynomials made of those, for example,

$$e_0 = 1, \quad e_1 = \sum_i x_i, \quad e_2 = \sum_{1\le i<j\le n} x_i x_j. \tag{6.12}$$

The Newton-Girard formula shows how the roots form the symmetric polynomials,

$$\prod_{i=1}^{n}(x - x_i) = \sum_{k=0}(-1)^k e_k x^{n-k}\,. \tag{6.13}$$

To obtain the eigenvalues of ρ_A, we can replace the LHS of Eq. (6.13), by $\det\{(xI - \rho_A)\}$, where x will be the eigenvalues or Schmidt probabilities. Then it is evident that $e_1 = \mathrm{Tr}(\rho_A)$, and we can understand what is e_2, by investigating the structure of

$$\begin{aligned} R_2 &= \mathrm{Tr}(\rho_A^2) = \sum_i x_i^2, \\ e_2 &= \sum_{1\le i<j\le n} x_i x_j = \left((\underbrace{\sum_i x_i}_{=1})^2 - \sum_i x_i^2 \right)/2 = \frac{1}{2}(1 - R_2). \end{aligned} \tag{6.14}$$

Similarly, we can see that for $n = 3$,

$$R_3 = \sum_i x_i^3, \quad e_3 = \sum_{1\le i<j<k\le n} x_i x_j x_k, \tag{6.15}$$

and using basic algebra, we can see that,

$$\begin{aligned} (\sum_i x_i)^3 &= \sum_{i=1}^{n} x_i^3 + 3 \underbrace{\sum_{i,j=1, i\neq j}^{n} x_i^2 x_j}_{=(\sum_{i=1}^n x_i)(\sum_{i=1}^n x_i^2) - \sum_{i=1}^n x_i^3} + 6 \sum_{1\le i<j<k\le n} x_i x_j x_k \\ \Rightarrow 1 &= R_3 + 3(R_2 - R_3) + 6e_3 \\ \Rightarrow e_3 &= \frac{1 - 3R_2 + 2R_3}{6}. \end{aligned} \tag{6.16}$$

One can generalize this relation between e_k and R_k by defining a matrix,

$$E_k = \begin{pmatrix} 1 & 1 & 0 & \dots \\ R_2 & 1 & 2 & \dots \\ R_3 & R_2 & 1 & \dots \\ \dots & & & \end{pmatrix} \Rightarrow e_k = \frac{\det E_k}{k!}, \tag{6.17}$$

where E_k is defined as the $(k \times k)$ matrix of the top-left corner, and we can easily recover the above relations between e_k and R_k. As a final equation,

$$\det(xI - \rho_A) = \sum_{k=0}^{n} \frac{(-1)^k}{k!} \det(E_k) x^{n-k}, \tag{6.18}$$

and the roots of the above polynomials (RHS) are nothing but the Schmidt coefficients. Now, we can see that to obtain all the Schmidt coefficients (in order to either calculate von-Neumann entropy or entanglement spectrum), one needs to have multiple copies of the same state, which becomes complicated in the experiment. However, measurement of R_n is dominated by λ_1 as $\lambda_1^{2n}[1 + (\lambda_2^2/\lambda_1^2)^n + \dots]$.

> For p largest eigenvalues ($\lambda_1^2 > \lambda_2^2 > \cdots > \lambda_p^2$) need upto p-copies, and hence $\mathcal{O}(pN)$ qubits with a parallel circuit depth of $\mathcal{O}\left[p\left(\frac{\lambda_1^2}{\lambda_p^2}\right)^p\right]$ to resolve the Schmidt values [469].

6.2.3 Schmidt values to GGM

From the complication of obtaining all the Schmidt coefficients, it is obvious that von-Neumann entropy needs more resources. Instead, either one can estimate the Rényi entropy, or, due to the ordering of the Schmidt values (coming from roots of the polynomial), the maximum of it can be used to obtain $1 - \lambda_{max}^2$, which becomes the GGM (sec. 2.6.4) on the optimal bipartition. As it requires only two copies of the state, it is more hardware-friendly.

Recall the definition of GGM from Eq. (2.66),

$$G_2(|\psi\rangle) = 1 - \max_{\mathcal{A}:\mathcal{B}} (\lambda_{\mathcal{A}:\mathcal{B}}^{\max})^2. \tag{6.19}$$

Now, the challenge is to maximize over all bipartitions $\mathcal{A} : \mathcal{B}$, which is experimentally expensive because:

1. the number of possible bipartitions increases with system size,

2. with increasing size of partition $\mathcal{A}$, a larger number of C-SWAPs need to be implemented, which increases depth

3. given the limited connectivity in the devices, the distance between qubits in partitions to the ancilla can increase, and qubit routing becomes necessary, which also affects the quality of the result.

All such problems can be set aside if we consider a fixed partition, where the qubits in the partition are at a minimal distance from the ancilla on the device. Although this does not confirm genuinely multipartite entanglement, as we have not optimized over all possible bipartitions, it still reveals meaningful entanglement characteristics of the system. Moreover, as observed in Fig. 5.6, in quantum optimization algorithms such as QAOA and quantum annealing, the Schmidt values do not differ significantly across different bipartitions; hence, empirically, we may not be far away from the actual GGM[1].

To be more concrete, instead of optimizing over all partitions, we define on partition $\mathcal{A}$ as

$$G_{\mathcal{A}} = 1 - (\lambda_{\mathcal{A}:\bar{\mathcal{A}}}^{\max})^2. \tag{6.20}$$

[1]Note, this will be an upper bound on the actual GGM

6.3 Benchmarking the method

To obtain the entanglement from the circuit in Fig. 6.2, one has to run the circuit multiple times to get enough count statistics, such that one can trust the probability to obtain a good result, with less error bar. To test if this way of circuit evaluation works, we first compare the $G_{\mathcal{A}}$ obtained from the circuit with the numerical value obtained by doing singular-value decomposition.

6.3.1 Fixed partition

We consider a random brick-wall circuit and generate states with variable depth, obtaining 100 different circuits with distinct GGM. Note that we choose only those circuits where the optimal partition is $\mathcal{A} = [0]$, so $G_{\mathcal{A}} = G_2$. In Fig. 6.3, we can observe that in an ideal noiseless simulation using 10000 shots, we can obtain the same GGM as numerically obtained, with a small errorbar, which benchmarks our method to be accurate for a wide range of GGM values. However, if we perform a noisy simulation using the noise model of the IBM hardware, we can observe a constant upward shift, which we believe is reminiscent of the noise introduced by the measurement circuit involving the C-SWAP part. We will see later that if one can account for this bias error, one can get closer to the ideal values. We also check if one can obtain a better result using zero-noise extrapolation (see Sec. 3.6.3) on a noisy simulation; however, as we can see, even after $3X$ and $5X$ CNOT insertion, the results do not improve sufficiently, compared to the cost of doing it in hardware.

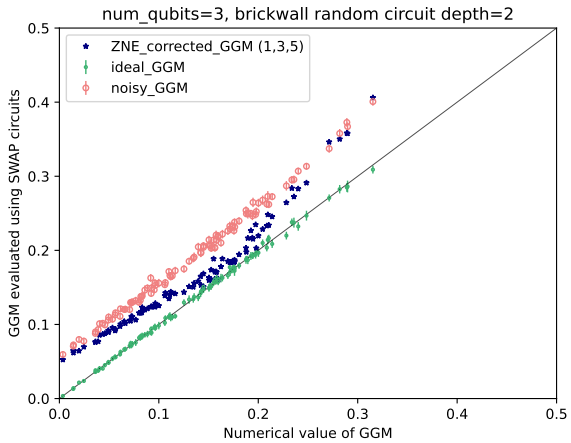

Figure 6.3. Benchmarking the circuit method of estimating GGM: From a random circuit of 3 qubits, we generated states with numerical values of GGM spanning from 0 to 0.4. We then estimate the GGM using the circuit by measuring the ancilla 10,000 times to obtain the y-axis values. The noiseless data matches well with the numerical GGM, while the noisy simulation data shows an upward shift. Zero-noise extrapolation does not consistently correct the deviation across all GGM values.

6.3.2 All partitions

In Section 6.2.3, we explained why working with all partitions is complicated and more errors can be introduced due to their distance from the ancilla. In Fig. 6.4, we show that through experimental data. Comparing with $(0), (1), (2)$, we can see that as the distance increases from the ancilla, which is near (0), the calibration error increases. With a larger number of qubits in the subsystem, the number of C-SWAPs has to increase, and the error also increases, as can be seen by comparing one-qubit partition with two-qubit partitions.

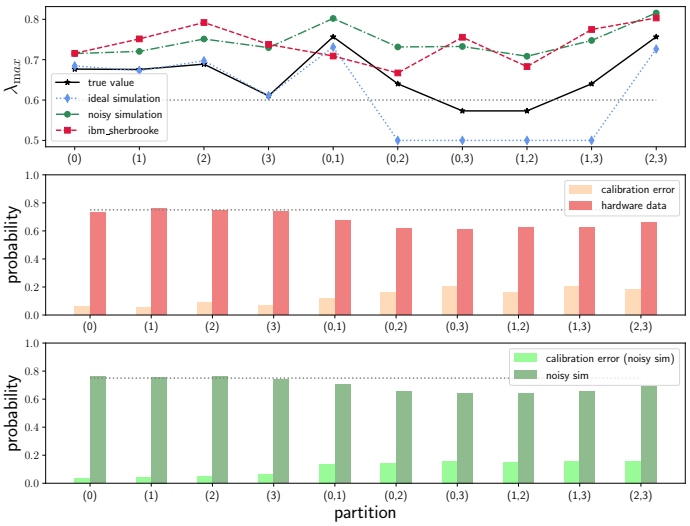

Figure 6.4. Performance over all bipartitions on quantum hardware. The protocol was implemented across several partitions (for 4 qubits, this corresponds to 10 partitions), and the results reflect the noise accumulation due to C-SWAPs and limited hardware connectivity, as we can see in the calibration error increases as the partition is far away from (0), and also when more qubits are involved in partition.

6.3.3 Noise accumulation from C-SWAP

As indicated by both the noisy simulations and hardware results in Fig. 6.4, the C-SWAP gate can be a significant source of error. This is because, when executed on hardware using its native gate set, it involves several error-prone two-qubit gates, which significantly contribute to the overall noise.

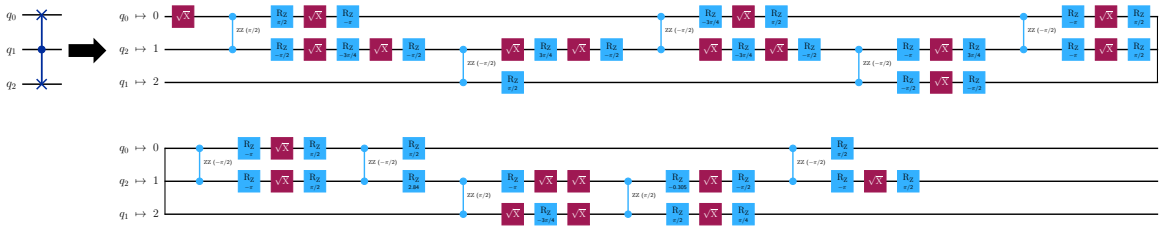

Figure 6.5. Transpiled C-SWAP circuit: A simple C-SWAP acting on only one qubit in the partition for each copy becomes a long circuit with multiple R_{ZZ} gates on the hardware.

6.3.4 Can circuit cutting help in measuring entanglement?

The main challenge in using the SWAP circuit is its increased circuit depth after transpilation. In this scenario, one can consider advanced techniques, such as circuit cutting [285, 474]. It is a technique that was devised to allow longer circuits to run on quantum hardware by cutting into sub-circuits that are suitable for execution on hardware, at the cost of additional sampling overhead [475, 476]. Then, one has to measure part of the circuit multiple times with a sampling overhead and post-process to obtain the target quantum channel [477, 478],

$$U = \sum_i a_i F_i \,, \tag{6.21}$$

where U is the target quantum channel, and each F_i is executable on hardware. The coefficients a_i come from quasi-probability decomposition (qpd).

Circuit cutting can perform two types of cuts:

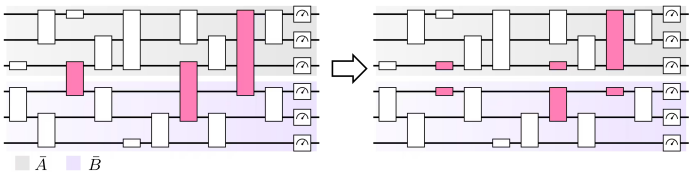

Figure 6.6. Example of circuit cutting via a gate cut. The full circuit is divided into two smaller subcircuits, $\bar{A}$ and $\bar{B}$, each with fewer qubits. The overall output is reconstructed by mid-circuit measurements on each subpart (Adapted from Qiskit Circuit Cutting [479]).

- Gate (space-like) cut: cut through a multi-qubit gate, to make smaller subcircuits with fewer qubits
- Wire (time-like) cut: cut directly through a qubit wire (essentially a single-qubit identity gate that has been cut into two pieces) to fight against coherence time

Cutting comes with sampling overhead, which is exponential in the number of cuts. For example, a CNOT gate cut incurs a sampling overhead of 9X, compared to an original CNOT.

Figure 6.7. Example of a cut-circuit for C-SWAP: We can see the number of R_{ZZ} gates significantly reduces, and mid-circuit measurements of quasi-probability decompositions are introduced.

We use circuit cutting on the C-SWAP gate to obtain the cut circuits in a way that eliminates the need for ancilla, and the circuit depth is significantly reduced (see Fig. 6.7). However, we need to run 8 more such circuits, with their sampling overheads, which makes the method costly. Despite the overhead, we implemented the circuit-cutting approach but found that it offers no clear advantage over standard C-SWAP transpilation. This is primarily because circuit cutting requires repeated measurements of both qubit subsets coming from mid-circuit measurements (see Fig. 6.7), which are highly sensitive to readout errors. To examine this effect, we used a product state in a test setup and scaled the readout error channel by a factor of η. Using noisy simulations, we then extracted the ancilla measurement probabilities (see Fig. 6.8). The results show that while the standard (uncut) method is relatively insensitive to readout errors, the circuit cutting (CC) approach improves only as η decreases, highlighting its strong dependence on readout fidelity. Since current IBM devices typically exhibit readout errors that are 3–4 times higher than the R_{ZZ} gate error, introducing additional R_{ZZ} gates proves to be a more practical alternative than relying on readout-intensive techniques like circuit cutting. Therefore, for the remainder of the chapter, we do not employ circuit-cutting techniques and instead rely on the standard transpilation of the C-SWAP gate.

6.4 Obtaining entanglement in QAOA from hardware

With these methods in place, we are now equipped to measure the entanglement generated in QAOA and to explore how it is utilized during the algorithm. We consider

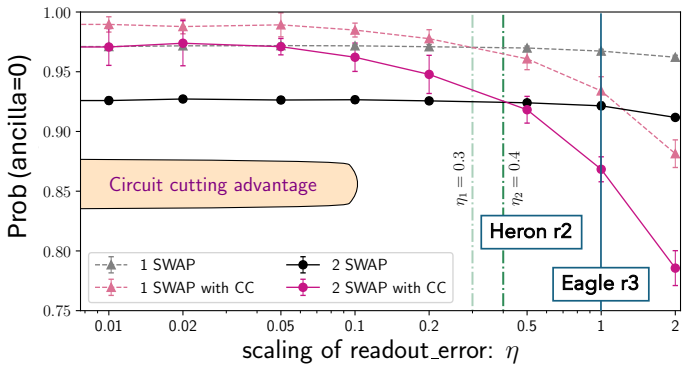

Figure 6.8. Readout error-regions of the advantage of circuit cutting. Circuit cutting offers advantages over without CC for 2-CSWAP at $\eta = 0.4$, which is just below where our current Heron r2 devices stand, and 1-CSWAP needs even better readout error.

the hardware-native MaxCut problem[2] with randomly chosen coefficients on the edges $\{-1, +1\}$, with a small bias field Z to break the degeneracy on the qubit considered in the bipartition $\mathcal{A}$ -

$$H_C = fZ_{[\mathcal{A}]} + \sum_{i,j \in \text{coupling map}} J_{ij} Z_i Z_j \,; \quad J_{ij} \in \{-1, +1\}, \; f = 0.01 \,. \tag{6.22}$$

6.4.1 Choosing qubit arrangement

As the device has limited connectivity, in this case heavy-hex [Fig. 6.9(b)], keeping the ancilla close to the qubits in bipartitions $\mathcal{A}$ would avoid needing to add multiple SWAPs for connectivity. We choose qubits such that ancilla (red) can be close to and in between $\mathcal{A}$ (blue) and $\mathcal{A}'$ (orange) [see Fig. 6.9(b)], which implies in the circuit the 1st copy of the QAOA is flipped [see Fig. 6.9(a)]. Out of multiple possibilities of such subgraphs or substructures in the full heavy-hex map, we choose the best one comparing total gate-fidelity and readout-error of ancilla qubit, as detailed in Sec. 3.6.2.

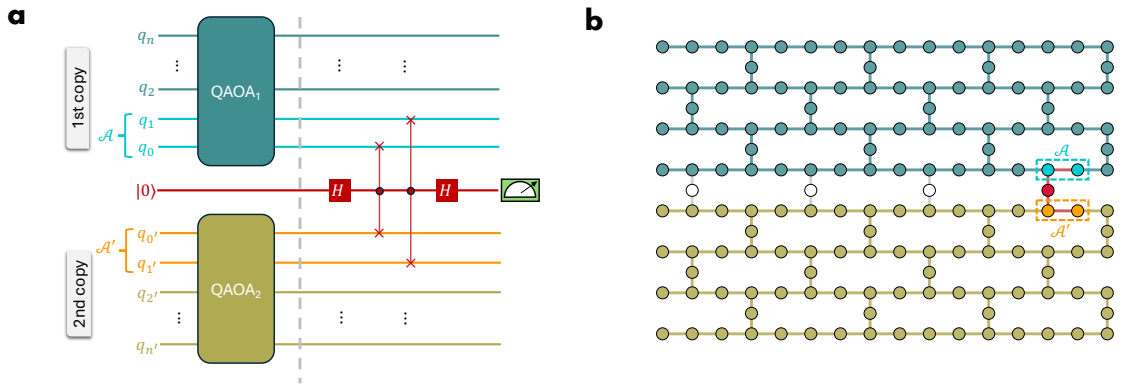

Figure 6.9. Qubit positions are chosen based on Sec. 3.6.2 from the possible set of subgraph structures where the ancilla qubit is in between the qubits of $\mathcal{A}$ and $\mathcal{A}'$ to keep them closer. (a) In the circuit, the order of the qubits in the 1st copy is flipped, so that $\mathcal{A}$ becomes closer to the ancilla. (b) One example of chosen qubit positions, with the ancilla being in between $\mathcal{A}$ and $\mathcal{A}'$.

[2] A hardware-native MaxCut problem is a MaxCut instance specifically designed or mapped to align with a quantum device's native qubit connectivity and gate set, minimizing overhead and enabling more efficient quantum execution.

6.4.2 Reducing circuit depth using SWAP-strategies

Superconducting qubit devices have limited connectivity and cross-talk, usually resulting in a planar coupling map where two-qubit gates can only be applied between neighboring qubits. To overcome this limitation, additional SWAP gates are inserted for qubit routing, that is, to bring distant qubits next to each other so they can effectively interact. If not transpiled efficiently, the circuit depth and gate count can increase significantly; however, this can be mitigated by using optimized SWAP strategies [290, 301]. The basic idea of this method is shown in Fig. 6.10. Fortunately, as we are already considering hardware-native problems, we do not need any extra SWAPs for qubit routing; however, we use a strategy to reorder the gates and reduce the circuit depth, as shown in Fig. 6.11.

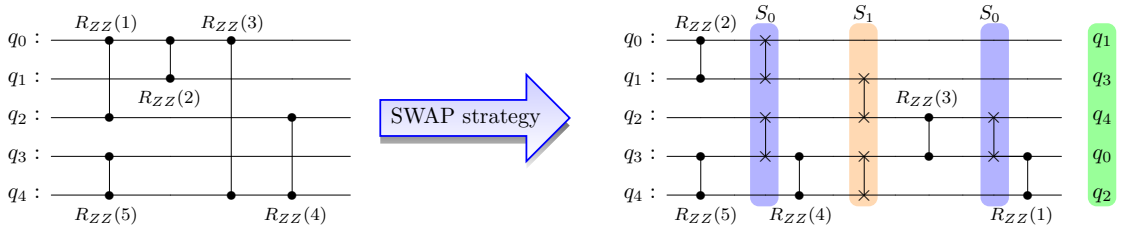

Figure 6.10. A five-qubit $\exp(-i\gamma H_C)$ circuit (left) is transpiled to a linear coupling map using the swap sets $\mathcal{S} = \{S_0, S_1\}$, where $S_0 = \{\text{SWAP}_{0,1}, \text{SWAP}_{2,3}\}$ and $S_1 = \{\text{SWAP}_{1,2}, \text{SWAP}_{3,4}\}$ alternate. In the final transpiled circuit (right), a redundant $\text{SWAP}_{0,1}$ from the last layer is removed. The final qubit mapping is shown in green.(Taken from Ref. [301])

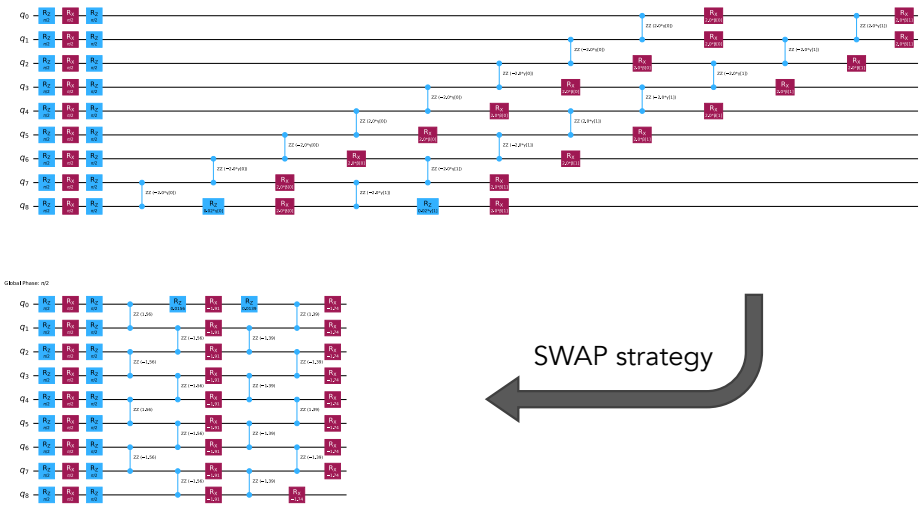

Figure 6.11. A 9-qubit QAOA with depth 2, if transpiled without SWAP strategies has a longer sparse circuit compared to using SWAP strategies, which provides a shorter dense circuit, advantageous for experimental run.

For more such tools for running quantum optimization algorithms on superconducting qubits using Qiskit, please refer to the *q-optimization-best-practices* guide in the Qiskit community [480].

6.4.3 Optimization strategies for QAOA

We optimize the QAOA parameters using *qaoa-training-pipelines* [265]. The idea is to grid-search over the full parameter space of (β_1, γ_1) for depth-one QAOA, and interpolate the parameter to higher depth as an initial guess. Then, we optimize the parameters using COBYLA [481]. For larger system sizes beyond the exact diagonalization capability, we use Matrix Product State (MPS) [74] with low bond-dimension to evaluate the expectation value of energy.

Algorithm 1 QAOA Training Loop (Pseudocode)

Input: Cost operator: `sp_op`, max depth: $p_{\max}$

Initialize `logs` ← [ ], `opt_params` ← [ ], `old_energy` ← `None`

for $p = 1$ to $p_{\max}$ **do**
    Create `run_log` with `p` and `cost_operator`

    if $p = 1$ **then**
        Initialize `evaluator` ← EfficientDepthOneEvaluator()
        `scan_trainer` ← DepthOneScanTrainer(evaluator)
        `scan_result` ← `scan_trainer.train(sp_op, num_points=100)`
        `opt_params` ← `scan_result[optimized_params]`
        Store `scan_result` in `run_log`
        `scipy_trainer` ← ScipyTrainer(evaluator, method=COBYLA)
        `result` ← `scipy_trainer.train(sp_op, opt_params)`
    else
        `evaluator` ← MPSEvaluator(bond_dim, use_vidal_form, threshold)
        `scipy_trainer` ← ScipyTrainer(evaluator, method=COBYLA)
        `recursion_trainer` ← RecursionTrainer(scipy_trainer, interpolate)
        `result` ← `recursion_trainer.train(sp_op, opt_params, reps=p)`

    end if

    `opt_params` ← `result[optimized_params]`
    `energy` ← `result[energy]`
    Store `opt_params`, `energy`, and `result` in `run_log`

    Compute `approx_ratio` using `solve_max_cut(sp_op, energy)`
    Store `approx_ratio` in `run_log`

    Append `run_log` to `logs`
    `old_energy` ← `energy`

end for

Save `logs` to disk as `qaoa_training_logs_{num_qubits}_p_{p_max}.pkl`

6.5 Entanglement from IBM device

6.5.1 Results for 9 qubits QAOA on a line

For all the experimental data, we obtain three sets of data, each with 10000 shots, to obtain the mean and error bar on the result. Due to the long C-SWAP measurements, it introduces error, as we have observed in Fig. 6.3. To tackle this issue, we first measure the initial state $|+\rangle^N$ ($p = 0$ in figures), which is a product state, and renormalize the probability counts (the probability of the ancilla being $|0\rangle$) for all p with respect to the $p = 0$ counts. For example,

$$P_{\text{raw}} = [P_0, P_1, \ldots, P_d] \to P_{\text{renorm}} = [1, \frac{P_1}{P_0}, \ldots, \frac{P_d}{P_0}]. \tag{6.23}$$

The motivation behind this renormalization is to ensure that the initial product states are unentangled, as expected at $P = 1$, and so any deviation can be attributed to the C-SWAP measurement circuit. More fundamentally, the renormalized probability can be interpreted as a conditional probability to the condition that the circuit produces the correct product state with no entanglement for $p = 0$ (denoted as P_0).

For a fixed partition and fixed depth

We begin by analyzing smaller systems, such as 9-qubit chains, using a bipartition of the form $[1] : [2, 3, 4, 5, 6, 7, 8, 9]$, see Fig. 6.12(a). As shown in Fig. 6.12(b), the entanglement grows steadily with QAOA-layer up to $p = 10$. We compute the quantity $G_{\mathcal{A}=[1]}$ numerically (denoted as exact) and compare it with experimental data from the *ibm kingston* quantum device, as well as with noisy simulations based on its hardware noise model. Up to $p = 8$, the experimental results closely follow the exact value, indicating that the device generates entanglement as expected. Beyond that point, deviations appear likely due to limitations in the device's coherence time. Additionally, we observe that the numerically obtained GGM, G_2, optimized over all bipartitions, remains close in value to $G_{\mathcal{A}=[1]}$ in our results, suggesting that the choice of bipartition does not significantly affect the outcome in this case. The fact that the difference only emerges toward the end of the circuit suggests that using a fixed bipartition, such as $[1] : [\text{rest}]$, already provides sufficient information to benchmark the quantumness of the hardware.

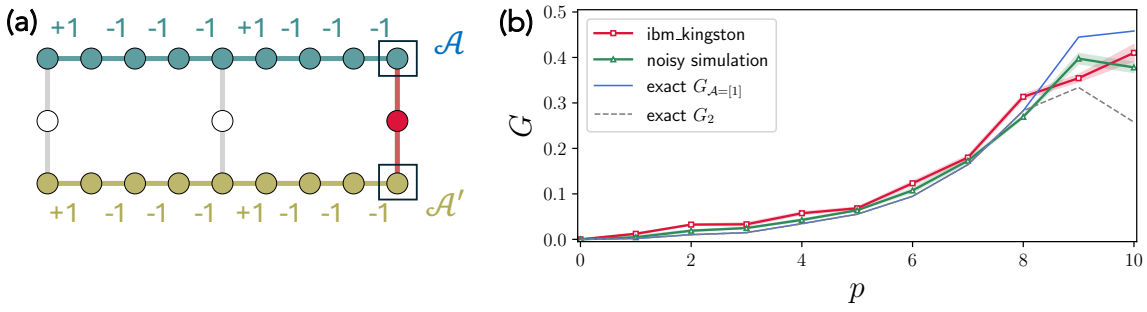

Figure 6.12. GGM on 9 qubits QAOA: (a) The chosen qubits are in filled circles, qaoa copy-1 in teal ($\mathcal{A}$) and qaoa copy-2 in olive color ($\mathcal{A}'$), where only one qubit is in the partition. (b) The experimental data and noisy simulation follow the exact value up to the 8th layer, after which entanglement starts decreasing, as expected from the finite coherence time of noisy hardware.

Dependence on depth

For QAOA, increasing depths typically improves the solution quality [81], captured by the approximation ratio[3] . To understand whether the entanglement also changes depending on the different depths considered, we also measured entanglement at these depths. In Fig. 6.13(a), we can see that with more allowed depth, the final G can increase to higher entanglement, although the slope of entanglement growth in layers is slower for larger depth. This behavior of the slope can be understood by examining how $\{\gamma_p\}$s change with different depths, as it controls the strength of the cost function, i.e., the entangling part of the evolution. We can see in Fig. 6.13(b) that the behavior of γ is similar to the growth of entanglement. However, the entanglement does not follow the noiseless value up to arbitrary layers, and it deviates to a lower entanglement close to larger layers, as expected, see inset of Fig. 6.13(a).

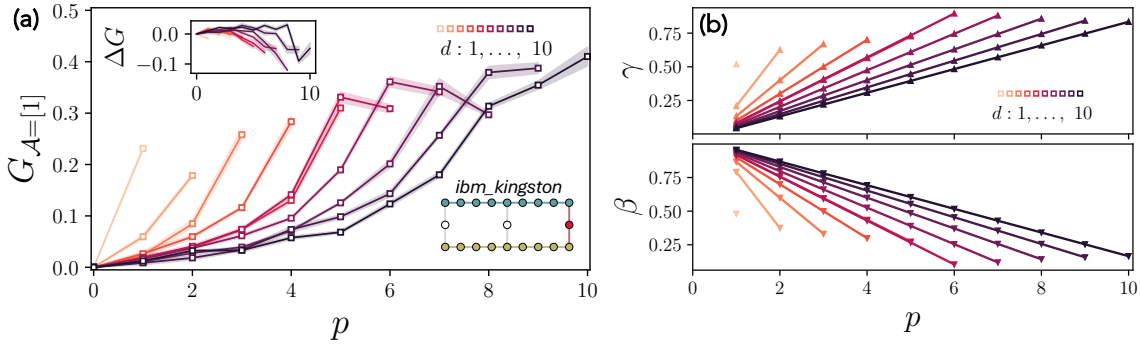

Figure 6.13. Entanglement for different depths. (a) With increasing depth d, the final entanglement reaches higher values, although with slower growth slopes, similar to the optimal γ_p parameters of QAOA, shown in (b). The measured entanglement deviates from the ideal noiseless one at larger depth, as shown in the inset of (a), where $\Delta G = G[\text{experiment}] - G[\text{ideal}]$. The numerically obtained approximation ratios for different depths are: 0.729, 0.784, 0.836, 0.867, 0.883, 0.898, 0.908, 0.918, 0.928, 0.934, respectively.

Dependence on partitions

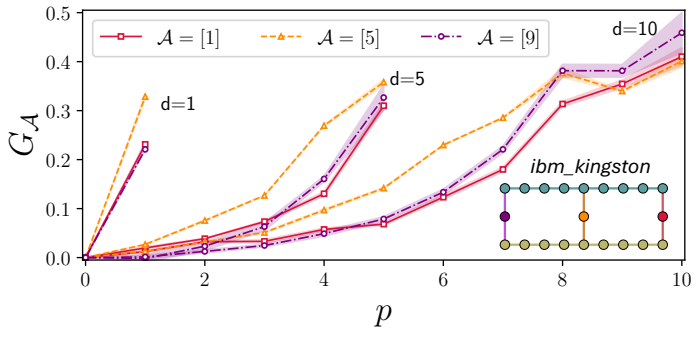

Figure 6.14. Entanglement from $\mathcal{A} = [1]$ is similar or lower than other chosen partitions for all the layers for depth $d = 1, 5, 10$.

[3]The approximation ratio is defined as

$$\text{Approximation Ratio} = \frac{C_{\text{QAOA}} - C_{\min}}{C_{\max} - C_{\min}},$$

where $C_{\text{QAOA}} = E + \frac{1}{2}\sum_{(i,j)} w_{ij}$, with E representing the QAOA energy and w_{ij} the edge weights. This ratio measures how close the QAOA solution is to the optimal maximum cut.

We motivated earlier that instead of calculating $G_{\mathcal{A}}$ for all partitions, choosing one is probably enough. In experiments, we utilize the ancilla between the two copies (see purple, orange, red in Fig. 6.14) without compromising the quality of the result due to their close distance. Though the results for $\mathcal{A} = [1], [5], [9]$ qualitatively follow similar patterns, there are some quantitative differences, with $\mathcal{A} = [1]$ exhibiting the lowest or comparable $G_{\mathcal{A}}$ compared to the other partitions, for all depths considered.

6.5.2 Results for 12 and 30 qubit QAOA

As the method works well, we extended it to 12 and 30-qubit QAOA. For the 12-qubit case, even the small depth can reach comparatively stronger entanglement, and when we compare with exact values, the deviation is higher than before at larger depths. We speculate if it can be related to the closed structure (heavy-hex) of the subgraph [Fig. 6.15(a)].

On the other hand, for 30 qubits (3 heavy-hex), the entanglement for smaller depth almost overlaps with the entanglement for the larger depth, i.e., they are of similar slopes [Fig. 6.15(b)]. Note that calculating entanglement in a 30-qubit system is already beyond the scope of a laptop simulation.

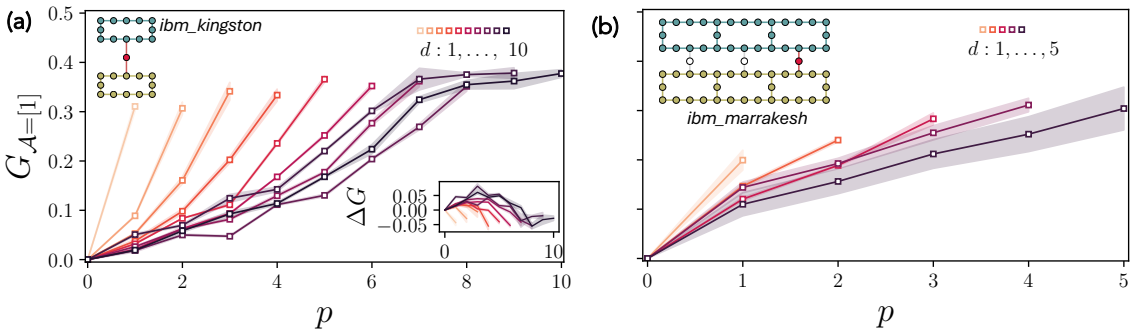

Figure 6.15. (a) For 12 qubits QAOA, entanglement grows with layer. A smaller depth has a faster slope of growth. Final G is similar for all depths. The approximation ratios corresponding to depths $d = 1, 2, 3, 4, 5, 6, 7, 8, 9, 10$ are $0.747, 0.824, 0.879, 0.912, 0.926, 0.927, 0.931, 0.939, 0.958, 0.970$, respectively. (b) For 30-qubit QAOA, entanglement growth in smaller depth overlaps with the entanglement growth in larger depth. The approximation ratios corresponding to depths $d = 1, 2, 3, 4, 5$ are $0.752, 0.832, 0.876, 0.907, 0.925$, respectively.

6.5.3 Results for 76 qubit QAOA

For the 156-qubit IBM Heron device, we push the limit of measuring the entanglement of a 76-qubit system, which can be nicely fit with its second copy on the chip [Fig. 6.16(a)]. In this case, entanglement grows rapidly during the first layer across all depths d, followed by a gradual increase up to the final layer [Fig. 6.16(b)]. The similarity in entanglement across different depths resembles the 30-qubit case, though it is even more pronounced here.

6.6 Summary and outlook

In this chapter, we addressed a fundamental question in the study of hybrid quantum-classical algorithms: to what extent does the Quantum Approximate Optimization

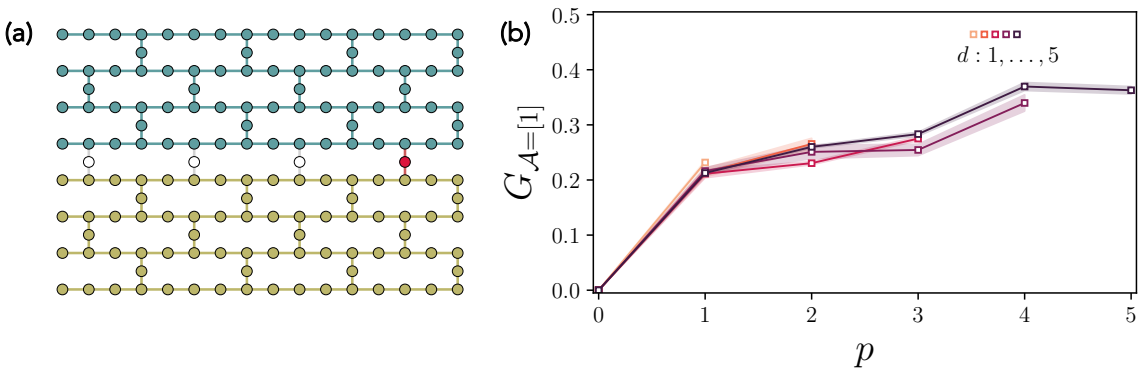

Figure 6.16. Measuring entanglement in 76-qubit QAOA. (a) Chosen coupling map for QAOA-1, ancilla, and QAOA-2 fits to the full device. (b) Entanglement for each depth almost overlaps with the others as it grows up to the final depths. The approximation ratios here are $0.752, 0.836, 0.886, 0.924, 0.947$ for $d = 1, 2, 3, 4, 5$, respectively.

Algorithm (QAOA) exploit genuinely quantum effects from the quantum processing unit (QPU)? Using a SWAP-circuit-based method, we estimated a geometric measure of entanglement (GGM)-like measure, all within the constraints of current noisy intermediate-scale quantum (NISQ) devices.

We built our approach around a SWAP-test-based method, carefully designed to extract a GGM-like entanglement measure that could be implemented within the tight constraints of NISQ devices. We first tested this method on random quantum circuits, validating our results against exact numerical simulations. We then shifted focus to QAOA, applying the same technique to circuits with up to 76 qubit QAOA (and the whole circuit consists of 153 qubits) on IBM's Heron device. Across different depths and system sizes, the entanglement we measured closely mirrored what noiseless simulations predicted, for the systems where we could simulate until hardware noise began to dominate at larger depths. This provided direct experimental evidence that QAOA is not simply following classical heuristics, but generating genuine quantum entanglement.

Along the way, we discovered practical insights. A fixed bipartition was often enough to capture the essential structure of entanglement, reducing the overhead of optimization over multiple partitions. We also saw how entanglement growth correlated with the evolution of QAOA parameters and how hardware-aware strategies like optimized qubit mapping, careful transpilation of C-SWAP gates, and calibration of measurement outcomes were vital for success. Techniques like circuit cutting and zero-noise extrapolation offered limited benefit due to dominant readout noise. But perhaps the most compelling outcome was not just that we could measure entanglement, but that we could do so at scales where classical simulation becomes intractable. This opens the door to using entanglement not only for evidence for quantumness but also as a benchmarking tool to guide the design and improvement of future quantum algorithms and hardware.

Looking forward, the methods we have developed can be extended to other variational quantum algorithms [231] or quantum machine learning models [482], helping us understand how and when quantum correlations play a role in performance. The entanglement may become a cornerstone in certifying quantum advantage as a physically meaningful and experimentally accessible way to verify that a quantum processor is doing something no classical computer can.

Chapter 7

Role of nonstabilizerness in quantum optimization

Can quantum optimization outperform stabilizer computations?

7.1 Introduction

Combinatorial optimization problems are ubiquitous, spanning from science to industry [232,483–487]. Hence, achieving any improvement over state-of-the-art classical algorithms through quantum computing could yield a substantial impact, making quantum optimization a leading candidate for practical uses of quantum technologies [248]. In particular, the quantum approximate optimization algorithm (QAOA) [81] offers a promising strategy in the era of noisy quantum devices [87, 301, 488–490]. Despite many successful applications [237, 491–499], it remains unclear to what extent such algorithms truly leverage non-classical quantum resources [47]. This is essential to understand as it defines whether quantum optimization can outperform classical computations or not. In this context, entanglement—a defining feature and a key resource in quantum information processing [89, 500, 501]—has been extensively studied, both in the form of bipartite [414, 417, 435, 437–439] and multipartite entanglement [325, 361, 502, 503]. However, entanglement alone does not ensure a quantum advantage. Stabilizer states can exhibit large entanglement yet remain efficiently simulable classically via Clifford circuits, as guaranteed by the Gottesman–Knill theorem [148–150]. Nonstabilizerness [504]—the degree to which a nonstabilizer state, also called a magic state, deviates from the set of stabilizer states—is thus a crucial property to unlock a potential quantum advantage [160, 504–508]. Based on the discrete Wigner function [509], many measures for this quantum resource have been introduced [181, 510–515]; among which Mana [85, 181] and the Stabilizer Rényi Entropy (SRE) [169, 171, 516] are notable for being efficiently computable and experimentally accessible. In recent years, the study of nonstabilizerness has seen many applications from many-body physics [517–523] over random circuits [172, 524, 525] to conformal field theory [526–528]. Yet, its role in variational quantum optimization remains largely unexplored.

In this chapter, we address this gap by analyzing nonstabilizerness in QAOA applied to combinatorial problems, focusing on both SRE and Mana. We study the performance of QAOA on the paradigmatic Sherrington–Kirkpatrick (SK) model [529], which combines computational hardness with statistical complexity. Our simulations reveal the presence of a "magic barrier"—a transient build-up of nonstabilizerness that occurs during the QAOA run, akin to previously observed entanglement barriers [414, 418, 503]. We find that while QAOA begins and ends with low-magic (sta-

bilizer) states, it must pass through a regime of increased magic in order to achieve high fidelity with the target solution. This behavior appears in both qubit and qutrit versions of the algorithm. We find that magic curves corresponding to different depths collapse under a simple rescaling, and we identify a similar magic barrier in quantum annealing. Furthermore, we analyze how the success probability of QAOA correlates with the final nonstabilizerness, uncovering characteristic trends and structure in the fidelity-magic plane. Using analytical calculations on *ansatz* states, made of few-component superpositions, we explain the observed features and clarify under what conditions low-magic solutions may or may not correspond to high-fidelity outcomes.

Through this chapter, we illuminate the role and significance of nonstabilizerness in quantum optimization, providing deeper insight into its influence on algorithmic performance and complementing existing studies on entanglement and coherence [418, 439, 503]. The results also have practical relevance, as measurements of magic can provide a figure of merit for estimating the performance of variational or optimization algorithms performed on concrete quantum hardware, such as superconducting qubits [530], trapped ions [173], and Rydberg atoms [531].

7.2 Quantifying nonstabilizerness for qudits

Here we recall two measures of nonstabilizerness from Sec. 2.7.4: the stabilizer Rényi entropy (SRE) [169, 171] and Mana [85, 181].

7.2.1 Stabilizer Rényi Entropy

The SRE [169] characterizes how a pure state $|\psi\rangle$ of N qudits spreads over the basis of Pauli strings $\mathcal{P}_N$:

$$M_n(|\psi\rangle) = \frac{1}{1-n} \log_2 \left[\sum_{P \in \mathcal{P}_N} \frac{|\langle\psi|P|\psi\rangle|^{2n}}{D^N} \right]. \tag{7.1}$$

M_n is non-negative and equals zero if and only if $|\psi\rangle$ is a stabilizer state [171, 532]. An important feature of Eq. (7.1) is that it is experimentally computable [173]. The SRE defined in Eq. (7.1) satisfies all properties (i-iii) necessary to be a valid magic measure [169] For $d > 2$, the Pauli operators are no longer Hermitian, and thus their expectation values can be complex. For this reason, the absolute values are taken in Eq. (7.1). Throughout this chapter, we use M_2 as our measure.

7.2.2 Mana

Defining Mana requires knowledge of two other concepts: Heisenberg–Weyl operators, and discrete Wigner functions, which we have discussed in Sec. 2.7.3. Then, the negativity of the discrete Wigner function provides another quantifier of nonstabilizerness [160, 533]. Specifically, the log-negativity of the Wigner function W_ρ associated with a quantum state ρ defines a quantity known as Mana [85]:

$$\text{Mana} = \log \sum_{\vec{V}} |W_\rho(\vec{V})| \,. \tag{7.2}$$

For pure states $\rho = |\psi\rangle\langle\psi|$, as considered here, the set of states with non-negative Wigner representation coincides precisely with the set of pure stabilizer states [160], in which case the Mana vanishes.

7.3 QAOA on SK model

As illustrated in Fig. 7.2(a), QAOA prepares a trial state $|\psi(\boldsymbol{\beta}, \boldsymbol{\gamma})\rangle$ by applying d layers of alternating unitaries, $\exp\left(-i\beta_p \hat{H}_M\right) \exp\left(-i\gamma_p \hat{H}_C\right)$, starting from the ground state of the mixer Hamiltonian $\hat{H}_M$ [534], see Sec. 3.3.4 for more details. Originally developed for qubits, the Quantum Approximate Optimization Algorithm (QAOA) can be generalized to qudit systems with any local dimension D [497], thereby expanding its range of potential applications [497, 499, 535, 536]. As the initial state is non-magical [1] and the solution state of a classical problem with a unique optimum is also non-magical, QAOA offers a natural setting to test the buildup and role of magic during the quantum optimization procedure.

The model of our interest is the Sherrington–Kirkpatrick (SK) model, a variant of the Ising model with all-to-all interactions randomly drawn from independent Gaussian distributions. Initially introduced as a solvable mean-field model to describe the spin-glass phase [529, 537], it serves as a prototype for real-world optimization problems, which often involve a diverse set of random variables [538, 539]. We use the SK model generalized to qudits (specifically, we study qubits and qutrits),

$$\hat{H}_{\mathrm{SK}} = \sum_{i \neq j} J_{ij} (Z_i Z_j^\dagger + Z_i^\dagger Z_j) + \hat{H}_{\mathrm{bias}} \,, \tag{7.3}$$

where the coefficients J_{ij} are chosen randomly from a normal distribution with unit variance, and Z_i is the generalized phase operator. The Hermitian conjugate term is necessary to ensure the Hermiticity of the Hamiltonian in the qutrit case. Since we aim to understand the magic generated solely through QAOA, it is crucial to remove any degeneracy, as it may contribute additional magic arising from a superposition of equally valid solution states rather than the algorithm itself. For that purpose, we add bias magnetic field terms $\hat{H}_{\mathrm{bias}}$.

7.3.1 Degeneracy breaking in SK model

The Hamiltonian term without bias $\sum_{i \neq j} J_{ij}(Z_i Z_j^\dagger + Z_i^\dagger Z_j)$ has symmetry under reflection, $Z_i \leftrightarrow -Z_i$, thus creating two degenerate states. The reflection degeneracy can be lifted by adding a longitudinal field, $\hat{H}_{\mathrm{bias},2} = \sum_i h_i (Z_i + Z_i^\dagger)$, which is reduced to $\sum_i 2h_i Z_i$ for the qubit case.

However, for qutrits, this term is furthermore symmetric under $Z_i \to cZ_i$, where $c \in \{\pm 1, \pm\omega, \pm\omega^2\}$, which introduces 4 additional symmetries. For example, $Z_i Z_j^\dagger \xrightarrow{+\omega} (\omega Z_i)(\omega Z_j)^\dagger = (\omega Z_i)(\omega^2 Z_j^\dagger) = Z_i Z_j^\dagger$. Thus, the qutrit Hamiltonian contains 6 degenerate eigenstates, equivalent to permutation among the local basis of qutrits,

[1] The $|+\rangle = \frac{1}{\sqrt{D}} \sum_{i=0}^{D-1} |i\rangle$ qudit state is a stabilizer state because it is a $(+1)$ eigenstate of a d-element subgroup of the Pauli group; for example, it is $\{I, X\}$ for $d = 2$. Using the additive property, $\mathcal{M}(|+\rangle^{\otimes N}) = N\mathcal{M}(|+\rangle) = 0$.

which contains $3! = 6$ degenerate states. The longitudinal field $\hat{H}_{\text{bias},2}$ removes the degeneracy between $|0\rangle$ and $\{|1\rangle, |2\rangle\}$ but retains the degeneracy between $|1\rangle$ and $|2\rangle$, as $(Z + Z^\dagger) = \text{diag}(2, -1, -1)$. To lift this degeneracy, we add another term $\sum_i ih'_i(Z_i - Z_i^\dagger)$, as $i(Z - Z^\dagger) = \text{diag}(0, -\sqrt{3}, +\sqrt{3})$. In our numerics, h_i and h'_i are chosen randomly from a normal distribution with variance 0.3.

7.3.2 Optimization procedure

We execute all QAOA simulations using a custom implementation. To find the optimal parameters $\{\boldsymbol{\beta}, \boldsymbol{\gamma}\}$, we employ the Constrained Optimization BY Linear Approximation (COBYLA) algorithm [481], a gradient-free method that solves the problem by linearly approximating the cost function. The parameters are initialized using the Trotterized Quantum Annealing (TQA) strategy [256]. The classical optimizer stops when the trust-region radius decreases below the specified tolerance of 10^{-4}. For each random realization of the SK model, we simulate a QAOA protocol using exact numerics, where we select the best outcome from 20 independent QAOA runs initialized using Trotterized quantum annealing initialization [256], and average the results over 50 such realizations. The SRE is computed exactly, with computational cost scaling as D^{2N} due to the exponential growth in the number of Pauli strings, where D is the qudit dimension and N is the number of qudits.

7.4 Magic barrier

When targeting the non-degenerate ground state of the SK model, QAOA starts—and ideally ends—in stabilizer states with zero magic. The relevant performance metrics—such as the relative energy $(E_{\text{QAOA}}(p) - E_{\text{exact}})/E_{\text{exact}}$ (in Fig. 7.1 (b1,b2)) reflects that the QAOA energy reaches values close to the ground state, and the fidelity with the ground state $\mathcal{F}(p) = |\langle\psi_{\text{exact}}|\psi_{\text{QAOA}}(p)\rangle|^2$ (in Fig. 7.1 (a1,a2)) improve monotonically with the number of QAOA layers p, though being far from equal to one.

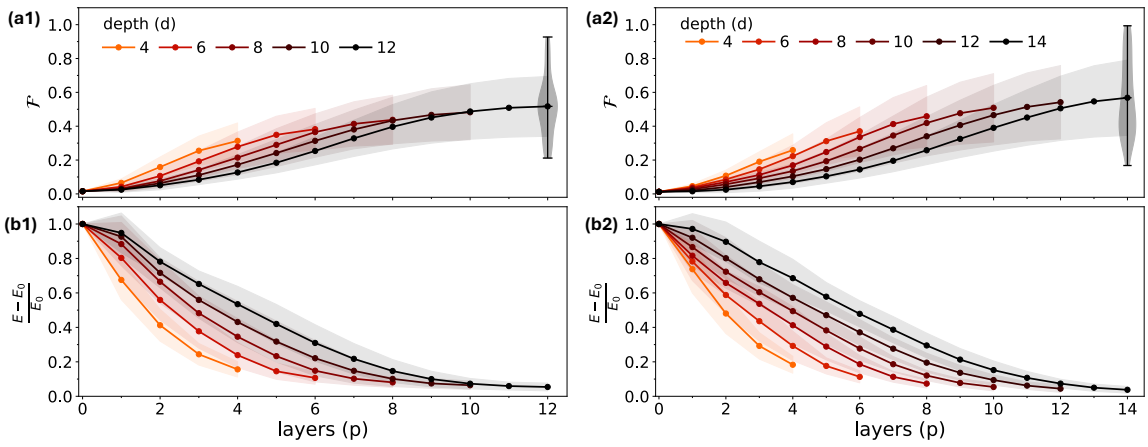

Figure 7.1. (a1) Mean value of the fidelity over 50 different realizations, with relative standard deviation, for each layer at different depths of the 6-qubit system. The violin plot for the curve at depth 12, using the full 12-layer wave function, highlights the high fidelity achieved by some realizations. (b1) Mean value of the relative energy under the same conditions. (a2) and (b2) show the corresponding results for a 4-qutrit system.

In contrast, the evolution of magic, quantified by SRE and Mana, follows a non-monotonic behavior: it initially rises rapidly as the first QAOA layers are applied, reaches a maximum, and then decreases as the algorithm approaches the final state. We define this structure as the *magic barrier*, marking the necessity of traversing highly nonstabilizer states during the QAOA algorithm. Therefore, the quantum computational resources required during the intermediate steps of QAOA significantly exceed what would be expected from monotonic growth. This additional "cost" in non-stabilizerness emerges inherently from the QAOA ansatz structure; thus, it becomes crucial to account for this elevated resource demand in the design and benchmarking of fault-tolerant quantum devices.

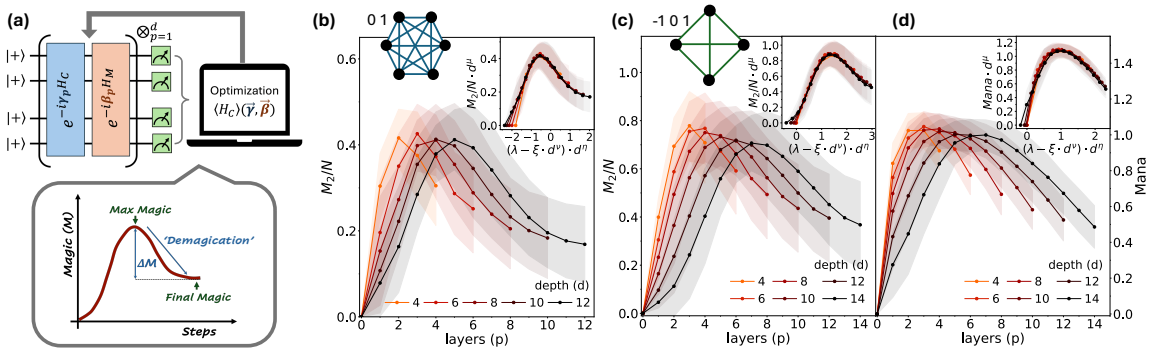

Figure 7.2. Magic barrier in QAOA. (a) Quantum Approximate Optimization Algorithm (QAOA) scheme and a pictorial representation of the magic barrier: initially, magic rises up to a maximal value, after which it decreases, an effect we call "demagication." (b) SRE density as a function of the layer number during a QAOA protocol, for a system of 6 qubits and different depths (i.e., total number of layers). Inset: Using a simple scaling function, the magic barrier collapses onto a universal curve. (c,d) Same plot of panel b for a system of 4 qutrits, showing SRE density (c) and Mana (d) as a function of the layer number. The universal collapses in the insets in (b-d) use the scaling function $\mathcal{M} = d^{-\mu} f[(\lambda - \xi \cdot d^{\nu}) \cdot d^{\eta}]$.

A pictorial representation of the magic barrier is shown in Fig. 7.2(a). Remarkably, this phenomenon is observed consistently across different systems and for both SRE and Mana. For instance, Fig. 7.2(b) depicts the evolution of the SRE density (M_2/N) for a 6-qubit system at varying QAOA depths. A distinct peak emerges at approximately half the total depth, indicating the point of maximal nonstabilizerness. A comparable scenario arises in the 4-qutrit system, for both SRE and mana [see Fig. 7.2(c,d)].

Notably, for a fixed system size, the maximum value of magic encountered remains approximately constant across different QAOA circuit depths, suggesting that the magic peak is independent of circuit depth. Moreover, even at its peak, the generated magic remains below that of a typical state in the corresponding Hilbert space, such as given by the Haar-random value– $M_2^{\text{Haar}} = -\log_2(\frac{4}{2^N+3})$ for qubit, and $-\log_2(\frac{3}{3^N+2})$ for qutrit systems [168, 524]. This suggests that for a device to successfully run a QAOA, it is sufficient if it can build up a limited amount of magic.

7.4.1 Scaling of nonstabilizerness

The states generated by QAOA strongly depend on the circuit depth, optimization parameters, and system size, and yet we observe a qualitatively uniform behavior of

the magic barrier in Fig. 7.2. In particular, for a fixed N, while the magic curve varies with the QAOA depth, certain patterns emerge consistently: (1) the barrier height remains nearly unchanged, and (2) as the depth increases, the curve appears to stretch horizontally. These observations motivate the search for a scaling collapse of the magic barrier, which could offer valuable insights into the underlying behavior.

We begin by seeking a simple scaling function $f[\cdot]$ for fixed N,

$$\frac{\mathcal{M}\left(|\psi_{\mathrm{QAOA_d}}(p)\rangle\right)}{N} = d^{-\mu} f\left[(\lambda - \xi \cdot d^{\nu}) \cdot d^{\eta}\right]; \mu, \xi, \nu, \eta \in \mathbb{R}; \quad \lambda = \frac{p}{d}. \tag{7.4}$$

where μ and η control the stretching along the y- and x-axes, respectively. The curves only collapse onto each other when centered around a depth (d)-dependent parameter, which we achieve through the introduction of ξ and ν. We use these parameters to rescale the data for different depths and observe whether the curves align. The collected scaling parameters for different *qubit* system sizes are reported in Table 7.1, which includes the values of μ, ξ, ν, and η obtained from numerical fits for $N = 4, 6, 8$ qubit systems. Similarly, Table 7.2 shows scaling parameters for *qutrits*. Indeed, shown in the insets of Fig. 7.2(b–d), the data for different depths, both for average SRE density and Mana, collapse onto a single curve.

N	μ	ξ	ν	η
4	−0.07	0.02	0.76	0.23
6	0.01	1.28	−0.34	0.60
8	−0.07	0.02	0.95	0.86

Table 7.1. Scaling parameters μ, ξ, ν, and η used for data collapse at fixed system size N (qubits), using Eq. (7.4). Values obtained from fitting QAOA magic curves for $N = 4, 6, 8$.

$N = 4$	μ	ξ	ν	η
SRE	−0.08	0.00	3.49	0.46
Mana	0.03	0.00	5.50	0.34

Table 7.2. Scaling parameters μ, ξ, ν, and η used for data collapse at $N = 4$ *qutrits* using Eq. (7.4). Values are shown for both SRE and mana.

For qubit systems, we find a scaling exponent μ close to zero, suggesting that the peak value of SRE remains independent of both the QAOA circuit depth and the number of qubits. Interestingly, for the qubit cases, we find that the scaling formulation can be simplified by replacing the combined term $\xi \cdot d^{\nu}$ with a constant critical point λ_c, leading to the alternative scaling form

$$\frac{\mathcal{M}\left(|\psi_{\mathrm{QAOA_d}}(p)\rangle\right)}{N} = d^{-\mu} \tilde{f}\left[(\lambda - \lambda_c) \cdot d^{\eta}\right]; \mu, \lambda_c, \eta \in \mathbb{R}; \quad \lambda = \frac{p}{d}. \tag{7.5}$$

This revised form uses the scaling variable $\lambda = p/d$ and centers the collapse around a critical point λ_c. In systems exhibiting universality–such as those undergoing phase transitions–the central parameter (around which the scaling occurs) becomes a constant, signaling a universal or critical point, similar to λ_c. The goal is then to determine whether such a λ_c can be found consistently across system sizes, as a signature of universal behavior. Table 7.3 reports the corresponding values of μ, λ_c, and η obtained from scaling collapses performed using Eq. (7.5) for $N = 4, 6, 8$ qubit systems. Remarkably, the extracted values of λ_c are rather consistent around 0.2 across system sizes, suggesting the existence of a constant point in the qubit case, even at small system sizes. This behavior is in contrast to the qutrit case, where no such consistent value of λ_c is observed. The exponent η, which governs the width rescaling, lies

within a relatively narrow range for both the 6-qubit and 4-qutrit systems. Moreover, η increases with the number of qubits, suggesting a sharper magic barrier in larger systems.

N	μ	λ_c	η
4	−0.07	0.27	0.23
6	0.01	0.27	0.59
8	−0.10	0.29	0.92

Table 7.3. Fitted scaling parameters μ, λ_c, and η using the critical-point form in Eq. (7.5). Results shown for $N = 4, 6, 8$ qubits.

7.5 Final magic and fidelity

The ultimate determinant of the success of QAOA lies in the fidelity of the final state with the target solution. As the QAOA approaches the final layer, successful instances reach a high overlap with a classical state, implying—in the absence of degenerate solutions—one can associate high-fidelity QAOA instances with low magic. This behavior is indeed what we observe in randomly sampled instances for different system sizes and depths, shown in Fig. 7.3. The opposite, however, is not necessarily true: a QAOA sweep can end up in a stabilizer state, including any computational basis state distinct from the solution state, and thus can have small magic while reaching only low fidelity.

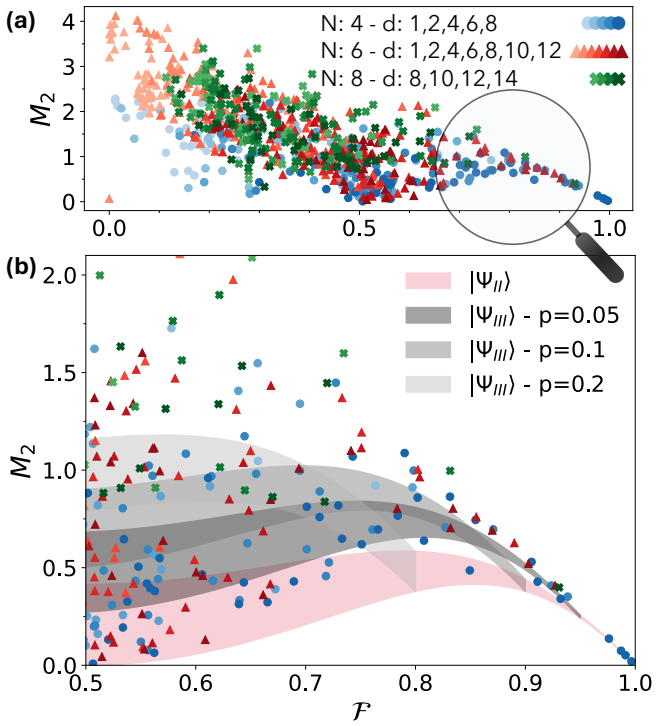

Figure 7.3. Relation between final magic and fidelity (qubits). (a) Magic of the final state as a function of final fidelity $\mathcal{F}$ for randomly sampled instances with varying numbers of qubits and QAOA depths. (b) Zoom-in on the region $\mathcal{F} \geq 0.5$. The red shaded area marks the upper limit of SRE achievable by superpositions of two computational basis states. The grey regions correspond to the SRE of wavefunctions spanning three basis states with varying amplitudes. While higher regions could be reachable with more complex *ansatz* states, the empty area below is forbidden.

Focusing on instances with $\mathcal{F} \geq 0.5$ [Fig. 7.3(b)], one observes a void region at the lower axis. The pattern can be explained as follows. At the end of a rather successful QAOA, we expect the state to consist of the final solution $|\phi_0\rangle$ with potentially a small contamination, typically from the first excited state, which is another computational basis states $|\phi_1\rangle$ or/and $|\phi_2\rangle$. In those cases, we can obtain an analytical expression relating magic and final-fidelity as shown in the following sections.

7.5.1 For superposition of two states (qubit)

Here, we consider an *ansatz* state

$$|\psi_{\mathrm{II}}\rangle = \sqrt{\mathcal{F}}\,|\phi_0\rangle + e^{i\theta}\sqrt{1-\mathcal{F}}\,|\phi_1\rangle\,, \quad \theta \in [0, 2\pi]\,, \tag{7.6}$$

where the probability amplitude to reach the desired solution is $\sqrt{\mathcal{F}}$, and where we allowed for a relative phase $e^{i\theta}$. Using the additivity of M_2 and permutational invariance, one can show that for any number of qubits:

$$M_2\left(|\psi_{\mathrm{II}}\rangle\right) = -\log_2\left[1 - 4\mathcal{F}(1-\mathcal{F}) + 2\mathcal{F}^2(1-\mathcal{F})^2(7+\cos 4\theta)\right]. \tag{7.7}$$

The result is symmetric around $\mathcal{F} = 0.5$. The minima (maxima) at $\theta = 0$ ($\theta = \pi/4$) describe a bounded region in the fidelity–magic plane, within which all instances that reach the above *ansatz* are confined, independent of peculiarities of the protocol such as qubit number or circuit depth.

Proof. Consider a system composed of n qubits. Since the states $|\phi_0\rangle$ and $|\phi_1\rangle$ are in the computational basis, we can define Hamming weight distance, let's say h. Assuming $h < n$, we can write the state $|\psi_{\mathrm{II}}\rangle$ as $|\psi'_{\mathrm{II}}\rangle_h \otimes |d\rangle_{n-h}$. Here, $|d\rangle = |0\rangle^{\otimes(n-h)}$ or $|1\rangle^{\otimes(n-h)}$. By the additive property of SRE, $M_n(|\psi_{\mathrm{II}}\rangle) = M_n(|\psi'_{\mathrm{II}}\rangle_h) + M_n(|d\rangle_{n-h})$. $M_n(|d\rangle_{n-h}) = 0$, so only $M_n(|\psi'_{\mathrm{II}}\rangle_h)$ contributes to SRE. We can write $|\psi'_{\mathrm{II}}\rangle_h$ as $\sqrt{\mathcal{F}}\,|a\rangle_n + e^{i\theta}\sqrt{1-\mathcal{F}}\,|\bar{a}\rangle_n$. This is SRE-equivalent to $\sqrt{\mathcal{F}}\,|0\rangle^{\otimes n} + e^{i\theta}\sqrt{1-\mathcal{F}}\,|1\rangle^{\otimes n}$ via bit-flip operations $X_{\vec{j}}$ at the appropriate positions $(\vec{j})$. This is equivalent to using $P'_i = X_{\vec{j}} P_i X_{\vec{j}}$ on the earlier states. As the Pauli group is invariant under such an operation, we can compute the magic for the latter state without any loss of generality. The formula is n-independent because what counts is the number of states in superposition, not the dimension of the system or which two basis states constitute the state. We can write all four terms appearing in the expectation values as,

$$\begin{aligned} &\mathcal{F}\cdot\langle 0|^{\otimes n} P_i\,|0\rangle^{\otimes n}\,, \quad (1-\mathcal{F})\cdot\langle 1|^{\otimes n} P_i\,|1\rangle^{\otimes n}\,, \\ &\sqrt{\mathcal{F}(1-\mathcal{F})}e^{i\theta}\cdot\langle 0|^{\otimes n} P_i\,|1\rangle^{\otimes n}\,, \quad \sqrt{\mathcal{F}(1-\mathcal{F})}e^{-i\theta}\cdot\langle 1|^{\otimes n} P_i\,|0\rangle^{\otimes n}\,, \quad \forall i\,. \end{aligned} \tag{7.8}$$

The first two terms are non-zero only when the involved string P_i is built only from combinations of $\{I, Z\}$ Pauli operators. In that case, the last two terms are zero. When P_i contains a number k of Z operators, there are $\binom{n}{k}$ terms contributing to the sum. These will cumulatively contribute to

$$\sum_{k=0}^{n}\binom{n}{k}\left|\mathcal{F} + (-1)^k(1-\mathcal{F})\right|^4 = 2^{n-1}[1 + (2\mathcal{F}-1)^4]\,. \tag{7.9}$$

Similarly, the last two terms are non-zero when the $P_i = Y^{\otimes k}X^{\otimes n-k}$. Thus,

$$\sum_{k=0}^{n}\binom{n}{k}\mathcal{F}^2(1-\mathcal{F})^2|e^{i\theta}(-i)^k + e^{-i\theta}(+i)^k|^4 = 2^{n-1}\mathcal{F}^2(1-\mathcal{F})^2 2^4[\cos^4\theta + \sin^4\theta]\,. \tag{7.10}$$

By summing these two contributions and performing some simple algebra, one obtains the final equation of Eq. (7.7).

7.5.2 For superposition of three states (qubit)

Motivated by the n independence of the previous result, we further refine this *ansatz* by considering a superposition of three computational basis states,

$$|\psi_{\mathrm{III}}\rangle = \sqrt{\mathcal{F}}\,|\phi_0\rangle + e^{i\theta_1}\sqrt{p}\,|\phi_1\rangle + e^{i\theta_2}\sqrt{1-\mathcal{F}-p}\,|\phi_2\rangle\,, \quad p \in [0, 1-\mathcal{F}],\ \theta_{1/2} \in [0, 2\pi]\,, \tag{7.11}$$

for which we can again calculate M_2 analytically. For different system sizes, we find an expression consistent for different N with the following:

$$\begin{aligned} M_2 = -\log_2\Big[&1 + 14f^4 + 28f^3(p-1) + 2(p-1)p\,(2 + 7p(p-1)) \\ &+ 6f^2\,(3 + p(7p-6)) + 4f(p-1)\,(1 + p(7p-6)) \\ &+ 2f^2(f+p-1)^2\cos(4\phi) + 4p^2f^2\cos(2\phi)\cos(2\phi - 4\theta) \\ &+ 2p^2(p-1)(2f+p-1)\cos(4\phi - 4\theta)\Big]\,. \end{aligned} \tag{7.12}$$

Similar to the case of magic computed for a superposition of two computational basis states, the analytical expression derived here remains valid for states of arbitrary dimension. The generalization of the Eq. (7.7) and (7.12) to any dimension systems is shown in Fig. 7.4, where random benchmarks are used for this purpose.

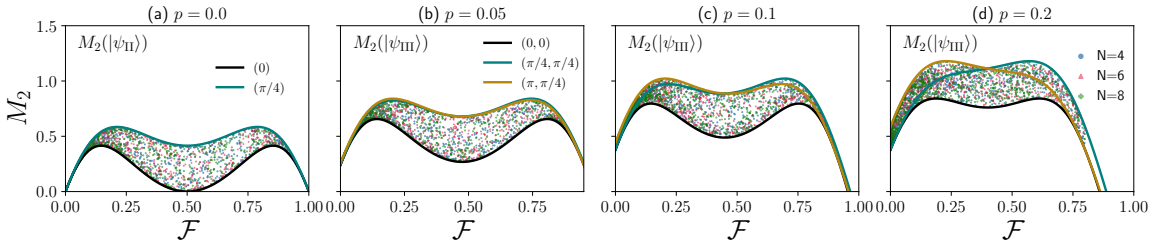

Figure 7.4. SRE vs. fidelity for a superposition of two (a) and three (b,c,d) states at different values of p. Continuous lines represent analytic bounds given by Eq. (7.7) and (7.12), respectively. Dots represent numerically computed SRE for random states of the form $|\psi_{\mathrm{II}}\rangle$ [Eq. (7.7) for (a)] and $|\psi_{\mathrm{III}}\rangle$[Eq. (7.12) for (b,c,d)]. The points are clearly enclosed within the bounds given by the continuous lines, certifying the validity of Eq. (7.7) and Eq. (7.12).

7.5.3 Relation to the QAOA fidelity

The shaded regions in Fig. 7.3(b) correspond to M_2 contained in the *ansatz* states $|\psi_{\mathrm{II,III}}\rangle$ for varying $\mathcal{F}, \theta, p$, as detailed in Eq. (7.7) and Eq. (7.12). Since *ansätze* with a further increased number of basis states will only lead to higher magic, these analytic considerations also explain why no instances are found numerically in the empty region at the bottom of the figure. Moreover, they suggest a reduced likelihood of obtaining a medium-to-high-fidelity state $\mathcal{F} \sim (0.6 - 0.9)$ with low magic, further indicating that QAOA has to go through a high-magic state to reach a good solution.

7.5.4 For superposition of qutrit states

Motivated by the qubit superposition, we also calculated how SRE behaves for the superposition of two qutrit states. The pauli group for qutrits is defined as $P =$

$\{X^r Z^j | r, j \in (0,1,2)\}$. So, for a qutrit state $|\psi\rangle = \sqrt{\mathcal{F}}\,|a\rangle + e^{i\theta}\sqrt{1-\mathcal{F}}\,|b\rangle$, we get

$$\langle\psi| P_i |\psi\rangle = \mathcal{F}\,\langle a| P_i |a\rangle + (1-\mathcal{F})\,\langle b| P_i |b\rangle \tag{7.13}$$

$$+ e^{i\theta}\sqrt{\mathcal{F}(1-\mathcal{F})}\,\langle a| P_i |b\rangle + e^{-i\theta}\sqrt{\mathcal{F}(1-\mathcal{F})}\,\langle b| P_i |a\rangle\ . \tag{7.14}$$

The first two terms will be different from zero when $a = 0$, while the second two terms will be different from zero when $a \neq 0$. Thus, we have

$$e^{-M_2} = \sum_{j=0,1,2} |\mathcal{F}\,\langle a| Z^j |a\rangle + (1-\mathcal{F})\,\langle b| Z^j |b\rangle\,|^4 \tag{7.15}$$

$$+ \sum_{r=1,2;j=0,1,2} |e^{i\theta}\sqrt{\mathcal{F}(1-\mathcal{F})}\,\langle a| X^r Z^j |b\rangle + e^{-i\theta}\sqrt{\mathcal{F}(1-\mathcal{F})}\,\langle b| X^r Z^j |a\rangle\,|^4$$

$$= 1 + |\omega^a \mathcal{F} + (1-\mathcal{F})\omega^b|^4 + |\omega^{2a}\mathcal{F} + (1-\mathcal{F})\omega^{2b}|^4 \tag{7.16}$$

$$+ \mathcal{F}^2(1-\mathcal{F})^2 \sum_{r=1,2;j=0,1,2} |e^{i\theta}\omega^{jb}\delta_{a,b\oplus r} + e^{-i\theta}\omega^{ja}\delta_{b,a\oplus r}|^4\,. \tag{7.17}$$

Notice that for a qutrit, $a = b \oplus r$ and $b = a \oplus r$ cannot be satisfied at the same time. This will remove any dependence on the relative phase θ between the two basis states ($\oplus$ indicated sum mod d). Considering $a = 0, b = 1$ we get

$$e^{-M_2} = 1 + |\mathcal{F} + (1-\mathcal{F})\omega|^4 + |\mathcal{F} + (1-\mathcal{F})\omega^2|^4 + 3\mathcal{F}^2(1-\mathcal{F})^2\,. \tag{7.18}$$

Figure 7.5 (a-b) presents the values of nonstabilizerness vs. fidelity of the optimized QAOA state for 4-qutrit systems. However, we do not find any similarity of our QAOA data with such an equation, suggesting that it may be due to the less successful instance of QAOA, or it is too naive to expect a superposition of two states in the qutrit basis without any knowledge of the cost function.

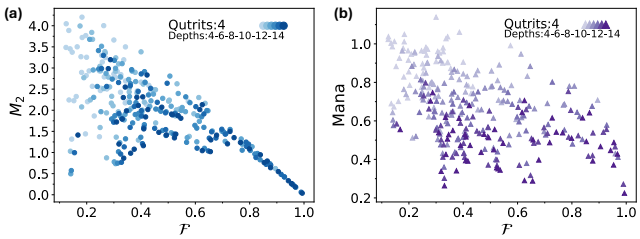

Figure 7.5. SRE (a) and Mana (b) as a function of fidelity for a system of four qutrits. Different shades correspond to different depths of the QAOA algorithm.

7.6 Demagication and success of QAOA

One may wonder whether the effect of demagication, i.e., the amount by which SRE decreases after the barrier, $\Delta M = M_2^{\max} - M_2^{\text{final}}$, is related to the success fidelity. To analyze this question, we calculate the conditional probability ($\mathcal{P}_{\text{cond}}[f_{\text{th}}, \epsilon]$) of obtaining a fidelity greater than some f_{th}, provided that the QAOA has shown some minimum amount of demagication, $\Delta M > \epsilon$:

$$\mathcal{P}_{\text{cond}}\Big[F > f_{\text{th}}\Big|\Delta M > \epsilon\Big] = \frac{\mathcal{P}\Big[(F > f_{\text{th}}) \cap (\Delta M > \epsilon)\Big]}{\mathcal{P}\Big[\Delta M > \epsilon\Big]}. \tag{7.19}$$

For qubits. As we see in Fig. 7.6, a larger demagication (larger ϵ), appears to result in a higher probability of solving the QAOA with high fidelity. Additionally, the probability of reaching or surpassing a given fidelity also increases (shifts to the right) as the depth increases, which is to be expected.

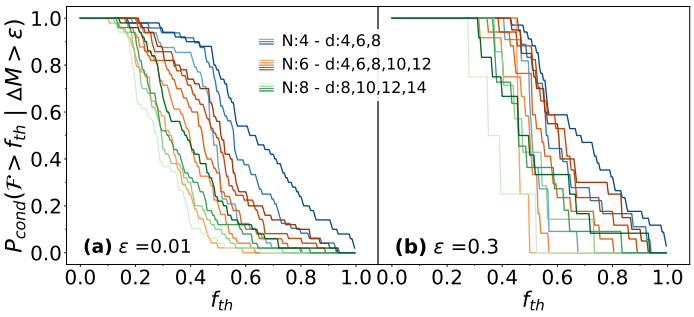

Figure 7.6. Conditional probability of achieving high final fidelity $f \geq f_{\text{th}}$ given a demagication ΔM (difference between peak and final magic) exceeding a threshold ϵ, for different system sizes and QAOA depths. (a) $\epsilon = 0.01$. (b) $\epsilon = 0.3$. The rightward shift in (b) relative to (a) shows that stronger demagication correlates with a higher chance of high fidelity. Darker lines represent deeper QAOA circuits.

For qutrits. Similarly, for qutrits, Fig. 7.7 (a-b) shows the conditional probability of achieving a fidelity above a given threshold, provided the QAOA reaches a minimum amount of demagication.

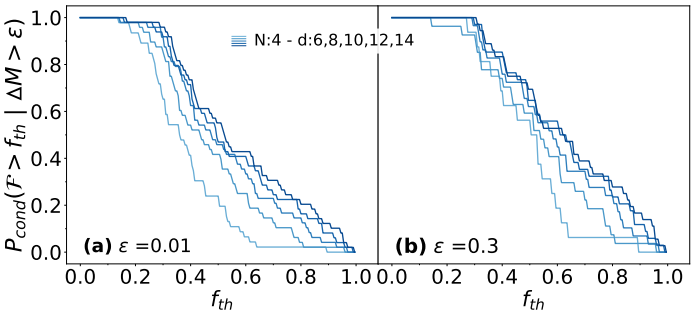

Figure 7.7. (a) Conditional probability curve for $\epsilon = 0.01$ and (b) for $\epsilon = 0.3$, obtained for four qutrits at QAOA depths 6, 8, 10, 12, and 14.

7.7 Magic barrier in quantum annealing

To assess the generality of the magic barrier beyond QAOA, we analyze its emergence in continuous-time quantum annealing protocols [236, 242, 540] (see Sec. 3.3.2). To simulate the stationary regime of the annealing protocol, we employ tensor network techniques, specifically matrix product state (MPS) methods [91, 541–543], which allow us to compute numerically the exact ground state $|\psi(\lambda)\rangle$ of the instantaneous Hamiltonian $H(\lambda = t/T)$, at arbitrary points along the interpolation, with small bond dimension χ (we fixed $\chi = 60$ in our simulation, at which value the result is converged). This framework also enables efficient computation of SRE using the Pauli Matrix Product State (Pauli MPS) formalism [544], with bond dimension up to $\chi_P = 1024$. To make the computation tractable, we truncate the fully connected spin-glass interactions in the cost Hamiltonian to fifth-neighbor couplings. We verified that this truncation does not qualitatively affect the key features of the observed magic dynamics.

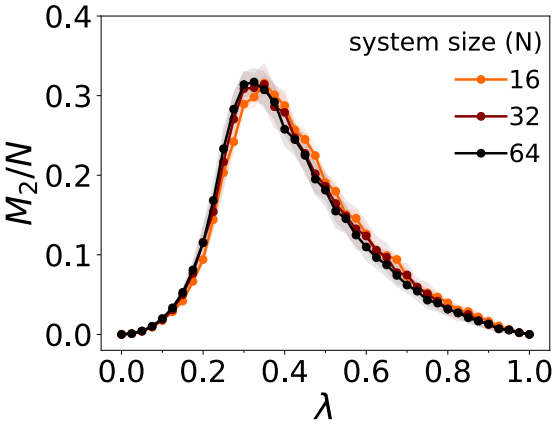

Figure 7.8. Magic barrier in quantum annealing The SRE density, computed on the ground state of the instantaneous Hamiltonian (ideal adiabatic quantum annealing, $\lambda \in [0, 1]$), exhibits a magic barrier around $\lambda \sim 0.35$. The nearly overlapping curves for $N = 16, 32, 64$ indicate the SRE density traces a barrier largely independent of system size.

The resulting SRE profile, shown in Fig. 7.8, reveals a clear magic barrier: magic rises during the early stages of the sweep, peaks around intermediate λ, and decreases as the system approaches the classical solution. This behavior closely mirrors the magic evolution observed in QAOA.

7.8 Evolution of magic during classical optimization loop

To reach a more complete understanding of the role of nonstabilizerness in solving optimization problems using variational quantum algorithms, we analyze how it evolves throughout the optimization process. QAOA heavily relies on classical optimization to determine optimal parameters, requiring repeated execution of quantum circuits [Fig. 7.2(a)] that include non-Clifford gates, making them resource-intensive in terms of quantum magic. By studying how magic evolves during the optimization of circuit parameters, we extract information about the resources required to achieve convergence. In particular, we consider 50 problem instances, each defined by different Hamiltonian coefficients, and run 50 QAOA optimizations per instance, initialized with annealing-inspired parameters (increasing γ, decreasing β) [256]. For each instance, we select the run achieving the lowest energy as the best-performing optimization.

Figure 7.9 shows energy values and nonstabilizerness measures as a function of the optimization steps for the best-performing QAOA run of each of the 50 realizations. Panels (a1) and (b1) refer to results for a 6-qubit system using a QAOA with a circuit depth of 12, while panels (a2) and (b2) report results for a 4-qutrit system using a QAOA circuit with depth 14. The success of QAOA is measured here using the approximation ratio, defined as $\frac{E-E_0}{E_0}$, where E is the expectation value of the Hamiltonian for the optimized state, and E_0 represents the minimum energy obtained through exact diagonalization. During optimization, the energy initially increases, crosses a barrier, and eventually converges close to E_0 for nearly all problem instances. Despite the initial parameterization ensuring a good starting point, the optimization process allows the algorithm to escape local minima and reach a lower-energy minimum, closer to the ground state. This energy barrier is accompanied by a peak in magic, suggesting that crossing a high-nonstabilizerness region is required for convergence. A similar pattern is observed for the Mana in the 4-qutrit case, shown in Fig. 7.9(b2).

Although magic, like energy, shows a barrier during optimization, it captures a

different property: the distance from stabilizer states in the Clifford group. As such, it is not necessarily expected to follow the energy landscape directly. While the energy approximation ratio consistently approaches zero across different instances, indicating convergence toward the ground state [254], the final magic values remain widely spread. This highlights a key point: although the ground state has zero magic, optimized QAOA states often retain finite magic, showing that energy convergence does not imply convergence to the exact solution. Moreover, our Hamiltonians are non-degenerate and thus their ground state are product-states with zero magic. This suggests that even near the exact solution energy, QAOA may converge to a superposition of low-lying eigenstates. This occurs when energy level splittings—which depend on the external field strength—are small, preventing the algorithm from entirely collapsing onto the actual ground state.

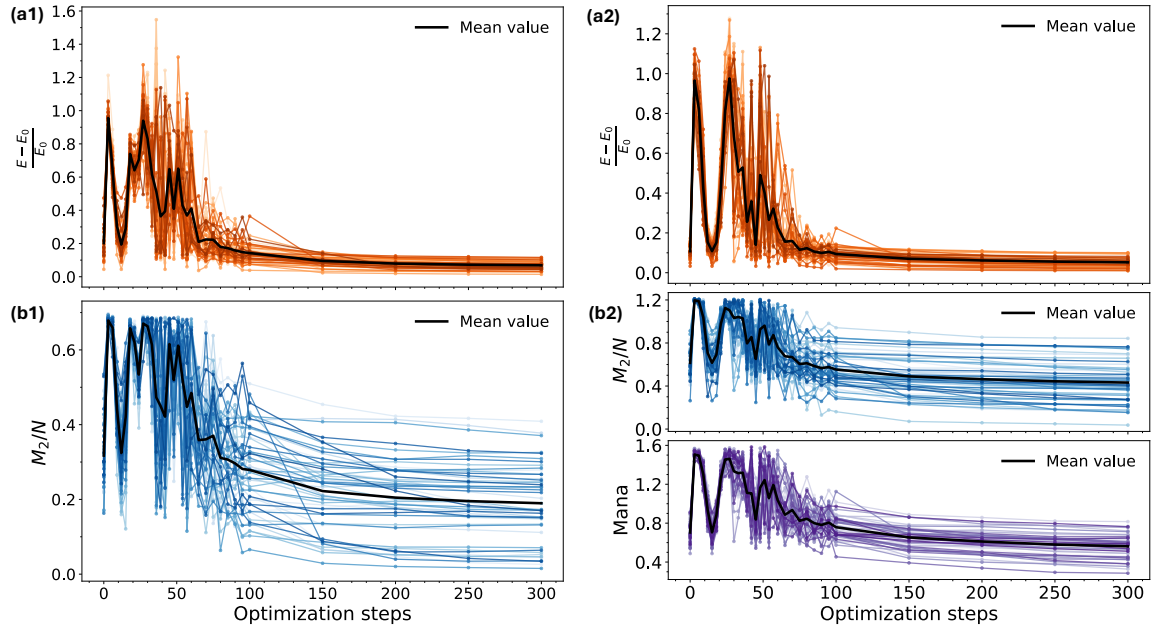

Figure 7.9. Energy and magic barrier during classical optimization. The black curves represent the mean values calculated over 50 realizations. (a1), (a2) Energy ratio as a function of the number of optimization steps during a QAOA run of each problem realization for 6-qubit and 4-qutrit systems, respectively. (b1) Magic as a function of optimization steps of each QAOA run for the qubit system. (b2) Magic in the upper plot and Mana in the lower plot as a function of optimization steps for the qutrit system.

7.9 Summary and outlook

To summarize, magic arises in QAOA even when the target problem has a non-magical solution. Irrespective of the depth of the QAOA, magic rises to a peak and, in a well-performing run, falls towards the end of the protocol, incurring an extra resource cost to overcome, a phenomenon we call the magic barrier. This peak consistently appears near the middle of the QAOA, and upon rescaling, the average magic collapses onto a universal curve across different depths, for both qubits and qutrits, and for SRE and Mana. The fidelity of the final state has a characteristic relation to the final magic, whose qualitative behavior can be explained analytically through the dependence on probability amplitude and local phase of a simple *ansatz* state.

While in current noisy devices non-Clifford gates are not necessarily more expensive than Clifford gates, the situation is different in early fault-tolerant machines, where non-Clifford operations constitute a significant bottleneck [505, 545–548]. In such cases, the emergence of a magic barrier in QAOA becomes a crucial factor. This motivates the question of whether QAOA can be parameterized to reach the solution state while remaining close to the convex hull of stabilizer states, thus minimizing magic generation.

A natural next step is to test these findings on a quantum processor such as one based on superconducting qubits, cold atoms, or trapped ions, which would also provide a figure of merit for the performance characteristics of a given device. Trapped ions, e.g., appear well suited for a direct test, as they naturally implement long-range interactions as occur in the Sherrington–Kirkpatrick model studied here, and they have recently permitted for measuring nonstabilizerness [173], and for the implementations of quantum optimization protocols [549, 550]

Part III

Resources in Disordered Systems

Chapter 8

Disorder-averaged qudit dynamics

emergence of non-Markovian dynamics from symmetry and disorder

8.1 Introduction

The effective use of the quantum resources within an engineered quantum device requires precise control. However, even in cases where the device is almost perfectly isolated from its surroundings, uncontrolled and uncertain parameters can significantly restrict the accuracy and efficiency of the quantum device, a challenge shared across experimental platforms. The effect of the lack of certainty and control on the system's evolution is often modeled via disorder, described by random system parameters [551–557]. In condensed matter, disordered systems are ubiquitous, and their fundamental and technological importance makes them a longstanding subject of research [362, 558–564]. In quantum-information-processing devices, the disorder may arise because of imperfect sample production, finite accuracy of control electronics, imprecise gate rotations, or slow drifts of system parameters. In this context, understanding disordered dynamics may be key for the mitigation of errors, e.g., suppressing charge-noise decoherence in superconducting charge qubits [565], boosting coherence via non-ergodicity [566], determining optimal readout times, reducing gate errors [567], tracking drift errors in quantum processors [568], and mitigating sample-to-sample fluctuations in quantum dots [569]. Disorder also plays a key role in quantum annealing [236,243,570,571], environment enhanced quantum transport [572,573], and the memory effect of disorder-induced localization can even be used to protect against errors [574–576].

While looking for a solution to a disordered model, one is often not interested in an individual disorder realization, either because it is too specific or because the disorder in the physical system is not sufficiently characterized. In such situations, one can derive information about the typical behavior of the quantum system by investigating disorder-averaged ensembles. However, the dynamics of disordered systems are difficult to compute in general, and reaching a converged average often requires considerable numerical effort to acquire sufficient independent samples. In such scenarios, it can be useful to have an effective equation for describing the averaged dynamics, either in the form of a dynamical map or a differential evolution equation. Interestingly, the effective dynamics of the disorder-averaged ensemble can behave as if it were an open system [577]. For various cases, a master equation has been formulated that governs the disorder-averaged evolution, e.g., in the context of a qubit under spectral disorder [578], anisotropic decoherence of qubits [579], relaxation of a qubit under coupling [580], Dirac particles with mass perturbations [201], many-body boson dynamics [581], simulations of the spin-boson model using a disordered

ensemble [582], transport properties in imperfect waveguides [583], obtaining robust control pulses [200], quantum parameter estimation [584], equilibration dynamics of the Sachdev–Ye–Kitaev model [585], and operator spreading [586]. For the case where the dynamical map describing the time-evolved ensemble density matrix can be inverted, Kropf *et al.* [578] discuss a formalism to obtain a master equation of Lindblad form using a matrix-based approach. However, deriving such an exact master equation is not always possible [587].

Here, we discuss an analytical method to find dynamical maps to describe the exact disorder-averaged evolution dynamics. Our framework is valid for arbitrary times and for any unbiased disorder distribution (mean zero), without necessitating a master equation. The Hamiltonians of the considered systems can be Hermitian or non-Hermitian, but they have to be periodic modulo a scalar factor, i.e., $H^p \propto \mathbb{I}$ or, more generally, $H^p \propto H^q$, with p and q integers such that $q < p$. In particular, this property covers periodic Hamiltonian matrices with non-trivial base q, also called (q, p)-potent [588, 589]. Prominent examples are the tensor-product Hamiltonians of two-level systems, corresponding to involutary matrices with $p = 2$ and $q = 0$, or multi-level clock operators [590, 591], such as $p = 3$, $q = 0$. Periodic Hamiltonians are ubiquitous in quantum technologies, e.g., as generators of single- and multi-qubit [372, 592, 593] or qudit gates in quantum computing [594], as stabilizer operators in quantum error correction [148, 595, 596], in error modeling of noisy quantum devices [597], in noisy quantum algorithms [598], etc.

In what follows, we analytically derive the dynamical map giving the disorder-averaged density matrix for such periodic Hamiltonians at any given time and extract common structures for three example cases. The effective equations are characterized by several quantities relevant in quantum information theory, including various witnesses of non-Markovianity [183, 188, 599]. Although solving for the dynamics of each individual realization of the chosen example Hamiltonians is relatively simple, they are non-self-averaging[1]. Therefore, already for somewhat restricted evolution times, numerous independent disorder realizations can be needed to obtain converged results; in one of our example cases, even up to more than 10^7 realizations. In such scenarios, having the exact analytic results at one's disposal provides significant benefits. In some cases, we can also derive a master equation [182] by inverting the underlying dynamical map, the result of which matches with Ref. [578]. Thus, our results further our understanding of how dynamics typically associated with dissipative systems can emerge in deterministic disorder averages, and it may be useful in extracting exact behavior in simple but ubiquitous situations.

The structure of the rest of this chapter is as follows: Section 8.2 presents the analytical approach for deriving the disorder-averaged dynamics, supplemented by examples as well as several quantities that we use to characterize the dynamics, including non-Markovianity witnesses. Next, we delve into three specific cases in detail: $(p = 2, q = 0)$, as described, e.g., by single-qubit operators or products of Pauli matrices (Sec. 8.3); $(p = 3, q = 0)$, which we exemplify through non-Hermitian qutrit operators (Sec. 8.4); and $(p = 3, q = 1)$, describing, e.g., spin-1 operators (Sec. 8.5). Finally, Sec. 8.7 concludes by highlighting the key features of the analytical method and discussing potential future research directions.

[1] A self-averaging property in a disordered system is one that can be accurately described by averaging over a sufficiently large number of samples [600].

8.2 Disorder-averaged dynamics

To set the stage, in this section, we formally derive the dynamical map[2] describing a disorder-averaged ensemble (Sec. 8.2.1). Finding a closed analytical solution is, in general, infeasible, but from its form, one can recognize a drastic simplification if the Hamiltonian matrix fulfills a specific structure, namely if it has a period (Sec. 8.2.2). Before discussing several examples in detail, which we postpone to the next section, we also introduce several quantities estimating quantum informational content of the state, including some witnesses of non-Markovianity (Sec. 8.2.3), which we will use in the later part of the chapter to characterize the disorder-averaged dynamics.

8.2.1 Disorder-averaged dynamical map: formal solution

Given a Hamiltonian $\hat{H}$, irrespective of it being Hermitian or non-Hermitian, and an initial state $\hat{\rho}(0)$, the final state after evolution until a time t is given by

$$\hat{\rho}(t) = e^{-i\hat{H}t}\hat{\rho}(0)e^{i\hat{H}^\dagger t}\,, \tag{8.1}$$

(note the dagger at the right of $\hat{\rho}(0)$, necessary for the correct description of non-Hermitian dynamics [601]). The system's dynamics follow the differential equation

$$\partial_t\hat{\rho}(t) = -i\hat{H}\rho(t) + i\rho(t)\hat{H}^\dagger\,, \tag{8.2}$$

which in the Hermitian case ($\hat{H} = \hat{H}^\dagger$), turns into the well-known von Neumann equation: $\partial_t\hat{\rho}(t) = -i[\hat{H}, \hat{\rho}(t)]$.

For a general Hamiltonian $\hat{H}$, solving Eq. (8.1) is not effortless. The situation becomes even more complicated if $\hat{H} = \hat{H}[h]$ describes an ensemble of Hamiltonians with a random variable h over which we have to average, a procedure we denote by $\mathbb{E}[\cdot]$. In particular, one has in general $\mathbb{E}[e^{-i\hat{H}t}] \neq e^{-i\mathbb{E}[\hat{H}]t}$, making it challenging to apply the ensemble average to the evolved state. This chapter aims to get a handle on the disorder-averaged density matrix for a specific but ubiquitous class of Hamiltonians useful for quantum information processing.

To calculate the disorder average irrespective of the initial state, it is advantageous to use the super-operator techniques [182, 602] that map between the matrix $\hat{\rho}$ and a vector $\vec{\rho}$. Any left and right multiplications to $\hat{\rho}$ can be vectorized as column vectors by the following rules

$$\hat{A}\hat{\rho} \leftrightarrow (\mathbb{I}\otimes\hat{A})\vec{\rho} \quad \text{and} \quad \hat{\rho}\hat{B} \leftrightarrow (B^T\otimes\mathbb{I})\vec{\rho}\,. \tag{8.3}$$

By series expanding on both exponentials in Eq. (8.1) and using the super-operator notation above, we derive (see below for full derivation)

$$\vec{\rho}(t) = \sum_{n=0}^{\infty}\frac{(-it)^n}{n!}\sum_{k=0}^{n}\binom{n}{k}(-\hat{H}^*)^{n-k}\otimes\hat{H}^k\vec{\rho}(0)\,, \tag{8.4}$$

where $(\,)^*$ denotes complex conjugation.

[2] The dynamical map of a quantum system describes how an initial density matrix evolves over time, mapping it to the system's state at a later moment.

Derivation. By series expanding the evolved density operator $\rho(t)$ of Eq. (8.1), we obtain

$$\rho(t) = e^{-iHt}\rho(0)e^{+iH^\dagger t} \tag{8.5}$$

$$= \sum_{k=0}^{\infty} \frac{(-it)^k}{k!} H^k \rho(0) \sum_{j=0}^{\infty} \frac{(it)^j}{j!} (H^\dagger)^j \tag{8.6}$$

$$= \sum_{n=0}^{\infty} \frac{(-it)^n}{n!} \sum_{k=0}^{n} \frac{n!}{(n-k)!k!} H^k \rho(0) (-H^\dagger)^{n-k} \,. \tag{8.7}$$

Now, we can go to the super-operator notation by using Eq. (8.3) to take the initial state towards the right and extract an evolution term that is independent of the initial state. Note that, the term $((-H^\dagger)^{n-k})^T = ((-H^\dagger)^T)^{n-k} = (-H^*)^{n-k}$, and thus we obtain

$$\vec{\rho}(t) = \sum_{n=0}^{\infty} \frac{(-it)^n}{n!} \sum_{k=0}^{n} \binom{n}{k} (\mathbb{I} \otimes H^k)((-H^*)^{n-k} \otimes \mathbb{I})\vec{\rho}(0) \tag{8.8}$$

$$= \sum_{n=0}^{\infty} \frac{(-it)^n}{n!} \sum_{k=0}^{\infty} \binom{n}{k} (-H^*)^{n-k} \otimes H^k \vec{\rho}(0) \,. \tag{8.9}$$

This equation facilitates the Hamiltonian terms to be separated from the initial state by taking $\vec{\rho}(0)$ outside operator products. Such an expansion of the exponential in the power series of the density operator has previously been used to derive exact equations for the dynamics in multiple scenarios, including the evolution of a classical many-body system [603] as well as an exact generalized master equation for a quantum-mechanical system [604]. It is a procedure quite analogous to the diagrammatic cluster expansion used in statistical mechanics [605].

We denote the disorder-averaged density matrix as $\mathbb{E}[\vec{\rho}(t)] \equiv \tilde{\vec{\rho}}(t)$. Assuming no disorder in the initial state $\rho(0)$[3], we arrive at an equation where disorder averaging acts directly on different powers of the Hamiltonian and its complex conjugate,

$$\tilde{\vec{\rho}}(t) = \sum_{n=0}^{\infty} \frac{(-it)^n}{n!} \sum_{k=0}^{n} \binom{n}{k} \mathbb{E}\left[(-\hat{H}^*)^{n-k} \otimes \hat{H}^k\right] \vec{\rho}(0) \equiv \Lambda_t[\vec{\rho}(0)] \,. \tag{8.10}$$

Here, a family of linear quantum dynamical maps $\{\Lambda_t\}_{t\geq 0}$ from the set of density matrices to itself formally describes the dynamics. In Sec. 8.3-8.5 below, we derive explicit expressions of the disorder-averaged evolution from this equation for the specific cases when the Hamiltonian is periodic, the property we introduce in the next section.

Before that, it is illustrative to establish a formal connection between the ensemble-averaged evolution and that of an open quantum system. In the time-local description of dynamics in an open quantum system, the family of dynamical maps satisfies a differential equation of the form, $\partial_t \Lambda_t[\cdot] = \mathcal{L}_t \circ \Lambda_t[\cdot]$, where $\mathcal{L}_t$ is the Lindbladian that generates the dynamics [182]. Alternatively, using the Nakajima–Zwanzig projective techniques, one can derive an integro-differential master equation involving a memory

[3]Note that our derivation can be extended for the disordered initial state as well, where the disorder averaging should be done together with $\rho(0)$ if it follows the same disorder distribution as the Hamiltonian or has a correlated disorder.

kernel ($\mathcal{K}$) [182]. The general conditions on $\mathcal{L}_t$ or $\mathcal{K}$ that ensure the resulting dynamical map Λ_t is valid, i.e., completely positive and trace-preserving, is still under research, with only certain cases fully understood (see, e.g., Refs. [606–616]). As a result, a general rule for constructing master equations is not always available. However, when the dynamical map is invertible, it is always possible to construct the time-local description, i.e., find $\mathcal{L}_t$ [190]. For example, from Eq. (8.10), we can obtain the following equations by replacing $\vec{\rho}(0) = \Lambda_t^{-1}[\tilde{\vec{\rho}}(t)]$ in the second equality,

$$\partial_t \tilde{\vec{\rho}}(t) = \partial_t \Lambda_t \left[\vec{\rho}(0)\right] = \partial_t \Lambda_t \circ \Lambda_t^{-1} \left[\tilde{\vec{\rho}}(t)\right] \equiv \mathcal{L}_t \left[\vec{\rho}(t)\right], \tag{8.11}$$

where $\circ$ denotes map composition, and we can identify $\mathcal{L}_t$ as the Lindbladian. Kropf et al. [578] obtain similar master equations based on a matrix formalism [190, 587] when Λ_t^{-1} exists, which forms the foundation for the exact dynamics in their cases. Here, instead, we focus on obtaining the dynamical map Λ_t, which is enough to exactly describe the ensemble-averaged dynamics (i.e., $\tilde{\rho}(t)$), and our method is independent of the representation of the Hamiltonian in any particular basis. When Λ_t^{-1} exists, we also write down the corresponding master equation.

8.2.2 Periodic Hamiltonians

The general formal solution achieved above in Eq. (8.10) does often not help much to extract the physical properties of the system, as one has to calculate arbitrary powers of $\hat{H}$ to obtain $\tilde{\vec{\rho}}(t)$, at least when one wants to go beyond a perturbative short-time expansion. However, for Hamiltonian matrices with a special structure, namely, if there exists a pair of integers p and q (with $p > q$) for which

$$\hat{H}^p = h^{p-q} \hat{H}^q, \tag{8.12}$$

Eq. (8.10) can be solved exactly.

In the literature, matrices with such a property (modulo the prefactor h^{p-q}) are called periodic with period $p - q$ and base q [588] or (q, p)-potent [589]. Special cases are periodic matrices with $q = 1$, called p-potent, and with $q = 1, p = 2$ (i.e., $\hat{H}^2 = \hat{H}$) called idempotent. If the matrix is non-singular, $\hat{H}^{p'} = h^{p'-q'} \hat{H}^{q'}$ implies the simpler relation $\hat{H}^p = h^p \mathbb{I}$, with $p = p' - q'$, which can be seen as a special case of Eq. (8.12) with $q = 0$. Matrices with $q = 0$ and $p = 2$ are called involutary. Physically, the periodicity of the Hamiltonian implies that the full dynamics are generated by a finite number of distinct operators. Here, we will use this property to reduce the infinite sums in Eq. (8.10) to a finite, tractable number of terms.

As some instructive examples, in Sec. 8.3 to Sec. 8.5, we will consider single-qubit Pauli and single-qutrit clock operators ($q = 0$ and $p = 2, 3$) as well as spin-1 operators ($q = 1$ and $p = 3$). For each case, we analytically derive the dynamics of the disorder-averaged density operator and calculate several quantities to characterize it, including non-Markovianity witnesses, as described in the next section. Such analysis can be helpful in determining noise channels [617] and error correction protocols [584]. As the spin-1 operator can be used as an alternative representation for qutrits [497], we can also compare how the symmetry ($\mathbb{Z}_3$ for clock operators, and SU(2) for spin-1) affects its dynamics. Before we go into the details of the results, we introduce several quantities, including witnesses of non-Markovianity, that we will use to analyze the ensuing dynamics.

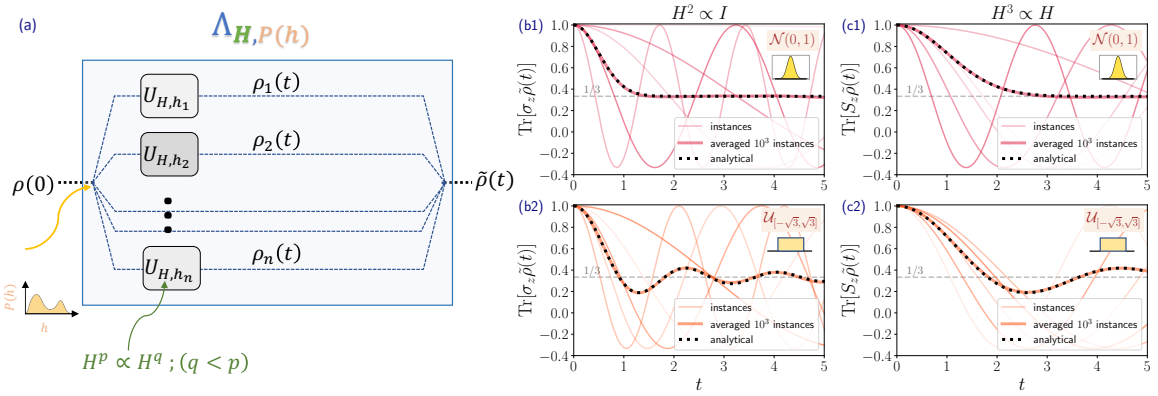

Figure 8.1. (a) An initial state $\rho(0)$ is evolved under an ensemble of disordered Hamiltonians with a finite period ($H^p \propto H^q$, $q < p$). Each instance is generated from a closed-system time evolution, with disorder h_i chosen from an arbitrary disorder distribution $P(h)$. The disorder averaging induces the effective dynamics of $\tilde{\rho}(t)$ defined by the dynamical map $\Lambda_{H,P(h)}$, which is determined by the period of the Hamiltonian and the probability distribution $P(h)$ of the disorder. (b1-c2) Time evolution of the expectation value of an observable [(b1,b2) σ_z, (c1,c2) S_z] for dynamics governed by periodic Hamiltonians [(b1,b2): $H^2 \propto \mathbb{I}$, (c1,c2): $H^3 \propto H$] with Gaussian (top) and uniform (bottom) disorder distributions. The initial state corresponds to $|+1\rangle$ of the corresponding observables. The evolutions numerically averaged over 10^3 samples match very well with the analytical expectation values derived with the disorder-averaged state $\tilde{\rho}$. The averaged observables for Gaussian disorder decay monotonically (b1,c1), whereas for the uniform disorder, their expectation value oscillates, with twice the period for $H^3 \propto H$ (c2) compared to $H^2 \propto I$ (b2). Nonetheless, in all the cases, the observables reach 1/3 for a long time. Directly using the averaged evolution operator can be advantageous, as it obviates the need for sufficient sampling over individual realizations to reach full convergence.

8.2.3 Quantum information theoretic quantities and witnesses of non-Markovianity

Disorder averaging can generate effective dynamics that reproduce effects typical of dissipative systems [578, 585], see Fig. 8.1. It is interesting to question whether the effective dynamics are compatible with a Markovian description. To explore this query, we will analyze several key quantities that serve as important measures in quantum information, which can also act as witnesses of non-Markovianity [599, 618]. Different and inequivalent notions of non-Markovianity exist. We have discussed such quantities in Sec. 2.8.2. In this chapter, we will use trace distance (BLP criterion), logarithmic negativity (RHP criterion), and Purity.

Note that all the above-mentioned witnesses are non-linear functions of $\rho(t)$. This property implies that the disorder-averaged witness, calculated from the disorder-averaged state $\tilde{\rho}$, differs from the average witness of individual disorder realizations $\rho(t)$, i.e, $W[\tilde{\rho}] \neq \mathbb{E}[W[\rho]]$, where W denotes the non-linear witness function (in contrast to standard observables that are linear functions of the state). Which averaging procedure is the more relevant one can depend on the situation at hand. E.g., often the disorder varies from shot to shot, making ρ hardly accessible and rendering the ensemble $\tilde{\rho}$ a potentially better description of the system. As each independent sample describes a fully unitary evolution, $\mathbb{E}[W[\rho]]$ will return only trivial results. In contrast, as we will see further below, $W[\tilde{\rho}]$ can yield striking differences between the various disorder distributions considered. The non-Markovian witnesses can thus serve as a tool to illuminate the characteristics of the emergent quantum dynamics.

8.3 Case I: $\hat{H}^2 = h^2\mathbb{I}$

In this section, we derive the exact quantum dynamics for one of the simplest possible classes covered by our framework, $\hat{H}^2 = h^2\mathbb{I}$, i.e., involutary matrices with $p = 2, q = 0$. Particular examples are

1. A single spin $S = 1/2$ or qubit,

$$\hat{H}_1 = h\vec{n}\cdot\vec{\sigma}\,, \tag{8.13}$$

   where $\vec{n}$ is a three-dimensional unit vector and $\vec{\sigma} = (\sigma_x, \sigma_y, \sigma_z)$ is the vector of Pauli matrices. For concreteness, in what follows, we choose without the restriction of generality $\vec{n} = (1, 1, 1)/\sqrt{3}$;

2. Many-body tensor products of Pauli matrices

$$\hat{H}_N = h\bigotimes_{i=1}^{N}(\hat{H}_{1i}/h)\,; \tag{8.14}$$

3. Tensor products of σ_α at different positions, P_α, where $\sigma_\alpha = \{\mathbb{I}, \sigma_x, \sigma_y, \sigma_z\}$. For example, $\sigma_x \otimes \mathbb{I} \otimes \sigma_y$.

Such Hamiltonians are ubiquitous in quantum mechanics, ranging from textbook examples such as Stern–Gerlach experiments on single spins to building blocks of advanced quantum technologies in cold-atom and quantum-computing platforms (e.g., single qubit operations are described by $\hat{H}_1$, while two-qubit gates such as the Mølmer–Sørensen gate are described by $\hat{H}_2$ [619]). The parity checking operator for quantum error detection and corrections belongs to P_α [595]. Here, we want to analyze analytically the effects of disorder on such systems in general.

8.3.1 Effective evolution and master equations

We only consider mean-zero disorder distributions. As a consequence, $\mathbb{E}[h^{2m+1}] = 0$ with $m \in \mathbb{N}$, and we are left with the terms of even n's of Eq. (8.10). On top of that, as $\hat{H}^2 = h^2\mathbb{I}$, all powers of $\hat{H}$ are either proportional to $\mathbb{I}$ (even) or $\hat{H}$ (odd). These constitute the dynamics of $\tilde{\rho}(t) = \mathbb{E}[\rho(t)]$

$$\tilde{\vec{\rho}}(t) = \left[\left(\frac{1+G(t)}{2}\right)\mathbb{I}\otimes\mathbb{I} + \left(\frac{1-G(t)}{2}\right)\tilde{H}^*\otimes\tilde{H}\right]\vec{\rho}(0) \equiv \Lambda_t\vec{\rho}(0)\,, \tag{8.15}$$

where $\tilde{H} = \hat{H}/h$ is the disorder-free part of the Hamiltonian. Note that Eq. (8.15) needs only two operators out of four possible combinations possible from $\{\mathbb{I}$ and $\tilde{H}\}$ because both $\mathbb{I}\otimes\tilde{H}$ and $\tilde{H}^*\otimes\mathbb{I}$ are associated to odd powers of h, and thus vanish after disorder averaging for a distribution with mean 0. For completeness, we present the derivation of the above equation below.

Derivation. To start with, we note that only terms even in t (i.e., even in h) in Eq. (8.9) will survive disorder averaging. So, we only need to take care of the even n terms. Further splitting these terms into even and odd k, we find

$$\begin{aligned}
&\left[\sum_{k=0}^{2n}\binom{2n}{k}(-H^*)^{2n-k}\otimes H^k\vec{\rho}(0)\right]\\
&=\left[\sum_{k=0}^{n}\binom{2n}{2k}(-H^*)^{2n-2k}\otimes H^{2k}+\sum_{k=0}^{n-1}\binom{2n}{2k+1}(-H^*)^{2n-2k-1}\otimes H^{2k+1}\right]\vec{\rho}(0)\\
&=\left[h^{2n}\mathbb{I}\otimes\mathbb{I}\Big(\frac{2^{2n}+\delta_{n0}}{2}\Big)-h^{2n-2}\tilde{H}^*\otimes\tilde{H}\Big(\frac{2^{2n}}{2}\Big)\right]\vec{\rho}(0)\,.
\end{aligned} \tag{8.16}$$

Note that the entire simplification of the terms is due to the periodicity of the Hamiltonian. Now, we can perform the average over the disorder,

$$\tilde{\vec{\rho}}(t)=\left[\sum_{n=0}^{\infty}\frac{(-it)^{2n}}{(2n)!}\mathbb{E}[h^{2n}]\Big(\frac{2^{2n}+\delta_{n0}}{2}\Big)\mathbb{I}\otimes\mathbb{I}-\sum_{n=1}^{\infty}\frac{(-it)^{2n}}{(2n)!}\mathbb{E}[h^{2n}]\Big(\frac{2^{2n}}{2}\Big)\tilde{H}^*\otimes\tilde{H}\right]\vec{\rho}(0)\,. \tag{8.17}$$

From here, using the moments of the disorder distributions, we will derive the exact analytical form of the equation Eq. (8.15).

The general form in Eq. (8.15) is independent of the type of disorder distribution, whose entire effect is encapsulated in the time-dependent function $G(t)$. For the present case of $p=2, q=0$, we have $G(t)=\mathbb{E}[e^{-2iht}]=\int dhp(h)e^{-2iht}$, i.e., it is given by the Fourier transform of the probability distribution with time $t'=2t$, and thus corresponds to the characteristic function[4] containing the behavior and properties of the probability distribution. In Tab. 8.1, we give the exact form of $G(t)$ for Gaussian and homogeneous uniform disorder distributions.

Quantities	Gaussian $\mathcal{N}(0,\sigma^2)$	Uniform $\mathcal{U}_{[-b,b]}$
Prob. dist. function: $P(h)$	$\frac{1}{\sigma\sqrt{2\pi}}e^{-\frac{1}{2}h^2/\sigma^2}$	$\frac{1}{2b}$
Characteristic function: $\varphi_x(t')$	$e^{-\sigma^2t'^2/2}$	$\frac{\sin bt'}{bt'}$
Disorder moments: $\mathbb{E}[h^{2n}]$	$\sigma^{2n}(2n-1)!!$	$b^{2n}/(2n+1)$
Time-dependent function: $G(t)$	$e^{-2\sigma^2t^2}$	$\frac{\sin 2bt}{2bt}$
Decay rate: $\gamma(t)$	$2\sigma^2t$	$\frac{1}{2}\Big(\frac{1}{t}-2b\cot 2bt\Big)$

Table 8.1. Relevant quantities describing the exact evolution depending on the disorder distributions: probability distribution function, the characteristic function of the distribution, disorder-averaged moments, $G(t)$, emergent decay rate governing the master equation (8.26). The last two quantities are specific to the case $p=2, q=0$, such as the single-qubit Hamiltonian H_1.

[4]The characteristic function is the Fourier transform of a probability distribution, encoding all its statistical moments.

Gaussian disorder: In the special case of a Gaussian distribution $(0, \sigma^2)$, we have $\mathbb{E}[h^{2n}] = \sigma^{2n}(2n-1)!!$, and therefore

$$\frac{(-it)^{2n}}{(2n)!}\mathbb{E}[h^{2n}] = \frac{(-i\sigma t)^{2n}}{(2n)!!} = \frac{1}{n!}\left(\frac{-\sigma^2 t^2}{2}\right)^n . \tag{8.18}$$

Inserting this to Eq. (8.17), we obtain

$$\sum_{n=0}^{\infty}\frac{1}{n!}\left(\frac{-\sigma^2 t^2}{2}\right)^n\left(\frac{2^{2n}+\delta_{n0}}{2}\right) = \frac{1}{2}\left[1 + e^{-2\sigma^2 t^2}\right] \tag{8.19}$$

and

$$\sum_{n=1}^{\infty}\frac{1}{n!}\left(\frac{-\sigma^2 t^2}{2}\right)^n\left(\frac{2^{2n}}{2}\right) = \frac{1}{2}\left[e^{-2\sigma^2 t^2} - 1\right] . \tag{8.20}$$

The final equation for the average time-evolved state in the case of Gaussian disorder thus becomes

$$\tilde{\vec{\rho}}(t) = \frac{1}{2}\left[\left(1 + e^{-2\sigma^2 t^2}\right)\mathbb{I}\otimes\mathbb{I} + \left(1 - e^{-2\sigma^2 t^2}\right)\tilde{H}^*\otimes\tilde{H}\right]\vec{\rho}(0) . \tag{8.21}$$

Uniform disorder: For a uniform box distribution in the interval $[-b, b]$, we have $\mathbb{E}[h^{2n}] = b^{2n}/(2n+1)$. Thus,

$$\frac{(-it)^{2n}}{(2n)!}\mathbb{E}[h^{2n}] = \frac{(-ibt)^{2n}}{(2n+1)!} . \tag{8.22}$$

Hence, we obtain

$$\sum_{n=0}^{\infty}\frac{(-ibt)^{2n}}{(2n+1)!}\left(\frac{2^{2n}+\delta_{n0}}{2}\right) = \frac{1}{2}\left[1 + \frac{\sin 2bt}{2bt}\right] . \tag{8.23}$$

In this case, the disorder-averaged time-evolved state is

$$\tilde{\vec{\rho}}(t) = \frac{1}{2}\left[\left(1 + \frac{\sin 2bt}{2bt}\right)\mathbb{I}\otimes\mathbb{I} + \left(1 - \frac{\sin 2bt}{2bt}\right)\tilde{H}^*\otimes\tilde{H}\right]\vec{\rho}(0) . \tag{8.24}$$

To illustrate the accuracy of our analytical method, we consider the Hamiltonian H_1 given above, with $\tilde{H} = \vec{n}\cdot\vec{\sigma}$, and calculate the average magnetization $\mathrm{Tr}[\sigma_z\tilde{\rho}(t)]$ using the disorder-averaged state $\tilde{\rho}(t)$ from the analytical solution. For the considered initial state $|\uparrow\rangle = (1,0)^T$, the analytical calculation gives

$$\mathrm{Tr}[\sigma_z\tilde{\rho}(t)] = \frac{1}{3}\left(1 + 2G(t)\right) . \tag{8.25}$$

In Fig. 8.1(b1,b2), we plot the cases of Gaussian disorder (top) as well as uniform disorder (bottom). For a reasonable comparison, we set both the variances of the uniform and the Gaussian distribution to unity, i.e., $b^2/3 = 1$ and $\sigma^2 = 1$. While the ensemble-averaged magnetization dynamics for the Gaussian disorder decays monotonically compared to the value corresponding to an infinite-temperature state [Fig. 8.1(b1)], the dynamics for other distributions can be more complicated, illustrated by the oscillations visible in the case of uniform disorder [Fig. 8.1(b2)]. For both types of

distributions, the exact dynamics over the considered time range match very well with the numerically calculated disorder-averaged magnetization of 10^3 instances.

Furthermore, from Eq. (8.15), we can derive a dynamical master equation for the disorder-averaged density matrix following Eq. (8.11). To this end, by inverting the dynamical map in Eq. (8.15), we obtain a time-local master equation

$$\partial_t \tilde{\rho}(t) = -\frac{\partial_t G(t)}{2G(t)}\left[\tilde{H}\ \tilde{\rho}(t)\ \tilde{H}^\dagger - \frac{1}{2}\left\{(\tilde{H})^\dagger \tilde{H}\ ,\ \tilde{\rho}(t)\right\}\right]. \tag{8.26}$$

Deriving the master equation: From the analytic expression of the time-evolved state, given above and in Eq. (8.15), we can also obtain a von-Neumann type evolution equation for the disorder-averaged $\tilde{\rho}(t)$. We rewrite Eq. (8.15) in terms of $\hat{A}$ and $\hat{B}$ as defined below,

$$\begin{aligned}\tilde{\vec{\rho}}(t) &= \frac{1}{2}\left[\underbrace{\left(\mathbb{I}\otimes\mathbb{I} + \tilde{H}^*\otimes\tilde{H}\right)}_{\hat{A}} + G(t)\underbrace{\left(\mathbb{I}\otimes\mathbb{I} - \tilde{H}^*\otimes\tilde{H}\right)}_{\hat{B}}\right]\vec{\rho}(0) \\ \Rightarrow \Lambda_t &= \frac{1}{2}\left(\hat{A} + G(t)\hat{B}\right).\end{aligned} \tag{8.27}$$

Following the steps in Eq. (8.11), we first obtain time derivative of $\tilde{\vec{\rho}}(t)$,

$$\partial_t \tilde{\vec{\rho}}(t) = \frac{\partial_t G(t)}{2}\hat{B}\vec{\rho}(0)\,. \tag{8.28}$$

To replace $\vec{\rho}(0) = \Lambda_t^{-1}\tilde{\vec{\rho}}(t)$, we evaluate the inverse, which has the form,

$$\Lambda_t^{-1} = \frac{1}{2}\left(\hat{A} + \frac{\hat{B}}{G(t)}\right), \tag{8.29}$$

following from the fact that, $\tilde{H}^2 = \mathbb{I}$ and thus $\hat{A}^2 = 2\hat{A}, \hat{B}^2 = 2\hat{B}, \hat{A}\hat{B} = \hat{B}\hat{A} = 0$, as well as from $\Lambda_0 = \mathbb{I}$ whence $\frac{1}{2}(\hat{A}+\hat{B}) = \mathbb{I}$. Thus, finally, we obtain,

$$\partial_t \tilde{\vec{\rho}}(t) = \frac{\partial_t G(t)}{2G(t)}\hat{B}\tilde{\vec{\rho}}(t)\,. \tag{8.30}$$

By replacing $\hat{B} = (\mathbb{I}\otimes\mathbb{I} - \tilde{H}^*\otimes\tilde{H})$ and going back from super-operator to matrix notation, we obtain Eq. (8.26).

From this equation, it becomes apparent that the $\tilde{H}$ coupled to the disordered field assumes the role of jump operators of a corresponding master equation in Lindblad form. Moreover, the effective decay rate $\gamma(t) \equiv -\frac{\partial_t G(t)}{2G(t)}$ is given entirely by the temporal rate of change of the time-dependent function $G(t)$, which in turn is determined by the disorder distribution (see Tab. 8.1 for explicit forms).

For Gaussian disorder, $G(t)$ and $\gamma(t)$ are always non-negative analytic functions (see Tab 8.1). In contrast, for uniform disorder, $G(t)$ periodically switches sign, and $\gamma(t)$ can have negative values [see Fig. 8.2(b)]. Such dynamics can no longer be $P-$divisible [620], and hence it is also not $CP-$divisible (see more in Ref. [599]), and thus a negative decay rate can also witness non-Markovianity [190], as we discuss in more detail in Sec. 8.3.3.

8.3.2 Relation to error channels

Quantum states are highly fragile and can easily be disrupted by environmental interactions [621,622], hardware imperfections, or operational gate errors [623]. Adequately understanding the dominant error channels of a given quantum hardware is essential for designing fault-tolerant architectures and error-correction codes, making it one of the critical steps in building reliable quantum computing firmware. To estimate the effects of such sources on quantum devices, one typically constructs noise models using quantum channels, e.g., depolarizing, dephasing, amplitude damping, etc. The present framework can be used to derive analytic descriptions of error channels that originate from uncontrolled gate operations.

To illustrate the main idea, consider a generic dephasing channel defined by

$$\rho \to \rho' = (1 - p_d)\rho + p_d \sigma_z \rho \sigma_z \,, \tag{8.31}$$

where with probability p_d the state dephases, while with probability $(1 - p_d)$ it remains unchanged. Interestingly, Eq. (8.31) coincides with Eq. (8.15) when setting $\tilde{H} = \sigma_z$ and choosing the dephasing probability $p_d = \frac{1-G(t)}{2}$. As mentioned above, $G(t)$ is the ensemble-averaged rotation generated by the disorder, $G(t) = \mathbb{E}[e^{-2iht}]$. Thus, if the system is subject to uncontrolled disorder, one can immediately determine the associated noise channel and its probability p_d by only characterizing the type of disorder, here $\exp(-iht\sigma_z)$, and the distribution of the pulse areas ht. This knowledge of disorder can further be used to determine suitable parameters for counteracting disorder-induced dephasing [581]. Similar considerations also hold for qudit systems [587, 617].

8.3.3 Non-Markovianity from disorder distributions

The analytical form of the disorder-averaged state [Eq. (8.15)] permits us to analytically compute the witnesses of non-Markovianity introduced in Sec. 8.2.3. They can be expressed as a function of $G(t)$, starting from any initial state, for example,–

$$\begin{aligned} \mathrm{Tr}(\tilde{\rho}^2) &= \frac{1}{3}(2 + G^2(t)) \,, \quad |\rho_0\rangle = |0\rangle\langle 0| \,; \\ D(\tilde{\rho}_1, \tilde{\rho}_2; t) &= \sqrt{\frac{1 + 2G^2(t)}{3}} \,, \quad |\rho_0\rangle = |0\rangle\langle 0| \,, |\rho_1\rangle = |1\rangle\langle 1| \,; \\ E_N(\tilde{\rho}_{\mathrm{SA}}) &= \log_2(1 + |G(t)|) \quad \rho_{\mathrm{SA},(t=0)} = \frac{1}{\sqrt{2}}(|00\rangle + |11\rangle). \end{aligned} \tag{8.32}$$

In order to see the difference between Gaussian and uniform distribution, we insert the corresponding form of $G(t)$ as detailed in Eq. (8.32) into the witness functions.

With Gaussian disorder, purity, trace distance, and entanglement negativity decrease and saturate to a particular constant (see Fig. 8.2). This behavior is compatible with a complete Markovianity of the evolution. In contrast, with uniform disorder, the non-Markovian witnesses show significant oscillations and only at late times settle to the same long-time value as that obtained for Gaussian disorder. The periodicity of the oscillation is determined by the periodicity of $|G(t)|$, i.e., $\frac{\pi}{2b}$. One can define the strength of non-Markovianity as the number of times the revival of these witnesses happens. This number is inversely proportional to the periodicity of $|G(t)|$ and thus proportional to the standard deviation of the disorder distribution [624]. Thus, the

revival frequency can be controlled by controlling the standard deviation of the disorder, which might be exploited for information-processing tasks [625, 626]. Moreover, with non-Markovian features, the evolution dynamics can be sped up [627], or the capacity of a quantum channel can be enhanced [628]. Note that, in this case, since the dynamical map is unital (see Section 8.6), purity can be used as a witness of non-Markovianity. It functions just as effectively as other witnesses and exhibits similar behavior.

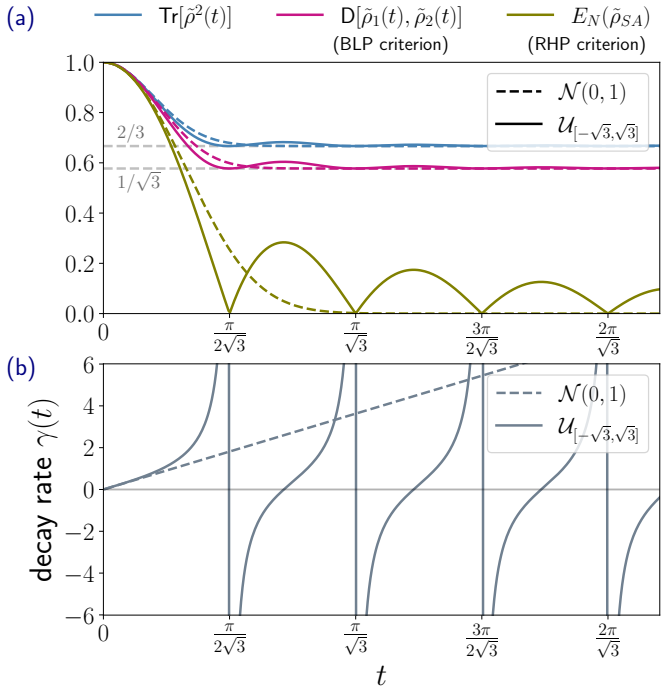

Figure 8.2. (a) Non-Markovian witnesses evaluated for the time-evolved disorder-averaged state for the case $p = 2, q = 0$ (qubit Hamiltonian) for Gaussian (dashed line) and uniform (solid line) distribution: Purity (blue), trace distance (violet), and entanglement negativity (green). All quantities are consistent with Markovian behavior for Gaussian disorder, but they show distinct non-Markovian features (revivals) for uniform disorder with a period of $\pi/2b$. (b) The decay rate in the master Eq. (8.26) also detects non-Markovianity. For the Gaussian disorder, it is always positive, indicating Markovianity, while for the uniform disorder, it assumes negative values in regions where the non-Markovian witnesses show revivals.

8.3.4 Multi-qubit operators

A multi-qubit operator such as $\hat{H}_N$ as given in Eq. (8.14) also fulfills $\hat{H}^2 \propto \mathbb{I}$. Thus, the same analytical solutions as above hold. For concreteness, we consider the multi-qubit Hamiltonian

$$\hat{H}_N = h \bigotimes_{i=1}^{N} \left(\frac{1}{\sqrt{3}} \sum_{\alpha=x,y,z} \sigma_\alpha \right)_i . \tag{8.33}$$

To illustrate the effect of increasing N, we calculate the purity for Gaussian disorder.

As the table in Fig. 8.3(a) details, the purity consists of a time-independent constant and a time-dependent part given by $G(t)$. With increasing N, the ratio between the corresponding coefficients decreases, e.g., from 2 for $N = 2$ to 5/4 for $N = 3$. The general ratio is $(3^N + 1)/(3^N - 1)$, showing that both contributions attain equal weight at $N \to \infty$. As N increases, the purity saturates at a lower value (see Fig. 8.3) and ultimately reaches 1/2 (see inset of Fig. 8.3). (Due to the special form of $\hat{H}_N$, the dynamics is non-ergodic, and the saturation value remains far from $1/2^N$, the value corresponding to a maximally mixed state.)

(a)

n	Purity
1	$(2+G^2)/3$
2	$(5+4G^2)/9$
3	$(14+13G^2)/27$
...	...
N	$\{(3^N+1)/2+(3^N-1)G^2/2\}/3^N$
∞	$(1+G^2)/2$

(b)

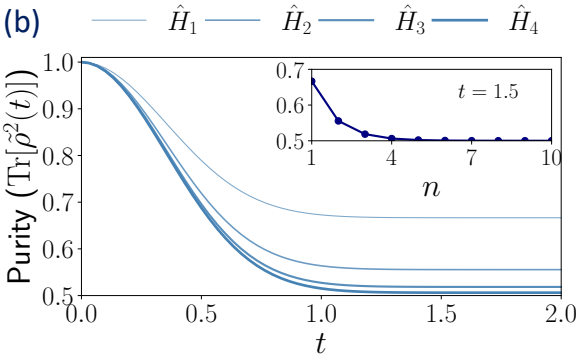

Figure 8.3. (a) Exact formulas for the purity of the disorder-averaged state under the evolution of $\hat{H}_N$ for the initial state $|\uparrow\rangle^{\otimes N}$. The ratio between the terms proportional to $\mathbb{I}\otimes\mathbb{I}$ and $\hat{H}^T\otimes\hat{H}$ is $(3^N+1)/(3^N-1)$, which approaches 1 as N increases. (b) Exact dynamics of the purity for $N = 1, 2, 3, 4$ with Gaussian disorder. As N increases, the final purity plateau approaches 1/2.

8.4 Case II: $\hat{H}^3 = h^3\mathbb{I}$

Until now, we have focused on Hamiltonians generating gates on single or multiple qubits. However, there is currently a significant drive towards developing the use of quantum-information carriers with more than $d > 2$ levels, so-called qudits [629–636]. The basic operations for qudit computations [594] are typically defined via the generalized Pauli operators, also known as Potts or clock operators in a statistical physics context. These operators present examples of (q, p)-potent Hamiltonians with $p = d, q = 0$.

Qudit operations can be defined by two generators, the shift operator τ, which moves the qudit state from $|i\rangle$ to $|i-1\rangle$, and the phase operator σ, which feeds d-different eigenvalues that are defined by the $d-$th root of unity, $\omega \equiv e^{2\pi i/d}$. In matrix form, they read

$$\sigma = \begin{pmatrix} 1 & 0 & 0 & \dots & 0 \\ 0 & \omega & 0 & \dots & 0 \\ 0 & 0 & \omega^2 & \dots & 0 \\ \vdots & \vdots & & \vdots & \\ 0 & 0 & 0 & \dots & \omega^{d-1} \end{pmatrix}, \quad \tau = \begin{pmatrix} 0 & 0 & \dots & 0 & 1 \\ 1 & 0 & \dots & 0 & 0 \\ 0 & 1 & \dots & 0 & 0 \\ \vdots & \vdots & & 0 & \vdots \\ 0 & 0 & \dots & 1 & 0 \end{pmatrix}, \tag{8.34}$$

and they fulfill the relations

$$\sigma^d = \tau^d = 1, \ \sigma^\dagger = \sigma^{d-1}, \ \tau^\dagger = \tau^{d-1}, \ \sigma\tau = \omega\tau\sigma\,. \tag{8.35}$$

Notice that the operators σ, τ are both non-Hermitian. Such non-Hermitian operators have been considered, e.g., in constructing a model of Feynman's clock [637] and in the context of topological insulators [638]. Another example of such operators also appears in the context of $\mathbb{Z}_d$ para-fermions, which have instead non-local commutation relations and can also be used for quantum computing [639]. Recently, effective non-Hermitian qudit Hamiltonians have been realized in trapped ions [640, 641].

In this chapter, for the analytical calculation's tractability, we stick to the case of

qutrits, i.e., $d = 3$. We consider a generic single qutrit Hamiltonian as a sum of both shift and phase operators,

$$\hat{H} = \frac{h}{2^{1/3}}(\sigma + \tau) = h\tilde{H}\,. \tag{8.36}$$

This Hamiltonian fulfils $\hat{H}^3 = h^3\mathbb{I}$. In this case, due to the existence of three independent operators $\{\mathbb{I}, \tilde{H}, \tilde{H}^2\}$, we can have at most 9 possible operators contributing to the evolution of the state $\tilde{\rho}(t)$. Unlike the $H^2 \propto \mathbb{I}$ case, where the terms of odd order in h vanish, in the present case, all the 9 terms contribute. For simplicity, we focus on Gaussian disorder, for which we can write the final disorder-averaged state $\tilde{\bar{\rho}}(t)$ as

$$\begin{aligned}\tilde{\bar{\rho}}(t) = \frac{1}{9}\Big[&3\left(\mathbb{I}\otimes\mathbb{I} + \tilde{H}^{*2}\otimes\tilde{H} + \tilde{H}^{*}\otimes\tilde{H}^2\right)\\ &+ \underbrace{\vec{v}(t)\cdot(1,1,1)^T}_{G_1(t)}\left(2\mathbb{I}\otimes\mathbb{I} - \tilde{H}^{*2}\otimes\tilde{H} - \tilde{H}^{*}\otimes\tilde{H}^2\right)\\ &+ \underbrace{\vec{v}(t)\cdot(1,\omega^2,\omega)^T}_{G_2(t)}\left(2\tilde{H}^{*}\otimes\tilde{H} - \tilde{H}^{*2}\otimes\mathbb{I} - \mathbb{I}\otimes\tilde{H}^2\right)\\ &+ \underbrace{\vec{v}(t)\cdot(1,\omega,\omega^2)^T}_{G_3(t)}\left(2\tilde{H}^{*2}\otimes\tilde{H}^2 - \tilde{H}^{*}\otimes\mathbb{I} - \mathbb{I}\otimes\tilde{H}\right)\Big]\,\vec{\rho}(0)\,,\end{aligned} \tag{8.37}$$

where for convenience we have defined the vector $\vec{v}(t) \equiv (e^{\frac{3}{2}\sigma^2t^2}, e^{\frac{3}{2}\omega\sigma^2t^2}, e^{\frac{3}{2}\omega^2\sigma^2t^2})$. Note, for a non-Hermitian system, the state $\tilde{\rho}$ has to be normalized by $\mathrm{Tr}(\tilde{\rho})$ in order to obtain normalized probabilities. See the derivation below for a concrete understanding.

To see how this analytical equation regulates the dynamics, we first look at $t = 0$, where $\vec{v}(0) = (1, 1, 1)$. In this limit, only the first two lines of Eq. (8.37) survive and add up to give $\mathbb{I}\otimes\mathbb{I}\,\vec{\rho}(0)$, as expected. Similar to the qubit case, we can also identify the time-dependent functions $G_1(t), G_2(t), G_3(t)$, which govern the full dynamics at $t > 0$ and which differ only by the combinations of coefficients $\{1, \omega, \omega^2\}$.

Derivation. For the case $\hat{H}^3 = h^3\mathbb{I}$, we can write more generally $H^k = h^k\tilde{H}^{k\ (\mathrm{mod}\ 3)}$. As before, the terms in Eq. (8.10) that are odd in h vanish, and thus we are left with

$$\begin{aligned}&\left[\sum_{k=0}^{2n}\binom{2n}{k}(-H^*)^{2n-k}\otimes H^k\vec{\rho}(0)\right]\\ &= \left[\sum_{k=0}^{2n}\binom{2n}{k}h^{2n}(-1)^{2n-k}\tilde{H}^{*(2n-k)\ (\mathrm{mod}\ 3)}\otimes\tilde{H}^{k\ (\mathrm{mod}\ 3)}\vec{\rho}(0)\right].\end{aligned} \tag{8.38}$$

As $\tilde{H}^3 \propto \mathbb{I}$, the dynamics is generated by $\{\mathbb{I}, \tilde{H}, \tilde{H}^2\}$ and its complex conjugates, thus when written in super-operator formalism like $B^*\otimes A$, where $A, B \in \{\mathbb{I}, \tilde{H}, \tilde{H}^2\}$, there are 9 possible terms. Now, we can use $\omega^3 = 1$, to have a closed form of the combinatorial terms,

$$\begin{aligned}
\binom{n}{0} - \binom{n}{3} + \binom{n}{6} \ldots\ldots &= \frac{0^n + (1-\omega)^n + (1-\omega^2)^n}{3} \equiv W_{(n,1)}\,, \\
-\binom{n}{1} + \binom{n}{4} - \binom{n}{7} \ldots\ldots &= \frac{1}{3}\left(\frac{\delta_{n0}}{1} + \frac{(1-\omega)^n}{\omega} + \frac{(1-\omega^2)^n}{\omega^2}\right) \equiv W_{(n,\omega)}\,, \\
\binom{n}{2} - \binom{n}{5} + \binom{n}{8} \ldots\ldots &= \frac{1}{3}\left(\frac{\delta_{n0}}{1} + \frac{(1-\omega)^n}{\omega^2} + \frac{(1-\omega^2)^n}{\omega}\right) \equiv W_{(n,\omega^2)}\,.
\end{aligned} \tag{8.39}$$

Using the above simplifications, the disorder-averaged density matrix is

$$\begin{aligned}
\tilde{\rho}(t) = \sum_{n=0}^{\infty} \Bigg[&\frac{(-it)^{6n}}{(6n)!}\mathbb{E}[h^{6n}]\Big\{W_{(6n,1)}\mathbb{I}\otimes\mathbb{I} + W_{(6n,\omega)}\tilde{H}^{*2}\otimes\tilde{H} + W_{(6n,\omega^2)}\tilde{H}^{*}\otimes\tilde{H}^2\Big\} \\
&+ \frac{(-it)^{6n+2}}{(6n+2)!}\mathbb{E}[h^{6n+2}]\Big\{W_{(6n+2,1)}\tilde{H}^{*2}\otimes\mathbb{I} + W_{(6n+2,\omega)}\tilde{H}^{*}\otimes\tilde{H} + W_{(6n+2,\omega^2)}\mathbb{I}\otimes\tilde{H}^2\Big\} \\
&+ \frac{(-it)^{6n+4}}{(6n+4)!}\mathbb{E}[h^{6n+4}]\Big\{W_{(6n+4,1)}\tilde{H}^{*}\otimes\mathbb{I} + W_{(6n+4,\omega)}\mathbb{I}\otimes\tilde{H} + W_{(6n+4,\omega^2)}\tilde{H}^{*2}\otimes\tilde{H}^2\Big\}\Bigg]\vec{\rho}(0)\,.
\end{aligned} \tag{8.40}$$

Using $(1-\omega)^{6n} = (-3)^{3n}$ in Eq. (8.39), we can further simplify the $W(6n,\cdot)$ terms,

$$\begin{aligned}
W_{(6n,1)} &= \frac{\delta_{n0} + 2(-3)^{3n}}{3}, \quad W_{(6n,\omega)} = W_{(6n,\omega^2)} = \frac{\delta_{n0} - (-3)^{3n}}{3}, \\
W_{(6n+2,1)} &= W_{(6n+2,\omega^2)} = \frac{-(-3)^{3n+1}}{3}, \quad W_{(6n+2,\omega)} = \frac{2(-3)^{3n+1}}{3}, \\
W_{(6n+4,1)} &= W_{(6n+4,\omega)} = \frac{-(-3)^{3n+2}}{3}, \quad W_{(6n+4,\omega^2)} = \frac{2(-3)^{3n+2}}{3}\,.
\end{aligned} \tag{8.41}$$

Note, the δ_{n0} terms in the coefficients corresponding to the operators $\mathbb{I}\otimes\mathbb{I}, \tilde{H}^{*2}\otimes\tilde{H}, \tilde{H}^{*}\otimes\tilde{H}^2$ are responsible for the time-independent terms in Eq. (8.37). The factor of 2 in front of $\mathbb{I}\otimes\mathbb{I}$, $\tilde{H}^{*}\otimes\tilde{H}$ and $\tilde{H}^{*2}\otimes\tilde{H}^2$, and -1 in all the other terms of the time-dependent part are also due to the above relation in Eq. (8.41). Now, we need to simplify the time-dependent term along with disorder-averaging $\mathbb{E}[h^{\#}]$. In the case of uniform disorder, the result can be expressed in terms of a hypergeometric function. For Gaussian disorder, using $\mathbb{E}[h^{2n}] = \sigma^{2n}(2n-1)!!$, one obtains rather compact expressions such as

$$\begin{aligned}
\sum_{n=0}^{\infty}\frac{(-it)^{6n}}{(6n)!}\mathbb{E}[h^{6n}] &= \sum_{n=0}^{\infty}\frac{(-it)^{6n}}{(6n)!}\sigma^{6n}(6n-1)!! \\
&= \sum_{n=0}^{\infty}\frac{(-i\sigma t)^{6n}}{(6n)!!} = \sum_{n=0}^{\infty}\frac{(-\sigma^2t^2)^{3n}}{2^{3n}(3n)!} = \sum_{n=0}^{\infty}\frac{(-\frac{1}{2}\sigma^2t^2)^{3n}}{(3n)!}\,,
\end{aligned} \tag{8.42}$$

and similarly for the terms with $3n$ replaced by $3n+1$ and $3n+2$. The resulting infinite series can be expressed as the sum of three exponentials having permutations of $(1,\omega,\omega^2)$ in the exponents,

$$\sum_{n=0}^{\infty}\frac{x^{3n+j}}{(3n+j)!} = \frac{e^x + \omega^{2j}e^{\omega x} + \omega^{4j}e^{\omega^2 x}}{3}\,, \quad \text{for } j = 0,1,2\,, \tag{8.43}$$

These relations allow us to express the three time-dependent functions G_1, G_2, G_3 in terms of $\vec{v} = (e^x, e^{\omega x}, e^{\omega^2 x})$ and the three vectors $(1,1,1)^T$, $(1,\omega^2,\omega)^T$, $(1,\omega,\omega^2)^T$, leading to the Eq. (8.37) describing the disorder-averaged time evolution of a qutrit.

In Fig. 8.4a, we plot the expectation value of a Hermitian observable, the spin-1 magnetization $S_z = \mathrm{Diag}(1, 0, -1)$ [see Eq. (8.47)] with an initial statevector $|\psi_0\rangle = (1, 0, 0)^T$. Its time evolution can be analytically expressed as

$$\frac{\mathrm{Tr}(S_z\tilde{\rho}(t))}{\mathrm{Tr}(\tilde{\rho}(t))} = \frac{12 + 2G_1 - 2^{5/3}G_3}{15 + e^{\frac{3}{2}\sigma^2 t^2} + 2^{\frac{4}{3}}G_2 + 2^{\frac{2}{3}}G_3}\,, \tag{8.44}$$

which can be compared to the evolution of σ_z in the Hermitian qubit case, see Eq. (8.25). Again, the evolution averaged over the Gaussian distribution decreases monotonically. The numerical average over 10^4 trajectories agrees qualitatively with the analytical prediction for the average, but even at 10^7 independent samples, slight deviations are still visible at the longest times of $t \sim 3$ considered.

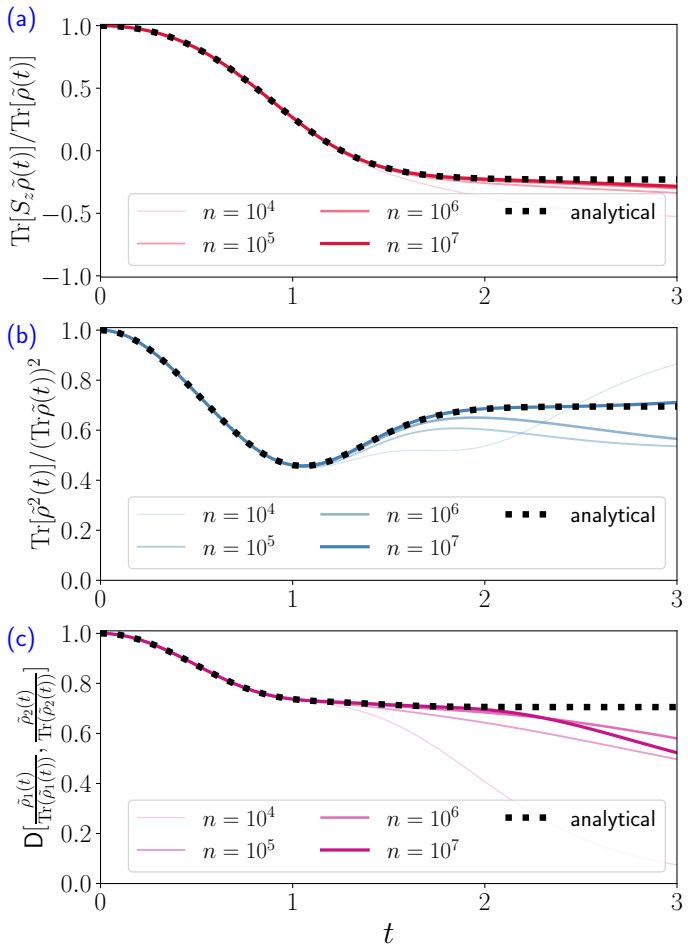

Figure 8.4. (a) The magnetization of the disorder-averaged qutrit state reaches a plateau for Gaussian disorder, whereas (b) the purity reaches a dip around $t \simeq 1$, followed by an increase and a final plateau. However, the dynamical map being non-unital, it does not witness non-Markovianity. (c) The trace distance does not witness non-Markovianity, as it decays monotonically, without any revival. Beyond very early times, for all the quantities of magnetization, purity, and trace distance, the numerical average converges to the analytical solution only when using a large number of disorder realizations.

Moreover, we calculate the purity of the normalized state [642],

$$\begin{aligned}\frac{\mathrm{Tr}[\tilde{\rho}^2(t)]}{(\mathrm{Tr}\tilde{\rho}(t))^2} =& 3\Big(81 - 6G_1 + 6\cdot 2^{1/3}G_2 + 5G_1^2 + 4\cdot 2^{2/3}G_2^2 \\ &+ 6\cdot 2^{1/3}G_3^2 - 2^{4/3}G_1G_2 - 4G_2G_3 - 2^{8/3}G_1G_3\Big) \\ &/\left(15 + e^{\frac{3}{2}\sigma^2 t^2} + 2^{\frac{4}{3}}G_2 + 2^{\frac{2}{3}}G_3\right)^2 .\end{aligned} \tag{8.45}$$

As we can see in Fig. 8.4b, the purity has a dip around $t \simeq 1$, after which it rises again to finally saturate in a plateau (we have checked that the dip does not derive

from the normalization, which monotonically increases in time as an exponential). This behavior is unlike the qubit case, where the purity of the averaged state monotonically decays. In contrast to the qubit case, the dynamical map generated by the non-Hermitian qutrit Hamiltonian ensemble is non-unital (see Section 8.6), meaning that the non-monotonic behavior of the purity in this case is not a good witness for non-Markovianity. To study a potential non-Markovianity, we also plot the trace distance in Fig. 8.4c. Its monotonous decay with time is compatible with a Markovian evolution.

These quantities do, however, illustrate an interesting aspect: Even at 10^6 independent disorder samples, considerable deviations become visible already at around $\sim 1.75 - 2$. With 10^7 samples, the purity reaches good convergence during the time frame considered, while the trace distance continues to display significant deviations. As this example shows, a vast number of realizations can be needed to match the numerical ensemble average to the analytical predictions, even for relatively short times. Thus, even in simple systems, it can be a considerable asset to be able to analytically extract converged results without the need for extensive numerical averaging.

8.5 Case III: $\hat{H}^3 = h^2\hat{H}$

In the examples above, we have considered cases where finite powers of the Hamiltonian return to $\mathbb{I}$. As mentioned in Sec. 8.2.2, we can derive similar analytical predictions also in the case when $\hat{H}^p = h^q\hat{H}^q$, with $q < p$. In this section, we illustrate this possibility for $\hat{H}^3 = h^2\hat{H}$, i.e., $p = 3$ and $q = 1$. The simplest instance of this case is given by 3×3 matrices describing spin-1 operators, S_α, $\alpha = x, y, z$. They follow the commutation relations $[S_\alpha, S_\beta] = i\hbar\epsilon_{\alpha\beta\gamma}S_\gamma$ [643], and we choose the matrix representation

$$S_x = \frac{1}{\sqrt{2}}\begin{pmatrix} 0 & 1 & 0 \\ 1 & 0 & 1 \\ 0 & 1 & 0 \end{pmatrix}, S_y = \frac{1}{\sqrt{2}}\begin{pmatrix} 0 & -i & 0 \\ i & 0 & -i \\ 0 & i & 0 \end{pmatrix}, S_z = \begin{pmatrix} 1 & 0 & 0 \\ 0 & 0 & 0 \\ 0 & 0 & -1 \end{pmatrix}. \tag{8.46}$$

Interestingly, these spin-1 operators also form a universal basis for qutrit computation [490, 497, 644]. However, they follow a different symmetry than the qutrit or Potts operators. In particular, they are Hermitian, and they obey $(S_\alpha)^3 = S_\alpha$. It is, therefore, interesting to investigate the difference in the time-evolution these operators generate after disorder averaging.

In similarity to the qubit case, Eq. (8.13), we choose a Hamiltonian describing a rotation around a specific axis,

$$\hat{H} = \frac{h}{\sqrt{3}}(S_x + S_y + S_z) \Rightarrow \hat{H}^3 = h^2\hat{H}\,. \tag{8.47}$$

Using similar techniques to the previous cases, we can write down the final equation,

$$\begin{aligned}\tilde{\vec{\rho}}(t) = \Big[&\mathbb{I}\otimes\mathbb{I} + (G'-1)\left\{\tilde{H}^{*2}\otimes\mathbb{I} + \mathbb{I}\otimes\tilde{H}^2\right\} \\ &+ \frac{1}{2}(1-G)\,\tilde{H}^*\otimes\tilde{H} + \frac{1}{2}(3+G-4G')\,\tilde{H}^{*2}\otimes\tilde{H}^2\Big]\vec{\rho}(0)\,,\end{aligned} \tag{8.48}$$

where G is identical to the qubit case (Tab. 8.1), and G' has a similar form as G but with $t \to t/2$.

Derivation. As in the previous cases, terms of odd order in h vanish. Thus, starting from the Eq. (8.10), we are left with

$$\sum_{n=0}^{\infty} \frac{(-iht)^{2n}}{(2n)!} \left[\sum_{k=0}^{2n} \binom{2n}{k} (-\tilde{H}^*)^{2n-k} \otimes \tilde{H}^k \right] . \tag{8.49}$$

One can consider the terms $n = 0, 1, 2, \ldots$ one by one and, by putting the terms together, can find the following equation:

$$\begin{aligned} &\mathbb{I} \otimes \mathbb{I} + \sum_{n=1}^{\infty} \frac{(-iht)^{2n}}{(2n)!} \underbrace{\binom{2n}{0}}_{=1} \tilde{H}^{*2} \otimes \mathbb{I} - \sum_{n=1}^{\infty} \frac{(-iht)^{2n}}{(2n)!} \underbrace{\sum_{k=0}^{n-1} \binom{2n}{2k+1}}_{=2^{2n-1}} \tilde{H}^* \otimes \tilde{H} \\ &+ \sum_{n=2}^{\infty} \frac{(-iht)^{2n}}{(2n)!} \underbrace{\sum_{k=1}^{n-1} \binom{2n}{2k}}_{=2^{2n-1}-2} \tilde{H}^{*2} \otimes \tilde{H}^2 + \sum_{n=1}^{\infty} \frac{(-iht)^{2n}}{(2n)!} \underbrace{\binom{2n}{2n}}_{=1} \mathbb{I} \otimes \tilde{H}^2 . \end{aligned} \tag{8.50}$$

For the Gaussian disorder case, using Eq. (8.18), disorder averaging yields

$$\begin{aligned} &\mathbb{I} \otimes \mathbb{I} + \left(e^{-\sigma^2 t^2/2} - 1 \right) \tilde{H}^{*2} \otimes \mathbb{I} - \frac{1}{2} \left(e^{-2\sigma^2 t^2} - 1 \right) \tilde{H}^* \otimes \tilde{H} \\ &+ \frac{1}{2} \left(3 + e^{-2\sigma^2 t^2} - 4 e^{-\sigma^2 t^2/2} \right) \tilde{H}^{*2} \otimes \tilde{H}^2 + \left(e^{-\sigma^2 t^2/2} - 1 \right) \mathbb{I} \otimes \tilde{H}^2 . \end{aligned} \tag{8.51}$$

For the uniform disorder case, using Eq. (8.22), we obtain

$$\begin{aligned} &\mathbb{I} \otimes \mathbb{I} + \left(\frac{\sin bt}{bt} - 1 \right) \tilde{H}^{*2} \otimes \mathbb{I} - \frac{1}{2} \left(\frac{\sin 2bt}{2bt} - 1 \right) \tilde{H}^* \otimes \tilde{H} \\ &+ \frac{1}{2} \left(3 + \frac{\sin 2bt}{2bt} - 4 \frac{\sin bt}{bt} \right) \tilde{H}^{*2} \otimes \tilde{H}^2 + \left(\frac{\sin bt}{bt} - 1 \right) \mathbb{I} \otimes \tilde{H}^2 . \end{aligned} \tag{8.52}$$

Thus, we obtain the Eq. (8.48) with two time-dependent functions $G(t)$ and $G'(t)$.

Choosing the initial statevector $|\psi_0\rangle = (1, 0, 0)^T$, the expectation value of S_z and the purity take the following forms:

$$\begin{aligned} \mathrm{Tr}(S_z \tilde{\rho}(t)) &= \frac{1}{3} \left(1 + 2G'(t) \right) , \\ \mathrm{Tr}(\tilde{\rho}^2(t)) &= \frac{1}{18} \left(9 + G^2(t) + 8G'^2(t) \right) . \end{aligned} \tag{8.53}$$

Figures 8.1 and 8.5 respectively compare the time-evolution for both quantities for the Gaussian and uniform distribution. For the Gaussian distribution, both observables monotonously decay to a plateau. The one of the magnetization, $\mathrm{Tr}(S_z \tilde{\rho}(t \to \infty)) = 1/3$, matches with the long-time plateau obtained in the qubit case, see Eq. (8.25), although the approach towards it is delayed, as it is governed by $G'(t)$ in the case of

spin-1 instead of $G(t)$ as was the case for qubits. For the uniform distribution, both the magnetization and purity of the disorder-averaged state oscillate, with a period that is twice that of the qubit case (see Fig. 8.1 for magnetization, and Fig. 8.2 and 8.5 for purity). In the long-time limit, the oscillation dies out, and the dynamics approach the plateau obtained in the case of Gaussian disorder. As discussed in Sec. 8.2.3, as the map in the present case is unital (see Section 8.6), the oscillations of the purity indicate an emergent non-Markovianity of the averaged time evolution.

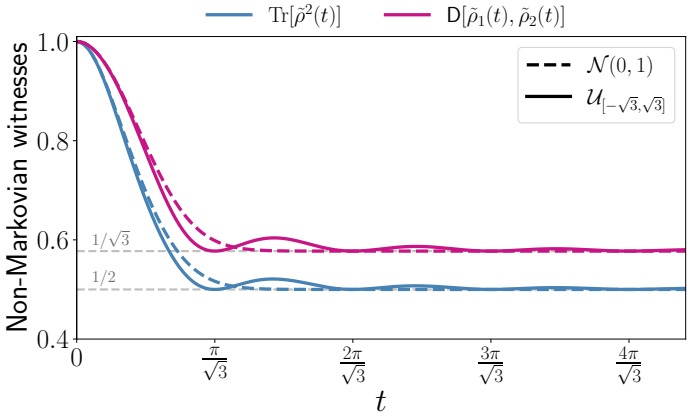

Figure 8.5. Time evolution of purity and trace distance of the disorder-averaged state for Gaussian (dashed line) and uniform (solid line) distribution. The time scales governing the evolution are twice those of the corresponding qubit dynamics (Fig. 8.2).

8.6 Unitality of the dynamical maps

A dynamical map is called unital when $\Lambda_t[\mathbb{I}] = \mathbb{I}$, i.e., a fully mixed state remains fully mixed. Here, Λ_t acts on the density matrix, not on its vectorized form. We now show that the map for the qubit and spin-1 cases is unital, while it is non-unital for the non-Hermitian qutrit case considered.

Case I: For the qubit case, from Eq. (8.15) we have

$$\Lambda_t[\mathbb{I}] = \left(\frac{1+G(t)}{2}\right)\mathbb{I} + \left(\frac{1-G(t)}{2}\right)\tilde{H}\mathbb{I}\tilde{H}^\dagger = \mathbb{I}\,, \tag{8.54}$$

where we used the fact that $\tilde{H}^\dagger = \tilde{H}$ and $\tilde{H}^2 = \mathbb{I}$, showing that the dynamical map for the qubit system is unital. Hence, purity can act as a non-Markovian witness (see Fig. 8.2 and behaves similarly to trace-distance).

Case II: For the qutrit ($\mathbb{Z}_3$) case, from Eq. (8.37) we have

$$\begin{aligned}\Lambda[\mathbb{I}] = \frac{1}{3}\left(\mathbb{I} + \tilde{H}\tilde{H}^{\dagger 2} + \tilde{H}^2\tilde{H}^\dagger\right) + \frac{G_1(t)}{9}\left(2\mathbb{I} - \tilde{H}\tilde{H}^{\dagger 2} - \tilde{H}^2\tilde{H}^\dagger\right)\\ + \frac{G_2(t)}{9}\left(2\tilde{H}\tilde{H}^\dagger - \tilde{H}^{\dagger 2} - \tilde{H}^2\right) + \frac{G_3(t)}{9}\left(2\tilde{H}^2\tilde{H}^{\dagger 2} - \tilde{H}^\dagger - \tilde{H}\right).\end{aligned} \tag{8.55}$$

As all the coefficients of $G_i(t)$ (in the bracket) remain non-zero, the dynamical map corresponding to a qutrit is non-unital. Hence, purity can not act as a non-Markovian witness (see Fig. 8.4 that purity behaves differently from trace-distance).

Case III: For the spin-1 case, from Eq. (8.48) we have

$$\begin{aligned}\Lambda_t[\mathbb{I}] = \mathbb{I} &+ (G'-1)(\tilde{H}^{\dagger 2} + \tilde{H}^2) \\ &+ \frac{1}{2}(1-G)\tilde{H}\tilde{H}^\dagger + \frac{1}{2}(3+G-4G')\tilde{H}^2\tilde{H}^{\dagger 2}\,.\end{aligned} \tag{8.56}$$

Note that $\tilde{H}^{\dagger 2} + \tilde{H}^2 - 2\tilde{H}^2\tilde{H}^{\dagger 2} = 0$ and $\tilde{H}^2\tilde{H}^{\dagger 2} - \tilde{H}\tilde{H}^\dagger = 0$ as $\tilde{H}^\dagger = \tilde{H}$ and $\tilde{H}^3 = \tilde{H}$. Thus, we can rewrite the above equation as

$$\Lambda_t[\mathbb{I}] = \mathbb{I} - (\tilde{H}^{\dagger 2} + \tilde{H}^2) + \frac{1}{2}\tilde{H}\tilde{H}^\dagger + \frac{3}{2}\tilde{H}^2\tilde{H}^{\dagger 2} = \mathbb{I}\,, \tag{8.57}$$

and thus the dynamical map for the spin-1 system is unital. Hence, purity can act as a non-Markovian witness (see Fig. 8.5 that purity behaves similarly to trace-distance).

8.7 Summary

In this chapter, we have derived an exact equation for the disorder-averaged dynamics of periodic Hamiltonians, independent of the initial states, applicable for Hermitian and non-Hermitian systems, and valid for arbitrary evolution times. These equations rely not on the specific representation of the Hamiltonians but rather only on their (q,p)-potency class as defined by the relation $\hat{H}^p \propto \hat{H}^q$. The effect of the disorder is then entirely captured in a few analytic functions derived from the disorder moments, which can be easily exchanged in the final equations according to the disorder at hand. This analytic approach significantly reduces the numerical overhead typically associated with disorder averaging. As often occurs in such a scenario [200, 201, 577–583], the disorder averaging induces open-system-like dynamics even in inherently closed systems. In cases where the equation defining the time-evolved state can be inverted, we have also derived a master equation governing the disorder-averaged system dynamics. Moreover, even without a formal master equation, we have shown how non-Markovian characteristics emerge as a function of the disorder distribution and its strength. These factors determine the periodicity of revivals observed in non-Markovian witnesses. Such phenomena could be leveraged when using an ensemble of disordered Hamiltonians to simulate open system dynamics [582, 645] as well as for applications in quantum-information processing [200, 201, 625–628]. It is an interesting question to ask what it means to witness non-Markovianity in a closed system without a genuine bath, and how the associated backflow of information should be interpreted.

The analytic expressions may help form a better understanding of errors in quantum computing by enabling insights into noise modeling or aiding in reverse-engineering disorder distributions tailored for specific applications. Another application can be in qudit-based quantum computations, where the effect of the disorder depends not only on the hardware implementation but also on the specific representation of the qudit operator. It thus becomes crucial to investigate which combinations of qudit dimension d, related to q, p, and disorder distributions $P(h)$ offer better resilience against decay caused by averaging over uncontrolled disorder in the qudit gates. Finally, in the context of optimal control, the optimal gate pulses for noisy hardware can be modified, knowing the decay rate caused by specific errors [646]. Beyond an intrinsic interest in analytic solutions to disorder problems, such investigations could thus guide the development of more robust quantum computing systems.

Chapter 9

Complexity transitions in chaotic quantum systems

complexity or resources are not one-size-fits-all

9.1 Introduction

The interplay between interactions and disorder [564] in quantum many-body systems gives rise to complex systems with extremely rich phenomenology, characterized by varying degrees of chaoticity and ergodicity [647, 648, 648–651]. Although analytical approaches are available in certain limits of ergodic [652–655] and localized regimes [656–659], and while quantum simulations [75, 90, 318, 660] have explored various regimes of disordered interacting systems [661–668], their treatment remains a significant challenge both for theory and experiment. In order to translate that difficulty into a measurable quantity, various notions have been proposed [91, 669–671]. Notable examples of such "complexity markers" include entanglement entropy [672] and stabilizer Rényi entropy [169], which have clear implications both for the difficulty of numerically treating [91, 154, 167, 542, 673–677] the system under study as well as for the quantum resources [47] an experiment needs in order to generate the target state [678, 679]. Such markers are also deeply connected to the question of what actually defines a quantum system as complex [172, 176, 680–682]. As a disordered quantum many-body system enters into respectively less ergodic and more localized regimes, the number of basis states involved is reduced (see Fig. 9.1**b**), suggesting intuitively a suppression of quantum complexity. As of yet, it remains, however, an open question how precisely ergodicity transitions are related to changes in complexity markers, and in particular, whether these define qualitatively different complexity regimes.

In this chapter, we map out complexity quantifiers (see Fig. 9.1) in prototypical disordered models that exhibit multiple distinct regimes: the Rosenzweig–Porter (RP) model [683, 684], the Power-Law Random Banded Matrix (PLRBM) model [685], and the Sachdev–Ye–Kitaev (SYK) [686, 687] model coupled to an Ising chain (see Fig. 9.3). The RP and PLRBM are paradigmatic models of chaotic systems that interpolate between ergodic and non-ergodic regimes, and they are central to the understanding of Anderson localization [558, 688] and (multi)fractal states [656, 689, 690]. The SYK model is a prototypical example of a maximally chaotic quantum many-body system [691], which plays a key role in the phenomenological description of non-Fermi liquid behavior [686, 692] and in the study of quantum black holes through the holographic principle [693, 694]. We scrutinize these models using three different markers of complexity: (i) The fractal dimension [695–699], a key observable for identifying

localized regions and mobility edges, quantifies how much a state is spread over a computational basis. (ii) The entanglement entropy across half–half bipartitions estimates a state's quantumness in terms of its inability to be expressed as a direct product state [91]. However, not all entangled states are computationally challenging. An outstanding example is the class of stabilizer states, which contain highly-entangled states but can be tackled efficiently classically thanks to the Gottesman–Knill theorem [149,150]. In contrast, non-stabilizer states fall outside this framework and are exponentially hard to represent on a classical computer. To capture this distinction, we use as the third measure (iii) the nonstabilizerness [85] (or "magic") of a state, quantified through the stabilizer Rényi entropy (SRE) [169]. While the fractal dimension and entanglement entropy have been instrumental in characterizing non-ergodic quantum systems already for some time [685,700–702], magic is currently emerging as a powerful tool in various contexts, including the study of ergodicity [168,521,524,703–706], quantum chaos [525,707,708], and as a sensitive probe for identifying quantum phase transitions [518,526,528,709–712].

In our work, we find that all three complexity markers show sharp phase transitions, separating regimes of different levels of complexity. Notably, the phase transition points are distinct when an extended fractal phase is present, as in the bulk of the RP spectrum. In contrast, when such a phase is absent, as in the ground state of the RP model, all considered markers detect the transition points close to each other, see Fig. 9.1**c**. Furthermore, an analysis of the SYK_4+Ising model reveals that the SRE exhibits a richer structure than the other markers and, in particular, is significantly more sensitive to underlying symmetries of the many-body systems, such as fermion parity and time reversal. Overall, this comparative analysis suggests that no single marker can independently describe all relevant regimes of the system, which may undergo distinct complexity transitions. These results not only yield insights into the physics of disordered quantum many-body systems but also help identify the complexity marker best suited to capture the computational hardness across different phases [676,677,682,713,714], guiding the selection of appropriate simulation methods.

Finally, our studies complement ongoing research on several complexity markers in ergodic and integrable/localized systems, including Krylov complexity [715–719], logarithmic multifractality [640], operator spreading [720], holographic complexity [721], or quantum-computational complexity [722].

The remainder of the chapter is structured as follows. In Sec. 9.2, we present the complexity markers used to characterize the various quantum phases explored in this study. In Secs. 9.3 and 9.4, we apply these markers to analyze random matrix models, specifically the Rosenzweig–Porter model and the power-law random banded matrix model. In Sec. 9.5, we investigate the Sachdev–Ye–Kitaev model interpolated towards the integrable Ising model. Our main findings and possible future research directions are presented in Sec. 9.8. We also find that the self-averaging properties of the considered complexity markers (Section 9.6.2) can also detect similar phase transitions.

9.2 Complexity markers

A plethora of different approaches exists to simulate quantum states, each with varying regimes of validity and efficiency, making it essential to scrutinize the complex-

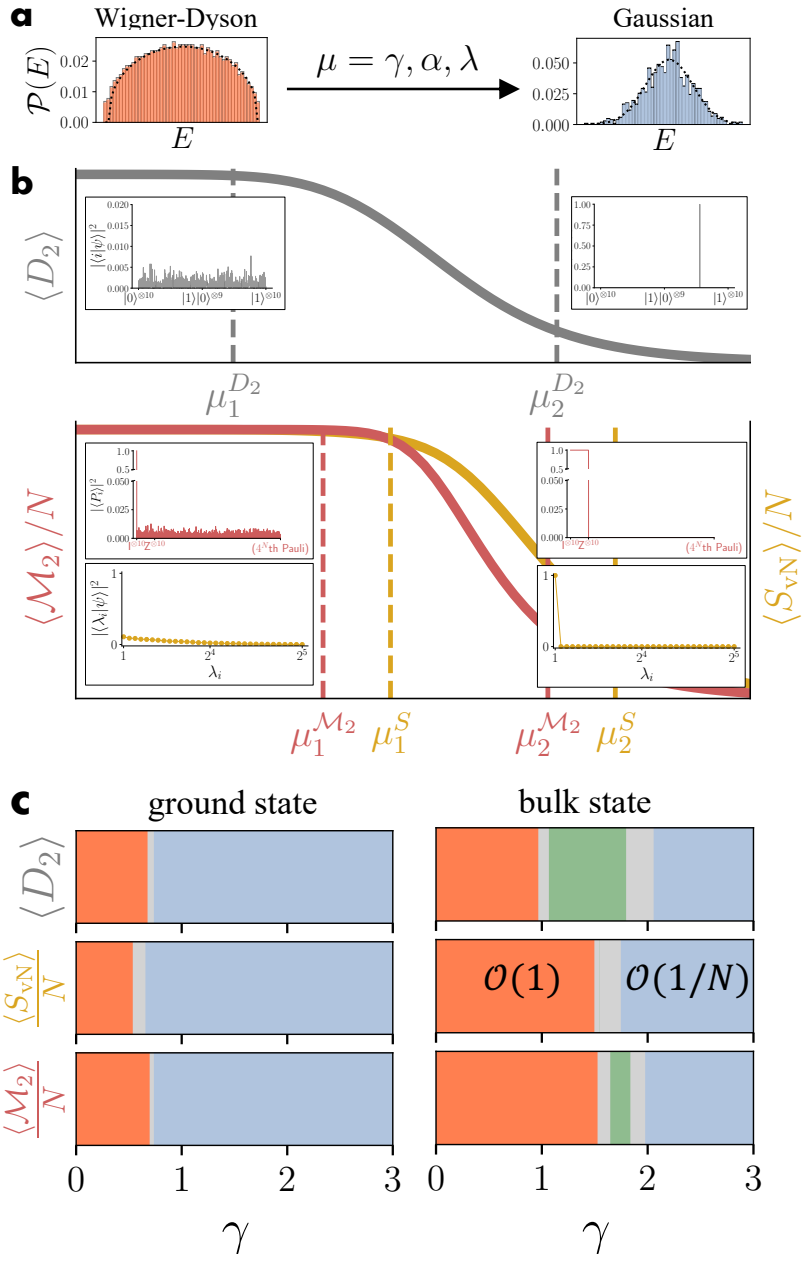

Figure 9.1. Complexity markers across a transition from a chaotic (ergodic) to an integrable (localized) phase. **(a)** As the control parameter μ drives a random matrix model towards localization, the eigenvalue distribution evolves from the Wigner–Dyson semicircle to a Gaussian profile. **(b)** Comparison of three complexity markers (data for the RP model). A high (low) fractal dimension D_2 indicates delocalization (localization) in the computational basis. High (low) magic $\mathcal{M}_2$ implies support over an extensive set of 4^N Pauli strings (concentration on a limited subset). Strong (weak) entanglement S_{vN} reflects high (low) Schmidt rank and the presence of many (few) computational basis states in the superposition. While all three markers feature a high-complexity regime, the transition towards intermediate- or low-complexity regimes can happen at distinct points ($\mu_{1,2}^{D_2} \neq \mu_{1,2}^{\mathcal{M}_2} \neq \mu_{1,2}^{S}$). Regimes of different complexity thus overlap but do not coincide. **(c)** The phase transition points in the RP model, obtained through finite-size scaling analysis, differ across the three complexity markers (orange: high [$\mathcal{O}(1)$] complexity; green: intermediate; blue: low complexity [$\mathcal{O}(1/N)$]). Faded regions indicate numerical uncertainty in determining regime boundaries. Notably, the ground state exhibits a sharp transition directly from high to low complexity, bypassing the intermediate regime. In contrast, bulk eigenstates display a well-defined intermediate phase, with a significant variation in transition points across the considered markers.

ity of quantum states through multiple markers. This section introduces the main markers we will employ to analyze how the system evolves from an ergodic to an integrable/localized regime, the fractal dimension, the maximal entanglement entropy, and the stabilizer Rényi entropy (SRE).

9.2.1 Fractal dimension

The fractal dimension can be derived from the inverse participation ratio (IPR), and quantifies the spread of the wavefunction in a given basis, which in our case will be provided by the computational basis states $\{|i\rangle\}_{i=1}^{L}$, L being the Hilbert space dimension. Fractal dimension and IPR are commonly used markers to investigate many-body localization [651, 688, 690, 695, 699], as a state that has support on just a few elements of the basis will be in the localized phase, while an ergodic wavefunction will be spread over many states of any generic basis, as shown in Fig. 9.1**b**. In computational terms, a highly localized state implies a smaller part of the Hilbert space needs to be handled, making it easier to simulate classically [723, 724].

For a wavefunction $|\psi\rangle$ expressed in terms of the computational basis with coefficients $\psi(i) = \langle i|\psi\rangle$, the q^{th} IPR is defined as

$$I_q(\psi) = \sum_{i=1}^{L} |\psi(i)|^{2q}, \qquad q > 1, \tag{9.1}$$

where $L = 2^N$ is the Hilbert space dimension for a space of N qubits. The fractal dimension D_q is defined from the IPR as [696–698]

$$D_q = \lim_{L\to\infty} \frac{\log_L(I_q)}{(1-q)}. \tag{9.2}$$

Typically, one considers $L \gg 1$ and the limit is dropped, such that the fractal dimension is given by

$$D_q = \frac{\log_2(I_q)}{N(1-q)}. \tag{9.3}$$

When the wavefunction ψ is confined to a small region of the Hilbert space, the system is considered to be in the localized phase, marked by $D_q = 0$ in the thermodynamic limit. For a fully extended state, in contrast, where the wavefunction spreads uniformly over all basis states, one obtains $D_q = 1$. States in the ergodic phase, however, are usually not entirely uniformly distributed. Instead, they can be approximated by Haar-random states[1], which do not saturate the fractal dimension for finite system sizes. For $q = 2$, the corresponding fractal dimension is given by [725]

$$D_2^{\text{Haar}} = -\frac{1}{N}\log_2\left(\frac{2}{2^N+1}\right). \tag{9.4}$$

For $N \to \infty$, one recovers $D_2^{\text{Haar}} \to 1$. For non-extended states, as are expected to occur in non-ergodic but delocalized phases, just a fraction of the volume will be occupied, and we will have $D_q < 1$. If D_q is a constant across all values of q, the state

[1] A Haar random state refers to a quantum state that is sampled uniformly at random from the set of all possible pure quantum states in a given Hilbert space, according to the Haar measure.

is called single-fractal (or just fractal), which is the case for the Rosenzweig–Porter model in the non-ergodic extended regime [689]. In the general case, D_q is a function of q. Such a state is called multi-fractal. An example occurs in the power-law random banded model at the Anderson transition [685, 688]. Here, we focus on $q = 2$ only.

9.2.2 Entanglement entropy

The second marker we consider is the entanglement entropy maximized with respect to all possible equal-sized (half–half) bipartitions of the state in the computational basis. The maximal entanglement entropy is a key measure of quantum correlations between subsystems. The presence of entanglement has been identified as one of the first limitations for efficient classical simulations of quantum states [154, 726, 727], and entanglement entropy provides an estimate of the bond dimension required in tensor-network methods [91, 542, 673, 674]. Moreover, it is widely used to probe many-body localization and quantum phase transitions [728–732].

Given a bipartition of the Hilbert space $\mathcal{H} = \mathcal{H}_A \otimes \mathcal{H}_B$ and a pure state $|\psi\rangle \in \mathcal{H}$, the von Neumann entropy is defined as $S(\rho_A) = -\mathrm{Tr}(\rho_A \log \rho_A)$, with $\rho_A = \mathrm{Tr}_B |\psi\rangle \langle\psi|$ the reduced density matrix for subsystem A. The maximal entanglement entropy is then defined as the von Neumann entropy maximized over all possible half–half bipartitions of the system,

$$S_{\max} = \max_{L_A = \lfloor N/2 \rfloor} S(\rho_A) \,. \tag{9.5}$$

For Haar-random states, the entanglement entropy follows the Page curve [733], which for $L_A \leq L_B$ reads

$$S^{\mathrm{page}}_{L_A, L_B} = \sum_{k=L_B+1}^{L_A L_B} \left(\frac{1}{k}\right) - \frac{L_A - 1}{2L_B} \,, \tag{9.6}$$

where $L_{A,B}$ is the Hilbert space dimension of $\mathcal{H}_{A,B}$. In this chapter, we work in the convention where logarithms are in base 2, so that $S^{\mathrm{page}}_{L_A, L_B}/N \approx \frac{1}{2}$ in the large-N limit.

9.2.3 Stabilizer Rényi entropy (SRE)

The last complexity marker we consider is the stabilizer Rényi entropy (SRE). Recall from Sec. 2.7.5 that the SRE captures how a state is distributed when expressed in the basis of Pauli operators $P \in \mathcal{P}_N$, where $\mathcal{P}_N$ represents the Pauli group for n-qubits. Stabilizer states, which are common eigenstates of a maximal set of mutually commuting Pauli operators, exhibit a highly concentrated probability distribution of the Pauli expectation values, confined to a subset of 2^N operators, and thus are easily simulable [148, 149, 151, 158, 166, 167]. In contrast, a Haar-random state has approximately equal weight on all P's [168]. Thus, a natural way to quantify the nonstabilizerness of a state $|\psi\rangle$ is by assessing the spread of this distribution using the q-th order stabilizer Rényi entropy,

$$\mathcal{M}_q(\psi) = \frac{1}{1-q} \log_2 \sum_{P \in \mathcal{P}_N} \frac{|\langle\psi|P|\psi\rangle|^{2q}}{2^N} \,. \tag{9.7}$$

In this work, we will use the second-order Rényi entropy, $q = 2$. The SRE vanishes for a stabilizer state and grows as the state exhibits increasing degrees of magic.

SRE in Haar-random states

For unitary-invariant Haar-random states, the expectation value of Pauli strings can be easily calculated analytically by averaging over Haar-random states. Using the formula [734]

$$\int |\psi\rangle \langle\psi|^{\otimes k} \, d\psi = \frac{(L-1)!}{(L+k-1)} \sum_{\pi \in S_k} W_\pi \,, \tag{9.8}$$

where S_k is the permutation group and W_π is the replica-permutation operator and $L = 2^N$, we find

$$\int |\langle\psi| P_i |\psi\rangle|^2 d\psi = \begin{cases} 1 & i = 0, \\ \frac{1}{2^N+1} & i \neq 0. \end{cases} \tag{9.9}$$

The stabilizer Rényi entropy (SRE) can be calculated using similar techniques [168] and takes the following analytical forms depending on the ensemble with respect to which the Haar measure is invariant:

$$\begin{aligned} \mathcal{M}_2^{\text{Haar}}(\text{GUE}) =& \mathcal{M}_2^{\text{Haar}}(\text{GSE}) = -\log_2\left(\frac{4}{3+2^N}\right), \\ \mathcal{M}_2^{\text{Haar}}(\text{GOE}) =& -\log_2\left(\frac{7}{6+2^N}\right). \end{aligned} \tag{9.10}$$

This value approaches the maximal value of 1 in the thermodynamic limit.

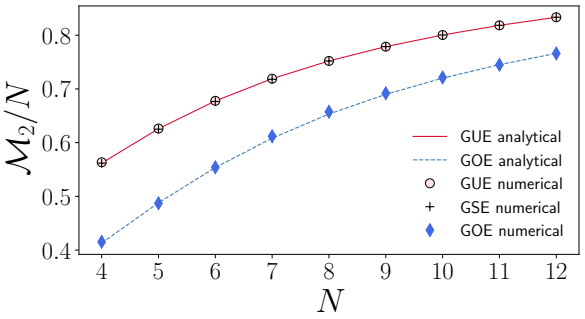

Figure 9.2. The magic computed for GUE and GSE ensembles exhibits similar behavior, while the GOE shows a distinct trend. The numerically obtained values are in excellent agreement with the corresponding analytical predictions.

In random matrix theory, the Gaussian ensembles—GOE, GUE, and GSE—are distinguished by their symmetry classes and the associated Dyson index $\beta \in \{1, 2, 4\}$, corresponding to real symmetric, complex Hermitian, and quaternionic self-dual Hermitian matrices, respectively [735]. Let H be an $N \times N$ Hermitian matrix. The probability distribution over the ensemble is given by $P(H) \propto \exp\left(-\frac{\beta}{4\sigma^2} \operatorname{Tr}(H^2)\right)$, where $\beta = 1$ corresponds to GOE, $\beta = 2$ to GUE, and $\beta = 4$ to GSE. The choice of β determines the symmetry class of the matrices:

- GOE ($\beta = 1$): $H \in \mathbb{R}^{N\times N}$, with $H = H^T$ (real symmetric).
- GUE ($\beta = 2$): $H \in \mathbb{C}^{N\times N}$, with $H = H^\dagger$ (complex Hermitian).
- GSE ($\beta = 4$): H is quaternionic Hermitian (self-dual), which can be represented by $2N \times 2N$ complex matrices with symplectic structure.

In what follows, we investigate how the three complexity markers discussed above evolve as a system transitions from a chaotic random matrix regime to a localized phase. We consider three representative models: the generalized Rosenzweig–Porter (RP) model (Sec. 9.3), the Power-Law Random Banded Matrix (PLRBM) model (Sec. 9.4), and the Sachdev–Ye–Kitaev (SYK_4) model coupled to an Ising chain

(Sec. 9.5). These models are characterized by a single tunable parameter, which controls the interpolation between chaotic and localized behavior. Moreover, the RP and PLRBM models exhibit Anderson criticality and support multifractal eigenstates [656, 689], providing a fertile ground for analyzing the distinct responses of the complexity markers.

9.3 Rosenzweig-Porter model

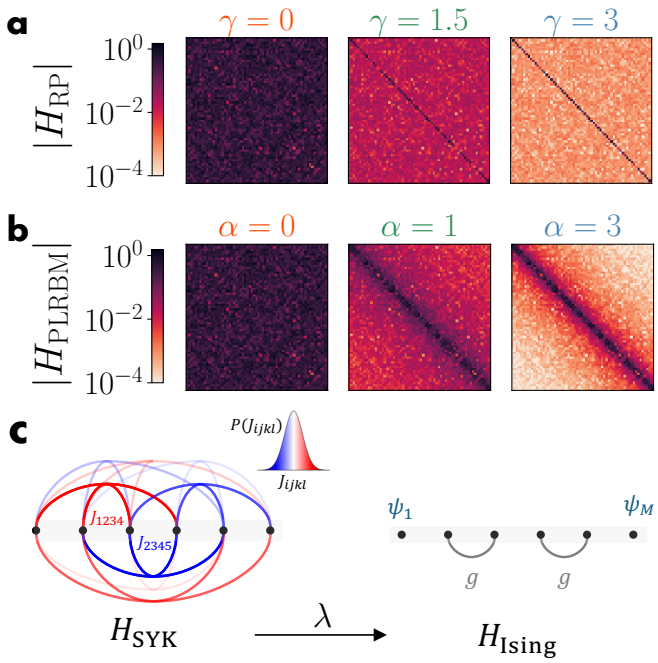

Figure 9.3. Three model Hamiltonians exhibiting a transition from chaotic (ergodic) to localized phases, controlled by tunable parameters. **(a)** Rosenzweig–Porter (RP) model: A random matrix ensemble where the off-diagonal elements have decreasing weight as the parameter γ increases. **(b)** Power-Law Random Banded Matrix (PLRBM) model: Characterized by off-diagonal elements that decay with a power-law determined by the exponent α. **(c)** SYK$_4$+Ising hybrid model: The coupling strength λ interpolates between the Sachdev–Ye–Kitaev (SYK$_4$) model with all-to-all random four-body interactions drawn from a Gaussian distribution (left, $\lambda = 0$) and an Ising chain, expressed in Majorana fermions (right, $\lambda = 1$).

In this section, we study the above complexity markers for the Rosenzweig–Porter (RP) model, both for bulk and ground states. By numerically analyzing varying system sizes, we identify sharp transitions that occur at different points for different markers, and we find distinct behavior in the bulk and ground state.

9.3.1 Model

The RP model is an ensemble of $L \times L$ random Hermitian matrices defined as [683]

$$H_{ij} = \delta_{ij} h_i + \frac{1}{L^{\gamma/2}} V_{ij}(1 - \delta_{ij}) \,. \tag{9.11}$$

Here, h_i as well as V_{ij} are independent random Gaussian variables (real for h_i and complex for V_{ij}) with mean zero and standard deviation 1. At $\gamma = 0$, the RP model recovers a Random Matrix Theory (RMT), which in the case of the above choices is given by the Gaussian unitary ensemble (GUE). Upon increasing γ, the model interpolates between this RMT and a diagonal Hamiltonian reached at $\gamma \to \infty$, whose eigenvalues are completely uncorrelated.

The relative simplicity of the RP model enables an analytical treatment of both its spectral properties [689, 736] and eigenvector statistics [737–739], allowing for a

comprehensive characterization of the model in the bulk of the energy spectrum. In the ergodic phase, which spans the range $0 \leq \gamma < 1$, the model behaves like an RMT, with Wigner–Dyson level spacing and Porter–Thomas statistics for the eigenvector probability distribution, signaling quantum chaos and ergodicity in Hilbert space. At $\gamma = 1$, a transition to non-ergodic behavior occurs, and at $\gamma = 2$ Anderson localization sets in. In the regime $2 < \gamma < \infty$, wavefunctions are localized within a small region of Hilbert space, and the level spacing distribution exhibits Poissonian statistics. A key feature of the RP model is the presence of an intermediate regime between the ergodic and localized phases, in the range $1 < \gamma < 2$, where wavefunctions remain extended but occupy only a fraction of the full Hilbert space, exhibiting fractal behavior that deviates from conventional ergodicity without being fully localized. The fractal dimension defined in Eq. (9.3) is a particularly effective marker for these transitions [689], leading to the characterization

$$\langle D_q \rangle = \begin{cases} 1 & \gamma < 1\,, \\ 2-\gamma & 1 \leq \gamma \leq 2\,, \\ 0 & \gamma > 2\,. \end{cases} \tag{9.12}$$

The same phase transitions have been confirmed not only through eigenvalue and eigenstate statistics but also via dynamical properties, such as diffusion characteristics [740,741], as well as survival and return probabilities [742,743]. Given the presence of different well-established regimes, the RP model serves as an ideal benchmark for evaluating how the behavior of the various complexity markers across different phases, as we discuss in detail in the following section.

9.3.2 Results

In this section, we comparatively study the behavior of eigenvectors—both ground state and bulk states—undergoing a localization transition using the complexity markers defined in Sec. 9.2: fractal dimension $\langle D_2 \rangle$, maximum half-chain von-Neumann entanglement entropy $\langle S_{\text{vN}} \rangle$, and stabilizer Rényi entropy $\langle \mathcal{M}_2 \rangle$, where the angular brackets denote ensemble averaging. We first analyze the bulk eigenstates of the RP model in detail before extending our discussion to the ground state. We focus on the parameter range $\gamma \in [0, 3]$ for varying system size $N = 4$ to 12 (corresponding to matrix dimension $2^N \times 2^N$), averaged over multiple samples.

Bulk state analysis: To characterize the bulk behavior of the RP model, we compute each complexity marker by averaging over the central 20% [2] of the ordered eigenstates. At $\gamma = 0$, the system effectively behaves like a Haar-random ensemble, with all three markers saturating their respective analytical values, as described in Sec. 9.2. In the opposite limit, as $\gamma \to \infty$, the Hamiltonian becomes fully diagonal, leading to eigenstates that are localized in the computational basis. In this regime, both the fractal dimension D_2 and the entanglement entropy S_{vN} vanish. Furthermore, since the diagonal Hamiltonian commutes with all 2^N Pauli strings composed of only I and Z, these are the only ones contributing to the Pauli spectrum. Hence,

[2] We obtain the same result if more than 20% of the bulk eigenstates are choosen instead, see Section 9.3.3.

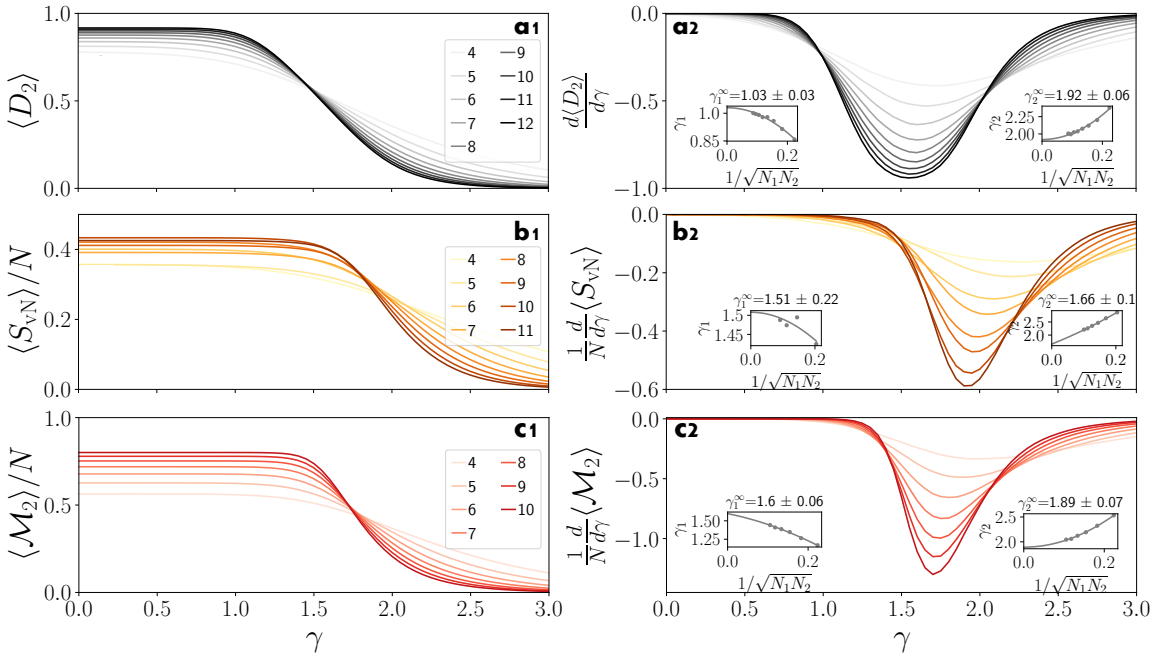

Figure 9.4. (**a1-c1**) Complexity markers (normalized with respect to N), averaged over the central 20% of the bulk eigenstates of the RP model for different system sizes from $N = 4$ up to $N = 12$, and averaged over samples from 20000 for $N = 4$ to 500 for $N = 12$. All markers plateau at the maximum value in an extended regime at small γ, overlapping with the model's ergodic regime. The N-dependent value matches with predictions from the GUE ensemble that is exactly recovered at $\gamma = 0$. The plateau's extent in terms of γ depends on the marker: the plateau is largest for $S_{\rm vN}$ and smallest for D_2. At large γ, the model enters a localized regime, characterized by a low value of all markers. The slope at which the model goes from the ergodic to the localized regime is different for all markers, as becomes clear from the derivatives **(a2-c2)**. The crossings in the derivatives (insets in **a2-c2**) determine two different transition points γ_1 and γ_2. There are, therefore, three different regimes of high, intermediate, and low complexity, which do not coincide for the different complexity markers used.

every eigenstate is a stabilizer state, resulting in vanishing magic. The Pauli spectra for different regimes are shown in Section 9.7.

For the fractal dimension, two critical points are known within $\gamma \in (0, 3)$, corresponding to transitions from ergodic to non-ergodic at $\gamma_1^c = 1$ and then to the localized phase at $\gamma_2^c = 2$ [Eq. (9.12)]. However, it is not a priori clear that entanglement and magic should exhibit the identical behavior. As can be seen in Fig. 9.4**b1**,**c1**, at small γ they exhibit $\mathcal{O}(1)$ scaling, indicating a high-complexity regime that one may expect in an ergodic phase. At a marker-dependent value γ_1, the complexity begins to decay, signaling entry into the non-ergodic regime. This decay continues until a second point γ_2, beyond which the markers eventually stabilize to a $\mathcal{O}(1/N)$ plateau as $N \to \infty$, indicating a low-complexity regime consistent with a large degree of localization. Within the intermediate regime $\gamma_1 < \gamma < \gamma_2$, all markers display fractal-like scaling of the form $\mathcal{O}(N^\delta)$ with $-1 < \delta < 0$.

Notably, the points γ_1 and γ_2, and therefore the parameter ranges corresponding to high- and low-complexity behavior, differ significantly between markers. For example, as shown in Fig. 9.4, the entanglement entropy features the broadest high-complexity plateau (panel **b1**), while the fractal dimension shows the narrowest (panel **a1**). We can make the separation into distinct regimes more precise by examining the first derivative of each marker with respect to γ. The intersection of these derivatives for

different system sizes N provides a reliable signature of emerging non-analytic behavior, indicating the onset of a sharp transition in the thermodynamic limit. We extract the transition points by extrapolating the crossing positions between two consecutive system sizes, N_1 and N_2, as a function of the inverse geometric mean, $1/\sqrt{N_1 N_2}$ [744]. These extrapolations are shown in the insets of Fig. 9.4**a2-c2**.

In the case of $\frac{d\langle D_2\rangle}{d\gamma}$, the crossing points for consecutive system sizes lie within a relatively narrow range, see the insets of Fig. 9.4**a2**. By applying a quadratic fit to the crossing locations as a function of $1/\sqrt{N_1 N_2}$ [3], we extract the transition points in the thermodynamic limit as $\gamma_1^\infty[D_2] = 1.03 \pm 0.03$ and $\gamma_2^\infty[D_2] = 1.92 \pm 0.06$. These values are in excellent agreement with the analytically predicted transition points from Eq. (9.12), thereby validating our numerical method. The quoted uncertainties are derived from the covariance matrix of the fit parameters.

In the half-system entanglement entropy, an even–odd behavior is observed in the $\mathcal{O}(1)$ regime: In this regime, the system assumes a volume-law entanglement determined by the subsystem size $\lfloor N/2 \rfloor$, leading to nearly identical half-system entanglement densities for N and $N+1$. However, once the system departs from the $\mathcal{O}(1)$ regime, this pairing breaks down, as the volume law no longer holds (see Fig. 9.4**b1**). Considering this effect, we use only even N when extracting γ_1^∞ via finite-size scaling, while we include all available N for determining γ_2^∞. Given the limited number of even-sized systems, the estimate for $\gamma_1^\infty[S_{\mathrm{vN}}] = 1.51 \pm 0.22$ has a comparatively larger uncertainty. Even when taking these error bars into account, we have that $\gamma_1^\infty[S_{\mathrm{vN}}] > \gamma_1^\infty[D_2]$. Conversely, we find $\gamma_2^\infty[S_{\mathrm{vN}}] = 1.66 \pm 0.10$, which is smaller than $\gamma_1^\infty[D_2]$, indicating that the intermediate regime identified by the entanglement entropy is significantly narrower than the non-ergodic fractal regime.

The behavior of magic is smoother across system sizes. The scaling of its crossing points yields a transition point $\gamma_1^\infty[\mathcal{M}_2] = 1.60 \pm 0.06$ in the same range as that of the entanglement entropy. However, the transition to the low-complexity $\mathcal{O}(1/N)$-regime occurs at a higher value, $\gamma_2^\infty[\mathcal{M}_2] = 1.89 \pm 0.07$, rather more closely aligned with that of the fractal dimension $\gamma_2^\infty[D_2]$.

Among all the transition points, the most notable contrast lies in γ_1^∞, where S_{vN} and $\mathcal{M}_2$ display a new phase transition that occurs significantly later than $\gamma = 1$ and that is undetected by D_2. A similar trend is evident in their self-averaging behavior (see Section 9.6.2), which undergoes abrupt changes that reinforce this observation. This behavior may stem from the fact that fractal states, while non-ergodic, can still exhibit high entanglement and high magic [706], causing these markers to remain large even after the system departs from full ergodicity. Consequently, the extended regime between $\gamma_1^\infty[D_2]$ and $\gamma_1^\infty[\mathcal{M}_2]$ represents a distinct non-ergodic phase, where the states remain highly entangled and highly magical, yet are no longer fully ergodic. This aligns with the intuition that the non-ergodic fractal phase can host highly complex states.

[3] To find the transition points in the thermodynamic limit, we fit a second-order polynomial curve to the crossing point with respect to $1/\sqrt{N_i N_{i+1}}$, of the form

$$\gamma = a + b\frac{1}{\sqrt{N_i N_{i+1}}} + c\frac{1}{N_i N_{i+1}}\,. \tag{9.13}$$

By extrapolating to $N \to \infty$, we obtain the transition points $\gamma^\infty = a$. To obtain the correct points after scaling, we found it crucial to set the acceptable parameter range of b and c while fitting the curve. For obtaining γ_1, the fitted curve should move to higher γ with increasing N, i.e., $b, c \leq 0$, while for γ_2, it should move to smaller γ, i.e., $b, c \geq 0$.

Finally, we highlight an additional noteworthy observation. As discussed in Section 9.6.2, among the various complexity markers, the SRE exhibits superior self-averaging properties across nearly all regimes, except in the interval $(\gamma_1^\infty[D_2], \gamma_1^\infty[\mathcal{M}_2])$, where the entanglement entropy shows faster convergence. This enhanced self-averaging behavior makes the SRE a particularly reliable probe for identifying transitions in finite-size systems, where statistical fluctuations are significant. At the same time, the fact that entanglement entropy outperforms SRE in a specific regime underscores the complementary nature of these markers in capturing the structure of complex quantum states.

Comparison between IPR and D_2: Although the fractal dimension D_2 can be formally related to the inverse participation ratio (IPR) I_2, defined in Eq. (9.1), via the expression $D_q = \frac{\log_2(I_q)}{N(1-q)}$, relying solely on I_q to detect phase transitions in such models can be challenging. This is because the multifractal nature of the wavefunctions manifests through the scaling relation $I_q \propto 1/L^{D_q(q-1)}$ [685, 688, 690, 695, 699], which can be captured in D_q instead of I_q. As illustrated in Fig. 9.5, the averaged IPR $\langle I_2 \rangle$ reveals only the transition near $\gamma \simeq 2$, corresponding to the non-ergodic to localized transition, while it fails to resolve the ergodic to non-ergodic transition. This limitation highlights the advantage of using the fractal dimension as a more sensitive diagnostic of intermediate, multifractal phases.

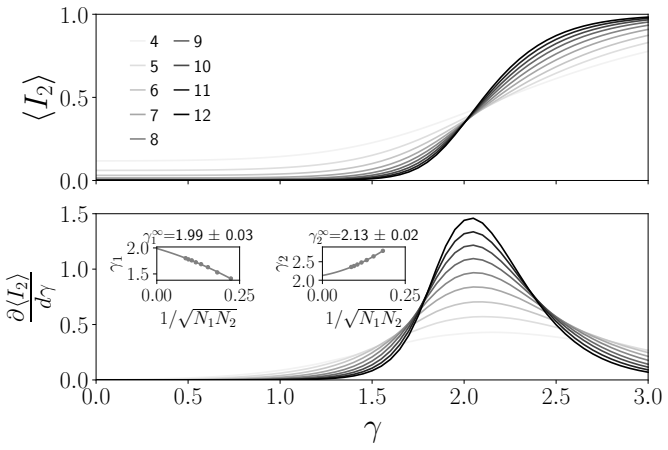

Figure 9.5. Unlike the fractal dimension, the average IPR does not resolve two distinct transition points in the bulk phase diagram of the RP model (Fig. 9.4). Instead, the derivative crossings yield nearly coincident transition points, suggesting a single transition point at $\gamma_c \simeq 2$.

Ground state analysis: The analysis of random matrix models is traditionally focused on the properties of the full eigenspectrum. However, their ground state tends to be more sensitive to ergodicity breaking, giving rise to a mobility edge [649,745–750] and motivating a dedicated analysis.

As shown in Fig. 9.6, again all complexity markers approach their Haar-random values in the small-γ regime, with complexity scaling as $\mathcal{O}(1)$. However, they begin to deviate from this value at a smaller γ than their bulk counterparts. Such an earlier transition point in the ground state compared to the bulk indicates the presence of a mobility edge (see Section 9.3.3). Furthermore, all markers transition more rapidly to a $\mathcal{O}(1/N)$ scaling than was the case in the bulk. As a result, in the large-N limit, the intermediate region with scaling $\mathcal{O}(1/N^\delta)$ appears to vanish entirely, giving rise to a sharp, first-order-like transition directly from $\mathcal{O}(1)$ to $\mathcal{O}(1/N)$ scaling. These abrupt

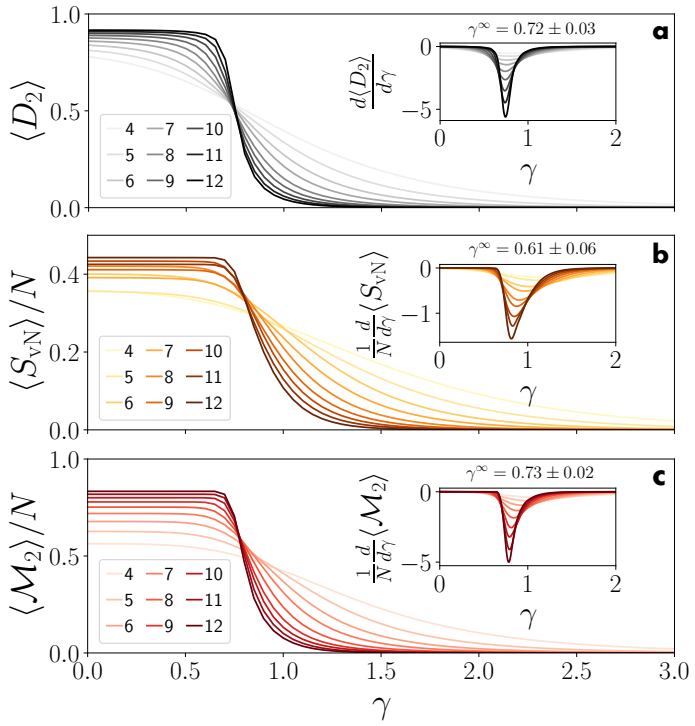

Figure 9.6. Complexity markers for the ground state of the RP model. Inset: first derivative with respect to γ. A direct transition from an ergodic to a localized phase is observed. The transition points detected through fractal dimension D_2 (a) and SRE density $\mathcal{M}_2/N$ (c) coincide within error bars. The entanglement entropy $S_{\rm vN}$ (b) indicates the transition at a slightly smaller value of γ, but with a larger error bar due to the even–odd effect.

transitions are identified by extrema in the derivatives of the complexity markers [4], signaling non-analytic behavior in the thermodynamic limit (see insets of Fig. 9.6). After finite-size scaling, we find that both the fractal dimension and magic detect the ground-state transition at around the same value, $\gamma^\infty[D_2] = 0.72 \pm 0.03$ and $\gamma^\infty[\mathcal{M}_2] = 0.73 \pm 0.02$, respectively. In contrast, for entanglement it appears somewhat earlier, at $\gamma^\infty[S_{\rm vN}] = 0.61 \pm 0.06$, but again with a larger error bar. Given the relative vicinity between the different transition points, we cannot exclude the possibility that they identify the same phase transition. Above, we found that the transitions in $S_{\rm vN}$ and $\mathcal{M}_2$ occurred well within the fractal regime. One may thus conjecture that all transition points agree when an intermediate fractal regime is missing.

9.3.3 Mobility edge in the energy spectrum

The transition to the localized phase can be energy-dependent, a phenomenon referred to as a mobility edge [649, 746–750]. For instance, low-energy states can become localized at lower values of the parameter regime compared to states near the middle of the spectrum. Random banded models are known to exhibit such a mobility edge [745]. A similar trend is observed in our numerical analysis of the RP model (see Fig. 9.1**c**). As a result, for certain values of the control parameter, low-energy states may already be localized while high-energy states remain ergodic. Given this sensitivity to the energy window, it is crucial to investigate how different complexity markers respond to variations in the chosen spectral region.

In Fig. 9.7**a1**–**c1**, we analyze consecutive 5% segments of the energy spectrum. Since the spectrum is symmetric on average, we focus only on the lower half. As we move toward the center of the spectrum, the transition curves systematically shift to

[4] Similar to bulk states, the derivatives of the ground state's complexity marker for systems of size N and $N+1$ intersect at two distinct points. However, after finite-size scaling, these crossings converge to a single transition point, which is consistently identified by the extrema of the derivative.

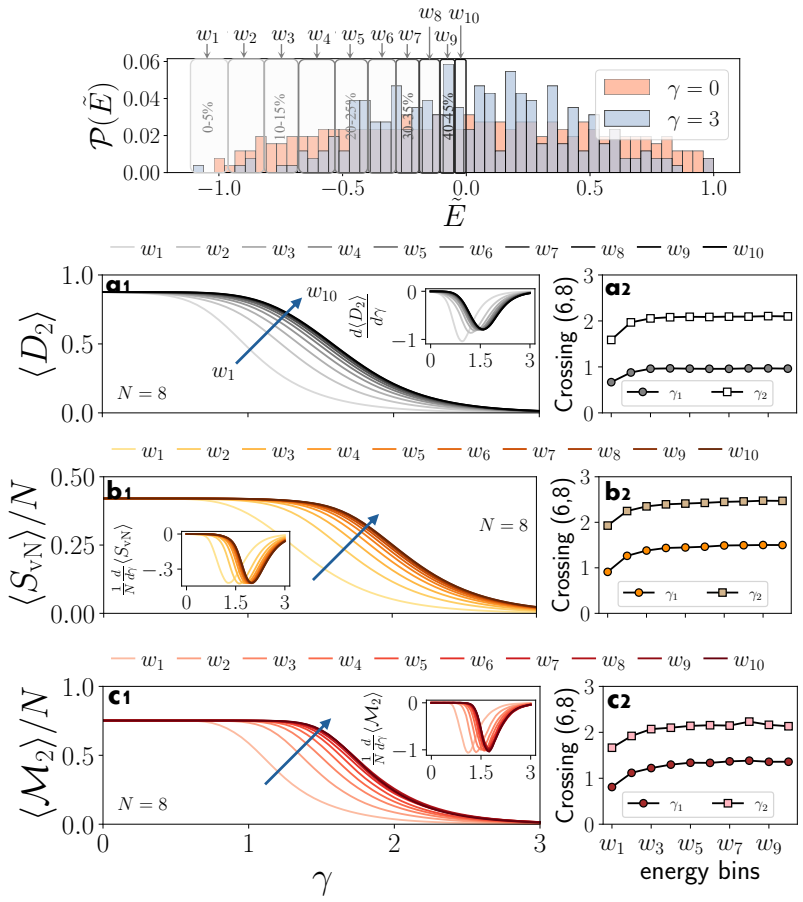

Figure 9.7. Dependence of the ergodic regime on energy window in the RP model. Top panel: The eigenenergies span a broad range, with densely packed, nearly degenerate states located in the spectral bulk, while the edges are populated by relatively few states. In the ergodic phase ($\gamma = 0$), the energy distribution is flatter as compared to the localized phase ($\gamma = 3$). The eigenstates are ordered in ascending energy, and the lower half of the spectrum is divided into 10 equal windows, labeled w_1 to w_{10}, each containing 5% of all eigenstates. As the energy window shifts toward the spectral center (thin to thick lines), the $\mathcal{O}(1)$ ergodic plateau and corresponding transition points γ_1 and γ_2 move to higher γ values for all complexity markers **(a1–c1)**. This shift saturates beyond approximately w_3 **(a2–c2)**, indicating that the crossing points remain essentially unchanged when averaging over bulk regions ranging from as narrow as the central 10% to as broad as 90% of the spectrum. Data shown for $N = 6$ (10000 samples) and $N = 8$ (4000 samples). Insets of **(a1-c1** show the derivative of the complexity markers, from which the crossing points are calculated.

the right, indicating that the transition point occurs at higher values of the control parameter, consistent with the presence of a mobility edge. Additionally, the curves corresponding to higher-energy windows quickly collapse onto one another, suggesting rapid convergence. This behavior supports our choice of using the central 20% of the spectrum for the bulk calculations in section 9.3.2, as this range already displays stable and converged behavior.

The rapid convergence becomes even clearer when examining the evolution of the crossing points of the derivatives of the complexity markers, which we used to pinpoint the transitions. As shown in Fig. 9.7**a2–c2**, these crossing points quickly stabilize to a constant value above the energy window 10%–15%, confirming the robustness of our choice.

9.4 Power-Law Random Banded Matrix model

To further deepen our understanding of the complexity transitions in random matrix models, in this section we examine another paradigmatic model—the Power-Law Random Banded Matrix (PLRBM) model.

9.4.1 Model

The PLRBM model [685] is conceptually similar to the RP model, as it is a random matrix model with suppressed off-diagonal elements. Nevertheless, its physics and phase diagram have distinct features from the RP model. The PLRBM model is a random matrix ensemble whose elements are given by

$$H_{ij} = G_{ij} a(|i-j|)\,. \tag{9.14}$$

In our case, G is chosen as a GUE matrix. The coefficients $a(r)$ implement a polynomial decay of the off-diagonal elements beyond a certain range,

$$a(r) = \begin{cases} 1 & r < b, \\ (r/b)^{-\alpha} & r \geq b, \end{cases} \tag{9.15}$$

where b is called the bandwidth parameter and α is the decay exponent. In this work, we set $b = 1$, i.e., only terms adjacent to the diagonal remain intact, and α remains the single tunable parameter.

The model is known to behave like a random matrix theory for $\alpha < \frac{1}{2}$ [685,751]. In the regime $\frac{1}{2} < \alpha < 1$, the eigenvectors depart from the Porter–Thomas distribution and follow a generalized hyperbolic distribution [752], signaling the presence of a weakly-ergodic regime distinct from that of the RP model. A recent study on the variable-range SYK_2 model reveals clear signatures of this non-ergodic transition at $\alpha = \frac{1}{2}$ in the many-body spectral statistics [753]. There is an Anderson critical point at $\alpha = 1$ [685, 754], where the eigenvectors display proper multifractal behavior that has been intensively studied in the literature [656, 688, 690]. In the range $1 < \alpha < \frac{3}{2}$, the PLRBM enters a localized yet superdiffusive phase, while it becomes fully localized for $\alpha > \frac{3}{2}$.

The differences between the PLRBM and RP models provide a valuable framework for a comparative analysis of how the complexity markers behave in the different regimes, as we will see in what follows. In this section, we focus on the bulk, again considering the central 20% of the energy eigenstates.

9.4.2 Results

The numerical results for the three complexity markers as a function of $\alpha \in [0, 3]$ are plotted in Fig. 9.8. Note that compared to the RP model, the PLRBM model has more significant fluctuations across realizations due to the persistence of some long-range correlations, which do not vanish in the large N limit (see Fig. 9.3**b**). For instance, while 1000 samples suffice for the RP model, we use 10000 samples for the PLRBM at $N = 8$ (see Section 9.6.1) when computing the SRE—the most self-averaging of the three markers—yet noticeable fluctuations persist.

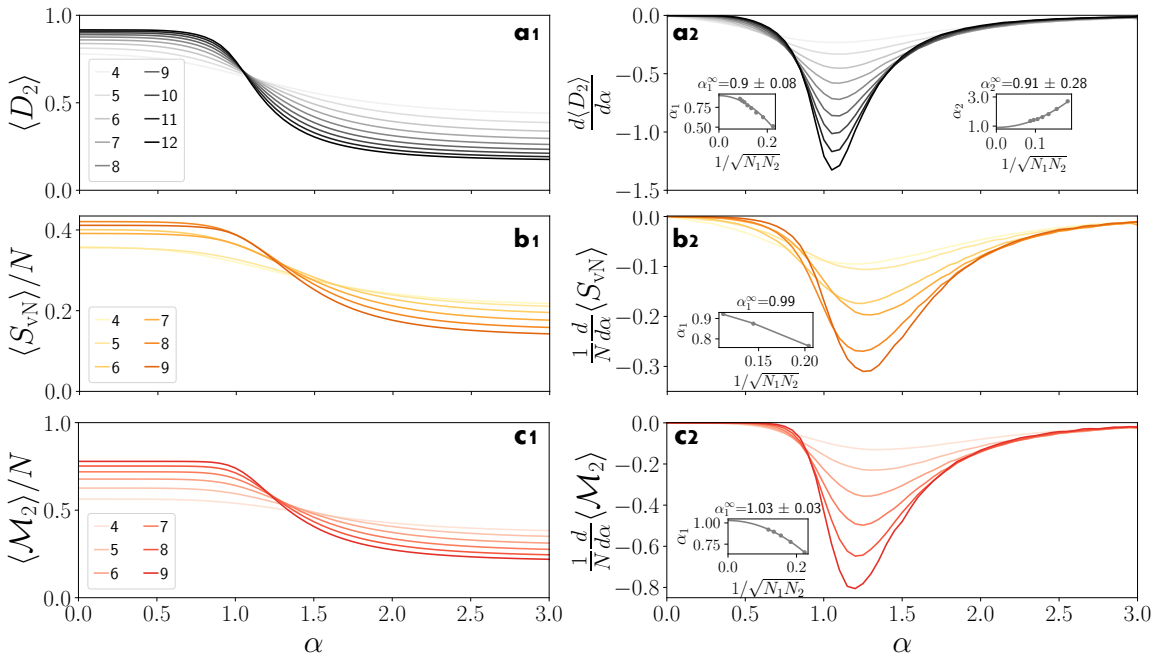

Figure 9.8. (**a1-c1**) Complexity markers (normalized with respect to N), averaged over the central 20% of bulk eigenstates of the PLRBM model for $N = 4$ up to $N = 9$ ($N = 12$ for the fractal dimension) averaged over different sample sizes of 35000 to 3000, respectively. Throughout an extended regime at small α, all markers plateau at the value matching predictions from the GUE ensemble (recovered by the model at $\alpha = 0$). At large α, the model transitions to a localized regime, characterized by a lower value of all the markers. The transition point can be deduced from the derivatives of the complexity markers (**a2-c2**). The crossings in the derivatives (insets **a2-c2**) effectively find only one distinct transition point. Therefore, in contrast to the RP model, there are only two different regimes of high and low complexity that coincide with the ergodic and localized phases, respectively.

At $\alpha = 0$, the state behaves again equal to a Haar-random state and reaches the maximal value for all complexity markers, similar to the RP model. This value extends up to around $\alpha = 1$, creating a plateau with value $\mathcal{O}(1)$ and indicating the extended ergodic regime of the model. Depending on the marker, the complexity begins to decay at a specific value α_1, signaling the entry of the system into the non-ergodic regime. In the limit for $\alpha \to \infty$, the PLRBM model becomes a tridiagonal matrix. Hence, it does not commute with all the 2^N diagonal Pauli strings and, consequently, the magic is nonzero (see Section 9.7). For the same reason, the eigenstates cannot completely localize in the computational basis. Indeed, in Fig. 9.8 we see that for large values of α the markers do not vanish and still show a finite N-dependence. As before, we identify the phase transition points for each complexity marker by considering the positions of the crossing points of the first derivatives in the thermodynamic limit.

For the fractal dimension, we find two crossing points $\alpha_1^\infty[D_2] = 0.90 \pm 0.08$ and $\alpha_2^\infty[D_2] = 0.91 \pm 0.28$, indicating that, in the large N limit, they will collapse to the same value. The curves for entanglement entropy and magic at different system sizes cross just at one transition point $\alpha_1^\infty[S_{\rm vN}] = 0.99$[5] and $\alpha_1^\infty[\mathcal{M}_2] = 1.03 \pm 0.03$.

[5]For $S_{\rm vN}$, the entanglement entropy exhibits even-odd effects even in the $\mathcal{O}(1)$ regime, prompting us to focus on even N values to locate the transition. To improve resolution near the critical point, we compute additional data for $N = 10$, resulting in three crossing points—(4,6), (6,8), and (8,10). These enable a quadratic fit that recovers the Anderson localization transition at $\alpha = 1$, although the limited number of points precludes a reliable error estimate.

Note there might be a second crossing point that remains undetected due to the more sizable fluctuations in the localized regime for large α. Thus, in contrast to the RP model, our analysis does not detect an intermediate regime that is non-ergodic but delocalized. Rather, the available data suggest a direct transition from the delocalized to the localized phase close to the Anderson critical point at $\alpha = 1$.

Although the analysis of the PLRBM model is restricted to smaller system sizes and exhibits larger fluctuations, it supports what we conjectured for the RP model: the complexity markers assume distinct values across the ergodic-to-non-ergodic transition only in the presence of a genuine fractal (or multifractal) phase. Indeed, within error bars, in the PLRBM model, the transition points identified by all three complexity markers coincide (or almost coincide) with the Anderson critical point, the only transition captured by the fractal dimension in the thermodynamic limit. We do not report here the results for the ground state behavior of the PLRBM model since they qualitatively resemble that of the RP model considered in Sec. 9.3.2: the transitions occur earlier than in the bulk [755], yet no intermediate phase is observed. This is consistent with expectations, as the markers used do not reveal a clear extended non-ergodic regime even in the bulk of the PLRBM model.

9.5 SYK_4+Ising model

In this section, we consider a quantum many-body model subject to a chaotic–integrable transition to contrast with the random-matrix behavior. For this, we choose a hybrid model consisting of the SYK model interpolating towards the Ising model. The SYK model, originally introduced as a phenomenological model for non-Fermi liquids [686], is a quantum mechanical system consisting of M Majorana fermions with random q-body interactions. It has accumulated significant attention due to the combination of strong interactions and solvability in the large-M limit [687, 756], making it a paradigmatic system to study quantum chaos beyond RMT. Moreover, randomly interacting many-body systems, like the SYK model, are known to behave drastically differently from RMT near the edge of their energy spectrum [757]. This makes it particularly interesting to compare the complexity markers for the ground state of this model to those of the RP model of Sec. 9.3.2. Further, the SYK model is a prototypical system in the study of black holes and quantum gravity [693,694] through the AdS/CFT correspondence [758,759]. Indeed, at low energies, it exhibits an emergent conformal symmetry and is effectively described by a Schwarzian action [756], mirroring the behavior of Jackiw–Teitelboim gravity [760]. Since the duality becomes manifest in the infrared, it is of particular interest to understand the ground-state properties of the model in order to assess the stability of the holographic phase under perturbations.

9.5.1 Model

The system under study is composed of M interacting Majorana fermions, described by operators ψ_i fulfilling the commutation relations $\{\psi_i, \psi_j\} = \delta_{ij}$. The Hilbert space of the model is isomorphic to that of $N = M/2$ qubits. The interactions between the fermions are chosen to interpolate between a chaotic Hamiltonian at $\lambda = 0$, provided

by the SYK model, and a fully localized, integrable Ising chain reached at $\lambda = 1$,

$$H = (1-\lambda)H_{\mathrm{SYK}_4} + \lambda H_{\mathrm{Ising}}\,. \tag{9.16}$$

The SYK$_q$ model is a system with M all-to-all interacting Majorana fermions with random q-body interactions, (see Fig. 9.3**c** where $q = 4$) , defined as

$$H_{\mathrm{SYK}_q} = (i)^{q/2} \sum_{1\le i_1<\cdots<i_q\le M} J_{i_1\ldots i_q}\psi_{i_1}\ldots\psi_{i_q}\,, \tag{9.17}$$

where the couplings $J_{i_1\ldots i_q}$ are independent and identically distributed random variables drawn from a Gaussian distribution with zero mean and variance given by $\langle J^2_{i_1\ldots i_q}\rangle = J^2(q-1)!/M^{q-1}$. In this article, we work with $q = 4$.

The Ising Hamiltonian is given by an anti-ferromagnetic ZZ spin chain without a magnetic field, $H_{\mathrm{Ising}} = \sum_{i=1}^{N-1} g\sigma_i^z\sigma_{i+1}^z$. It can be written in terms of Majorana operators using the Jordan–Wigner transformation, which maps each Majorana operator to a Pauli string consisting of N Pauli matrices [761],

$$\psi_{2i-1} = \sigma_1^x \otimes \ldots \otimes \sigma_{i-1}^x \otimes \sigma_i^z \otimes \mathbb{I}_{i+1} \otimes \ldots \otimes \mathbb{I}_N, \tag{9.18}$$

$$\psi_{2i} = \sigma_1^x \otimes \ldots \otimes \sigma_{i-1}^x \otimes \sigma_i^y \otimes \mathbb{I}_{i+1} \otimes \ldots \otimes \mathbb{I}_N\,. \tag{9.19}$$

Using $\psi_{2i}\psi_{2i+1} = \mathbb{I}_1 \otimes \ldots \otimes \mathbb{I}_{i-1} \otimes -i\sigma_i^z \otimes \sigma_{i+1}^z \otimes \mathbb{I}_{i+2} \otimes \ldots \mathbb{I}_N$, we obtain

$$H_{\mathrm{Ising}} = i \sum_{i=1}^{M/2-1} g\psi_{2i}\psi_{2i+1}\,, \tag{9.20}$$

where only interactions between even-odd Majorana fermions remain, see Fig. 9.3**c**.

The Ising contribution to the model in Eq. (9.20) introduces purely neighboring and equal-strength interactions between the Majorana fermions. Thus, an increasing λ gradually suppresses the disordered all-to-all interactions characteristic of the ergodic SYK$_4$ regime. The effect is reminiscent of the suppression of off-diagonal terms in the RP model in Eq. (9.11) considered above.

The symmetries of this model play an important role in understanding the behavior of complexity markers, as will be discussed in detail in the following section. Both the SYK$_4$ and Ising model Hamiltonian commute with the fermion parity operator

$$(-1)^{\mathrm{F}} = (i)^M\psi_1\ldots\psi_M = (\sigma^x)^{\otimes M}\,. \tag{9.21}$$

In addition, H_{SYK_4} commutes with the anti-unitary time reversal operator $\mathcal{T}$. The interplay between $(-1)^{\mathrm{F}}$ and $\mathcal{T}$ determines the RMT ensemble and degeneracy of the ground state of the SYK model [762]: for M mod $4 = 2$ the ensemble corresponds to GUE, for M mod $8 = 0$ the corresponding ensemble is GOE, and for M mod $8 = 4$ it is GSE [6] In contrast, H_{Ising} as given in Eq. (9.20) anticommutes with $\mathcal{T}$ due to the presence of the imaginary unit in the Hamiltonian, lifting for $\lambda \neq 0$ the symmetry class to GUE for all M.

[6] The Gaussian symplectic ensemble describes the random $L \times L$ Hermitian quaternionic matrices. The numerical results were obtained by representing the GSE matrices as $2L \times 2L$ complex matrices. For consistency, when comparing the SYK$_4$ results falling in the GSE symmetry class with the corresponding Haar-random value, we take an ensemble of dimension L^{N-1} such that the Hilbert space dimension of SYK$_4$ matches the dimension of the complex GSE representation.

9.5.2 Results

Similarly to the RP and PLRBM models, we carry out a comparative analysis of three complexity markers for the SYK_4 + Ising model. Additionally, we present a more detailed study of magic across different M, which turns out to be sensitive to the model's symmetries introduced above. To be consistent with the rest of the chapter, we consider the number of qubits $N = M/2$ instead of the number of Majorana fermions when calculating the density of the markers.

In the integrable Ising model at $\lambda = 1$, the ground state is doubly degenerate. However, introducing a small perturbation from the SYK Hamiltonian, $\lambda \lesssim 1$, lifts this degeneracy. Due to the fermion parity symmetry of the full Hamiltonian, the system selects a specific ground state: an equal superposition of the two antiferromagnetic

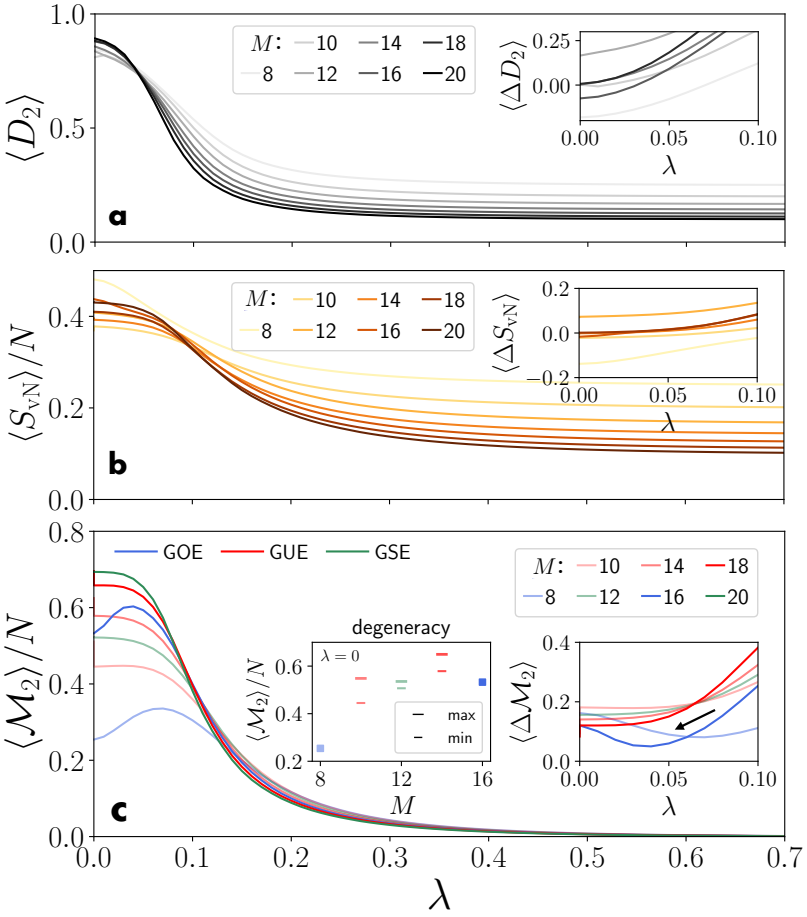

Figure 9.9. Ensemble averaged complexity markers for the groundstate of the SYK_4 + Ising model for different number of Majorana fermions M. (**a**) The fractal dimension D_2 starts to decrease for any non-zero λ and approaches the asymptotic value of the Ising model relatively quickly. Inset: Difference of D_2 to the Haar-random value, indicating that for sufficiently large M, D_2 saturates this value at $\lambda = 0$. (**b**) The S_{vN}-density shows a small remnant of a plateau around the SYK_4 limit ($\lambda = 0$). Inset: for large M also the S_{vN}-density approaches the Haar-random value at small λ. (**c**) For $\lambda \gtrsim 0.5$, the average magic remains zero, while it reaches its maximum near $\lambda \sim 0$, except for states corresponding to the GOE ensemble (which reflects the symmetry of the SYK model at $\lambda = 0$), where the peak occurs away from zero. Left inset: At $\lambda = 0$, the ground states corresponding to the GUE and GSE ensembles are degenerate, where a range of SRE values is possible; however, as soon as λ deviates from zero, it chooses the minimum. Right inset: The difference to the Haar-random value is larger than for D_2 and S_{vN}.

spin configurations, with a relative phase of ± 1. As a result, in this limit, the fractal dimension and maximal von-Neumann entropy density approach the values of $1/N$. In contrast, the magic tends to zero since this superposition is a stabilizer state (see Section 9.5.3). All considered markers approach the values of the $\lambda \sim 1$ limit relatively rapidly without appreciable changes beyond $\lambda \gtrsim 0.5$, see Fig. 9.9.

In the chaotic regime for $\lambda \gtrsim 0$, unlike in the RP ground state, we cannot a priori know if the complexity markers saturate the Haar-random values since we are now considering a many-body system. The deviation from the Haar-random value is quantified by

$$\langle \Delta \mathcal{C} \rangle = \frac{\langle \mathcal{C}_{\text{Haar}} \rangle}{N} - \frac{\langle \mathcal{C} \rangle}{N}, \tag{9.22}$$

where $\mathcal{C}$ denotes one of the three markers D_2, S_{vN}, or $\mathcal{M}_2$. As shown in the insets of Fig. 9.9, for sufficiently large M, $\langle \Delta D_2 \rangle$ and $\langle \Delta S_{\text{vN}} \rangle$ tend to zero as $\lambda \to 0$, whereas $\langle \Delta \mathcal{M}_2 \rangle$ is strictly larger than zero. This behavior can be understood by the fact that, similarly to what we have seen for $\lambda \sim 1$, the ground state for small λ has fixed fermion parity, which means that only Pauli strings composed of the product of an even number of Majorana operators (those that preserve the symmetry) contribute to a non-zero $\mathcal{M}_2$. Since these comprise only half of all possible Pauli strings, the overall $\mathcal{M}_2$ is smaller than the Haar-random value. The situation is, however, a bit more subtle in the strict $\lambda = 0$ case since in pure SYK$_4$ the ground state is not always unique. For $M = 0 \bmod 8$ (GOE), there is just one ground state with fixed fermion parity. In contrast, for GUE and GSE, $M \neq 0 \bmod 8$, the presence of degeneracy allows for the superposition of the two ground states with opposite fermion parity, which can enhance the SRE. We numerically determine the maximum and minimum values of this linear combination [7], as shown in the left inset of Fig. 9.9. Notably, the minima coincide with the values shown in the main plot (**c**) at small but non-zero λ, confirming that the Ising Hamiltonian breaks the degeneracy and selects one specific parity.

Moreover, the SRE exhibits a peculiar M-dependent behavior at small λ, which can be attributed to the characteristics of the underlying RMT ensembles [694, 763]. Specifically, when $M \bmod 8 = 0$, $\mathcal{M}_2$ begins at a lower value, and then rises to a peak at some small nonzero λ, followed by a monotonic decrease. This behavior can be comprehended in the following way: for finite-size systems, the GOE ensemble yields lower magic than GUE or GSE for Haar-random states (see Eq. (9.10) and Fig. 9.2 in Section 9.2.3). As contributions from the Ising Hamiltonian kick in at $\lambda \neq 0$, the symmetry class is lifted from GOE to GUE, leading to a rise of the value for the SRE in the case of $M \bmod 8 = 0$. In contrast, for $M \bmod 4 = 2$ and $M \bmod 8 = 4$, the SRE starts at its maximal value, and the addition of the Ising contribution only decreases it.

As we move further away from $\lambda \sim 0$, all three markers start deviating from their ergodic value without exhibiting a long plateau as in the RP model—indicating that the ground state is rather susceptible to perturbations by the Ising contribution (see Fig. 9.9), unlike the $\lambda \gtrsim 0.5$ regime. Such fragility of the SYK$_4$ ground state resembles

[7] Given the two ground states GS_1 and GS_2 with opposite fermion parity and a generic linear combination

$$|\psi\rangle = \sin\theta\, |\text{GS}_1\rangle + e^{i\phi} \cos\theta\, |\text{GS}_2\rangle\,, \tag{9.23}$$

we numerically optimize $\langle \mathcal{M}_2(\psi) \rangle$ over a 200×200 grid in the (θ, ϕ) plane to determine the maximum and minimum values.

recent observations in a related model interpolating between SYK_4 and SYK_2 [711], which implements a crossover from many-body chaos to single-body chaos, while always maintaining volume-law magic in the ground state. In our model, the perturbed Ising ground state is a stabilizer state; therefore, the transition in magic appears sharper, reminiscent of the transition observed in the RP ground state (Fig. 9.6).

We expect the ensemble-dependent features discussed above to disappear in the $M \to \infty$ limit. Indeed, the $M \bmod 8 = 0$ peak seems to progressively move to smaller values of λ and $\Delta\mathcal{M}_2$ progressively decreases if we compare the same ensembles. Nonetheless, such finite-size effects are particularly relevant for characterizing realistic many-body chaotic systems beyond random matrix universality [757, 764]. The analysis highlights the utility of the SRE as a diagnostic tool due to its sensitivity to the model's symmetry structure, distinguishing it from other markers such as the fractal dimension and entanglement entropy.

9.5.3 Complexity markers for superposition of two computational basis states

It is instructive to examine the behavior of the three complexity markers for a simple superposition of two computational basis states. Consider the following N-qubit state:

$$|\psi\rangle = \sin\theta\,|a\rangle + e^{i\phi}\cos\theta\,|\bar{a}\rangle\ , \tag{9.24}$$

where $|a\rangle$ and $|\bar{a}\rangle$ are N-qubit orthogonal computational basis states differing by a Hamming distance of N, i.e., they are locally orthogonal at each qubit site. For such a state, the complexity markers are given by:

$$D_2 = -\frac{1}{N}\log_2\left(\sin^4\theta + \cos^4\theta\right), \tag{9.25}$$

$$S_{\mathrm{vN}} = -\left[\cos^2\theta\log_2\left(\cos^2\theta\right) + \sin^2\theta\log_2\left(\sin^2\theta\right)\right]\ . \tag{9.26}$$

The SRE is given by [765]:

$$\mathcal{M}_2 = -\log_2\left(\frac{1+\cos^4 2\theta + \sin^4 2\theta\left(\cos^4\phi + \sin^4\phi\right)}{2}\right)\ . \tag{9.27}$$

Among the three markers, only the SRE is sensitive to the relative phase ϕ. In the special case of an equal superposition with ± 1 difference, i.e., $\sin\theta = \cos\theta = \frac{1}{\sqrt{2}}$ and $\phi = 0, \text{or } \pi$, the complexity markers simplify to

$$D_2 = \frac{1}{N}, \quad \frac{S_{\mathrm{vN}}}{N} = \frac{1}{N}, \quad \frac{\mathcal{M}_2}{N} = 0\,. \tag{9.28}$$

Such a superposition state appears in the $\lambda \to 1$ limit of the SYK+Ising model. Due to the fermion parity symmetry of the full Hamiltonian, the ground state has double degeneracy and forms a superposition of two degenerate states connected by $(-1)^F$:

$$(-1)^F\,|\mathrm{GS}_1\rangle = +\,|\mathrm{GS}_2\rangle\ . \tag{9.29}$$

Moreover, the symmetry ensures that they form equal superpositions without any complex relative phase, as explained in the following way. Consider the generic su-

perposition

$$|\psi\rangle = \sin\theta\,|\mathrm{GS}_1\rangle + e^{i\phi}\cos\theta\,|\mathrm{GS}_2\rangle\ . \tag{9.30}$$

As $|\psi\rangle$ should also be symmetric under $(-1)^F$ with possible eigenvalues ± 1,

$$(-1)^F\,|\psi\rangle \stackrel{!}{=} \pm\,|\psi\rangle \Rightarrow \theta = \pi/4, \phi = 0, \pi. \tag{9.31}$$

Now, close to $\lambda \to 1$, as both ground states are computational basis states, we can use the above Eq. (9.28). That is, we expect fractal dimension and von-Neumann entropy density to scale as $1/N$ and SRE to vanish, which is exactly what we observe in Fig. 9.9**c**.

9.6 Effects of samples

Analyzing disordered systems requires averaging over several random disorder instances to eliminate instance dependence, i.e., reduce the variance of results. However, it is often a model, its phase, and an observable dependent. For example, a highly ergodic phase with a self-averaging observable requires fewer samples compared to a localized phase to obtain the same order of variance. In this section, first, we discuss the number of samples we use for each model and complexity markers. Then we discuss how the self-averaging property of the complexity markers also contains the information of the phase transition.

9.6.1 Details on number of samples

For numerical reproducibility, we provide detailed tables listing the exact number of disorder realizations used for the results for different models (see Tables 9.1-9.3). To keep the numerical effort manageable under the exponential growth of the Hilbert-space dimension with system size N, we progressively reduced the number of realizations with increasing N. However, this reduction does not compromise the accuracy of our results, as the observables become increasingly self-averaging with larger N (see Fig. 9.10**a1,b1,c1**).

Moreover, we adapted the number of samples for the marker under consideration. The computational complexity for computing the maximum entanglement grows as $\binom{N}{N/2} \times \mathrm{construction}(\rho_A) \times \mathrm{diag}(\rho_A) = \frac{2^{5/2N}}{\sqrt{N}}$. Similarly, the complexity for computing the Stabilizer Rényi Entropy (SRE) scales as $\mathcal{O}(2^{2N})$, due to the size of the Pauli group. In comparison, the computational complexity for calculating the fractal dimension is more modest, scaling as $\mathcal{O}(2^N)$, permitting us to increase the number of samples to even further improve the quality of the results.

Among the considered models, we found the most substantial sample-to-sample fluctuations in the PLRBM model, making a larger number of realizations necessary to achieve satisfactory statistical accuracy. In contrast, due to the large density of states in the bulk, a comparatively smaller number of realizations was sufficient for the RP bulk model as compared to studies on its ground state. For the SYK+Ising model, we maintained a comparable sample size to that of the RP bulk case across all markers.

Model / N	4	5	6	7	8	9	10	11	12
RP bulk	20000	15000	10000	5000	4000	3000	2000	1000	500
RP gs	20000	15000	10000	5000	4000	3000	2000	1000	500
PLRBM bulk	20000	15000	10000	5000	4000	3000	2000	1000	500
SYK+Ising	5000	4000	3000	2000	1000	500	100	–	–

Table 9.1. Number of samples used for fractal dimension estimates across different models and system sizes N.

Model / N	4	5	6	7	8	9	10	11	12
RP bulk	5000	4000	3000	2000	1000	800	100	30	–
RP gs	20000	15000	10000	5000	4000	3000	500	100	50
PLRBM bulk	35000	24000	40000	16000	10000	3000	500	–	–
SYK+Ising	5000	4000	3000	2000	1000	500	100	–	–

Table 9.2. Number of samples used for maximum entanglement entropy estimates across different models and system sizes N.

Model / N	4	5	6	7	8	9	10	11	12
RP bulk	5000	4000	3000	2000	1000	500	80	–	–
RP gs	20000	15000	10000	5000	4000	1000	200	100	50
PLRBM bulk	35000	24000	20000	20000	10000	1500	–	–	–
SYK+Ising	5000	4000	3000	2000	1000	500	100	–	–

Table 9.3. Number of samples used for Stabilizer Rényi Entropy estimates across different models and system sizes N.

9.6.2 Self-averaging property

In disordered quantum many-body systems, the self-averaging property refers to the tendency of observables to converge to their ensemble-averaged (disorder-averaged) values as the system size increases. A physical quantity $\mathcal{C}$ is said to be self-averaging if its relative variance vanishes in the thermodynamic limit. This can be quantified by the dimensionless ratio

$$R_{\mathcal{C}} = \frac{\mathrm{Var}(\mathcal{C})}{\langle \mathcal{C} \rangle^2}\,, \tag{9.32}$$

where $\langle \cdot \rangle$ denotes the disorder average. In ergodic phases, where the system uniformly explores its Hilbert space, $R_{\mathcal{C}} \to 0$ as the system size increases, indicating strong self-averaging. In contrast, in non-ergodic or localized regimes, $R_{\mathcal{C}}$ can remain finite even in the thermodynamic limit, reflecting strong sample-to-sample fluctuations and the breakdown of ergodicity.

RP bulk states. In Fig. 9.10**a1**, we find that the complexity markers exhibit self-averaging behavior exclusively within the ergodic regime ($\gamma \leq 1$). Beyond this point, deviations begin to emerge. Notably, at $\gamma = 1.2$, the fractal dimension D_2 starts losing its self-averaging character due to its scaling as $\mathcal{O}(N^{\delta})$, whereas both the normalized von Neumann entropy S_{vN}/N and the magic $\mathcal{M}_2/N$, which remain $\mathcal{O}(1)$, continue

to exhibit self-averaging. At stronger disorder strengths, such as $\gamma = 1.8$, the entanglement remains more strongly self-averaging, consistent with a larger plateau in Fig. 9.4**b1** of the $\mathcal{O}(1)$ regime. At $\gamma = 3$, none of the markers remain self-averaging, in accordance with their $\mathcal{O}(N^{\delta})$ and $\mathcal{O}(1/N)$ scaling behaviors, respectively.

Furthermore, the strength of self-averaging can be inferred from the scaling behavior of $R_{\mathcal{C}}$ with system size $L = 2^N$, i.e.,

$$R_{\mathbf{C}} \propto L^{-\beta} = 2^{-N\beta} \,. \tag{9.33}$$

A system is *strongly self-averaging* if $\beta \geq 1$, and *weakly self-averaging* if $0 < \beta < 1$.Notably, Fig. 9.10**a2** shows that up to $\gamma = 1.5$, even in the non-ergodic phase, the system remains strongly self-averaging. Beyond $\gamma = 2.5$, all markers exhibit the same exponents. Additionally, $\mathcal{M}$ demonstrates stronger self-averaging in the ergodic regime and undergoes the most pronounced change around the transition points.

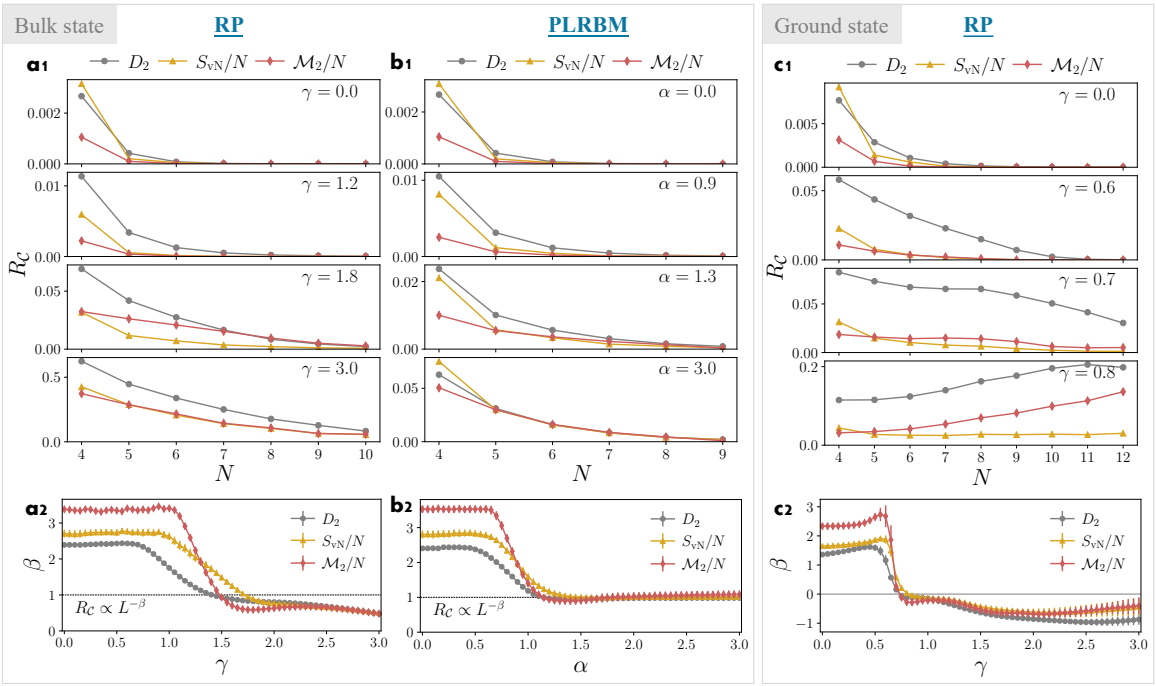

Figure 9.10. Self-averaging behavior of different complexity markers and their scaling exponents. **(a1)** For the bulk of the RP model, in the ergodic regime ($\gamma = 0$), all markers exhibit strong self-averaging, indicated by a vanishing relative variance. At intermediate disorder ($\gamma = 1.2$), D_2 already begins to deviate, showing non-self-averaging behavior, while others remain stable. At $\gamma = 1.8$ and $\gamma = 3$, none of the markers are self-averaging, consistent with the breakdown of ergodicity and the emergence of strong sample-to-sample fluctuations. **(a2)** Scaling exponent β as a function of γ for RP bulk states. All three markers exhibit strong self-averaging ($\beta > 1$) up to $\gamma = 1.5$, and after $\gamma = 2.5$, they show same β. Notably, $\mathcal{M}_2$ displays the steepest variation in β, indicating a more pronounced change in self-averaging across the transition. The deviation from the plateau region of constant β occurs in the same order, i.e., D_2 then S_{vN} and $\mathcal{M}_2$ as observed in Fig. 9.4. **(b1)** In the bulk states of the PLRBM model, complexity markers exhibit behavior analogous to the RP model, with magic showing the highest degree of self-averaging, followed by entanglement entropy, and fractal dimension displaying the least self-averaging in the ergodic phase. **(b2)** The scaling exponent of all the markers becomes weakly self-averaging ($\beta \sim 1$) close to $\alpha \sim 1$, and the $\alpha > 1$ regime is comparatively more self-averaging than the bulk states of the RP model. **(c1)** In the ground state of the RP model, all the markers stop exhibiting the self-averaging behavior after crossing the phase transition point $\gamma^{\infty} \sim 0.75$, leading to $\beta < 0$ as seen in **(c2)**.

RP ground states. A key distinction between the bulk and ground state phases is the absence of a fractal regime in the latter, where only ergodic and localized phases are detected via complexity markers. Notably, the ground state exhibits a first-order phase transition, raising the question of whether self-averaging behaves differently compared to the bulk. As shown in Fig. 9.10**c1**, self-averaging holds at $\gamma = 0$, but breaks down beyond the transition point at $\gamma = 0.8$, the marker even increases with N. This behavior is reminiscent of the vanishing marker values at large γ (see Fig. 9.6).

PLRBM bulk states. Similar to the RP bulk states, the PLRBM bulk state also shows the strongly self-averaging behavior, and near the Anderson critical point, at $\alpha = 1$, all the complexity markers still remain strongly self-averaging, i.e., $\beta = 1$ (see Fig. 9.10**b2**), which is a behavior quite different from that in the RP bulk states.

Since the scaling behavior of the self-averaging property in complexity markers reflects the ergodicity transitions observed in the markers themselves, one might speculate that in disordered systems where fluctuations play a crucial role, the self-averaging property could serve as a diagnostic tool for phase transitions.

9.7 Pauli spectrum for RP and PLRBM bulk states

The stabilizer Rényi entropy is defined as the Rényi entropy of a probability distribution constructed from the expectation values of Pauli strings on a given quantum state. Since a probability distribution inherently contains more information than any of its finite-order entropies, additional structure—particularly relevant in complex phases—is revealed by examining higher-order moments $\mathcal{M}_q$. Moreover, non-ergodic behavior is often captured by higher-order entropies, such as the fractal dimension D_q.

It is therefore worth investigating if relevant signatures can emerge from the *Pauli spectrum*, defined as the set of squared Pauli expectation values on the state [168,766]:

$$\mathrm{spec}(|\psi\rangle) = \left\{ |\langle\psi|P_i|\psi\rangle|^2,\ P_i \in \mathcal{P}_N;\ i = 0, 1, \ldots, 4^N - 1 \right\}. \tag{9.34}$$

The support of the Pauli spectrum, $i \in [0, 4^N - 1]$, changes depending on N. The *frequency distribution* of these expectation values,

$$\Pi_{\mathcal{P}}(|\psi\rangle) = \sum_i \frac{\delta(x - x_{P_i})}{4^N}, \qquad x_{P_i} = \langle\psi|P_i|\psi\rangle, \tag{9.35}$$

offers a diagnostic tool for understanding the ergodicity behavior independent of N. However, individual realizations would have different $\Pi_{\mathcal{P}}$, which can average away relevant features. Instead, we focus on the averaged Pauli spectrum, where the expectation value for each P_i is averaged over states from each realization. To better interpret its structure, we organize the Pauli strings by indexing i in a specific order: the first 2^N indices $i \in [0, 2^N - 1]$ correspond to diagonal operators $\{I, Z\}^{\otimes N}$, followed by all other (non-diagonal) strings. The overall ordering is then refined by sorting the values of $\langle P_i \rangle$ in descending order, using the localized state at $\alpha = 10$ or $\gamma = 10$ as a reference. This choice is motivated by the fact that localized states exhibit significant weight on the diagonal strings (see Fig. 9.11 **a2**, **b2**), and thus provide a natural order.

Ergodic states follow the Haar-random prediction (see Section 9.2.3) and exhibit an almost uniform distribution over Pauli strings around the value $\frac{1}{2^N+1}$, except for the identity component $I^{\otimes N}$, which saturates to 1, resulting in $\Pi_{\mathcal{P}}$ sharply peaked around zero (orange bars in Fig. 9.11 **a1**, **b1**) and low variance in the frequency distribution (orange shaded region in **a2**, **b2**). In contrast, localized states have only a few significant Pauli components (**a2**, **b2**), leading to larger individual $\langle P_i \rangle$ values and a broadened spectrum (blue bars in **a1**, **b1**).

Notably, exact stabilizer states yield Pauli expectation values of either $+1$ for all 2^N stabilizers, or a balanced set of $+1$ and -1 values [168], as can be observed in the RP bulk case (blue lines in **a2**). In the PLRBM model, however, bulk localized states do not align with the computational basis $\{I, Z\}^{\otimes N}$, resulting in a more dispersed Pauli spectrum (**b1**) compared to the RP model (**a1**). Even after averaging over random realizations, the PLRBM bulk state retains high variance in its Pauli spectrum across the non-ergodic and localized regimes, except in the ergodic phase where the distribution sharply concentrates [767].

In summary, the Pauli spectrum offers insight into why an ergodic state, which contains high magic, requires a larger number of basis states and is thus considered more complex, while a localized state, with non-zero contributing terms limited to a few Pauli strings, is considered less complex (see Fig. 9.1**b**). Furthermore, the difference between the RP and PLRBM models is clearly captured in the Pauli spectrum, where the less suppressed off-diagonal terms of the PLRBM model yield strong fluctuations even in the localized regime, thus providing a direct interpretation of the relatively high magic in the localized regime of PLRBM bulk states (see Fig. 9.8**c1**), compared to its RP counterpart.

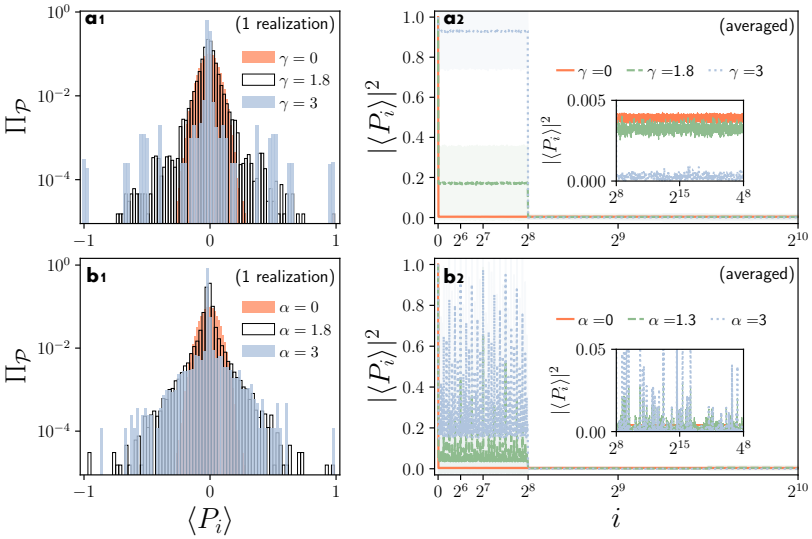

Figure 9.11. Frequency distribution for a single realization (left) and averaged Pauli-spectrum for a bulk state in the middle of the spectrum (right) of the RP (top) and PLRBM models (bottom). Data for $N = 8$ with 4000 and 8000 realizations, respectively. In the ergodic phase (orange), expectation values are nearly uniformly distributed over all Pauli strings with minimal variance (shaded regions in **a2, b2**), resulting in a distribution with small variance around $\langle P_i \rangle = 0$ in $\Pi_{\mathcal{P}}$ **(a1, b1)**. In contrast, localized states (blue) exhibit pronounced peaks in $\Pi_{\mathcal{P}}$, reflecting non-zero expectation values aligned with the stabilizer basis (notably within $i = [0, 2^N]$ in **a2, b2**). The intermediate regime shows partial delocalization with mixed features. These distinct distribution patterns are reflected in the magic values. Compared to RP, localization in PLRBM bulk states is weaker **(b1)** and exhibits reduced self-averaging behavior **(b2)**.

9.8 Summary and outlook

In this work, we have conducted a comparative study of various complexity markers across families of Hamiltonians that interpolate between ergodic, extended non-ergodic, and localized phases. When a fractal region in the parameter space is present, such as for states in the bulk of the Rosenzweig–Porter model spectrum, the different markers identify high and low complexity regimes in overlapping but distinct parameter regions. Both entanglement entropy and stabilizer Rényi entropy undergo a transition within the fractal phase that is not detected by the fractal dimension, indicating the existence of a non-ergodic yet complex regime with respect to these two markers. Moreover, the stabilizer Rényi entropy reveals an additional extended intermediate regime with non-maximal magic, before eventually dropping to low complexity in correspondence to the localization point. The presence of an extended fractal region seems to be crucial to the appearance of new complexity regimes: when such a region is absent, as in the ground state of the Rosenzweig–Porter model and the bulk of the power-law random banded model, the transition points identified by all complexity markers remain consistent. The behavior of the stabilizer Rényi entropy suggests that it can uncover subtle features in the quantum phase diagram that might otherwise go unnoticed using conventional localization markers. It would be interesting to corroborate these findings through analytical studies, e.g., of the Rosenzweig–Porter model akin to those employed for fractal dimensions [689].

Moreover, our analysis of the ergodic to integrable transition of the SYK_4 + Ising model suggests that stabilizer Rényi entropy may be a more sensitive marker to the underlying symmetries of the model, as indicated by its non-monotonic behavior as compared to the fractal dimension and the entanglement entropy. This observation motivates a more systematic investigation of the relationship between nonstabilizerness and symmetry classes in SYK-type models, extending beyond the cases considered in Refs. [762, 763]. Additionally, it would be valuable to study other quadratic perturbations of the SYK model to determine whether the complexity markers studied here can consistently capture the observed fragility of ground-state ergodicity. This is especially relevant for assessing the stability of the holographic phase, which has been argued to remain robust under deformations only within a vanishingly small region in the thermodynamic limit [768].

Investigating the presence of non-ergodic but highly complex regimes would not only shed light on the structure of the quantum phase diagram but also help assess the sensitivity of non-stabilizer magic to non-ergodic behavior and complexity transitions. This could be further pursued by analyzing many-body systems undergoing a many-body localization transition, where multifractal phases are expected to arise, such as disordered spin systems [769,770] and the Bose–Hubbard model [748,771]. Localization also plays a significant role in quantum optimization [243,570,571,574,772], whose target problems are often described by spin-glass models [236,529,538]. In these contexts, our work offers a promising perspective for probing complex characteristics of physical systems approaching the many-body localization transition.

The presence of distinct crossover values at finite system sizes is crucial for both classical and quantum simulations, as the feasible techniques are often constrained by available quantum resources. For instance, in noisy intermediate-scale quantum (NISQ) devices, the bottleneck is the ability to build up entanglement across the device [773], while in tensor networks, the reachable bond dimension constrains the

accessible entanglement entropy [91,542,673,674]. In contrast, the efficiency of classical calculations using the Gottesmann–Knill framework [148,149,151,158,166] as well as the cost of broad classes of fault-tolerant quantum computers [774, 775] is determined by the number of T-gates [167,545], which is related to the magic in a quantum state [165]. In this context, our analysis could guide the identification of the most efficient simulation strategies for each regime.

Chapter 10

Conclusions and Outlook

In this thesis, we demonstrated how various quantum resources enhance our understanding of quantum optimization and simulation, providing critical insights into the performance and capabilities of quantum technologies. After introducing the concepts of quantum resources and quantum optimization in Part I, we dedicated Part II entirely to quantum optimization and Part III to disordered systems.

We explored the quantumness of Quantum Approximate Optimization Algorithm (QAOA) and Quantum Annealing (QA) through squeezing, multipartite entanglement, and nonstabilizerness (magic), as well as experimentally measured entanglement on an IBM quantum device. We shed light on the role of quantum correlation in QAOA by connecting two fields of quantum technology: quantum computation and quantum metrology. The goal of metrology is to establish measurement protocols with increased sensitivity, and quantum computation aims to obtain the solution state with reduced uncertainty, both requiring a reduction in variance. By expressing the combinatorial MaxCut problem in terms of a collective spin basis, we are able to generate spin-squeezed states by finding optimal solutions to the MaxCut problem. We showed this both numerically and on the IBM Quantum chip. Then we connected this squeezing to quantum Fisher information and multipartite entanglement. Furthermore, squeezing generated by QAOA enabled us to propose a benchmark, where more squeezing is associated with a higher probability of the solution state, conventionally referred to as the approximation ratio of the quantum algorithm. Moreover, such squeezing can also detect errors in the circuit. We also extended this connection between the two fields to their benefits: using QAOA to generate arbitrary Dicke states, and using squeezed states to warm-start QAOA.

To understand the presence of multipartite entanglement in quantum optimization, we utilized the generalized geometric measure, a measure of genuine multipartite entanglement, in quantum annealing and QAOA. Using numerical benchmarks, we analyzed its occurrence in the annealing schedule in detail. We observed that entanglement increases with anneal time, and for successful instances, it decreases again, creating a multipartite entanglement barrier. We explored how such a barrier relates to the algorithm's success. We also proved how multipartite entanglement provides an upper bound to the overlap of the instantaneous state with an exact solution. Vice versa, the overlaps to the initial and final product states, which can be easily measured experimentally, offer upper bounds for the multipartite entanglement during the entire schedule.

Noisy devices raise the question of whether entanglement persists with longer circuit depth, as its absence would render the algorithm's success entirely dependent on classical algorithms. To validate such quantum effects in real devices, we chose

the new Heron processor from IBM Quantum to test entanglement generation in the QAOA layers, using the SWAP circuit. We first measured the purity of the subsystems, then extracted the maximum Schmidt coefficients, which served as a proxy for entanglement. We found that such entanglement persists even for large systems and significant depth, showing on the one hand that quantum effects play a role in the QAOA, as well as that current hardware is mature enough to run quantum optimization.

We also analyzed the presence of nonstabilizerness (a proxy for classical simulability) in QAOA. We found that both stabilizer Rényi entropy (SRE) and mana initially grow with circuit depth, peaking and then decreasing as the algorithm converges, creating a barrier that limits the algorithm's capability for shallow circuits. We found curves corresponding to different depths collapse under a simple rescaling, and we revealed a non-trivial relationship between the final SRE and the fidelity of final states. Finally, we identified a similar nonstabilizerness barrier also in quantum annealing.

In Part III, we turned to disordered systems. Since disorder mimics noise, understanding its effects helps model noisy devices. Averaging over disorder is computationally costly, so we developed an exact framework for disorder-averaged dynamics generated by periodic Hamiltonians (including (p, q)-potent ones). These results are valid for arbitrary initial states, evolution times, and even non-Hermitian systems. The ensemble dynamics resemble open-system evolution, with non-Markovian features depending on the disorder distribution and Hamiltonian periodicity. We illustrated this for systems built from spin-1/2, spin-1, and clock operators.

We also investigated complexity transitions in paradigmatic models such as the power-law random banded matrix model, the Rosenzweig–Porter model, and a hybrid SYK+Ising model. Using fractal dimension, von Neumann entropy, and SRE as markers, we identified sharp complexity transitions through finite-size scaling. These markers, while aligned in ergodic and localized regimes, diverged in intermediate phases. SRE in particular was highly sensitive to symmetries like fermion parity and time reversal. Our results show that no single marker suffices: combining different resources offers a better understanding of phase behavior and classical simulability.

Throughout this thesis, we explored various aspects of quantum resources and their exploitation in quantum optimization and many-body physics scenarios. Such quantum resources define what is easy and hard, given the free and resourceful operations within the resource theory. In quantum optimization, we observed that squeezing, multipartite entanglement, and nonstabilizerness all grow with the quantum run of the algorithm, validating that quantum algorithms are indeed quantum. Moreover, when asked for classical optimization problems, one is looking for a classical solution. In that case, all such resources must be reduced to the classical level, creating a resource barrier. The existence of such barriers makes the resource necessary for quantum algorithms, and understanding them is essential, as success is closely related to it. In many-body physics, such peaks can be related to phase transitions or crossovers, and it becomes interesting to understand if these barriers or transitions appear at the same transition points for different resources. As we discovered, this is not the case, suggesting that there may be multiple phases that require combining different resources for a comprehensive understanding. Our results provided more profound insights into how quantum resources influence quantum optimization, enabling a better understanding of the success of such algorithms and the recognition of new phases behind the wall of combined complexity markers arising from resource theories

in many-body physics.

We now turn to a discussion of possible future directions and outlooks based on the findings presented in this thesis. Since we had obtained squeezing for eight-qubit QAOA on IBM hardware, the quantum hardware architectures have evolved into over 100 qubits with substantially improved gate fidelities [460, 776]. Moreover, platforms based on trapped ions and neutral atoms have become increasingly accessible, making it feasible to perform cross-platform [777], large-scale benchmarks using squeezing as a diagnostic tool. Such an approach could potentially realize squeezed states with unprecedented precision [332]. This would not only validate the quantum nature of QAOA but also help identify the breakdown points of classical tensor-network simulations, offering a compelling case for quantum computational advantage. In parallel, growing attention has been devoted to understanding the behavior of quantum annealers [778] such as those developed by D-Wave [779, 780]. Exploring how different practical annealing schedules influence entanglement generation, and whether this entanglement correlates with the success of those schedules, could offer valuable insights into the behavior of quantum devices. While our study of nonstabilizerness in QAOA was limited to small system sizes due to computational overhead, recent advancements in tensor-network simulations of QAOA [265, 544] now open the door to probing larger system sizes. This would allow us to test the universality of the magic barrier observed across scales. Additionally, since SRE is, in principle, experimentally measurable [530], there is a clear opportunity to extend our entanglement-measurement pipeline to include nonstabilizerness; thereby concluding the empirical investigation of quantum resources explored in this thesis. A particularly intriguing avenue concerns the relationship between squeezing and non-classicality, specifically through the appearance of negative Wigner functions [781], which are also directly related to mana, a magic monotone. This raises the fundamental question of whether entanglement and magic are generated in a correlated manner within the QAOA framework. While several counterexamples suggest these resources can vary independently in other scenarios [522, 782, 783], if QAOA does exhibit correlated resource generation, it would represent a distinctive and possibly unique feature of the QAOA ansatz. This warrants deeper exploration, particularly in light of the discrete nature of the Clifford group and the challenge of designing QAOA evolutions that avoid magic generation entirely, allowing simulation through stabilizer formalism [151].

In the context of disorder-averaged dynamics, our focus was on exact analytical results, which led us to consider a specific type of Hamiltonian. Extending such analysis to other Hamiltonian classes, especially non-Hermitian systems [784], presents an exciting theoretical direction. In such regimes, fundamental questions arise: What constitutes a quantum resource under non-Hermitian dynamics? And do traditional criteria for non-Markovianity still apply? Furthermore, it is worth exploring whether experimental observation of non-Markovian features can facilitate a modelling method for the underlying disorder, which would be of interest for quantum control theory [785]. Our resource-based complexity analysis in random matrix models, encompassing entanglement, nonstabilizerness, and fractal dimensions, provides a comprehensive view of quantum complexity. Extending this multi-marker framework to other many-body systems and quantum optimization problems could uncover hidden structures in the non-ergodic regime, potentially leading to new classifications of quantum phases and a deeper understanding of quantum information structure in complex systems.

List of Publications

Peer-reviewed articles.

- **G. C. Santra**, F. Jendrzejewski, P. Hauke, D.J. Egger (2024). Squeezing and quantum approximate optimization.
  Physical Review A, 109(1), 012413 (**Editor's suggestion**) [325].
  Chapter 4
  Contribution: This project explores the connection between quantum squeezing and the Quantum Approximate Optimization Algorithm (QAOA), and uses this link to study the entanglement structure within QAOA. My contributions included performing numerical simulations of QAOA and squeezing, calculating the quantum Fisher information and multipartite entanglement, identifying the connection between squeezing and the proposed entanglement benchmark, and extending the analysis to arbitrary Dicke states. I also worked on implementing a warm-start approach for QAOA, contributed to the interpretation of the results, and participated in writing the manuscript.

- **G. C. Santra**, S.S. Roy, D.J. Egger, P. Hauke (2025). Genuine multipartite entanglement in quantum optimization.
  Physical Review A, 111(2), 022434. [503]
  Chapter 5
  Contribution: This project investigates the role of genuine multipartite entanglement in quantum optimization algorithms and its connection to algorithmic performance. My contributions included writing numerical code for entanglement measures and quantum annealing, generating and analyzing data, interpreting the results, and providing analytical proofs for the entanglement bounds. I also contributed to the project design and manuscript writing.

Preprints.

- **G. C. Santra**, P. Hauke (2024). Disorder-averaged Qudit Dynamics.
  arXiv preprint arXiv:2412.17519. [786]
  Chapter 8
  Contribution: This project aims to understand how open quantum system dynamics can emerge from disorder-averaged closed quantum systems. My contributions included deriving exact analytical calculations, executing numerical validations, and carrying out detailed calculations for all illustrative examples. I also contributed to the project design and manuscript writing.

- **G. C. Santra**, A. Windey, S. Bandyopadhyay, A. Legramandi, P. Hauke (2025). Complexity transitions in chaotic quantum systems.

arXiv preprint arXiv:2505.09707. [522]
Chapter 9
Contribution: This project investigates various complexity markers in disordered many-body quantum systems. My contributions included developing the numerical code for all complexity markers and random matrix models, running simulations for the Rosenzweig–Porter model in both the bulk and ground-state regimes, and preparing all figures for the manuscript. I also contributed to the project design and manuscript writing.

- C. Capecci, **G.C. Santra**, A. Bottarelli, E. Tirrito, P. Hauke (2025). Role of Nonstabilizerness in Quantum Optimization.
arXiv preprint arXiv:2505.17185. [765]
Chapter 7
Contribution. This project explores the role of nonstabilizerness in the Quantum Approximate Optimization Algorithm (QAOA). Together with the first author, I contributed to the development of the numerical code for evaluating nonstabilizerness markers in qudit systems. I contributed to the analytical calculations used to interpret the data, project design, and wrote parts of the manuscript.

Under preparation

- **G.C. Santra**, P. Hauke, D.J. Egger (2025). Validating quantum effects in quantum optimization
to be arXived
Chapter 6
Contribution. This project focuses on identifying and validating multipartite entanglement in quantum optimization algorithms on IBM hardware. My contributions included setting up the numerical framework for the experiments, gathering experimental data, conducting exact and noisy simulations, and analyzing data. I also contributed to the project design, interpretation of the results, and the writing of the manuscript.

Others (not included in the thesis)

- A.N. Madhusudan[1], **G.C. Santra**[1], I. Kaur, W. Li, R. Nath. (2024). Commensurate supersolids and re-entrant transitions in an extended Bose-Hubbard ladder.
arXiv preprint arXiv:2407.20107. [787]

- **G.C. Santra**, J. Mildenberger, E. Ballini, A. Bottarelli, M.M. Wauters, P. Hauke. Quantum Resource in Non-Abelian Lattice Gauge Theory
under preparation

- **G.C. Santra**, J. Mildenberger, P. Hauke, R.C. Almeida. Stabilizer Fisher Information
under preparation

[1]These authors contributed equally.

Bibliography

[1] J. Ignacio Cirac and Peter Zoller. Quantum computations with cold trapped ions. *Physical Review Letters*, 74(20):4091–4094, 1995. (cited on page 1)

[2] C. Monroe, D. M. Meekhof, B. E. King, W. M. Itano, and D. J. Wineland. Demonstration of a fundamental quantum logic gate. *Physical Review Letters*, 75(25):4714–4717, 1995. (cited on page 1)

[3] Rainer Blatt and David Wineland. Entangled states of trapped atomic ions. *Nature*, 453:1008–1015, 2008. (cited on page 1)

[4] Pieter Kok, W. J. Munro, Kae Nemoto, T. C. Ralph, Jonathan P. Dowling, and G. J. Milburn. Linear optical quantum computing with photonic qubits. *Reviews of Modern Physics*, 79(1):135–174, 2007. (cited on page 1)

[5] L. Isenhower, E. Urban, X. L. Zhang, A. T. Gill, T. Henage, T. A. Johnson, T. G. Walker, and M. Saffman. Demonstration of a neutral atom controlled-not quantum gate. *Physical Review Letters*, 104(1):010503, 2010. (cited on page 1)

[6] T. Wilk, A. Gaëtan, C. Evellin, J. Wolters, Y. Miroshnychenko, P. Grangier, and A. Browaeys. Entanglement of two individual neutral atoms using rydberg blockade. *Physical Review Letters*, 104(1):010502, 2010. (cited on page 1)

[7] John Clarke and Frank K. Wilhelm. Superconducting quantum bits. *Nature*, 453:1031–1042, 2008. (cited on page 1)

[8] David J. Wineland, C. Monroe, W. M. Itano, D. Leibfried, B. E. King, and D. M. Meekhof. Experimental issues in coherent quantum-state manipulation of trapped atomic ions. *Journal of Research of the National Institute of Standards and Technology*, 103(3):259–328, 1998. (cited on page 1)

[9] Jerry M. Chow, Jay M. Gambetta, Antonio D. Córcoles, Seth T. Merkel, Chad Rigetti, John A. Smolin, Jay M. Gambetta, Blake R. Johnson, Colm A. Ryan, Toyohiro Ohki, et al. Universal quantum gate set approaching fault-tolerant thresholds with superconducting qubits. *Physical Review Letters*, 109(6):060501, 2012. (cited on page 1)

[10] Michel H. Devoret and Robert J. Schoelkopf. Superconducting circuits for quantum information: An outlook. *Science*, 339(6124):1169–1174, 2013. (cited on page 1)

[11] Frank Arute, Kunal Arya, Ryan Babbush, Dave Bacon, Joseph C Bardin, Rami Barends, Rupak Biswas, Sergio Boixo, Fernando GSL Brandao, David A Buell, et al. Quantum supremacy using a programmable superconducting processor. *Nature*, 574(7779):505–510, 2019. (cited on pages 1 and 2)

[12] Morten Kjaergaard, Matthew E Schwartz, Johannes Braumüller, Philip Krantz, J. I. Jan Wang, Simon Gustavsson, and William D Oliver. Superconducting qubits: Current state of play. *Annual Review of Condensed Matter Physics*, 11:369–395, 2020. (cited on page 1)

[13] Rainer Blatt and Christian F Roos. Quantum simulations with trapped ions. *Nature Physics*, 8(4):277–284, 2012. (cited on page 1)

[14] Christopher Monroe and et al. Demonstration of a programmable two-qubit quantum processor. *Nature*, 536:63–66, 2016. (cited on page 1)

[15] Christopher Monroe and Jungsang Kim. Programmable quantum simulations of spin systems with trapped ions. *Science*, 339(6124):1164–1168, 2013. (cited on page 1)

[16] Hannes Bernien, Sebastian Schwartz, Alexander Keesling, Herbert Levine, Ahmed Omran, Hannes Pichler, Soonwon Choi, Alexander S. Zibrov, Manuel Endres, Markus Greiner, Vladan Vuletić, and Mikhail D. Lukin. Probing many-body dynamics on a 51-atom quantum simulator. *Nature*, 551:579–584, 2017. (cited on pages 1 and 4)

[17] Antoine Browaeys and Thierry Lahaye. Many-body physics with individually controlled rydberg atoms. *Nature Physics*, 16(2):132–142, 2020. (cited on page 1)

[18] Jeremy L. O'Brien. Photonic quantum technologies. *Nature Photonics*, 3:687–695, 2009. (cited on page 1)

[19] Stefano Pirandola, Ulrik L Andersen, Leonardo Banchi, Mario Berta, Darius Bunandar, Roger Colbeck, Dirk Englund, Tobias Gehring, Cosmo Lupo, Carlo Ottaviani, et al. Advances in quantum cryptography. *Advances in optics and photonics*, 12(4):1012–1236, 2020. (cited on page 1)

[20] Laura Clinton, Toby Cubitt, Brian Flynn, Filippo Maria Gambetta, Joel Klassen, Ashley Montanaro, Stephen Piddock, Raul A Santos, and Evan Sheridan. Towards near-term quantum simulation of materials. *Nature Communications*, 15(1):211, 2024. (cited on page 1)

[21] Raffaele Santagati, Alan Aspuru-Guzik, Ryan Babbush, Matthias Degroote, Leticia González, Elica Kyoseva, Nikolaj Moll, Markus Oppel, Robert M Parrish, Nicholas C Rubin, et al. Drug design on quantum computers. *Nature Physics*, 20(4):549–557, 2024. (cited on page 1)

[22] Amira Abbas, Andris Ambainis, Brandon Augustino, Andreas Bärtschi, Harry Buhrman, Carleton Coffrin, Giorgio Cortiana, Vedran Dunjko, Daniel J Egger, Bruce G Elmegreen, et al. Challenges and opportunities in quantum optimization. *Nature Reviews Physics*, pages 1–18, 2024. (cited on pages 1, 3, 41, 47, and 95)

[23] J. Zhang, G. Pagano, P. W. Hess, A. Kyprianidis, P. Becker, H. Kaplan, A. V. Gorshkov, Z.-X. Gong, and C. Monroe. Observation of a many-body dynamical phase transition with a 53-qubit quantum simulator. *Nature*, 551:601–604, 2017. (cited on page 1)

[24] Sepehr Ebadi, Tout T Wang, Harry Levine, Alexander Keesling, Giulia Semeghini, Ahmed Omran, Dolev Bluvstein, Rhine Samajdar, Hannes Pichler, Wen Wei Ho, et al. Quantum phases of matter on a 256-atom programmable quantum simulator. *Nature*, 595(7866):227–232, 2021. (cited on pages 1 and 4)

[25] Christian Gross and Immanuel Bloch. Quantum simulations with ultracold atoms in optical lattices. *Science*, 357(6355):995–1001, 2017. (cited on page 1)

[26] Zhihuang Luo, Yi-Zhuang You, Jun Li, Chao-Ming Jian, Dawei Lu, Cenke Xu, Bei Zeng, and Raymond Laflamme. Quantum simulation of the non-fermi-liquid state of sachdev-ye-kitaev model. *npj Quantum Information*, 5(1):53, 2019. (cited on page 1)

[27] Marcello Dalmonte and Peter Zoller. Quantum simulation of lattice gauge theories with ultracold atoms in optical lattices. *Reports on Progress in Physics*, 79(2):024401, 2016. (cited on page 1)

[28] Mari Carmen Banuls, Rainer Blatt, J. Ignacio Cirac, Marcello Dalmonte, Jens Eisert, Rick van Bijnen, Maciej Lewenstein, Simone Montangero, and U.-J. Wiese. Simulating lattice gauge theories within quantum technologies. *The European Physical Journal D*, 74:165, 2020. (cited on page 1)

[29] Julius Mildenberger, Wojciech Mruczkiewicz, Jad C Halimeh, Zhang Jiang, and Philipp Hauke. Confinement in a z 2 lattice gauge theory on a quantum computer. *Nature Physics*, 21(2):312–317, 2025. (cited on page 1)

[30] Michael Meth, Jinglei Zhang, Jan F Haase, Claire Edmunds, Lukas Postler, Andrew J Jena, Alex Steiner, Luca Dellantonio, Rainer Blatt, Peter Zoller, et al. Simulating two-dimensional lattice gauge theories on a qudit quantum computer. *Nature Physics*, pages 1–7, 2025. (cited on page 1)

[31] Tyler A Cochran, Bernhard Jobst, Eliott Rosenberg, Yuri D Lensky, Gaurav Gyawali, Norhan Eassa, Melissa Will, Aaron Szasz, Dmitry Abanin, Rajeev Acharya, et al. Visualizing dynamics of charges and strings in (2+ 1) d lattice gauge theories. *Nature*, pages 1–6, 2025. (cited on page 1)

[32] Daniel González-Cuadra, Majd Hamdan, Torsten V Zache, Boris Braverman, Milan Kornjača, Alexander Lukin, Sergio H Cantú, Fangli Liu, Sheng-Tao Wang, Alexander Keesling, et al. Observation of string breaking on a (2+ 1) d rydberg quantum simulator. *Nature*, pages 1–6, 2025. (cited on page 1)

[33] Arinjoy De, Alessio Lerose, De Luo, Federica M Surace, Alexander Schuckert, Elizabeth R Bennewitz, Brayden Ware, William Morong, Kate S Collins, Zohreh Davoudi, et al. Observation of string-breaking dynamics in a quantum simulator. *arXiv preprint arXiv:2410.13815*, 2024. (cited on page 1)

[34] Markus Reiher, Nathan Wiebe, Krysta M. Svore, Dave Wecker, and Matthias Troyer. Elucidating reaction mechanisms on quantum computers. *Proceedings of the National Academy of Sciences of the United States of America*, 114(29):7555–7560, 2017. (cited on page 1)

[35] Ieva Liepuoniute, Mario Motta, Thaddeus Pellegrini, Julia E Rice, Tanvi P Gujarati, Sofia Gil, and Gavin O Jones. Simulation of a diels–alder reaction on a quantum computer. *Physical Chemistry Chemical Physics*, 26(38):25181–25191, 2024. (cited on page 1)

[36] Brian Swingle. Entanglement renormalization and holography. *Physical Review D*, 86(6):065007, 2012. (cited on page 1)

[37] Xiao Mi, Matteo Ippoliti, Chris Quintana, Jonas A Gross, Thomas Schuster, Michael Block, Jens Koch, Matthew Reagor, Andrew W Cross, Dario Rosenberg, et al. Information scrambling in quantum circuits. *Science*, 374(6574):1479–1483, 2021. (cited on page 1)

[38] Martin Gärttner, Justin G Bohnet, Arghavan Safavi-Naini, Michael L Wall, John J Bollinger, and Ana Maria Rey. Measuring out-of-time-order correlations and multiple quantum spectra in a trapped-ion quantum magnet. *Nature Physics*, 13(8):781–786, 2017. (cited on page 1)

[39] Timothy Proctor, Kevin Young, Andrew D Baczewski, and Robin Blume-Kohout. Benchmarking quantum computers. *Nature Reviews Physics*, 7(2):105–118, 2025. (cited on page 1)

[40] Salonik Resch and Ulya R Karpuzcu. Benchmarking quantum computers and the impact of quantum noise. *ACM Computing Surveys (CSUR)*, 54(7):1–35, 2021. (cited on page 1)

[41] Jens Eisert, Dominik Hangleiter, Nathan Walk, Ingo Roth, Damian Markham, Rhea Parekh, Ulysse Chabaud, and Elham Kashefi. Quantum certification and benchmarking. *Nature Reviews Physics*, 2(7):382–390, 2020. (cited on page 1)

[42] Andreas Elben, Benoît Vermersch, Rick Van Bijnen, Christian Kokail, Tiff Brydges, Christine Maier, Manoj K Joshi, Rainer Blatt, Christian F Roos, and Peter Zoller. Cross-platform verification of intermediate scale quantum devices. *Physical review letters*, 124(1):010504, 2020. (cited on page 1)

[43] Jose Carrasco, Andreas Elben, Christian Kokail, Barbara Kraus, and Peter Zoller. Theoretical and experimental perspectives of quantum verification. *PRX Quantum*, 2(1):010102, 2021. (cited on page 1)

[44] Youngseok Kim, Andrew Eddins, Sajant Anand, Ken Xuan Wei, Ewout Van Den Berg, Sami Rosenblatt, Hasan Nayfeh, Yantao Wu, Michael Zaletel, Kristan Temme, et al. Evidence for the utility of quantum computing before fault tolerance. *Nature*, 618(7965):500–505, 2023. (cited on pages 1, 66, and 67)

[45] Nils Herrmann, Daanish Arya, Marcus W Doherty, Angus Mingare, Jason C Pillay, Florian Preis, and Stefan Prestel. Quantum utility–definition and assessment of a practical quantum advantage. In *2023 IEEE International Conference on Quantum Software (QSW)*, pages 162–174. IEEE, 2023. (cited on pages 1 and 2)

[46] Zhenyu Cai, Ryan Babbush, Simon C Benjamin, Suguru Endo, William J Huggins, Ying Li, Jarrod R McClean, and Thomas E O'Brien. Quantum error mitigation. *Reviews of Modern Physics*, 95(4):045005, 2023. (cited on page 1)

[47] Eric Chitambar and Gilad Gour. Quantum resource theories. *Rev. Mod. Phys.*, 91:025001, Apr 2019. (cited on pages 1, 2, 9, 96, 127, and 163)

[48] Max Planck. Über eine verbesserung der Wien'schen spektralgleichung. *Verhandlungen der Deutschen Physikalischen Gesellschaft*, 2:202–204, 1900. (cited on page 2)

[49] Max Planck. Zur theorie des gesetzes der energieverteilung im normalspectrum. *Verhandlungen der Deutschen Physikalischen Gesellschaft*, 2:237–245, 1900. (cited on page 2)

[50] Max Planck. Über das gesetz der energieverteilung im normalspectrum. *Annalen der Physik*, 4:553–563, 1901. (cited on page 2)

[51] Albert Einstein. Über einen die erzeugung und verwandlung des lichtes betreffenden heuristischen gesichtspunkt. *Annalen der Physik*, 322(6):132–148, 1905. (cited on page 2)

[52] Werner Heisenberg. Über quantentheoretische umdeutung kinematischer und mechanischer beziehungen. *Zeitschrift für Physik*, 33:879–893, 1925. (cited on page 2)

[53] Werner Heisenberg. Über den anschaulichen inhalt der quantentheoretischen kinematik und mechanik. *Zeitschrift für Physik*, 43(3–4):172–198, 1927. (cited on page 2)

[54] Erwin Schrödinger. Quantisierung als eigenwertproblem. *Annalen der Physik*, 79(4):361–376, 1926. (cited on page 2)

[55] P. A. M. Dirac. On the theory of quantum mechanics. *Proceedings of the Royal Society A*, 112:661–677, 1926. (cited on page 2)

[56] Max Born. Zur quantenmechanik der stoßvorgänge. *Zeitschrift für Physik*, 37:863–867, 1926. (cited on page 2)

[57] Niels Bohr. Das quantenpostulat und die neuere entwicklung der atomistik. *Naturwissenschaften*, 16:245–257, 1928. (cited on page 2)

[58] Paul A. M. Dirac. *The Principles of Quantum Mechanics*. Oxford University Press, 1930. (cited on page 2)

[59] John von Neumann. *Mathematische Grundlagen der Quantenmechanik*. Springer, 1932. (cited on page 2)

[60] Clinton Davisson and Lester H. Germer. Diffraction of electrons by a crystal of nickel. *Physical Review*, 30(6):705–741, 1927. (cited on page 2)

[61] Claus Jönsson. Elektroneninterferenzen an mehreren kunstlich hergestellten feinspalten. *Zeitschrift für Physik*, 161:454–474, 1961. (cited on page 2)

[62] Yuri Mannin. Computable and non-computable. *Sov. Radio*, 1980. (cited on page 2)

[63] Richard P. Feynman, Robert B. Leighton, and Matthew Sands. *The Feynman Lectures on Physics, Volume 3*. Addison-Wesley, Reading, MA, 1965. (cited on page 2)

[64] Richard P Feynman. Simulating physics with computers. *International Journal of Theoretical Physics*, 21(6-7):467–488, 1982. (cited on page 2)

[65] Charles H. Bennett and Gilles Brassard. Quantum cryptography: Public key distribution and coin tossing. In *Proceedings of IEEE International Conference on Computers, Systems and Signal Processing*, pages 175–179, 1984. (cited on page 2)

[66] Peter W Shor. Algorithms for quantum computation: discrete logarithms and factoring. In *Proceedings 35th annual symposium on foundations of computer science*, pages 124–134. Ieee, 1994. (cited on pages 2 and 45)

[67] Charles H. Bennett, F. Bessett, Gilles Brassard, Louis Salvail, and John A. Smolin. Experimental quantum cryptography. *Journal of Cryptology*, 5(1):3–28, 1992. (cited on page 2)

[68] Isaac L. Chuang, Neil Gershenfeld, Mark Kubinec, and David W. Leung. Experimental implementation of fast quantum searching. *Physical Review Letters*, 80(15):3408–3411, 1998. (cited on page 2)

[69] S. Deachapunya, Sengpis Chiangga, and Harald Weinfurter. Experimental Quantum Cryptography based on the BB84 Protocol. *Current Applied Science and Technology*, 1(1):80–83, 2001. (cited on page 2)

[70] Lieven M. K. Vandersypen, Matthias Steffen, Gregory Breyta, Costantino S. Yannoni, Mark H. Sherwood, and Isaac L. Chuang. Experimental realization of shor's quantum factoring algorithm using nuclear magnetic resonance. *Nature*, 414:883–887, 2001. (cited on page 2)

[71] Peter W. Shor. Scheme for reducing decoherence in quantum computer memory. *Physical Review A*, 52(4):R2493–R2496, 1995. (cited on page 2)

[72] Dorit Aharonov and Michael Ben-Or. Fault-tolerant quantum computation with constant error rate. *SIAM Journal on Computing*, 38(4):1207–1282, 2008. (cited on page 2)

[73] Frank Verstraete, Valentin Murg, and J. Ignacio Cirac. Matrix product states, projected entangled pair states, and variational renormalization group methods for quantum spin systems. *Advances in Physics*, 57(2):143–224, 2008. (cited on page 2)

[74] J. Ignacio Cirac, David Pérez-García, Norbert Schuch, and Frank Verstraete. Matrix product states and projected entangled pair states: Concepts, symmetries, theorems. *Rev. Mod. Phys.*, 93:045003, Dec 2021. (cited on pages 2 and 122)

[75] Andrew J Daley, Immanuel Bloch, Christian Kokail, Stuart Flannigan, Natalie Pearson, Matthias Troyer, and Peter Zoller. Practical quantum advantage in quantum simulation. *Nature*, 607(7920):667–676, 2022. (cited on pages 2, 4, and 163)

[76] Ryan LaRose. A brief history of quantum vs classical computational advantage. In *arXiv preprint*, 2024. (cited on page 2)

[77] Cupjin Huang, Fang Zhang, Michael Newman, Junjie Cai, Xun Gao, Zhengxiong Tian, Junyin Wu, Haihong Xu, Huanjun Yu, Bo Yuan, et al. Classical simulation of quantum supremacy circuits. *arXiv preprint arXiv:2005.06787*, 2020. (cited on page 2)

[78] Johnnie Gray and Stefanos Kourtis. Hyper-optimized tensor network contraction. *Quantum*, 5:410, 2021. (cited on page 2)

[79] Feng Pan and Pan Zhang. Simulating the sycamore quantum supremacy circuits. *arXiv preprint arXiv:2103.03074*, 2021. (cited on page 2)

[80] Yong Liu, Xin Liu, Fang Li, Haohuan Fu, Yuling Yang, Jiawei Song, Pengpeng Zhao, Zhen Wang, Dajia Peng, Huarong Chen, et al. Closing the" quantum supremacy" gap: achieving real-time simulation of a random quantum circuit using a new sunway supercomputer. In *Proceedings of the international conference for high performance computing, networking, storage and analysis*, pages 1–12, 2021. (cited on page 2)

[81] Edward Farhi, Jeffrey Goldstone, and Sam Gutmann. A quantum approximate optimization algorithm. *arXiv:1411.4028*, 2014. (cited on pages 2, 3, 48, 51, 52, 111, 124, and 127)

[82] Boaz Barak, Prasad Raghavendra, and David Steurer. Beating the random assignment on constraint satisfaction problems of bounded degree. *SIAM Journal on Computing*, 46(1):330–361, 2017. (cited on page 2)

[83] Matthew B. Hastings. Classical and quantum algorithms for the maxcut problem. *Quantum*, 3:156, 2019. (cited on page 2)

[84] V. Vedral, M. B. Plenio, M. A. Rippin, and P. L. Knight. Quantifying entanglement. *Phys. Rev. Lett.*, 78:2275–2279, Mar 1997. (cited on pages 3 and 17)

[85] Victor Veitch, S A Hamed Mousavian, Daniel Gottesman, and Joseph Emerson. The resource theory of stabilizer quantum computation. *New Journal of Physics*, 16(1):013009, jan 2014. (cited on pages 3, 29, 30, 32, 33, 127, 128, and 164)

[86] Christos H Papadimitriou and Kenneth Steiglitz. *Combinatorial optimization: algorithms and complexity*. Courier Corporation, 1998. (cited on page 3)

[87] John Preskill. Quantum computing in the nisq era and beyond. *Quantum*, 2:79, 2018. (cited on pages 3, 47, and 127)

[88] Richard Jozsa and Noah Linden. On the role of entanglement in quantum-computational speed-up. *Proceedings of the Royal Society of London. Series A: Mathematical, Physical and Engineering Sciences*, 459(2036):2011–2032, 2003. (cited on pages 3, 27, and 95)

[89] J Ignacio Cirac and Peter Zoller. Goals and opportunities in quantum simulation. *Nature physics*, 8(4):264–266, 2012. (cited on pages 3 and 127)

[90] Iulia M Georgescu, Sahel Ashhab, and Franco Nori. Quantum simulation. *Reviews of Modern Physics*, 86(1):153–185, 2014. (cited on pages 3 and 163)

[91] Román Orús. Tensor networks for complex quantum systems. *Nature Reviews Physics*, 1(9):538–550, 2019. (cited on pages 3, 137, 163, 164, 167, and 189)

[92] Brian M Austin, Dmitry Yu Zubarev, and William A Lester Jr. Quantum monte carlo and related approaches. *Chemical reviews*, 112(1):263–288, 2012. (cited on page 4)

[93] Adam L Shaw, Zhuo Chen, Joonhee Choi, Daniel K Mark, Pascal Scholl, Ran Finkelstein, Andreas Elben, Soonwon Choi, and Manuel Endres. Benchmarking highly entangled states on a 60-atom analogue quantum simulator. *Nature*, 628(8006):71–77, 2024. (cited on page 4)

[94] Mihir Kavishwar. Quantum computing 1: Breaking down the process, March 2024. (cited on page 5)

[95] Microsoft Copilot AI. Generated by microsoft copilot ai, 2025. AI-assisted citation generation. (cited on page 5)

[96] Ingemar Bengtsson and Karol Zyczkowski. A brief introduction to multipartite entanglement. *arXiv preprint arXiv:1612.07747*, 2016. (cited on pages 5, 19, 20, and 21)

[97] Juan Maldacena and Douglas Stanford. Remarks on the sachdev-ye-kitaev model. *Phys. Rev. D*, 94:106002, Nov 2016. (cited on page 5)

[98] M PA. Dynamical protein interaction pathways: A molecular root to diseases. 2024. (cited on page 5)

[99] NL Diaz, Antonio Anna Mele, Pablo Bermejo, Paolo Braccia, Andrew E Deneris, Martin Larocca, and M Cerezo. A unified approach to quantum resource theories and a new class of free operations. *arXiv preprint arXiv:2507.10851*, 2025. (cited on page 5)

[100] Charles H. Bennett, Gilles Brassard, Claude Crépeau, Richard Jozsa, Asher Peres, and William K. Wootters. Teleporting an unknown quantum state via dual classical and einstein-podolsky-rosen channels. *Phys. Rev. Lett.*, 70:1895–1899, Mar 1993. (cited on pages 11 and 18)

[101] Carlos Palazuelos. Superactivation of quantum nonlocality. *Phys. Rev. Lett.*, 109:190401, Nov 2012. (cited on pages 11 and 13)

[102] Kohdai Kuroiwa, Ryuji Takagi, Gerardo Adesso, and Hayata Yamasaki. Every quantum helps: Operational advantage of quantum resources beyond convexity. *Phys. Rev. Lett.*, 132:150201, Apr 2024. (cited on page 12)

[103] Michał Horodecki, Paweł Horodecki, and Ryszard Horodecki. Mixed-state entanglement and distillation: Is there a "bound" entanglement in nature? *Phys. Rev. Lett.*, 80:5239–5242, Jun 1998. (cited on page 12)

[104] Guifré Vidal. Entanglement monotones. *Journal of Modern Optics*, 47(2-3):355–376, 2000. (cited on page 13)

[105] Matthew J Donald, Michał Horodecki, and Oliver Rudolph. The uniqueness theorem for entanglement measures. *Journal of Mathematical Physics*, 43(9):4252–4272, 2002. (cited on page 14)

[106] Barbara Synak-Radtke and Michał Horodecki. On asymptotic continuity of functions of quantum states. *Journal of Physics A: Mathematical and General*, 39(26):L423, 2006. (cited on page 14)

[107] Mark Fannes. A continuity property of the entropy density for spin lattice systems. *Communications in Mathematical Physics*, 31(4):291–294, 1973. (cited on page 14)

[108] Koenraad MR Audenaert. A sharp continuity estimate for the von neumann entropy. *Journal of Physics A: Mathematical and Theoretical*, 40(28):8127, 2007. (cited on page 14)

[109] Alfréd Rényi. On measures of entropy and information. In *Proceedings of the fourth Berkeley symposium on mathematical statistics and probability, volume 1: contributions to the theory of statistics*, volume 4, pages 547–562. University of California Press, 1961. (cited on page 15)

[110] Dénes Petz. Quasi-entropies for finite quantum systems. *Reports on mathematical physics*, 23(1):57–65, 1986. (cited on page 15)

[111] V. Vedral. The role of relative entropy in quantum information theory. *Rev. Mod. Phys.*, 74:197–234, Mar 2002. (cited on page 15)

[112] Matthew J Donald and Michał Horodecki. Continuity of relative entropy of entanglement. *Physics Letters A*, 264(4):257–260, 1999. (cited on page 15)

[113] Carl W Helstrom. Quantum detection and estimation theory. *Journal of Statistical Physics*, 1:231–252, 1969. (cited on page 16)

[114] Alexander S Holevo. Statistical decision theory for quantum systems. *Journal of multivariate analysis*, 3(4):337–394, 1973. (cited on page 16)

[115] Abner Shimony. Degree of entanglement. *Annals of the New York Academy of Sciences*, 755(1):675–679, 1995. (cited on pages 16, 25, and 96)

[116] Howard Barnum and Noah Linden. Monotones and invariants for multi-particle quantum states. *Journal of Physics A: Mathematical and General*, 34(35):6787, 2001. (cited on pages 16, 25, and 96)

[117] Christopher A Fuchs and Jeroen Van De Graaf. Cryptographic distinguishability measures for quantum-mechanical states. *IEEE Transactions on Information Theory*, 45(4):1216–1227, 1999. (cited on page 16)

[118] Charles H. Bennett, Herbert J. Bernstein, Sandu Popescu, and Benjamin Schumacher. Concentrating partial entanglement by local operations. *Phys. Rev. A*, 53:2046–2052, Apr 1996. (cited on page 17)

[119] Sevag Gharibian. Strong np-hardness of the quantum separability problem. *arXiv preprint arXiv:0810.4507*, 2008. (cited on page 17)

[120] Ryszard Horodecki, Paweł Horodecki, Michał Horodecki, and Karol Horodecki. Quantum entanglement. *Rev. Mod. Phys.*, 81:865–942, Jun 2009. (cited on page 17)

[121] Charles H. Bennett, David P. DiVincenzo, Christopher A. Fuchs, Tal Mor, Eric Rains, Peter W. Shor, John A. Smolin, and William K. Wootters. Quantum nonlocality without entanglement. *Phys. Rev. A*, 59:1070–1091, Feb 1999. (cited on page 17)

[122] A. Einstein, B. Podolsky, and N. Rosen. Can quantum-mechanical description of physical reality be considered complete? *Phys. Rev.*, 47:777–780, May 1935. (cited on page 18)

[123] J. S. Bell. On the einstein podolsky rosen paradox. *Physics Physique Fizika*, 1:195–200, Nov 1964. (cited on page 18)

[124] Charles H. Bennett and Stephen J. Wiesner. Communication via one- and two-particle operators on einstein-podolsky-rosen states. *Phys. Rev. Lett.*, 69:2881–2884, Nov 1992. (cited on page 18)

[125] Artur K. Ekert. Quantum cryptography based on bell's theorem. *Phys. Rev. Lett.*, 67:661–663, Aug 1991. (cited on page 18)

[126] W. Dür, G. Vidal, and J. I. Cirac. Three qubits can be entangled in two inequivalent ways. *Phys. Rev. A*, 62:062314, Nov 2000. (cited on page 19)

[127] Daniel M Greenberger, Michael A Horne, and Anton Zeilinger. Going beyond bell's theorem. In *Bell's theorem, quantum theory and conceptions of the universe*, pages 69–72. Springer, 1989. (cited on page 20)

[128] Dik Bouwmeester, Jian-Wei Pan, Matthew Daniell, Harald Weinfurter, and Anton Zeilinger. Observation of three-photon greenberger-horne-zeilinger entanglement. *Physical Review Letters*, 82(7):1345, 1999. (cited on page 21)

[129] Ashish V Thapliyal. Multipartite pure-state entanglement. *Physical Review A*, 59(5):3336, 1999. (cited on page 21)

[130] Wolfgang Dür, Guifre Vidal, and J Ignacio Cirac. Three qubits can be entangled in two inequivalent ways. *Physical Review A*, 62(6):062314, 2000. (cited on page 21)

[131] Otfried Gühne, Géza Tóth, and Hans J Briegel. Multipartite entanglement in spin chains. *New Journal of Physics*, 7(1):229, 2005. (cited on page 22)

[132] Vittorio Giovannetti, Seth Lloyd, and Lorenzo Maccone. Quantum metrology. *Phys. Rev. Lett.*, 96:010401, Jan 2006. (cited on pages 23 and 73)

[133] C Radhakrishna Rao. Information and the accuracy attainable in the estimation of statistical parameters. In *Breakthroughs in Statistics: Foundations and basic theory*, pages 235–247. Springer, 1992. (cited on page 23)

[134] Harald Cramér. *Mathematical methods of statistics*, volume 9. Princeton university press, 1946. (cited on page 23)

[135] Ronald A Fisher. On the mathematical foundations of theoretical statistics. *Philosophical transactions of the Royal Society of London. Series A, containing papers of a mathematical or physical character*, 222(594-604):309–368, 1922. (cited on page 23)

[136] Ronald Aylmer Fisher. Theory of statistical estimation. In *Mathematical proceedings of the Cambridge philosophical society*, volume 22, pages 700–725. Cambridge University Press, 1925. (cited on page 23)

[137] Samuel L. Braunstein and Carlton M. Caves. Statistical distance and the geometry of quantum states. *Phys. Rev. Lett.*, 72:3439–3443, May 1994. (cited on pages 24 and 77)

[138] Samuel L Braunstein, Carlton M Caves, and Gerard J Milburn. Generalized uncertainty relations: Theory, examples, and lorentz invariance. *annals of physics*, 247(1):135–173, 1996. (cited on page 24)

[139] Philipp Hyllus, Wiesław Laskowski, Roland Krischek, Christian Schwemmer, Witlef Wieczorek, Harald Weinfurter, Luca Pezzé, and Augusto Smerzi. Fisher information and multiparticle entanglement. *Phys. Rev. A*, 85(2):022321, 2012. (cited on pages 25, 73, 76, 77, and 80)

[140] Géza Tóth. Multipartite entanglement and high-precision metrology. *Phys. Rev. A*, 85(2):022322, 2012. (cited on pages 25, 73, 77, 80, and 81)

[141] Tzu-Chieh Wei and Paul M. Goldbart. Geometric measure of entanglement and applications to bipartite and multipartite quantum states. *Phys. Rev. A*, 68:042307, Oct 2003. (cited on pages 25, 27, 96, and 110)

[142] Aditi Sen(De) and Ujjwal Sen. Channel capacities versus entanglement measures in multiparty quantum states. *Phys. Rev. A*, 81:012308, Jan 2010. (cited on pages 25, 26, 96, and 97)

[143] Anindya Biswas, R. Prabhu, Aditi Sen(De), and Ujjwal Sen. Genuine-multipartite-entanglement trends in gapless-to-gapped transitions of quantum spin systems. *Phys. Rev. A*, 90:032301, Sep 2014. (cited on pages 25, 26, 96, and 97)

[144] Ingemar Bengtsson and Karol Życzkowski. *Geometry of quantum states: an introduction to quantum entanglement*. Cambridge university press, 2017. (cited on page 26)

[145] D. Bures. An extension of Kakutani's theorem on infinite product measures to the tensor product of semifinite w^* -algebras. *Trans. Amer. Math. Soc.*, 135(2):199–212, 1969. (cited on page 26)

[146] Tamoghna Das, Sudipto Singha Roy, Shrobona Bagchi, Avijit Misra, Aditi Sen, Ujjwal Sen, et al. Generalized geometric measure of entanglement for multiparty mixed states. *Physical Review A*, 94(2):022336, 2016. (cited on pages 27 and 110)

[147] K. G. H. Vollbrecht and R. F. Werner. Entanglement measures under symmetry. *Phys. Rev. A*, 64:062307, Nov 2001. (cited on pages 27 and 110)

[148] Daniel Gottesman. Stabilizer codes and quantum error correction. *arXiv: quant-ph/9705052*, 1997. (cited on pages 27, 33, 127, 144, 167, and 189)

[149] Daniel Gottesman. The heisenberg representation of quantum computers. *arXiv quant-ph/9807006*, 1998. (cited on pages 27, 28, 30, 33, 127, 164, 167, and 189)

[150] Daniel Gottesman. Theory of fault-tolerant quantum computation. *Phys. Rev. A*, 57:127–137, Jan 1998. (cited on pages 27, 28, 47, 127, and 164)

[151] Scott Aaronson and Daniel Gottesman. Improved simulation of stabilizer circuits. *Physical Review A—Atomic, Molecular, and Optical Physics*, 70(5):052328, Nov 2004. (cited on pages 27, 30, 33, 167, 189, and 193)

[152] Richard Jozsa and Akimasa Miyake. Matchgates and classical simulation of quantum circuits. *Proceedings of the Royal Society A: Mathematical, Physical and Engineering Sciences*, 464(2100):3089–3106, 2008. (cited on pages 27 and 28)

[153] Simon Anders and Hans J. Briegel. Fast simulation of stabilizer circuits using a graph-state representation. *Phys. Rev. A*, 73:022334, Feb 2006. (cited on page 28)

[154] Guifré Vidal. Efficient classical simulation of slightly entangled quantum computations. *Phys. Rev. Lett.*, 91(14):147902, Oct 2003. (cited on pages 28, 163, and 167)

[155] Éloi Descamps and Borivoje Dakić. On the stabilizer formalism and its generalization. *Journal of Physics A: Mathematical and Theoretical*, 57(45):455301, 2024. (cited on page 28)

[156] Vlad Gheorghiu. Standard form of qudit stabilizer groups. *Physics Letters A*, 378(5-6):505–509, 2014. (cited on page 29)

[157] Utkarsh Azad. Efficient simulation of clifford circuits. `https://pennylane.ai/qml/demos/tutorial_clifford_circuit_simulations`, 04 2024. Date Accessed: 2025-07-18. (cited on page 29)

[158] M Nest. Classical simulation of quantum computation, the gottesman-knill theorem, and slightly beyond. *arXiv preprint arXiv:0811.0898*, 2008. (cited on pages 30, 33, 167, and 189)

[159] E. Wigner. On the quantum correction for thermodynamic equilibrium. *Phys. Rev.*, 40:749–759, Jun 1932. (cited on page 30)

[160] David Gross. Hudson's theorem for finite-dimensional quantum systems. *Journal of mathematical physics*, 47(12), 2006. (cited on pages 31, 127, 128, and 129)

[161] John Watrous. Understanding quantum information and computation. *arXiv preprint arXiv:2507.11536*, 2025. (cited on page 31)

[162] Andrew M Steane. Simple quantum error-correcting codes. *Physical Review A*, 54(6):4741, 1996. (cited on page 31)

[163] Bryan Eastin and Emanuel Knill. Restrictions on transversal encoded quantum gate sets. *Physical review letters*, 102(11):110502, 2009. (cited on page 31)

[164] Sergey Bravyi and Alexei Kitaev. Universal quantum computation with ideal clifford gates and noisy ancillas. *Phys. Rev. A*, 71:022316, Feb 2005. (cited on page 32)

[165] Xiaohui Li and Shunlong Luo. Optimality of t-gate for generating magic resource. *Communications in Theoretical Physics*, 75(4):045101, 2023. (cited on pages 32 and 189)

[166] Craig Gidney. Stim: a fast stabilizer circuit simulator. *Quantum*, 5:497, 2021. (cited on pages 33, 167, and 189)

[167] Sergey Bravyi, Dan Browne, Padraic Calpin, Earl Campbell, David Gosset, and Mark Howard. Simulation of quantum circuits by low-rank stabilizer decompositions. *Quantum*, 3:181, 2019. (cited on pages 33, 163, 167, and 189)

[168] Xhek Turkeshi, Anatoly Dymarsky, and Piotr Sierant. Pauli spectrum and nonstabilizerness of typical quantum many-body states. *Phys. Rev. B*, 111:054301, Feb 2025. (cited on pages 33, 131, 164, 167, 168, 186, and 187)

[169] Lorenzo Leone, Salvatore F. E. Oliviero, and Alioscia Hamma. Stabilizer rényi entropy. *Phys. Rev. Lett.*, 128(5):050402, Feb 2022. (cited on pages 33, 127, 128, 163, and 164)

[170] Lorenzo Leone and Lennart Bittel. Stabilizer entropies are monotones for magic-state resource theory. *Phys. Rev. A*, 110:L040403, Oct 2024. (cited on page 33)

[171] Tobias Haug and Lorenzo Piroli. Stabilizer entropies and nonstabilizerness monotones. *Quantum*, 7:1092, 2023. (cited on pages 33, 127, and 128)

[172] Tobias Haug, Leandro Aolita, and MS Kim. Probing quantum complexity via universal saturation of stabilizer entropies. *arXiv:2406.04190*, 2024. (cited on pages 33, 127, and 163)

[173] Christopher David Niroula, Pradeep andWhite, Qingfeng Wang, Sonika Johri, Daiwei Zhu, Christopher Monroe, Crystal Noel, and Michael J. Gullans. Phase transition in magic with random quantum circuits. *Nature Physics*, 20:1786–1792, 2024. (cited on pages 33, 128, and 140)

[174] Emanuele Tirrito, Poetri Sonya Tarabunga, Gugliemo Lami, Titas Chanda, Lorenzo Leone, Salvatore F. E. Oliviero, Marcello Dalmonte, Mario Collura, and Alioscia Hamma. Quantifying nonstabilizerness through entanglement spectrum flatness. *Phys. Rev. A*, 109:L040401, Apr 2024. (cited on page 33)

[175] Lorenzo Leone, Salvatore F. E. Oliviero, Gianluca Esposito, and Alioscia Hamma. Phase transition in stabilizer entropy and efficient purity estimation. *Phys. Rev. A*, 109:032403, Mar 2024. (cited on page 33)

[176] Lorenzo Leone, Salvatore F. E. Oliviero, and Alioscia Hamma. Nonstabilizerness determining the hardness of direct fidelity estimation. *Phys. Rev. A*, 107:022429, Feb 2023. (cited on pages 33 and 163)

[177] Marcel Hinsche, Marios Ioannou, Sofiene Jerbi, Lorenzo Leone, Jens Eisert, and Jose Carrasco. Efficient distributed inner product estimation via pauli sampling. *arXiv preprint arXiv:2405.06544*, 2024. (cited on page 33)

[178] Raphael Brieger, Markus Heinrich, Ingo Roth, and Martin Kliesch. Stability of classical shadows under gate-dependent noise. *Physical review letters*, 134(9):090801, 2025. (cited on page 33)

[179] Andi Gu, Lorenzo Leone, Soumik Ghosh, Jens Eisert, Susanne F. Yelin, and Yihui Quek. Pseudomagic quantum states. *Phys. Rev. Lett.*, 132:210602, May 2024. (cited on page 33)

[180] Tobias Haug, Kishor Bharti, and Dax Enshan Koh. Pseudorandom unitaries are neither real nor sparse nor noise-robust. *arXiv preprint arXiv:2306.11677*, 2023. (cited on page 33)

[181] Victor Veitch, Christopher Ferrie, David Gross, and Joseph Emerson. Negative quasi-probability as a resource for quantum computation. *New Journal of Physics*, 14(11):113011, 2012. (cited on pages 33, 127, and 128)

[182] Heinz-Peter Breuer, Francesco Petruccione, et al. *The theory of open quantum systems*. Oxford University Press on Demand, 2002. (cited on pages 35, 144, 145, 146, and 147)

[183] Heinz-Peter Breuer, Elsi-Mari Laine, and Jyrki Piilo. Measure for the degree of non-markovian behavior of quantum processes in open systems. *Phys. Rev. Lett.*, 103(21):210401, 2009. (cited on pages 36, 37, 38, and 144)

[184] Elsi-Mari Laine, Jyrki Piilo, and Heinz-Peter Breuer. Measure for the non-markovianity of quantum processes. *Phys. Rev. A*, 81:062115, Jun 2010. (cited on page 36)

[185] Francesco Buscemi, Rajeev Gangwar, Kaumudibikash Goswami, Himanshu Badhani, Tanmoy Pandit, Brij Mohan, Siddhartha Das, and Manabendra Nath Bera. Information revival without backflow: non-causal explanations for non-markovian quantum stochastic processes, 2024. (cited on page 36)

[186] S. C. Hou, X. X. Yi, S. X. Yu, and C. H. Oh. Alternative non-markovianity measure by divisibility of dynamical maps. *Phys. Rev. A*, 83:062115, Jun 2011. (cited on page 36)

[187] M. M. Wolf, J. Eisert, T. S. Cubitt, and J. I. Cirac. Assessing non-markovian quantum dynamics. *Phys. Rev. Lett.*, 101:150402, Oct 2008. (cited on page 36)

[188] Ángel Rivas, Susana F Huelga, and Martin B Plenio. Entanglement and non-markovianity of quantum evolutions. *Phys. Rev. Lett.*, 105(5):050403, 2010. (cited on pages 36, 38, and 144)

[189] Dariusz Chruciński and Andrzej Kossakowski. Non-markovian quantum dynamics: Local versus nonlocal. *Phys. Rev. Lett.*, 104:070406, Feb 2010. (cited on page 36)

[190] Michael J. W. Hall, James D. Cresser, Li Li, and Erika Andersson. Canonical form of master equations and characterization of non-markovianity. *Phys. Rev. A*, 89:042120, Apr 2014. (cited on pages 36, 37, 38, 147, and 152)

[191] Wei-Min Zhang, Ping-Yuan Lo, Heng-Na Xiong, Matisse Wei-Yuan Tu, and Franco Nori. General non-markovian dynamics of open quantum systems. *Phys. Rev. Lett.*, 109:170402, Oct 2012. (cited on page 36)

[192] Pinja Haikka and Sabrina Maniscalco. Non-markovian quantum probes. *Open Systems & Information Dynamics*, 21(01n02):1440005, 2014. (cited on page 36)

[193] Dariusz Chruściński, Chiara Macchiavello, and Sabrina Maniscalco. Detecting non-markovianity of quantum evolution via spectra of dynamical maps. *Phys. Rev. Lett.*, 118:080404, Feb 2017. (cited on page 37)

[194] Jing Liu, Xiao-Ming Lu, and Xiaoguang Wang. Nonunital non-markovianity of quantum dynamics. *Phys. Rev. A*, 87:042103, Apr 2013. (cited on pages 37 and 38)

[195] Richard Jozsa. Quantum effects in algorithms. *NASA International Conference on Quantum Computing and Quantum Communications*, pages 103–112, 1998. (cited on pages 37 and 95)

[196] Martin B. Plenio and S. Virmani. An introduction to entanglement measures, 2006. (cited on page 37)

[197] M. B. Plenio. Logarithmic negativity: A full entanglement monotone that is not convex. *Phys. Rev. Lett.*, 95:090503, Aug 2005. (cited on pages 37 and 38)

[198] DA Lidar, A Shabani, and Robert Alicki. Conditions for strictly purity-decreasing quantum markovian dynamics. *Chemical physics*, 322(1-2):82–86, 2006. (cited on page 38)

[199] Soroush Haseli, Shahriar Salimi, and AS Khorashad. A measure of non-markovianity for unital quantum dynamical maps. *Quantum Information Processing*, 14:3581–3594, 2015. (cited on page 38)

[200] Tenzan Araki, Franco Nori, and Clemens Gneiting. Robust quantum control with disorder-dressed evolution. *Phys. Rev. A*, 107(3):032609, 2023. (cited on pages 38, 144, and 162)

[201] Clemens Gneiting. Disorder-dressed quantum evolution. *Phys. Rev. B*, 101(21):214203, 2020. (cited on pages 38, 143, and 162)

[202] Igor Devetak and Jon Yard. Exact cost of redistributing multipartite quantum states. *Phys. Rev. Lett.*, 100:230501, Jun 2008. (cited on page 38)

[203] Kunal Sharma, Eyuri Wakakuwa, and Mark M. Wilde. Conditional quantum one-time pad. *Phys. Rev. Lett.*, 124:050503, Feb 2020. (cited on page 38)

[204] Mario Berta, Fernando G. S. L. Brandão, Christian Majenz, and Mark M. Wilde. Deconstruction and conditional erasure of quantum correlations. *Phys. Rev. A*, 98:042320, Oct 2018. (cited on page 38)

[205] Bogna Bylicka, Dariusz Chruściński, and Sabrina Maniscalco. Non-markovianity as a resource for quantum technologies. *arXiv preprint arXiv:1301.2585*, 2013. (cited on page 38)

[206] Graeme D Berk, Andrew JP Garner, Benjamin Yadin, Kavan Modi, and Felix A Pollock. Resource theories of multi-time processes: A window into quantum non-markovianity. *Quantum*, 5:435, 2021. (cited on page 38)

[207] David Applegate, Robert Bixby, William Cook, and Vasek Chvátal. On the solution of traveling salesman problems. *Rheinische Friedrich-Wilhelms-Universität Bonn*, 1998. (cited on page 42)

[208] David Applegate, Robert Bixby, Vašek Chvátal, and William Cook. *Finding tours in the TSP*. Universität Bonn. Institut für Ökonometrie und Operations Research, 1999. (cited on page 42)

[209] William J Cook, William H Cunningham, William R Pulleyblank, and Alexander Schrijver. Combinatorial optimization. *Unpublished manuscript*, 10:75–93, 1994. (cited on page 42)

[210] Jakob Puchinger, Günther R Raidl, and Ulrich Pferschy. The multidimensional knapsack problem: Structure and algorithms. *INFORMS Journal on Computing*, 22(2):250–265, 2010. (cited on page 42)

[211] Tom Packebusch and Stephan Mertens. Low autocorrelation binary sequences. *Journal of Physics A: Mathematical and Theoretical*, 49(16):165001, 2016. (cited on page 42)

[212] Daniel A Spielman and Shang-Hua Teng. Smoothed analysis: an attempt to explain the behavior of algorithms in practice. *Communications of the ACM*, 52(10):76–84, 2009. (cited on page 43)

[213] Teofilo F Gonzalez. *Handbook of approximation algorithms and metaheuristics*. Chapman and Hall/CRC, 2007. (cited on page 43)

[214] Ethan Bernstein and Umesh Vazirani. Quantum complexity theory. In *Proceedings of the twenty-fifth annual ACM symposium on Theory of computing*, pages 11–20, 1993. (cited on page 44)

[215] Richard M Karp. Reducibility among combinatorial problems. In *50 Years of Integer Programming 1958-2008: from the Early Years to the State-of-the-Art*, pages 219–241. Springer, 2009. (cited on page 45)

[216] David Gamarnik. The overlap gap property: A topological barrier to optimizing over random structures. *Proceedings of the National Academy of Sciences*, 118(41):e2108492118, 2021. (cited on page 45)

[217] Afonso Bandeira, Amelia Perry, and Alexander S Wein. Notes on computational-to-statistical gaps: predictions using statistical physics. *Portugaliae mathematica*, 75(2):159–186, 2018. (cited on page 45)

[218] Chris Marriott and John Watrous. Quantum arthur–merlin games. *computational complexity*, 14(2):122–152, 2005. (cited on page 46)

[219] Michel X Goemans and David P Williamson. Improved approximation algorithms for maximum cut and satisfiability problems using semidefinite programming. *Journal of the ACM (JACM)*, 42(6):1115–1145, 1995. (cited on page 46)

[220] Subhash Khot, Guy Kindler, Elchanan Mossel, and Ryan O'Donnell. Optimal inapproximability results for max-cut and other 2-variable csps? *SIAM Journal on Computing*, 37(1):319–357, 2007. (cited on page 46)

[221] Subhash Khot. On the power of unique 2-prover 1-round games. In *Proceedings of the thiry-fourth annual ACM symposium on Theory of computing*, pages 767–775, 2002. (cited on page 46)

[222] Dorit Aharonov, Itai Arad, Zeph Landau, and Umesh Vazirani. The detectability lemma and quantum gap amplification. In *Proceedings of the forty-first annual ACM symposium on Theory of computing*, pages 417–426, 2009. (cited on page 46)

[223] Dorit Aharonov and Tomer Naveh. Quantum np-a survey. *arXiv preprint quant-ph/0210077*, 2002. (cited on page 46)

[224] Dorit Aharonov, Itai Arad, and Thomas Vidick. Guest column: the quantum pcp conjecture. *Acm sigact news*, 44(2):47–79, 2013. (cited on page 46)

[225] Alexei Yu Kitaev, Alexander Shen, and Mikhail N Vyalyi. *Classical and quantum computation*, volume 47. American Mathematical Soc., 2002. (cited on page 46)

[226] Lov K Grover. A fast quantum mechanical algorithm for database search. *Proceedings of the twenty-eighth annual ACM symposium on Theory of computing*, pages 212–219, 1996. (cited on page 47)

[227] Edward Farhi, Jeffrey Goldstone, Sam Gutmann, and Michael Sipser. Quantum computation by adiabatic evolution. *arXiv preprint quant-ph/0001106*, 2000. (cited on pages 47 and 48)

[228] Lieven Vandenberghe and Stephen Boyd. Semidefinite programming. *SIAM review*, 38(1):49–95, 1996. (cited on page 47)

[229] Joran Van Apeldoorn, András Gilyén, Sander Gribling, and Ronald de Wolf. Quantum sdp-solvers: Better upper and lower bounds. In *2017 IEEE 58th Annual Symposium on Foundations of Computer Science (FOCS)*, pages 403–414. IEEE, 2017. (cited on page 47)

[230] Fernando GSL Brandão, Amir Kalev, Tongyang Li, Cedric Yen-Yu Lin, Krysta M Svore, and Xiaodi Wu. Quantum sdp solvers: Large speed-ups, optimality, and applications to quantum learning. *arXiv preprint arXiv:1710.02581*, 2017. (cited on page 47)

[231] Marco Cerezo, Andrew Arrasmith, Ryan Babbush, Simon C Benjamin, Suguru Endo, Keisuke Fujii, Jarrod R McClean, Kosuke Mitarai, Xiao Yuan, Lukasz Cincio, et al. Variational quantum algorithms. *Nature Reviews Physics*, 3(9):625–644, 2021. (cited on pages 47, 50, 95, and 126)

[232] Andrew Lucas. Ising formulations of many NP problems. *Frontiers in physics*, 2:5, 2014. (cited on pages 47, 48, and 127)

[233] Gary Kochenberger, Jin-Kao Hao, Fred Glover, Mark Lewis, Zhipeng Lü, Haibo Wang, and Yang Wang. The unconstrained binary quadratic programming problem: a survey. *Journal of combinatorial optimization*, 28(1):58–81, 2014. (cited on page 47)

[234] Fred Glover, Gary Kochenberger, and Yu Du. A tutorial on formulating and using qubo models. *arXiv preprint arXiv:1811.11538*, 2018. (cited on page 47)

[235] Abraham P Punnen. The quadratic unconstrained binary optimization problem. *Springer International Publishing*, 10:978–3, 2022. (cited on page 47)

[236] Philipp Hauke, Helmut G Katzgraber, Wolfgang Lechner, Hidetoshi Nishimori, and William D Oliver. Perspectives of quantum annealing: methods and implementations. *Reports on Progress in Physics*, 83(5):054401, may 2020. (cited on pages 48, 49, 95, 137, 143, and 188)

[237] Leo Zhou, Sheng-Tao Wang, Soonwon Choi, Hannes Pichler, and Mikhail D. Lukin. Quantum approximate optimization algorithm: Performance, mechanism, and implementation on near-term devices. *Phys. Rev. X*, 10:021067, Jun 2020. (cited on pages 48, 52, 111, and 127)

[238] Tadashi Kadowaki and Hidetoshi Nishimori. Quantum annealing in the transverse ising model. *Physical Review E*, 58(5):5355, 1998. (cited on page 48)

[239] Aleta Berk Finnila, Maria A Gomez, C Sebenik, Catherine Stenson, and Jimmie D Doll. Quantum annealing: A new method for minimizing multidimensional functions. *Chemical physics letters*, 219(5-6):343–348, 1994. (cited on page 48)

[240] Andrew J Sommese, Charles W Wampler, et al. *The Numerical solution of systems of polynomials arising in engineering and science*. World Scientific, 2005. (cited on page 48)

[241] M. H. S. Amin. Consistency of the adiabatic theorem. *Phys. Rev. Lett.*, 102:220401, Jun 2009. (cited on page 49)

[242] Satoshi Morita and Hidetoshi Nishimori. Mathematical foundation of quantum annealing. *Journal of Mathematical Physics*, 49(12), 2008. (cited on pages 50 and 137)

[243] Boris Altshuler, Hari Krovi, and Jérémie Roland. Anderson localization makes adiabatic quantum optimization fail. *Proceedings of the National Academy of Sciences*, 107(28):12446–12450, 2010. (cited on pages 50, 110, 143, and 188)

[244] Victor Bapst, Laura Foini, Florent Krzakala, Guilhem Semerjian, and Francesco Zamponi. The quantum adiabatic algorithm applied to random optimization problems: The quantum spin glass perspective. *Physics Reports*, 523(3):127–205, 2013. (cited on page 50)

[245] Sergey Knysh. Zero-temperature quantum annealing bottlenecks in the spin-glass phase. *Nature communications*, 7(1):12370, 2016. (cited on page 50)

[246] Troels F Rønnow, Zhihui Wang, Joshua Job, Sergio Boixo, Sergei V Isakov, David Wecker, John M Martinis, Daniel A Lidar, and Matthias Troyer. Defining and detecting quantum speedup. *science*, 345(6195):420–424, 2014. (cited on page 50)

[247] EJ Crosson and DA Lidar. Prospects for quantum enhancement with diabatic quantum annealing. *Nature Reviews Physics*, 3(7):466–489, 2021. (cited on page 50)

[248] Amira Abbas, Andris Ambainis, Brandon Augustino, Andreas Bärtschi, Harry Buhrman, Carleton Coffrin, Giorgio Cortiana, Vedran Dunjko, Daniel J Egger, Bruce G Elmegreen, et al. Challenges and opportunities in quantum optimization. *arXiv:2312.02279*, 2023. (cited on pages 51, 62, and 127)

[249] Lennart Bittel and Martin Kliesch. Training variational quantum algorithms is np-hard. *Phys. Rev. Lett.*, 127:120502, Sep 2021. (cited on page 50)

[250] John Golden, Andreas Bärtschi, Daniel O'Malley, and Stephan Eidenbenz. Numerical evidence for exponential speed-up of qaoa over unstructured search for approximate constrained optimization. In *2023 IEEE International Conference on Quantum Computing and Engineering (QCE)*, volume 1, pages 496–505. IEEE, 2023. (cited on page 50)

[251] Martin Larocca, Supanut Thanasilp, Samson Wang, Kunal Sharma, Jacob Biamonte, Patrick J Coles, Lukasz Cincio, Jarrod R McClean, Zoë Holmes, and M Cerezo. A review of barren plateaus in variational quantum computing. *arXiv preprint arXiv:2405.00781*, 2024. (cited on page 51)

[252] Jules Tilly, Hongxiang Chen, Shuxiang Cao, Dario Picozzi, Kanav Setia, Ying Li, Edward Grant, Leonard Wossnig, Ivan Rungger, George H Booth, et al. The variational quantum eigensolver: a review of methods and best practices. *Physics Reports*, 986:1–128, 2022. (cited on page 51)

[253] Jonathan Wurtz and Peter Love. Maxcut quantum approximate optimization algorithm performance guarantees for p> 1. *Physical Review A*, 103(4):042612, 2021. (cited on page 52)

[254] Edward Farhi, Jeffrey Goldstone, Sam Gutmann, and Leo Zhou. The quantum approximate optimization algorithm and the sherrington-kirkpatrick model at infinite size. *Quantum*, 6:759, 2022. (cited on pages 52 and 139)

[255] Joao Basso, Edward Farhi, Kunal Marwaha, Benjamin Villalonga, and Leo Zhou. The quantum approximate optimization algorithm at high depth for maxcut on large-girth regular graphs and the sherrington-kirkpatrick model. *arXiv preprint arXiv:2110.14206*, 2021. (cited on page 52)

[256] Stefan H Sack and Maksym Serbyn. Quantum annealing initialization of the quantum approximate optimization algorithm. *Quantum*, 5:491, July 2021. (cited on pages 52, 130, and 138)

[257] Andoni Agirre, Evert Van Nieuwenburg, and Matteo M Wauters. A monte carlo tree search approach to qaoa: finding a needle in the haystack. *New Journal of Physics*, 27(4):043014, 2025. (cited on page 52)

[258] Mahabubul Alam, Abdullah Ash-Saki, and Swaroop Ghosh. Accelerating quantum approximate optimization algorithm using machine learning. In *2020 Design, Automation & Test in Europe Conference & Exhibition (DATE)*, pages 686–689. IEEE, 2020. (cited on page 52)

[259] Matteo M Wauters, Emanuele Panizon, Glen B Mbeng, and Giuseppe E Santoro. Reinforcement-learning-assisted quantum optimization. *Physical Review Research*, 2(3):033446, 2020. (cited on page 52)

[260] Michael Streif and Martin Leib. Training the quantum approximate optimization algorithm without access to a quantum processing unit. *Quantum Science and Technology*, 5(3):034008, may 2020. (cited on pages 52 and 110)

[261] Tomislav Begušić, Kasra Hejazi, and Garnet Kin Chan. Simulating quantum circuit expectation values by clifford perturbation theory. *The Journal of Chemical Physics*, 162(15), 2025. (cited on page 52)

[262] Fernando GSL Brandao, Michael Broughton, Edward Farhi, Sam Gutmann, and Hartmut Neven. For fixed control parameters the quantum approximate optimization algorithm's objective function value concentrates for typical instances. *arXiv preprint arXiv:1812.04170*, 2018. (cited on page 53)

[263] Vishwanathan Akshay, Daniil Rabinovich, Ernesto Campos, and Jacob Biamonte. Parameter concentrations in quantum approximate optimization. *Physical Review A*, 104(1):L010401, 2021. (cited on page 53)

[264] Alexey Galda, Xiaoyuan Liu, Danylo Lykov, Yuri Alexeev, and Ilya Safro. Transferability of optimal qaoa parameters between random graphs. In *2021 IEEE International Conference on Quantum Computing and Engineering (QCE)*, pages 171–180. IEEE, 2021. (cited on page 53)

[265] Qiskit Community. qaoa_training_pipeline: A pipeline and methods to generate good parameters for qaoa ansatz circuits. `https://github.com/qiskit-community/qaoa_training_pipeline`, 2025. Accessed: 2025-07-07. (cited on pages 53, 122, and 193)

[266] Kostas Blekos, Dean Brand, Andrea Ceschini, Chiao-Hui Chou, Rui-Hao Li, Komal Pandya, and Alessandro Summer. A review on quantum approximate optimization algorithm and its variants. *Physics Reports*, 1068:1–66, 2024. (cited on page 53)

[267] Stuart Hadfield, Zhihui Wang, Bryan O'gorman, Eleanor G Rieffel, Davide Venturelli, and Rupak Biswas. From the quantum approximate optimization algorithm to a quantum alternating operator ansatz. *Algorithms*, 12(2):34, 2019. (cited on pages 53 and 62)

[268] Daniel J. Egger, Jakub Mareček, and Stefan Woerner. Warm-starting quantum optimization. *Quantum*, 5:479, June 2021. (cited on pages 53 and 62)

[269] Reuben Tate, Majid Farhadi, Creston Herold, Greg Mohler, and Swati Gupta. Bridging classical and quantum with sdp initialized warm-starts for qaoa. *ACM Transactions on Quantum Computing*, 4(2):1–39, 2023. (cited on pages 53 and 62)

[270] Sergey Bravyi, Alexander Kliesch, Robert Koenig, and Eugene Tang. Obstacles to variational quantum optimization from symmetry protection. *Physical review letters*, 125(26):260505, 2020. (cited on page 53)

[271] Linghua Zhu, Ho Lun Tang, George S Barron, FA Calderon-Vargas, Nicholas J Mayhall, Edwin Barnes, and Sophia E Economou. Adaptive quantum approximate optimization algorithm for solving combinatorial problems on a quantum computer. *Physical Review Research*, 4(3):033029, 2022. (cited on page 53)

[272] Aditi Misra-Spieldenner, Tim Bode, Peter K Schuhmacher, Tobias Stollenwerk, Dmitry Bagrets, and Frank K Wilhelm. Mean-field approximate optimization algorithm. *PRX quantum*, 4(3):030335, 2023. (cited on page 53)

[273] Colin D Bruzewicz, John Chiaverini, Robert McConnell, and Jeremy M Sage. Trapped-ion quantum computing: Progress and challenges. *Applied physics reviews*, 6(2), 2019. (cited on page 53)

[274] Philip Krantz, Morten Kjaergaard, Fei Yan, Terry P Orlando, Simon Gustavsson, and William D Oliver. A quantum engineer's guide to superconducting qubits. *Applied physics reviews*, 6(2), 2019. (cited on pages 53, 59, and 60)

[275] Mark Saffman, Thad G Walker, and Klaus Mølmer. Quantum information with rydberg atoms. *Reviews of modern physics*, 82(3):2313–2363, 2010. (cited on page 53)

[276] Sergei Slussarenko and Geoff J Pryde. Photonic quantum information processing: A concise review. *Applied physics reviews*, 6(4), 2019. (cited on page 53)

[277] Joseph B Altepeter, Daniel FV James, and Paul G Kwiat. qubit quantum state tomography. In *Quantum state estimation*, pages 113–145. Springer, 2004. (cited on page 58)

[278] Jens Koch, Terri M. Yu, Jay Gambetta, A. A. Houck, D. I. Schuster, J. Majer, Alexandre Blais, M. H. Devoret, S. M. Girvin, and R. J. Schoelkopf. Charge-insensitive qubit design derived from the cooper pair box. *Phys. Rev. A*, 76:042319, Oct 2007. (cited on page 61)

[279] Rami Barends, Julian Kelly, Anthony Megrant, Andrzej Veitia, Daniel Sank, Evan Jeffrey, Ted C White, Josh Mutus, Austin G Fowler, Brooks Campbell, et al. Superconducting quantum circuits at the surface code threshold for fault tolerance. *Nature*, 508(7497):500–503, 2014. (cited on page 61)

[280] Chad Rigetti and Michel Devoret. Fully microwave-tunable universal gates in superconducting qubits with linear couplings and fixed transition frequencies. *Physical Review B—Condensed Matter and Materials Physics*, 81(13):134507, 2010. (cited on page 61)

[281] David C McKay, Stefan Filipp, Antonio Mezzacapo, Easwar Magesan, Jerry M Chow, and Jay M Gambetta. Universal gate for fixed-frequency qubits via a tunable bus. *Physical Review Applied*, 6(6):064007, 2016. (cited on page 61)

[282] Marc Ganzhorn, G Salis, DJ Egger, A Fuhrer, Matthias Mergenthaler, Clemens Müller, Peter Müller, Stephan Paredes, M Pechal, Max Werninghaus, et al. Benchmarking the noise sensitivity of different parametric two-qubit gates in a single superconducting quantum computing platform. *Physical Review Research*, 2(3):033447, 2020. (cited on page 61)

[283] Maxime Dupont, Bram Evert, Mark J Hodson, Bhuvanesh Sundar, Stephen Jeffrey, Yuki Yamaguchi, Dennis Feng, Filip B Maciejewski, Stuart Hadfield, M Sohaib Alam, et al. Quantum-enhanced greedy combinatorial optimization solver. *Science Advances*, 9(45):eadi0487, 2023. (cited on page 62)

[284] Pranav Chandarana, Narendra N Hegade, Koushik Paul, Francisco Albarrán-Arriagada, Enrique Solano, Adolfo Del Campo, and Xi Chen. Digitized-counterdiabatic quantum approximate optimization algorithm. *Physical review research*, 4(1):013141, 2022. (cited on page 62)

[285] Tianyi Peng, Aram W Harrow, Maris Ozols, and Xiaodi Wu. Simulating large quantum circuits on a small quantum computer. *Physical review letters*, 125(15):150504, 2020. (cited on pages 62 and 118)

[286] Stefan H Sack and Daniel J Egger. Large-scale quantum approximate optimization on nonplanar graphs with machine learning noise mitigation. *Physical Review Research*, 6(1):013223, 2024. (cited on pages 63, 65, 66, and 68)

[287] Fei Hua, Yuwei Jin, Ang Li, Chenxu Liu, Meng Wang, Yanhao Chen, Chi Zhang, Ari Hayes, Samuel Stein, Minghao Guo, et al. A synergistic compilation workflow for tackling crosstalk in quantum machines. *arXiv preprint arXiv:2207.05751*, 2022. (cited on page 63)

[288] David C McKay, Ian Hincks, Emily J Pritchett, Malcolm Carroll, Luke CG Govia, and Seth T Merkel. Benchmarking quantum processor performance at scale. *arXiv preprint arXiv:2311.05933*, 2023. (cited on pages 63, 67, 68, and 111)

[289] Fei Hua, Yuwei Jin, Yanhao Chen, Suhas Vittal, Kevin Krsulich, Lev S Bishop, John Lapeyre, Ali Javadi-Abhari, and Eddy Z Zhang. Exploiting qubit reuse through mid-circuit measurement and reset. *arXiv preprint arXiv:2211.01925*, 2022. (cited on page 63)

[290] Atsushi Matsuo, Shigeru Yamashita, and Daniel J Egger. A sat approach to the initial mapping problem in swap gate insertion for commuting gates. *IEICE Transactions on Fundamentals of Electronics, Communications and Computer Sciences*, 106(11):1424–1431, 2023. (cited on pages 63, 65, and 121)

[291] Jun Zhang, Jiri Vala, Shankar Sastry, and K Birgitta Whaley. Minimum construction of two-qubit quantum operations. *Physical review letters*, 93(2):020502, 2004. (cited on page 65)

[292] Byron Drury and Peter Love. Constructive quantum shannon decomposition from cartan involutions. *Journal of Physics A: Mathematical and Theoretical*, 41(39):395305, 2008. (cited on page 65)

[293] Dmitri Maslov. Basic circuit compilation techniques for an ion-trap quantum machine. *New Journal of Physics*, 19(2):023035, 2017. (cited on page 65)

[294] David P DiVincenzo. The physical implementation of quantum computation. *Fortschritte der Physik: Progress of Physics*, 48(9-11):771–783, 2000. (cited on page 65)

[295] Gushu Li, Anbang Wu, Yunong Shi, Ali Javadi-Abhari, Yufei Ding, and Yuan Xie. Paulihedral: a generalized block-wise compiler optimization framework for quantum simulation kernels. In *Proceedings of the 27th ACM International Conference on Architectural Support for Programming Languages and Operating Systems*, pages 554–569, 2022. (cited on page 65)

[296] Liam Madden and Andrea Simonetto. Best approximate quantum compiling problems. *ACM Transactions on Quantum Computing*, 3(2):1–29, 2022. (cited on page 65)

[297] Ethan Smith, Marc Grau Davis, Jeffrey Larson, Ed Younis, Lindsay Bassman Oftelie, Wim Lavrijsen, and Costin Iancu. Leap: Scaling numerical optimization based synthesis using an incremental approach. *ACM Transactions on Quantum Computing*, 4(1):1–23, 2023. (cited on page 65)

[298] Gushu Li, Yufei Ding, and Yuan Xie. Tackling the qubit mapping problem for nisq-era quantum devices. In *Proceedings of the twenty-fourth international conference on architectural support for programming languages and operating systems*, pages 1001–1014, 2019. (cited on page 65)

[299] Alwin Zulehner, Alexandru Paler, and Robert Wille. An efficient methodology for mapping quantum circuits to the ibm qx architectures. *IEEE Transactions on Computer-Aided Design of Integrated Circuits and Systems*, 38(7):1226–1236, 2018. (cited on page 65)

[300] Alexander Cowtan, Silas Dilkes, Ross Duncan, Alexandre Krajenbrink, Will Simmons, and Seyon Sivarajah. On the qubit routing problem. *arXiv preprint arXiv:1902.08091*, 2019. (cited on page 65)

[301] Johannes Weidenfeller, Lucia C Valor, Julien Gacon, Caroline Tornow, Luciano Bello, Stefan Woerner, and Daniel J Egger. Scaling of the quantum approximate optimization algorithm on superconducting qubit based hardware. *Quantum*, 6:870, 2022. (cited on pages 65, 67, 75, 81, 84, 87, 110, 121, and 127)

[302] Yuwei Jin, Jason Luo, Lucent Fong, Yanhao Chen, Ari B Hayes, Chi Zhang, Fei Hua, and Eddy Z Zhang. A structured method for compilation of qaoa circuits in quantum computing. *arXiv preprint arXiv:2112.06143*, 2021. (cited on page 65)

[303] Mahabubul Alam, Abdullah Ash-Saki, and Swaroop Ghosh. Circuit compilation methodologies for quantum approximate optimization algorithm. In *2020 53rd Annual IEEE/ACM International Symposium on Microarchitecture (MICRO)*, pages 215–228. IEEE, 2020. (cited on page 65)

[304] Matthew P Harrigan, Kevin J Sung, Matthew Neeley, Kevin J Satzinger, Frank Arute, Kunal Arya, Juan Atalaya, Joseph C Bardin, Rami Barends, Sergio Boixo, et al. Quantum approximate optimization of non-planar graph problems on a planar superconducting processor. *Nature Physics*, 17(3):332–336, 2021. (cited on page 65)

[305] Antonio D Córcoles, Maika Takita, Ken Inoue, Scott Lekuch, Zlatko K Minev, Jerry M Chow, and Jay M Gambetta. Exploiting dynamic quantum circuits in a quantum algorithm with superconducting qubits. *Physical Review Letters*, 127(10):100501, 2021. (cited on page 65)

[306] Elisa Bäumer, Vinay Tripathi, Derek S Wang, Patrick Rall, Edward H Chen, Swarnadeep Majumder, Alireza Seif, and Zlatko K Minev. Efficient long-range entanglement using dynamic circuits. *PRX Quantum*, 5(3):030339, 2024. (cited on page 65)

[307] Anette Messinger, Michael Fellner, and Wolfgang Lechner. Constant depth code deformations in the parity architecture. In *2023 IEEE International Conference on Quantum Computing and Engineering (QCE)*, volume 1, pages 120–130. IEEE, 2023. (cited on page 65)

[308] Pradeep Niroula, Ruslan Shaydulin, Romina Yalovetzky, Pierre Minssen, Dylan Herman, Shaohan Hu, and Marco Pistoia. Constrained quantum optimization for extractive summarization on a trapped-ion quantum computer. *Scientific Reports*, 12(1):17171, 2022. (cited on page 65)

[309] Lorenza Viola and Seth Lloyd. Dynamical suppression of decoherence in two-state quantum systems. *Physical Review A*, 58(4):2733, 1998. (cited on page 66)

[310] David Vitali and Paolo Tombesi. Using parity kicks for decoherence control. *Physical Review A*, 59(6):4178, 1999. (cited on page 66)

[311] Bibek Pokharel, Namit Anand, Benjamin Fortman, and Daniel A Lidar. Demonstration of fidelity improvement using dynamical decoupling with superconducting qubits. *Physical review letters*, 121(22):220502, 2018. (cited on page 66)

[312] Elijah Pelofske, Andreas Bärtschi, and Stephan Eidenbenz. Short-depth qaoa circuits and quantum annealing on higher-order ising models. *npj Quantum Information*, 10(1):30, 2024. (cited on page 66)

[313] Daniel Gottesman. An introduction to quantum error correction and fault-tolerant quantum computation. *arXiv preprint arXiv:0904.2557*, 2009. (cited on page 66)

[314] Kristan Temme, Sergey Bravyi, and Jay M Gambetta. Error mitigation for short-depth quantum circuits. *Physical review letters*, 119(18):180509, 2017. (cited on pages 66 and 67)

[315] Abhinav Kandala, Kristan Temme, Antonio D Córcoles, Antonio Mezzacapo, Jerry M Chow, and Jay M Gambetta. Error mitigation extends the computational reach of a noisy quantum processor. *Nature*, 567(7749):491–495, 2019. (cited on pages 66, 67, and 68)

[316] Christophe Piveteau, David Sutter, and Stefan Woerner. Quasiprobability decompositions with reduced sampling overhead. *npj Quantum Information*, 8(1):12, 2022. (cited on page 66)

[317] Ewout Van Den Berg, Zlatko K Minev, Abhinav Kandala, and Kristan Temme. Probabilistic error cancellation with sparse pauli–lindblad models on noisy quantum processors. *Nature physics*, 19(8):1116–1121, 2023. (cited on pages 66 and 68)

[318] Philipp Hauke, Fernando M Cucchietti, Luca Tagliacozzo, Ivan Deutsch, and Maciej Lewenstein. Can one trust quantum simulators? *Reports on Progress in Physics*, 75(8):082401, 2012. (cited on pages 66 and 163)

[319] Ying Li and Simon C Benjamin. Efficient variational quantum simulator incorporating active error minimization. *Physical Review X*, 7(2):021050, 2017. (cited on page 66)

[320] Ryan LaRose, Andrea Mari, Sarah Kaiser, Peter J Karalekas, Andre A Alves, Piotr Czarnik, Mohamed El Mandouh, Max H Gordon, Yousef Hindy, Aaron Robertson, et al. Mitiq: A software package for error mitigation on noisy quantum computers. *Quantum*, 6:774, 2022. (cited on page 67)

[321] Almudena Carrera Vazquez, Daniel J Egger, David Ochsner, and Stefan Woerner. Well-conditioned multi-product formulas for hardware-friendly hamiltonian simulation. *Quantum*, 7:1067, 2023. (cited on page 67)

[322] Samantha V Barron, Daniel J Egger, Elijah Pelofske, Andreas Bärtschi, Stephan Eidenbenz, Matthis Lehmkuehler, and Stefan Woerner. Provable bounds for noise-free expectation values computed from noisy samples. *Nature Computational Science*, pages 1–11, 2024. (cited on page 68)

[323] Andrew Wack, Hanhee Paik, Ali Javadi-Abhari, Petar Jurcevic, Ismael Faro, Jay M Gambetta, and Blake R Johnson. Quality, speed, and scale: three key attributes to measure the performance of near-term quantum computers. *arXiv preprint arXiv:2110.14108*, 2021. (cited on page 68)

[324] Andrew W. Cross, Lev S. Bishop, Sarah Sheldon, Paul D. Nation, and Jay M. Gambetta. Validating quantum computers using randomized model circuits. *Phys. Rev. A*, 100:032328, Sep 2019. (cited on pages 68, 73, and 83)

[325] Gopal Chandra Santra, Fred Jendrzejewski, Philipp Hauke, and Daniel J. Egger. Squeezing and quantum approximate optimization. *Phys. Rev. A*, 109:012413, Jan 2024. (cited on pages 68, 95, 97, 109, 127, and 195)

[326] Edward Farhi, Jeffrey Goldstone, and Sam Gutmann. A quantum approximate optimization algorithm. *arXiv:1411.4028*, 2014. (cited on pages 73 and 95)

[327] Pietro Torta, Glen B. Mbeng, Carlo Baldassi, Riccardo Zecchina, and Giuseppe E. Santoro. Quantum approximate optimization algorithm applied to the binary perceptron. *arXiv:2112.10219*, 107:094202, Mar 2021. (cited on page 73)

[328] David Headley, Thorge Müller, Ana Martin, Enrique Solano, Mikel Sanz, and Frank K. Wilhelm. Approximating the quantum approximate optimisation algorithm. *arXiv:2002.12215*, 106:042446, Oct 2020. (cited on page 73)

[329] Michael Streif and Martin Leib. Comparison of qaoa with quantum and simulated annealing. *arXiv:1901.01903*, 2019. (cited on page 73)

[330] Jonathan Wurtz and Peter J. Love. Counterdiabaticity and the quantum approximate optimization algorithm. *Quantum*, 6:635, jan 2022. (cited on page 73)

[331] Luca Pezzé and Augusto Smerzi. Entanglement, nonlinear dynamics, and the Heisenberg limit. *Phys. Rev. Lett.*, 102:100401, Mar 2009. (cited on page 73)

[332] Luca Pezzè, Augusto Smerzi, Markus K. Oberthaler, Roman Schmied, and Philipp Treutlein. Quantum metrology with nonclassical states of atomic ensembles. *Rev. Mod. Phys.*, 90:035005, Sep 2018. (cited on pages 73, 78, 89, and 193)

[333] Christian L. Degen, Friedemann Reinhard, and Paola Cappellaro. Quantum sensing. *Rev. Mod. Phys.*, 89:035002, Jul 2017. (cited on page 73)

[334] Christian Gross, Tilman Zibold, Euler Nicklas, Jerome Estève, and Markus K. Oberthaler. Nonlinear atom interferometer surpasses classical precision limit. *Nature*, 464(7292):1165–1169, Apr 2010. (cited on page 73)

[335] Robert J. Sewell, Marco Koschorreck, Mario Napolitano, Brice Dubost, Naeimeh Behbood, and Morgan W. Mitchell. Magnetic sensitivity beyond the projection noise limit by spin squeezing. *Phys. Rev. Lett.*, 109:253605, Dec 2012. (cited on page 73)

[336] Lisa Barsotti, Jan Harms, and Roman Schnabel. Squeezed vacuum states of light for gravitational wave detectors. *Rep. Prog. Phys.*, 82(1):016905, 2018. (cited on page 73)

[337] Robert H. Dicke. Coherence in spontaneous radiation processes. *Phys. Rev.*, 93:99–110, Jan 1954. (cited on pages 73 and 78)

[338] Masahiro Kitagawa and Masahito Ueda. Squeezed spin states. *Phys. Rev. A*, 47:5138–5143, Jun 1993. (cited on pages 73, 75, and 76)

[339] Jian Ma, Xiaoguang Wang, Chang-Pu Sun, and Franco Nori. Quantum spin squeezing. *Phys. Rep.*, 509(2-3):89–165, 2011. (cited on pages 73 and 76)

[340] Petar Jurcevic, Ali Javadi-Abhari, Lev S. Bishop, Isaac Lauer, Daniela F. Bogorin, Markus Brink, Lauren Capelluto, Oktay Günlük, Toshinari Itoko, Naoki Kanazawa, and *et al.* Demonstration of quantum volume 64 on a superconducting quantum computing system. *Quantum Sci. Technol.*, 6(2):025020, mar 2021. (cited on pages 73, 82, and 83)

[341] Elijah Pelofske, Andreas Bärtschi, and Stephan Eidenbenz. Quantum volume in practice: What users can expect from NISQ devices. *IEEE Transactions on Quantum Engineering*, 3:1–19, 2022. (cited on pages 73 and 83)

[342] Ahmed Omran, Harry Levine, Alexander Keesling, Giulia Semeghini, Tout T. Wang, Sepehr Ebadi, Hannes Bernien, Alexander S. Zibrov, Hannes Pichler, Soonwon Choi, and *et al.* Generation and manipulation of Schrödinger cat states in Rydberg atom arrays. *Science*, 365(6453):570–574, aug 2019. (cited on page 73)

[343] Christian D. Marciniak, Thomas Feldker, Ivan Pogorelov, Raphael Kaubruegger, Denis V. Vasilyev, Rick van Bijnen, Philipp Schindler, Peter Zoller, Rainer Blatt, and Thomas Monz. Optimal metrology with programmable quantum sensors. *Nature*, 603(7902):604–609, Mar 2022. (cited on pages 73, 75, 89, and 93)

[344] Juan M. Arrazola, Ville Bergholm, Kamil Brádler, Thomas R. Bromley, Matt J. Collins, Ish Dhand, Alberto Fumagalli, Thomas Gerrits, Andrey Goussev, Lukas G. Helt, and *et al.* Quantum circuits with many photons on a programmable nanophotonic chip. *Nature*, 591(7848):54–60, Mar 2021. (cited on page 73)

[345] Andrew Lucas. Ising formulations of many NP problems. *Front. Phys.*, 2:5, 2014. (cited on pages 74 and 98)

[346] James C. Spall. An overview of the simultaneous perturbation method for efficient optimization. *Johns Hopkins APL technical digest*, 19(4):482–492, 1998. (cited on page 75)

[347] Jerome Esteve, Christian Gross, Andreas Weller, Stefano Giovanazzi, and Markus K. Oberthaler. Squeezing and entanglement in a Bose–Einstein condensate. *Nature*, 455(7217):1216–1219, 2008. (cited on page 75)

[348] Thomas P. Purdy, Pen-Li Yu, Robert W. Peterson, Nir S. Kampel, and Cindy A. Regal. Strong optomechanical squeezing of light. *Phys. Rev. X*, 3:031012, Sep 2013. (cited on page 75)

[349] Helmut Strobel, Wolfgang Muessel, Daniel Linnemann, Tilman Zibold, David B. Hume, Luca Pezzè, Augusto Smerzi, and Markus K. Oberthaler. Fisher information and entanglement of non-gaussian spin states. *Science*, 345(6195):424–427, Jul 2014. (cited on pages 75, 77, 78, 79, 81, 82, and 92)

[350] W. Muessel, H. Strobel, D. Linnemann, T. Zibold, B. Juliá-Díaz, and M. K. Oberthaler. Twist-and-turn spin squeezing in bose-einstein condensates. *Phys. Rev. A*, 92:023603, Aug 2015. (cited on page 75)

[351] Kai Xu, Yu-Ran Zhang, Zheng-Hang Sun, Hekang Li, Pengtao Song, Zhongcheng Xiang, Kaixuan Huang, Hao Li, Yun-Hao Shi, Chi-Tong Chen, Xiaohui Song, Dongning Zheng, Franco Nori, H. Wang, and Heng Fan. Metrological characterization of non-gaussian entangled states of superconducting qubits. *Phys. Rev. Lett.*, 128:150501, Apr 2022. (cited on page 75)

[352] Anders Sørensen, L.-M. Duan, Juan Ignacio Cirac, and Peter Zoller. Many-particle entanglement with Bose–Einstein condensates. *Nature*, 409(6816):63–66, 2001. (cited on page 75)

[353] Jaroslaw K. Korbicz, Ignacio J. Cirac, and Maciej Lewenstein. Spin squeezing inequalities and entanglement of n qubit states. *Phys. Rev. Lett.*, 95:120502, Sep 2005. (cited on page 75)

[354] Jaroslaw K. Korbicz, Otfried Gühne, Maciej Lewenstein, Hartmut Häffner, Christian F. Roos, and Rainer Blatt. Generalized spin-squeezing inequalities in n-qubit systems: Theory and experiment. *Phys. Rev. A*, 74:052319, Nov 2006. (cited on page 75)

[355] Otfried Gühne and Géza Tóth. Entanglement detection. *Phys. Rep.*, 474(1-6):1–75, 2009. (cited on page 75)

[356] Géza Tóth. Detection of multipartite entanglement in the vicinity of symmetric dicke states. *J. Opt. Soc. Am. B*, 24(2):275–282, 2007. (cited on pages 75, 76, and 80)

[357] Xiaoguang Wang, Anders Søndberg Sørensen, and Klaus Mølmer. Spin squeezing in the Ising model. *Phys. Rev. A*, 64:053815, Oct 2001. (cited on page 75)

[358] Helmut Strobel. *Fisher Information and entanglement of non-Gaussian spin states*. PhD thesis, Kirchhoff Institute for Physics, Universität Heidelberg, 2016. (cited on pages 76 and 79)

[359] Iagoba Apellaniz, Bernd Lücke, Jan Peise, Carsten Klempt, and Géza Tóth. Detecting metrologically useful entanglement in the vicinity of Dicke states. *New J. Phys.*, 17(8):083027, aug 2015. (cited on page 76)

[360] Bernd Lücke, Jan Peise, Giuseppe Vitagliano, Jan Arlt, Luis Santos, Géza Tóth, and Carsten Klempt. Detecting multiparticle entanglement of Dicke states. *Phys. Rev. Lett.*, 112(15):155304, 2014. (cited on page 76)

[361] Philipp Hauke, Markus Heyl, Luca Tagliacozzo, and Peter Zoller. Measuring multipartite entanglement through dynamic susceptibilities. *Nat. Phys.*, 12(8):778–782, 2016. (cited on pages 77, 106, and 127)

[362] Jacob Smith, Aaron Lee, Philip Richerme, Brian Neyenhuis, Paul W. Hess, Philipp Hauke, Markus Heyl, David A. Huse, and Christopher Monroe. Many-body localization in a quantum simulator with programmable random disorder. *Nat. Phys.*, 12(10):907–911, 2016. (cited on pages 77 and 143)

[363] Teng-Long Wang, Ling-Na Wu, Wen Yang, Guang-Ri Jin, Neill Lambert, and Franco Nori. Quantum fisher information as a signature of the superradiant quantum phase transition. *New Journal of Physics*, 16(6):063039, 2014. (cited on page 77)

[364] Shaoying Yin, Jie Song, Yujun Zhang, and Shutian Liu. Quantum fisher information in quantum critical systems with topological characterization. *Phys. Rev. B*, 100:184417, Nov 2019. (cited on page 77)

[365] George Mathew, Saulo L. L. Silva, Anil Jain, Arya Mohan, Devashi T. Adroja, V. G. Sakai, C. V. Tomy, Alok Banerjee, Rajendar Goreti, Aswathi V. N., Ranjit Singh, and D. Jaiswal-Nagar. Experimental realization of multipartite entanglement via quantum Fisher information in a uniform antiferromagnetic quantum spin chain. *Phys. Rev. Research*, 2:043329, Dec 2020. (cited on page 77)

[366] Pontus Laurell, Allen Scheie, Chiron J. Mukherjee, Michael M. Koza, Mechtild Enderle, Zbigniew Tylczynski, Satoshi Okamoto, Radu Coldea, D. Alan Tennant, and Gonzalo Alvarez. Quantifying and controlling entanglement in the quantum magnet Cs_2CoCl_4. *Phys. Rev. Lett.*, 127:037201, Jul 2021. (cited on page 77)

[367] Luca Pezze and Augusto Smerzi. Quantum theory of phase estimation. *arXiv:1411.5164*, 2014. (cited on page 77)

[368] Géza Tóth and Iagoba Apellaniz. Quantum metrology from a quantum information science perspective. *J. Phys. A: Math. Theor.*, 47(42):424006, 2014. (cited on page 77)

[369] Ricardo Costa de Almeida and Philipp Hauke. From entanglement certification with quench dynamics to multipartite entanglement of interacting fermions. *Phys. Rev. Research*, 3:L032051, Aug 2021. (cited on page 77)

[370] David Gross. Non-negative wigner functions in prime dimensions. *Appl. Phys. B*, 86(3):367–370, 2007. (cited on pages 77 and 79)

[371] Edward Farhi, David Gamarnik, and Sam Gutmann. The quantum approximate optimization algorithm needs to see the whole graph: A typical case. *arXiv preprint arXiv:2004.09002*, 2020. (cited on page 81)

[372] Anders Sørensen and Klaus Mølmer. Quantum computation with ions in thermal motion. *Phys. Rev. Lett.*, 82:1971–1974, Mar 1999. (cited on pages 82 and 144)

[373] Cass A Sackett, David Kielpinski, Brian E King, Christopher Langer, Volker Meyer, Christopher J Myatt, M Rowe, QA Turchette, Wayne M Itano, David J Wineland, et al. Experimental entanglement of four particles. *Nature*, 404(6775):256–259, 2000. (cited on pages 82 and 87)

[374] Ben P Lanyon, Cornelius Hempel, Daniel Nigg, Markus Müller, Rene Gerritsma, F Zähringer, Philipp Schindler, Julio T Barreiro, Markus Rambach, Gerhard Kirchmair, et al. Universal digital quantum simulation with trapped ions. *Science*, 334(6052):57–61, 2011. (cited on page 82)

[375] Max Werninghaus, Daniel J. Egger, Federico Roy, Shai Machnes, Frank K. Wilhelm, and Stefan Filipp. Leakage reduction in fast superconducting qubit gates via optimal control. *npj Quantum Inf.*, 7, 2021. (cited on page 82)

[376] Andrew Wack, Hanhee Paik, Ali Javadi-Abhari, Petar Jurcevic, Ismael Faro, Jay M. Gambetta, and Blake R. Johnson. Quality, speed, and scale: three key attributes to measure the performance of near-term quantum computers. *arxiv: 2110.14108*, 2021. (cited on page 82)

[377] I. Pogorelov, T. Feldker, Ch. D. Marciniak, L. Postler, G. Jacob, O. Krieglsteiner, V. Podlesnic, M. Meth, V. Negnevitsky, M. Stadler, B. Höfer, C. Wächter, K. Lakhmanskiy, R. Blatt, P. Schindler, and T. Monz. Compact ion-trap quantum computing demonstrator. *PRX Quantum*, 2:020343, Jun 2021. (cited on page 82)

[378] Philipp Schindler, Daniel Nigg, Thomas Monz, Julio T Barreiro, Esteban Martinez, Shannon X Wang, Stephan Quint, Matthias F Brandl, Volckmar Nebendahl, Christian F Roos, et al. A quantum information processor with trapped ions. *New Journal of Physics*, 15(12):123012, 2013. (cited on page 82)

[379] Easwar Magesan, Jay M. Gambetta, and Joseph Emerson. Scalable and robust randomized benchmarking of quantum processes. *Phys. Rev. Lett.*, 106:180504, May 2011. (cited on page 83)

[380] Easwar Magesan, Jay M. Gambetta, Blake R. Johnson, Colm A. Ryan, Jerry M. Chow, Seth T. Merkel, Marcus P. da Silva, George A. Keefe, Mary B. Rothwell, and *et al.* Efficient measurement of quantum gate error by interleaved randomized benchmarking. *Phys. Rev. Lett.*, 109:080505, Aug 2012. (cited on page 83)

[381] Antonio D. Córcoles, Jay M. Gambetta, Jerry M. Chow, John A. Smolin, Matthew Ware, Joel Strand, Britton L. T. Plourde, and Matthias Steffen. Process verification of two-qubit quantum gates by randomized benchmarking. *Phys. Rev. A*, 87:030301, Mar 2013. (cited on page 83)

[382] Jeremy L. O'Brien, Geoff J. Pryde, Alexei Gilchrist, Daniel F. V. James, Nathan K. Langford, Timothy C. Ralph, and Andrew G. White. Quantum process tomography of a controlled-NOT gate. *Phys. Rev. Lett.*, 93:080502, Aug 2004. (cited on page 83)

[383] Radoslaw C. Bialczak, Markus Ansmann, Max Hofheinz, Erik Lucero, Matthew Neeley, Aaron D. O'Connell, Daniel Sank, Haohua Wang, James Wenner, Matthias Steffen, and *et al.* Quantum process tomography of a universal entangling gate implemented with josephson phase qubits. *Nat. Phys.*, 6(6):409–413, Jun 2010. (cited on page 83)

[384] Frank Arute, Kunal Arya, Ryan Babbush, Dave Bacon, Joseph C. Bardin, Rami Barends, Sergio Boixo, Michael Broughton, Bob B. Buckley, David A. Buell, and *et al.* Hartree-Fock on a superconducting qubit quantum computer. *Science*, 369(6507):1084–1089, 2020. (cited on page 83)

[385] Marcello Benedetti, Delfina Garcia-Pintos, Oscar Perdomo, Vicente Leyton-Ortega, Yunseong Nam, and Alejandro Perdomo-Ortiz. A generative modeling approach for benchmarking and training shallow quantum circuits. *Npj Quantum Inf.*, 5(1):45, May 2019. (cited on page 83)

[386] Pierre-Luc Dallaire-Demers and Nathan Killoran. Quantum generative adversarial networks. *Phys. Rev. A*, 98:012324, Jul 2018. (cited on page 83)

[387] Amir H. Karamlou, William A. Simon, Amara Katabarwa, Travis L. Scholten, Borja Peropadre, and Yudong Cao. Analyzing the performance of variational quantum factoring on a superconducting quantum processor. *Npj Quantum Inf.*, 7(1):156, Oct 2021. (cited on page 83)

[388] Pierre-Luc Dallaire-Demers, Michał Stęchły, Jerome F Gonthier, Ntwali Toussaint Bashige, Jonathan Romero, and Yudong Cao. An application benchmark for fermionic quantum simulations. *arXiv preprint arXiv:2003.01862*, 2020. (cited on page 83)

[389] Philipp Schmoll and Román Orús. Kitaev honeycomb tensor networks: Exact unitary circuits and applications. *Phys. Rev. B*, 95:045112, Jan 2017. (cited on page 83)

[390] Guifre Vidal and Christopher M. Dawson. Universal quantum circuit for two-qubit transformations with three controlled-NOT gates. *Phys. Rev. A*, 69:010301, Jan 2004. (cited on page 83)

[391] Daniel S. França and Raul García-Patrón. Limitations of optimization algorithms on noisy quantum devices. *Nat. Phys.*, 17(11):1221–1227, Nov 2021. (cited on page 84)

[392] David C. McKay, Christopher J. Wood, Sarah Sheldon, Jerry M. Chow, and Jay M. Gambetta. Efficient z gates for quantum computing. *Phys. Rev. A*, 96:022330, Aug 2017. (cited on page 86)

[393] Philip Krantz, Morten Kjaergaard, Fei Yan, Terry P. Orlando, Simon Gustavsson, and William D. Oliver. A quantum engineer's guide to superconducting qubits. *Appl. Phys. Rev.*, 6(2):021318, 2019. (cited on page 86)

[394] MD Sajid Anis, Abby-Mitchell, Héctor Abraham, Adu Offei, Rochisha Agarwal, Gabriele Agliardi, Merav Aharoni, Ismail Yunus Akhalwaya, Gadi Aleksandrowicz, Thomas Alexander, and *et al.* Qiskit: An open-source framework for quantum computing. *Zenodo*, February 2021. (cited on page 87)

[395] Yuwei Jin, Jason Luo, Lucent Fong, Yanhao Chen, Ari B Hayes, Chi Zhang, Fei Hua, and Eddy Z Zhang. A structured method for compilation of qaoa circuits in quantum computing. *arXiv preprint arXiv:2112.06143*, 2021. (cited on page 87)

[396] Sarah Sheldon, Easwar Magesan, Jerry M. Chow, and Jay M. Gambetta. Procedure for systematically tuning up cross-talk in the cross-resonance gate. *Phys. Rev. A*, 93:060302, Jun 2016. (cited on page 87)

[397] Neereja Sundaresan, Isaac Lauer, Emily Pritchett, Easwar Magesan, Petar Jurcevic, and Jay M. Gambetta. Reducing unitary and spectator errors in cross resonance with optimized rotary echoes. *PRX Quantum*, 1:020318, Dec 2020. (cited on page 87)

[398] Nathan Earnest, Caroline Tornow, and Daniel J. Egger. Pulse-efficient circuit transpilation for quantum applications on cross-resonance-based hardware. *Phys. Rev. Research*, 3:043088, Oct 2021. (cited on page 87)

[399] Thomas Alexander, Naoki Kanazawa, Daniel J. Egger, Lauren Capelluto, Christopher J. Wood, Ali Javadi-Abhari, and David C. McKay. Qiskit pulse: programming quantum computers through the cloud with pulses. *Quantum Sci. Technol.*, 5(4):044006, aug 2020. (cited on page 87)

[400] Sergey Bravyi, Sarah Sheldon, Abhinav Kandala, David C. Mckay, and Jay M. Gambetta. Mitigating measurement errors in multiqubit experiments. *Phys. Rev. A*, 103:042605, Apr 2021. (cited on page 87)

[401] George S Barron and Christopher J Wood. Measurement error mitigation for variational quantum algorithms. *arXiv:2010.08520*, 2020. (cited on page 87)

[402] V. Meyer, M. A. Rowe, D. Kielpinski, C. A. Sackett, W. M. Itano, C. Monroe, and D. J. Wineland. Experimental demonstration of entanglement-enhanced rotation angle estimation using trapped ions. *Phys. Rev. Lett.*, 86:5870–5873, Jun 2001. (cited on page 87)

[403] Dietrich Leibfried, Brian DeMarco, Volker Meyer, David Lucas, Murray Barrett, Joe Britton, Wayne M Itano, B Jelenković, Chris Langer, Till Rosenband, et al. Experimental demonstration of a robust, high-fidelity geometric two ion-qubit phase gate. *Nature*, 422(6930):412–415, 2003. (cited on page 87)

[404] Dietrich Leibfried, Murray D Barrett, T Schaetz, Joseph Britton, J Chiaverini, Wayne M Itano, John D Jost, Christopher Langer, and David J Wineland. Toward heisenberg-limited spectroscopy with multiparticle entangled states. *Science*, 304(5676):1476–1478, 2004. (cited on page 87)

[405] Dietrich Leibfried, Emanuel Knill, Signe Seidelin, Joe Britton, R Brad Blakestad, John Chiaverini, David B Hume, Wayne M Itano, John D Jost, Christopher Langer, et al. Creation of a six-atom 'schrödinger cat'state. *Nature*, 438(7068):639–642, 2005. (cited on page 87)

[406] Thomas Monz, Philipp Schindler, Julio T. Barreiro, Michael Chwalla, Daniel Nigg, William A. Coish, Maximilian Harlander, Wolfgang Hänsel, Markus Hennrich, and Rainer Blatt. 14-qubit entanglement: Creation and coherence. *Phys. Rev. Lett.*, 106:130506, Mar 2011. (cited on page 87)

[407] Raphael Kaubruegger, Pietro Silvi, Christian Kokail, Rick van Bijnen, Ana Maria Rey, Jun Ye, Adam M. Kaufman, and Peter Zoller. Variational spin-squeezing algorithms on programmable quantum sensors. *Phys. Rev. Lett.*, 123:260505, Dec 2019. (cited on pages 89 and 93)

[408] Bálint Koczor, Suguru Endo, Tyson Jones, Yuichiro Matsuzaki, and Simon C Benjamin. Variational-state quantum metrology. *New Journal of Physics*, 22(8):083038, 2020. (cited on pages 89 and 93)

[409] Johannes Jakob Meyer, Johannes Borregaard, and Jens Eisert. A variational toolbox for quantum multi-parameter estimation. *npj Quantum Information*, 7(1):1–5, 2021. (cited on pages 89 and 93)

[410] ShengChao Ding and Zhi Jin. Review on the study of entanglement in quantum computation speedup. *Chinese Science Bulletin*, 52(16):2161–2166, 2007. (cited on page 95)

[411] Noah Linden and Sandu Popescu. Good dynamics versus bad kinematics: Is entanglement needed for quantum computation? *Phys. Rev. Lett.*, 87:047901, Jul 2001. (cited on page 95)

[412] Humberto Munoz Bauza and Daniel A. Lidar. Scaling advantage in approximate optimization with quantum annealing. *arXiv:2401.07184*, 2024. (cited on page 95)

[413] Atanu Rajak, Sei Suzuki, Amit Dutta, and Bikas K Chakrabarti. Quantum annealing: An overview. *Philosophical Transactions of the Royal Society A*, 381(2241):20210417, 2023. (cited on page 95)

[414] Philipp Hauke, Lars Bonnes, Markus Heyl, and Wolfgang Lechner. Probing entanglement in adiabatic quantum optimization with trapped ions. *Frontiers in Physics*, 3:21, 2015. (cited on pages 95, 96, 101, 108, and 127)

[415] Román Orús and José I. Latorre. Universality of entanglement and quantum-computation complexity. *Phys. Rev. A*, 69:052308, May 2004. (cited on pages 95, 96, and 106)

[416] Arun K Pati and Samuel L Braunstein. Role of entanglement in quantum computation. *Journal of the Indian Institute of Science*, 89(3):295–302, 2009. (cited on page 95)

[417] Maxime Dupont, Nicolas Didier, Mark J. Hodson, Joel E. Moore, and Matthew J. Reagor. Calibrating the classical hardness of the quantum approximate optimization algorithm. *PRX Quantum*, 3:040339, Dec 2022. (cited on pages 95, 96, 97, and 127)

[418] Maxime Dupont, Nicolas Didier, Mark J Hodson, Joel E Moore, and Matthew J Reagor. Entanglement perspective on the quantum approximate optimization algorithm. *Phys. Rev. A*, 106(2):022423, 2022. (cited on pages 95, 96, 97, 127, and 128)

[419] Sudipto S. Roy, Silvia N. Santalla, Javier Rodríguez-Laguna, and Germán Sierra. Entanglement as geometry and flow. *Phys. Rev. B*, 101:195134, May 2020. (cited on page 95)

[420] Sudipto Singha Roy, Silvia N Santalla, Germán Sierra, and Javier Rodríguez-Laguna. Link representation of the entanglement entropies for all bipartitions. *Journal of Physics A: Mathematical and Theoretical*, 54(30):305301, jun 2021. (cited on page 95)

[421] Gabriele De Chiara and Anna Sanpera. Genuine quantum correlations in quantum many-body systems: a review of recent progress. *Reports on Progress in Physics*, 81(7):074002, June 2018. (cited on page 95)

[422] Kurt Binder and A Peter Young. Spin glasses: Experimental facts, theoretical concepts, and open questions. *Rev. Mod. Phys.*, 58(4):801, 1986. (cited on page 95)

[423] Shu Tanaka, Ryo Tamura, and Bikas K Chakrabarti. Quantum spin glasses, annealing and computation. *Cambridge University Press*, 2017. (cited on page 95)

[424] Mark Hillery, Vladimír Bužek, and André Berthiaume. Quantum secret sharing. *Phys. Rev. A*, 59:1829–1834, Mar 1999. (cited on page 95)

[425] Ping-Xing Chen, Shi-Yao Zhu, and Guang-Can Guo. General form of genuine multipartite entanglement quantum channels for teleportation. *Phys. Rev. A*, 74:032324, Sep 2006. (cited on page 95)

[426] Michael Epping, Hermann Kampermann, Chiara macchiavello, and Dagmar Bruß. Multipartite entanglement can speed up quantum key distribution in networks. *New Journal of Physics*, 19(9):093012, sep 2017. (cited on page 95)

[427] Géza Tóth. Multipartite entanglement and high-precision metrology. *Phys. Rev. A*, 85:022322, Feb 2012. (cited on page 95)

[428] H. J. Briegel, D. E. Browne, W. Dür, R. Raussendorf, and M. Van den Nest. Measurement-based quantum computation. *Nature Physics*, 5(1):19–26, January 2009. (cited on page 95)

[429] D. Bruß and C. Macchiavello. Multipartite entanglement in quantum algorithms. *Phys. Rev. A*, 83:052313, May 2011. (cited on page 95)

[430] Piotr Badzia g, Časlav Brukner, Wiesław Laskowski, Tomasz Paterek, and Marek Żukowski. Experimentally friendly geometrical criteria for entanglement. *Phys. Rev. Lett.*, 100:140403, Apr 2008. (cited on page 96)

[431] David A. Meyer. Sophisticated quantum search without entanglement. *Phys. Rev. Lett.*, 85:2014–2017, Aug 2000. (cited on page 96)

[432] Eli Biham, Gilles Brassard, Dan Kenigsberg, and Tal Mor. Quantum computing without entanglement. *Theoretical Computer Science*, 320(1):15–33, 2004. (cited on page 96)

[433] Dan Kenigsberg, Tal Mor, and Gil Ratsaby. Quantum advantage without entanglement. *Quantum Inf. Comput.*, 6(7):606–615, 2006. (cited on page 96)

[434] Maarten Van den Nest. Universal quantum computation with little entanglement. *Phys. Rev. Lett.*, 110:060504, Feb 2013. (cited on page 96)

[435] Rishi Sreedhar, Pontus Vikstål, Marika Svensson, Andreas Ask, Göran Johansson, and Laura García-Álvarez. The quantum approximate optimization algorithm performance with low entanglement and high circuit depth. *arXiv:2207.03404*, 2022. (cited on pages 96, 97, and 127)

[436] Moein Naseri, Tulja Varun Kondra, Suchetana Goswami, Marco Fellous-Asiani, and Alexander Streltsov. Entanglement and coherence in the bernstein-vazirani algorithm. *Phys. Rev. A*, 106:062429, Dec 2022. (cited on pages 96 and 97)

[437] T. Lanting, A. J. Przybysz, A. Yu. Smirnov, F. M. Spedalieri, M. H. Amin, A. J. Berkley, R. Harris, F. Altomare, S. Boixo, P. Bunyk, N. Dickson, C. Enderud, J. P. Hilton, E. Hoskinson, M. W. Johnson, E. Ladizinsky, N. Ladizinsky, R. Neufeld, T. Oh, I. Perminov, C. Rich, M. C. Thom, E. Tolkacheva, S. Uchaikin, A. B. Wilson, and G. Rose. Entanglement in a quantum annealing processor. *Phys. Rev. X*, 4:021041, May 2014. (cited on pages 96 and 127)

[438] Pablo Díez-Valle, Diego Porras, and Juan José García-Ripoll. Quantum variational optimization: The role of entanglement and problem hardness. *Phys. Rev. A*, 104:062426, Dec 2021. (cited on pages 97 and 127)

[439] Yanzhu Chen, Linghua Zhu, Nicholas J. Mayhall, Edwin Barnes, and Sophia E. Economou. How much entanglement do quantum optimization algorithms require? *Quantum 2.0 Conference and Exhibition*, page QM4A.2, 2022. (cited on pages 97, 127, and 128)

[440] M. Rossi, D. Bruß, and C. Macchiavello. Scale invariance of entanglement dynamics in grover's quantum search algorithm. *Phys. Rev. A*, 87:022331, Feb 2013. (cited on page 97)

[441] Tameem Albash and Daniel A. Lidar. Adiabatic quantum computation. *Rev. Mod. Phys.*, 90:015002, Jan 2018. (cited on page 98)

[442] Artur Soriani, Pierre Nazé, Marcus V. S. Bonança, Bartłomiej Gardas, and Sebastian Deffner. Three phases of quantum annealing: Fast, slow, and very slow. *Phys. Rev. A*, 105:042423, Apr 2022. (cited on page 101)

[443] Alexander Miessen, Daniel J Egger, Ivano Tavernelli, and Guglielmo Mazzola. Benchmarking digital quantum simulations and optimization above hundreds of qubits using quantum critical dynamics. *arXiv:2404.08053*, 2024. (cited on pages 101 and 109)

[444] V Ivakhnenko, Sergey N Shevchenko, and Franco Nori. Nonadiabatic landau–zener–stückelberg–majorana transitions, dynamics, and interference. *Physics Reports*, 995:1–89, 2023. (cited on pages 101 and 110)

[445] Azar C. Nakhl, Thomas Quella, and Muhammad Usman. Calibrating the role of entanglement in variational quantum circuits. *Phys. Rev. A*, 109:032413, Mar 2024. (cited on page 109)

[446] Kosei Teramoto, Rudy Raymond, and Hiroshi Imai. The role of entanglement in quantum-relaxation based optimization algorithms. *2023 IEEE International Conference on Quantum Computing and Engineering (QCE)*, 1:543–553, 2023. (cited on page 109)

[447] Oliver Buerschaper, Artur García-Saez, Román Orús, and Tzu-Chieh Wei. Topological minimally entangled states via geometric measure. *Journal of Statistical Mechanics: Theory and Experiment*, 2014(11):P11009, 2014. (cited on page 110)

[448] Michael Hart and John McAllister. Quantum circuit cutting minimising loss of qubit entanglement. *Proceedings of the 21st ACM International Conference on Computing Frontiers*, pages 207–214, 2024. (cited on page 110)

[449] Lennart Bittel and Martin Kliesch. Training variational quantum algorithms is np-hard. *Phys. Rev. Lett.*, 127:120502, Sep 2021. (cited on page 110)

[450] David Guéry-Odelin, Andreas Ruschhaupt, Anthony Kiely, Erik Torrontegui, Sofia Martínez-Garaot, and Juan Gonzalo Muga. Shortcuts to adiabaticity: Concepts, methods, and applications. *Rev. Mod. Phys.*, 91(4):045001, 2019. (cited on page 110)

[451] Andrei Broder and Eli Shamir. On the second eigenvalue of random regular graphs. *28th Annual Symposium on Foundations of Computer Science (sfcs 1987)*, pages 286–294, 1987. (cited on page 110)

[452] Sergio Boixo, Vadim N Smelyanskiy, Alireza Shabani, Sergei V Isakov, Mark Dykman, Vasil S Denchev, Mohammad H Amin, Anatoly Yu Smirnov, Masoud Mohseni, and Hartmut Neven. Computational multiqubit tunnelling in programmable quantum annealers. *Nature communications*, 7(1):10327, 2016. (cited on page 110)

[453] E. Knill and R. Laflamme. Power of one bit of quantum information. *Phys. Rev. Lett.*, 81:5672–5675, Dec 1998. (cited on page 110)

[454] Dorit Aharonov, Alexei Kitaev, and Noam Nisan. Quantum circuits with mixed states. *Proceedings of the thirtieth annual ACM symposium on Theory of computing*, pages 20–30, 1998. (cited on page 110)

[455] Animesh Datta and Guifre Vidal. Role of entanglement and correlations in mixed-state quantum computation. *Phys. Rev. A*, 75:042310, Apr 2007. (cited on page 110)

[456] Thomas Schulte-Herbrüggen, Raimund Marx, Amr Fahmy, Louis Kauffman, Samuel Lomonaco, Navin Khaneja, and Steffen J Glaser. Control aspects of quantum computing using pure and mixed states. *Philosophical Transactions of the Royal Society A: Mathematical, Physical and Engineering Sciences*, 370(1976):4651–4670, 2012. (cited on page 110)

[457] Vittorio Giovannetti, Seth Lloyd, and Lorenzo Maccone. A quantum algorithm for estimating the determinant. *arXiv preprint arXiv:2504.11049*, 2025. (cited on page 111)

[458] Francisco JR Ruiz, Tuomas Laakkonen, Johannes Bausch, Matej Balog, Mohammadamin Barekatain, Francisco JH Heras, Alexander Novikov, Nathan Fitzpatrick, Bernardino Romera-Paredes, John van de Wetering, et al. Quantum circuit optimization with alphatensor. *Nature Machine Intelligence*, pages 1–12, 2025. (cited on page 111)

[459] Craig Gidney. How to factor 2048 bit rsa integers with less than a million noisy qubits. *arXiv preprint arXiv:2505.15917*, 2025. (cited on page 111)

[460] Google Quantum AI. Google unveils 'willow' quantum processor, achieves milestone in error correction. *Google Research Blog*, December 2024. Accessed July 2025. (cited on pages 111 and 193)

[461] Andrew D King, Alberto Nocera, Marek M Rams, Jacek Dziarmaga, Roeland Wiersema, William Bernoudy, Jack Raymond, Nitin Kaushal, Niclas Heinsdorf, Richard Harris, et al. Beyond-classical computation in quantum simulation. *Science*, 388(6743):199–204, 2025. (cited on page 111)

[462] Pedro Sales Rodriguez, John M Robinson, Paul Niklas Jepsen, Zhiyang He, Casey Duckering, Chen Zhao, Kai-Hsin Wu, Joseph Campo, Kevin Bagnall, Minho Kwon, et al. Experimental demonstration of logical magic state distillation. *Nature*, pages 1–3, 2025. (cited on page 111)

[463] Gary J Mooney, Gregory AL White, Charles D Hill, and Lloyd CL Hollenberg. Whole-device entanglement in a 65-qubit superconducting quantum computer. *Advanced Quantum Technologies*, 4(10):2100061, 2021. (cited on page 112)

[464] René Zander and Colin Kai-Uwe Becker. Benchmarking multipartite entanglement generation with graph states. *Advanced Quantum Technologies*, 8(1):2400239, 2025. (cited on page 112)

[465] John F Kam, Haiyue Kang, Charles D Hill, Gary J Mooney, and Lloyd CL Hollenberg. Characterization of entanglement on superconducting quantum computers of up to 414 qubits. *Physical Review Research*, 6(3):033155, 2024. (cited on page 112)

[466] Tiff Brydges, Andreas Elben, Petar Jurcevic, Benoît Vermersch, Christine Maier, Ben P Lanyon, Peter Zoller, Rainer Blatt, and Christian F Roos. Probing rényi entanglement entropy via randomized measurements. *Science*, 364(6437):260–263, 2019. (cited on page 112)

[467] Paweł Horodecki and Artur Ekert. Method for direct detection of quantum entanglement. *Phys. Rev. Lett.*, 89:127902, Aug 2002. (cited on page 112)

[468] Rajibul Islam, Ruichao Ma, Philipp M Preiss, M Eric Tai, Alexander Lukin, Matthew Rispoli, and Markus Greiner. Measuring entanglement entropy in a quantum many-body system. *Nature*, 528(7580):77–83, 2015. (cited on page 112)

[469] Sonika Johri, Damian S. Steiger, and Matthias Troyer. Entanglement spectroscopy on a quantum computer. *Phys. Rev. B*, 96:195136, Nov 2017. (cited on pages 112, 114, and 116)

[470] A. J. Daley, H. Pichler, J. Schachenmayer, and P. Zoller. Measuring entanglement growth in quench dynamics of bosons in an optical lattice. *Phys. Rev. Lett.*, 109:020505, Jul 2012. (cited on page 112)

[471] Adriano Barenco, André Berthiaume, David Deutsch, Artur Ekert, Richard Jozsa, and Chiara Macchiavello. Stabilization of quantum computations by symmetrization. *SIAM Journal on Computing*, 26(5):1541–1557, 1997. (cited on page 113)

[472] Harry Buhrman, Richard Cleve, John Watrous, and Ronald De Wolf. Quantum fingerprinting. *Physical review letters*, 87(16):167902, 2001. (cited on page 113)

[473] H. Francis Song, Stephan Rachel, Christian Flindt, Israel Klich, Nicolas Laflorencie, and Karyn Le Hur. Bipartite fluctuations as a probe of many-body entanglement. *Phys. Rev. B*, 85:035409, Jan 2012. (cited on page 114)

[474] Wei Tang, Teague Tomesh, Martin Suchara, Jeffrey Larson, and Margaret Martonosi. Cutqc: using small quantum computers for large quantum circuit evaluations. In *Proceedings of the 26th ACM International conference on architectural support for programming languages and operating systems*, pages 473–486, 2021. (cited on page 118)

[475] Kosuke Mitarai and Keisuke Fujii. Overhead for simulating a non-local channel with local channels by quasiprobability sampling. *Quantum*, 5:388, 2021. (cited on page 118)

[476] Lukas Schmitt, Christophe Piveteau, and David Sutter. Cutting circuits with multiple two-qubit unitaries. *Quantum*, 9:1634, 2025. (cited on page 118)

[477] Christophe Piveteau and David Sutter. Circuit knitting with classical communication. *IEEE Transactions on Information Theory*, 70(4):2734–2745, 2023. (cited on page 118)

[478] Lukas Brenner, Christophe Piveteau, and David Sutter. Optimal wire cutting with classical communication. *arXiv preprint arXiv:2302.03366*, 2023. (cited on page 118)

[479] IBM Quantum. Circuit cutting with qiskit. `https://quantum.cloud.ibm.com/docs/en/guides/qiskit-addons-cutting`, 2024. Accessed: 2025-07-31. (cited on page 119)

[480] Qiskit Community. Qiskit optimization best practices. `https://github.com/qiskit-community/qopt-best-practices`, 2023. Accessed: 2025-07-17. (cited on page 121)

[481] Michael JD Powell. *A direct search optimization method that models the objective and constraint functions by linear interpolation*. Springer, 1994. (cited on pages 122 and 130)

[482] Jacob Biamonte, Peter Wittek, Nicola Pancotti, Patrick Rebentrost, Nathan Wiebe, and Seth Lloyd. Quantum machine learning. *Nature*, 549(7671):195–202, 2017. (cited on page 126)

[483] Raimund Mannhold, Hugo Kubinyi, and Hendrik Timmerman. *Combinatorial Chemistry: A practical approach*. John Wiley & Sons, 2009. (cited on page 127)

[484] Gang Yu. *Industrial applications of combinatorial optimization*, volume 16. Springer Science & Business Media, 2013. (cited on page 127)

[485] Julius Beneoluchi Odili. Combinatorial optimization in science and engineering. *Current Science*, pages 2268–2274, 2017. (cited on page 127)

[486] Sheir Yarkoni, Elena Raponi, Thomas Bäck, and Sebastian Schmitt. Quantum annealing for industry applications: Introduction and review. *Reports on Progress in Physics*, 85(10):104001, 2022. (cited on page 127)

[487] Pei-Hua Wang, Jen-Hao Chen, Yu-Yuan Yang, Chien Lee, and Yufeng Jane Tseng. Recent advances in quantum computing for drug discovery and development. *IEEE Nanotechnology Magazine*, 17(2):26–30, 2023. (cited on page 127)

[488] Phillip C Lotshaw, Thien Nguyen, Anthony Santana, Alexander McCaskey, Rebekah Herman, James Ostrowski, George Siopsis, and Travis S Humble. Scaling quantum approximate optimization on near-term hardware. *Scientific Reports*, 12(1):12388, 2022. (cited on page 127)

[489] Elijah Pelofske, Andreas Bärtschi, and Stephan Eidenbenz. Quantum annealing vs. qaoa: 127 qubit higher-order ising problems on nisq computers. In *International Conference on High Performance Computing*, pages 240–258. Springer, 2023. (cited on page 127)

[490] Alberto Bottarelli, Sebastian Schmitt, and Philipp Hauke. Inequality constraints in variational quantum circuits with qudits. *arXiv preprint arXiv:2410.07674*, 2024. (cited on pages 127 and 159)

[491] Ruslan Shaydulin, Changhao Li, Shouvanik Chakrabarti, Matthew DeCross, Dylan Herman, Niraj Kumar, Jeffrey Larson, Danylo Lykov, Pierre Minssen, Yue Sun, et al. Evidence of scaling advantage for the quantum approximate optimization algorithm on a classically intractable problem. *Science Advances*, 10(22):eadm6761, 2024. (cited on page 127)

[492] Edward Farhi and Aram W Harrow. Quantum supremacy through the quantum approximate optimization algorithm. *arXiv:1602.07674*, 2016. (cited on page 127)

[493] Sami Boulebnane, Abid Khan, Minzhao Liu, Jeffrey Larson, Dylan Herman, Ruslan Shaydulin, and Marco Pistoia. Evidence that the quantum approximate optimization algorithm optimizes the sherrington-kirkpatrick model efficiently in the average case. *arXiv:2505.07929*, 2025. (cited on page 127)

[494] Sivaprasad Omanakuttan, Zichang He, Zhiwei Zhang, Tianyi Hao, Arman Babakhani, Sami Boulebnane, Shouvanik Chakrabarti, Dylan Herman, Joseph Sullivan, Michael A Perlin, et al. Threshold for fault-tolerant quantum advantage with the quantum approximate optimization algorithm. *arXiv:2504.01897*, 2025. (cited on page 127)

[495] Sebastian Brandhofer, Daniel Braun, Vanessa Dehn, Gerhard Hellstern, Matthias Hüls, Yanjun Ji, Ilia Polian, Amandeep Singh Bhatia, and Thomas Wellens. Benchmarking the performance of portfolio optimization with qaoa. *Quantum Information Processing*, 22(1):25, 2022. (cited on page 127)

[496] Gian Giacomo Guerreschi and Anne Y Matsuura. Qaoa for max-cut requires hundreds of qubits for quantum speed-up. *Scientific reports*, 9(1):6903, 2019. (cited on page 127)

[497] Yannick Deller, Sebastian Schmitt, Maciej Lewenstein, Steve Lenk, Marika Federer, Fred Jendrzejewski, Philipp Hauke, and Valentin Kasper. Quantum approximate optimization algorithm for qudit systems. *Phys. Rev. A*, 107(6):062410, Jun 2023. (cited on pages 127, 129, 147, and 159)

[498] Linus Ekstrom, Hao Wang, and Sebastian Schmitt. Variational quantum multiobjective optimization. *Phys. Rev. Res.*, 7:023141, May 2025. (cited on page 127)

[499] Sergey Bravyi, Alexander Kliesch, Robert Koenig, and Eugene Tang. Hybrid quantum-classical algorithms for approximate graph coloring. *Quantum*, 6:678, 2022. (cited on pages 127 and 129)

[500] Luigi Amico, Rosario Fazio, Andreas Osterloh, and Vlatko Vedral. Entanglement in many-body systems. *Rev. Mod. Phys.*, 80:517–576, May 2008. (cited on page 127)

[501] J. Eisert, M. Cramer, and M. B. Plenio. Colloquium: Area laws for the entanglement entropy. *Rev. Mod. Phys.*, 82:277–306, Feb 2010. (cited on page 127)

[502] Vittorio Vitale, Aniket Rath, Petar Jurcevic, Andreas Elben, Cyril Branciard, and Benoît Vermersch. Robust estimation of the quantum fisher information on a quantum processor. *PRX Quantum*, 5:030338, Aug 2024. (cited on page 127)

[503] Gopal Chandra Santra, Sudipto Singha Roy, Daniel J. Egger, and Philipp Hauke. Genuine multipartite entanglement in quantum optimization. *Phys. Rev. A*, 111:022434, Feb 2025. (cited on pages 127, 128, and 195)

[504] Sergey Bravyi and Alexei Kitaev. Universal quantum computation with ideal clifford gates and noisy ancillas. *Phys. Rev. A*, 71:022316, Feb 2005. (cited on page 127)

[505] Sergey Bravyi and Jeongwan Haah. Magic-state distillation with low overhead. *Phys. Rev. A*, 86:052329, Nov 2012. (cited on pages 127 and 140)

[506] Earl T Campbell, Barbara M Terhal, and Christophe Vuillot. Roads towards fault-tolerant universal quantum computation. *Nature*, 549(7671):172–179, 2017. (cited on page 127)

[507] Aram W Harrow and Ashley Montanaro. Quantum computational supremacy. *Nature*, 549(7671):203–209, 2017. (cited on page 127)

[508] William K Wootters. A wigner-function formulation of finite-state quantum mechanics. *Annals of Physics*, 176(1):1–21, 1987. (cited on page 127)

[509] V. Bužek, A. Vidiella-Barranco, and P. L. Knight. Superpositions of coherent states: Squeezing and dissipation. *Phys. Rev. A*, 45:6570–6585, May 1992. (cited on page 127)

[510] Sergey Bravyi and David Gosset. Improved classical simulation of quantum circuits dominated by clifford gates. *Phys. Rev. Lett.*, 116:250501, Jun 2016. (cited on page 127)

[511] Sergey Bravyi, Graeme Smith, and John A. Smolin. Trading classical and quantum computational resources. *Phys. Rev. X*, 6:021043, Jun 2016. (cited on page 127)

[512] Mark Howard and Earl Campbell. Application of a resource theory for magic states to fault-tolerant quantum computing. *Phys. Rev. Lett.*, 118:090501, Mar 2017. (cited on page 127)

[513] Markus Heinrich and David Gross. Robustness of magic and symmetries of the stabiliser polytope. *Quantum*, 3:132, 2019. (cited on page 127)

[514] Xin Wang, Mark M. Wilde, and Yuan Su. Efficiently computable bounds for magic state distillation. *Phys. Rev. Lett.*, 124:090505, Mar 2020. (cited on page 127)

[515] Arne Heimendahl, Felipe Montealegre-Mora, Frank Vallentin, and David Gross. Stabilizer extent is not multiplicative. *Quantum*, 5:400, 2021. (cited on page 127)

[516] Lorenzo Leone and Lennart Bittel. Stabilizer entropies are monotones for magic-state resource theory. *Phys. Rev. A*, 110:L040403, Oct 2024. (cited on page 127)

[517] Saubhik Sarkar, Chiranjib Mukhopadhyay, and Abolfazl Bayat. Characterization of an operational quantum resource in a critical many-body system. *New Journal of Physics*, 22(8):083077, 2020. (cited on page 127)

[518] Salvatore F. E. Oliviero, Lorenzo Leone, and Alioscia Hamma. Magic-state resource theory for the ground state of the transverse-field ising model. *Phys. Rev. A*, 106:042426, Oct 2022. (cited on pages 127 and 164)

[519] Zi-Wen Liu and Andreas Winter. Many-body quantum magic. *PRX Quantum*, 3:020333, May 2022. (cited on page 127)

[520] Michele Viscardi, Marcello Dalmonte, Alioscia Hamma, and Emanuele Tirrito. Interplay of entanglement structures and stabilizer entropy in spin models. *arXiv:2503.08620*, 2025. (cited on page 127)

[521] Pedro R Nicácio Falcão, Piotr Sierant, Jakub Zakrzewski, and Emanuele Tirrito. Magic dynamics in many-body localized systems. *arXiv:2503.07468*, 2025. (cited on pages 127 and 164)

[522] Gopal Chandra Santra, Alex Windey, Soumik Bandyopadhyay, Andrea Legramandi, and Philipp Hauke. Complexity transitions in chaotic quantum systems. *arXiv:2505.09707*, 2025. (cited on pages 127, 193, and 196)

[523] David Aram Korbany, Michael J Gullans, and Lorenzo Piroli. Long-range nonstabilizerness and phases of matter. *arXiv:2502.19504*, 2025. (cited on page 127)

[524] Xhek Turkeshi, Emanuele Tirrito, and Piotr Sierant. Magic spreading in random quantum circuits. *Nature Communications*, 16(1):2575, 2025. (cited on pages 127, 131, and 164)

[525] Naga Dileep Varikuti, Soumik Bandyopadhyay, and Philipp Hauke. Impact of clifford operations on non-stabilizing power and quantum chaos. *arXiv:2505.14793*, 2025. (cited on pages 127 and 164)

[526] Christopher David White, ChunJun Cao, and Brian Swingle. Conformal field theories are magical. *Phys. Rev. B*, 103:075145, Feb 2021. (cited on pages 127 and 164)

[527] Poetri Sonya Tarabunga. Critical behaviors of non-stabilizerness in quantum spin chains. *Quantum*, 8:1413, 2024. (cited on page 127)

[528] Masahiro Hoshino, Masaki Oshikawa, and Yuto Ashida. Stabilizer r\'enyi entropy and conformal field theory. *arXiv:2503.13599*, 2025. (cited on pages 127 and 164)

[529] Dmitry Panchenko. *The sherrington-kirkpatrick model*. Springer Science & Business Media, 2013. (cited on pages 127, 129, and 188)

[530] Salvatore FE Oliviero, Lorenzo Leone, Alioscia Hamma, and Seth Lloyd. Measuring magic on a quantum processor. *npj Quantum Information*, 8(1):148, 2022. (cited on pages 128 and 193)

[531] Dolev Bluvstein, Simon J Evered, Alexandra A Geim, Sophie H Li, Hengyun Zhou, Tom Manovitz, Sepehr Ebadi, Madelyn Cain, Marcin Kalinowski, Dominik Hangleiter, et al. Logical quantum processor based on reconfigurable atom arrays. *Nature*, 626(7997):58–65, 2024. (cited on page 128)

[532] David Gross, Sepehr Nezami, and Michael Walter. Schur–weyl duality for the clifford group with applications: Property testing, a robust hudson theorem, and de finetti representations. *Commun. Math. Phys.*, 385(3):1325–1393, 2021. (cited on page 128)

[533] William K Wootters. A wigner-function formulation of finite-state quantum mechanics. *Annals of Physics*, 176(1):1–21, 1987. (cited on page 128)

[534] Michael Streif and Martin Leib. Comparison of qaoa with quantum and simulated annealing. *arXiv:1901.01903*, 2019. (cited on page 129)

[535] Gabriel Bottrill, Mudit Pandey, and Olivia Di Matteo. Exploring the potential of qutrits for quantum optimization of graph coloring. *2023 IEEE International Conference on Quantum Computing and Engineering (QCE)*, 01:177–183, 2023. (cited on page 129)

[536] Márton Karácsony, László Oroszlány, and Zoltán Zimborás. Efficient qudit based scheme for photonic quantum computing. *SciPost Physics Core*, 7(2):032, 2024. (cited on page 129)

[537] David Sherrington and Scott Kirkpatrick. Solvable model of a spin-glass. *Phys. Rev. Lett.*, 35:1792–1796, Dec 1975. (cited on page 129)

[538] Davide Venturelli, Salvatore Mandrà, Sergey Knysh, Bryan O'Gorman, Rupak Biswas, and Vadim Smelyanskiy. Quantum optimization of fully connected spin glasses. *Phys. Rev. X*, 5:031040, Sep 2015. (cited on pages 129 and 188)

[539] Samuel Mugel, Carlos Kuchkovsky, Escolástico Sánchez, Samuel Fernández-Lorenzo, Jorge Luis-Hita, Enrique Lizaso, and Román Orús. Dynamic portfolio optimization with real datasets using quantum processors and quantum-inspired tensor networks. *Phys. Rev. R*, 4(1):013006, 2022. (cited on page 129)

[540] Giuseppe E. Santoro, Roman Martoňák, Erio Tosatti, and Roberto Car. Theory of quantum annealing of an ising spin glass. *Science*, 295(5564):2427–2430, 2002. (cited on page 137)

[541] Ulrich Schollwöck. The density-matrix renormalization group in the age of matrix product states. *Annals of physics*, 326(1):96–192, 2011. (cited on page 137)

[542] Román Orús. A practical introduction to tensor networks: Matrix product states and projected entangled pair states. *Annals of physics*, 349:117–158, 2014. (cited on pages 137, 163, 167, and 189)

[543] Shi-Ju Ran, Emanuele Tirrito, Cheng Peng, Xi Chen, Luca Tagliacozzo, Gang Su, and Maciej Lewenstein. *Tensor network contractions: methods and applications to quantum many-body systems*. Springer Nature, 2020. (cited on page 137)

[544] Poetri Sonya Tarabunga, Emanuele Tirrito, Mari Carmen Bañuls, and Marcello Dalmonte. Nonstabilizerness via matrix product states in the pauli basis. *Physical Review Letters*, 133(1):010601, 2024. (cited on pages 137 and 193)

[545] Joe O'Gorman and Earl T. Campbell. Quantum computation with realistic magic-state factories. *Phys. Rev. A*, 95:032338, Mar 2017. (cited on pages 140 and 189)

[546] Alexandre M Souza, Jingfu Zhang, Colm A Ryan, and Raymond Laflamme. Experimental magic state distillation for fault-tolerant quantum computing. *Nature communications*, 2(1):169, 2011. (cited on page 140)

[547] Michael Beverland, Earl Campbell, Mark Howard, and Vadym Kliuchnikov. Lower bounds on the non-clifford resources for quantum computations. *Quantum Science and Technology*, 5(3):035009, 2020. (cited on page 140)

[548] Earl T Campbell. Early fault-tolerant simulations of the hubbard model. *Quantum Science and Technology*, 7(1):015007, 2021. (cited on page 140)

[549] Guido Pagano, Aniruddha Bapat, Patrick Becker, Katherine S Collins, Arinjoy De, Paul W Hess, Harvey B Kaplan, Antonis Kyprianidis, Wen Lin Tan, Christopher Baldwin, et al. Quantum approximate optimization of the long-range ising model with a trapped-ion quantum simulator. *Proceedings of the National Academy of Sciences*, 117(41):25396–25401, 2020. (cited on page 140)

[550] P Huber, J Haber, P Barthel, JJ García-Ripoll, E Torrontegui, and C Wunderlich. Realization of a quantum perceptron gate with trapped ions. *arXiv:2111.08977*, 2021. (cited on page 140)

[551] CJ Reichhardt and C Reichhardt. Disorder in the wild. *Nature Physics*, 13(1):10–11, 2017. (cited on page 143)

[552] David G Bounds. New optimization methods from physics and biology. *Nature*, 329(6136):215–219, 1987. (cited on page 143)

[553] A Boschetti, L Pattelli, R Torre, and DS Wiersma. Perspectives and recent advances in super-resolution spectroscopy: Stochastic and disordered-based approaches. *Applied Physics Letters*, 120(25):250502, 2022. (cited on page 143)

[554] Jan-Michael Reiner, Sebastian Zanker, Iris Schwenk, Juha Leppäkangas, Frank Wilhelm-Mauch, Gerd Schön, and Michael Marthaler. Effects of gate errors in digital quantum simulations of fermionic systems. *Quantum Science and Technology*, 3(4):045008, 2018. (cited on page 143)

[555] Tameem Albash, Victor Martin-Mayor, and Itay Hen. Analog errors in ising machines. *Quantum Science and Technology*, 4(2):02LT03, 2019. (cited on page 143)

[556] P. V. Klimov, J. Kelly, Z. Chen, M. Neeley, A. Megrant, B. Burkett, R. Barends, K. Arya, B. Chiaro, Yu Chen, A. Dunsworth, A. Fowler, B. Foxen, C. Gidney, M. Giustina, R. Graff, T. Huang, E. Jeffrey, Erik Lucero, J. Y. Mutus, O. Naaman, C. Neill, C. Quintana, P. Roushan, Daniel Sank, A. Vainsencher, J. Wenner, T. C. White, S. Boixo, R. Babbush, V. N. Smelyanskiy, H. Neven, and John M. Martinis. Fluctuations of energy-relaxation times in superconducting qubits. *Phys. Rev. Lett.*, 121:090502, Aug 2018. (cited on page 143)

[557] Jonathan Brugger, Christian Seidel, Michael Streif, Filip A. Wudarski, Christoph Dittel, and Andreas Buchleitner. Output statistics of quantum annealers with disorder. *Phys. Rev. A*, 105:042605, Apr 2022. (cited on page 143)

[558] P. W. Anderson. Absence of diffusion in certain random lattices. *Phys. Rev.*, 109:1492–1505, Mar 1958. (cited on pages 143 and 163)

[559] Samuel Frederick Edwards and Phil W Anderson. Theory of spin glasses. *Journal of Physics F: Metal Physics*, 5(5):965, 1975. (cited on page 143)

[560] I Ya Korenblit and EF Shender. Ferromagnetism of disordered systems. *Soviet Physics Uspekhi*, 21(10):832, 1978. (cited on page 143)

[561] JA Mydosh. Spin glasses—recent experiments and systems. *Journal of Magnetism and Magnetic Materials*, 7(1-4):237–248, 1978. (cited on page 143)

[562] Ad Lagendijk, Bart van Tiggelen, and Diederik S Wiersma. Fifty years of anderson localization. *Physics today*, 62(8):24–29, 2009. (cited on page 143)

[563] Dmitry A Abanin, Ehud Altman, Immanuel Bloch, and Maksym Serbyn. Colloquium: Many-body localization, thermalization, and entanglement. *Rev. Mod. Phys.*, 91(2):021001, 2019. (cited on page 143)

[564] Thomas Vojta. Disorder in quantum many-body systems. *Annual Review of Condensed Matter Physics*, 10(1):233–252, 2019. (cited on pages 143 and 163)

[565] J. A. Schreier, A. A. Houck, Jens Koch, D. I. Schuster, B. R. Johnson, J. M. Chow, J. M. Gambetta, J. Majer, L. Frunzio, M. H. Devoret, S. M. Girvin, and R. J. Schoelkopf. Suppressing charge noise decoherence in superconducting charge qubits. *Phys. Rev. B*, 77:180502, May 2008. (cited on page 143)

[566] M. R. Delbecq, T. Nakajima, P. Stano, T. Otsuka, S. Amaha, J. Yoneda, K. Takeda, G. Allison, A. Ludwig, A. D. Wieck, and S. Tarucha. Quantum dephasing in a gated gaas triple quantum dot due to nonergodic noise. *Phys. Rev. Lett.*, 116:046802, Jan 2016. (cited on page 143)

[567] J. I. Colless, V. V. Ramasesh, D. Dahlen, M. S. Blok, M. E. Kimchi-Schwartz, J. R. McClean, J. Carter, W. A. de Jong, and I. Siddiqi. Computation of molecular spectra on a quantum processor with an error-resilient algorithm. *Phys. Rev. X*, 8:011021, Feb 2018. (cited on page 143)

[568] Timothy Proctor, Melissa Revelle, Erik Nielsen, Kenneth Rudinger, Daniel Lobser, Peter Maunz, Robin Blume-Kohout, and Kevin Young. Detecting and tracking drift in quantum information processors. *Nature communications*, 11(1):5396, 2020. (cited on page 143)

[569] KC Beverly, JL Sample, JF Sampaio, F Remacle, JR Heath, and RD Levine. Quantum dot artificial solids: Understanding the static and dynamic role of size and packing disorder. *Proceedings of the National Academy of Sciences*, 99(suppl_2):6456–6459, 2002. (cited on page 143)

[570] Sergey Knysh and Vadim Smelyanskiy. On the relevance of avoided crossings away from quantum critical point to the complexity of quantum adiabatic algorithm. *arXiv:1005.3011*, 2010. (cited on pages 143 and 188)

[571] Manuel Pino and Juan José García-Ripoll. Quantum annealing in spin-boson model: From a perturbative to an ultrastrong mediated coupling. *New Journal of Physics*, 20(11):113027, 2018. (cited on pages 143 and 188)

[572] Patrick Rebentrost, Masoud Mohseni, Ivan Kassal, Seth Lloyd, and Alán Aspuru-Guzik. Environment-assisted quantum transport. *New Journal of Physics*, 11(3):033003, 2009. (cited on page 143)

[573] Christine Maier, Tiff Brydges, Petar Jurcevic, Nils Trautmann, Cornelius Hempel, Ben P. Lanyon, Philipp Hauke, Rainer Blatt, and Christian F. Roos. Environment-assisted quantum transport in a 10-qubit network. *Phys. Rev. Lett.*, 122:050501, Feb 2019. (cited on page 143)

[574] Cyril Stark, Lode Pollet, Ata ç Imamoğlu, and Renato Renner. Localization of toric code defects. *Phys. Rev. Lett.*, 107:030504, Jul 2011. (cited on pages 143 and 188)

[575] James R Wootton and Jiannis K Pachos. Bringing order through disorder: Localization of errors in topological quantum memories. *Phys. Rev. Lett.*, 107(3):030503, 2011. (cited on page 143)

[576] Rahul Nandkishore and David A Huse. Many-body localization and thermalization in quantum statistical mechanics. *Annu. Rev. Condens. Matter Phys.*, 6(1):15–38, 2015. (cited on page 143)

[577] Clemens Gneiting, Felix R. Anger, and Andreas Buchleitner. Incoherent ensemble dynamics in disordered systems. *Phys. Rev. A*, 93:032139, Mar 2016. (cited on pages 143 and 162)

[578] Chahan M Kropf, Clemens Gneiting, and Andreas Buchleitner. Effective dynamics of disordered quantum systems. *Phys. Rev. X*, 6(3):031023, 2016. (cited on pages 143, 144, 147, 148, and 162)

[579] Hong-Bin Chen. Effects of symmetry breaking of the structurally-disordered hamiltonian ensembles on the anisotropic decoherence of qubits. *Scientific reports*, 12(1):2869, 2022. (cited on pages 143 and 162)

[580] Congwei Lu, Wanting He, Jun Wang, Haibo Wang, and Qing Ai. Sudden death of entanglement with a hamiltonian ensemble assisted by auxiliary qubits. *Phys. Rev. A*, 108:012621, Jul 2023. (cited on pages 143 and 162)

[581] Chahan M. Kropf. Protecting quantum coherences from static noise and disorder. *Phys. Rev. Res.*, 2:033311, Aug 2020. (cited on pages 143, 153, and 162)

[582] Hong-Bin Chen, Clemens Gneiting, Ping-Yuan Lo, Yueh-Nan Chen, and Franco Nori. Simulating open quantum systems with hamiltonian ensembles and the nonclassicality of the dynamics. *Phys. Rev. Lett.*, 120:030403, Jan 2018. (cited on pages 144 and 162)

[583] JungYun Han, Clemens Gneiting, and Daniel Leykam. Helical transport in coupled resonator waveguides. *Phys. Rev. B*, 99:224201, Jun 2019. (cited on pages 144 and 162)

[584] Yao Ma, Mi Pang, Libo Chen, and Wen Yang. Improving quantum parameter estimation by monitoring quantum trajectories. *Phys. Rev. A*, 99:032347, Mar 2019. (cited on pages 144 and 147)

[585] Soumik Bandyopadhyay, Philipp Uhrich, Alessio Paviglianiti, and Philipp Hauke. Universal equilibration dynamics of the sachdev-ye-kitaev model. *Quantum*, 7:1022, 2023. (cited on pages 144 and 148)

[586] Alessio Paviglianiti, Soumik Bandyopadhyay, Philipp Uhrich, and Philipp Hauke. Absence of operator growth for average equal-time observables in charge-conserved sectors of the sachdev-ye-kitaev model. *Journal of High Energy Physics*, 2023(3):1–23, 2023. (cited on page 144)

[587] Erika Andersson, James D Cresser, and Michael JW Hall. Finding the kraus decomposition from a master equation and vice versa. *Journal of Modern Optics*, 54(12):1695–1716, 2007. (cited on pages 144, 147, and 153)

[588] Zhongshan Li, Frank Hall, and Carolyn Eschenbach. On the period and base of a sign pattern matrix. *Linear Algebra and Its Applications*, 212:101–120, 1994. (cited on pages 144 and 147)

[589] Melvyn W Jeter and Wallace C Pye. Nonnegative (s, t)-potent matrices. *Linear Algebra and its Applications*, 45:109–121, 1982. (cited on pages 144 and 147)

[590] S. Ostlund. Incommensurate and commensurate phases in asymmetric clock models. *Phys. Rev. B*, 24:398–405, Jul 1981. (cited on page 144)

[591] David A. Huse. Simple three-state model with infinitely many phases. *Phys. Rev. B*, 24:5180–5194, Nov 1981. (cited on page 144)

[592] Markus Nünnerich, Daniel Cohen, Patrick Barthel, Patrick H. Huber, Dorna Niroomand, Alex Retzker, and Christof Wunderlich. Fast, robust and laser-free universal entangling gates for trapped-ion quantum computing, 2024. (cited on page 144)

[593] Michael A Nielsen and Isaac L Chuang. *Quantum computation and quantum information*. Cambridge university press, 2010. (cited on page 144)

[594] Yuchen Wang, Zixuan Hu, Barry C Sanders, and Sabre Kais. Qudits and high-dimensional quantum computing. *Frontiers in Physics*, 8:589504, 2020. (cited on pages 144 and 155)

[595] Daniel A Lidar and Todd A Brun. *Quantum error correction*. Cambridge university press, 2013. (cited on pages 144 and 149)

[596] Simon J Devitt, William J Munro, and Kae Nemoto. Quantum error correction for beginners. *Reports on Progress in Physics*, 76(7):076001, 2013. (cited on page 144)

[597] Konstantinos Georgopoulos, Clive Emary, and Paolo Zuliani. Modeling and simulating the noisy behavior of near-term quantum computers. *Phys. Rev. A*, 104:062432, Dec 2021. (cited on page 144)

[598] Daniel Shapira, Shay Mozes, and Ofer Biham. Effect of unitary noise on grover's quantum search algorithm. *Phys. Rev. A*, 67:042301, Apr 2003. (cited on page 144)

[599] Heinz-Peter Breuer, Elsi-Mari Laine, Jyrki Piilo, and Bassano Vacchini. Colloquium: Non-markovian dynamics in open quantum systems. *Rev. Mod. Phys.*, 88:021002, Apr 2016. (cited on pages 144, 148, and 152)

[600] Self-averaging. Wikipedia, The Free Encyclopedia. Accessed: 2025-08-01. (cited on page 144)

[601] Sudipto Singha Roy, Soumik Bandyopadhyay, Ricardo Costa de Almeida, and Philipp Hauke. Unveiling eigenstate thermalization for non-hermitian systems, 2023. (cited on page 145)

[602] Alexei Gilchrist, Daniel R. Terno, and Christopher J. Wood. Vectorization of quantum operations and its use, 2011. (cited on page 145)

[603] Jerome Weinstock. Cluster formulation of the exact equation for the evolution of a classical many-body system. *Phys. Rev.*, 132:454–469, Oct 1963. (cited on page 146)

[604] Jerome Weinstock. Generalized master equation for quantum-mechanical systems to all orders in the density. *Phys. Rev.*, 136:A879–A888, Nov 1964. (cited on page 146)

[605] Mehran Kardar. *Statistical physics of fields*. Cambridge University Press, 2007. (cited on page 146)

[606] Adrián A. Budini. Stochastic representation of a class of non-markovian completely positive evolutions. *Phys. Rev. A*, 69:042107, Apr 2004. (cited on page 147)

[607] Sonja Daffer, Krzysztof Wódkiewicz, James D. Cresser, and John K. McIver. Depolarizing channel as a completely positive map with memory. *Phys. Rev. A*, 70:010304, Jul 2004. (cited on page 147)

[608] Sabrina Maniscalco. Complete positivity of a spin-1⁄2 master equation with memory. *Phys. Rev. A*, 75:062103, Jun 2007. (cited on page 147)

[609] Bassano Vacchini. Non-markovian master equations from piecewise dynamics. *Phys. Rev. A*, 87:030101, Mar 2013. (cited on page 147)

[610] Bassano Vacchini. Generalized master equations leading to completely positive dynamics. *Phys. Rev. Lett.*, 117:230401, Nov 2016. (cited on page 147)

[611] Katarzyna Siudzińska and Dariusz Chruściński. Memory kernel approach to generalized pauli channels: Markovian, semi-markov, and beyond. *Phys. Rev. A*, 96:022129, Aug 2017. (cited on page 147)

[612] Björn Witt, Y Tanimura, F Mintert, et al. Exploring complete positivity in hierarchy equations of motion. *New Journal of Physics*, 19(1):013007, 2017. (cited on page 147)

[613] Viktor Reimer and Maarten Rolf Wegewijs. Density-operator evolution: Complete positivity and the Keldysh real-time expansion. *SciPost Phys.*, 7:012, 2019. (cited on page 147)

[614] Sergey N Filippov, AN Glinov, and Leevi Leppäjärvi. Phase covariant qubit dynamics and divisibility. *Lobachevskii Journal of Mathematics*, 41(4):617–630, 2020. (cited on page 147)

[615] Bassano Vacchini. Quantum renewal processes. *Scientific reports*, 10(1):5592, 2020. (cited on page 147)

[616] K. Nestmann, V. Bruch, and M. R. Wegewijs. How quantum evolution with memory is generated in a time-local way. *Phys. Rev. X*, 11:021041, May 2021. (cited on page 147)

[617] Supriyo Dutta, Subhashish Banerjee, and Monika Rani. Qudit states in noisy quantum channels. *Physica Scripta*, 98(11):115113, 2023. (cited on pages 147 and 153)

[618] Ángel Rivas, Susana F Huelga, and Martin B Plenio. Quantum non-markovianity: characterization, quantification and detection. *Reports on Progress in Physics*, 77(9):094001, 2014. (cited on page 148)

[619] Xiaoguang Wang, Anders Sørensen, and Klaus Mølmer. Multibit gates for quantum computing. *Phys. Rev. Lett.*, 86:3907–3910, Apr 2001. (cited on page 149)

[620] Andrzej Kossakowski. On quantum statistical mechanics of non-hamiltonian systems. *Reports on Mathematical Physics*, 3(4):247–274, 1972. (cited on page 152)

[621] Wojciech Hubert Zurek. Decoherence, einselection, and the quantum origins of the classical. *Rev. Mod. Phys.*, 75:715–775, May 2003. (cited on page 153)

[622] Andrea López-Incera, Pavel Sekatski, and Wolfgang Dür. All macroscopic quantum states are fragile and hard to prepare. *Quantum*, 3:118, 2019. (cited on page 153)

[623] Bartłomiej Gardas, Jacek Dziarmaga, Wojciech H Zurek, and Michael Zwolak. Defects in quantum computers. *Scientific reports*, 8(1):4539, 2018. (cited on page 153)

[624] Salvatore Lorenzo, Federico Lombardo, Francesco Ciccarello, and G Massimo Palma. Quantum non-markovianity induced by anderson localization. *Scientific reports*, 7(1):42729, 2017. (cited on page 153)

[625] Jin-Shi Xu, Kai Sun, Chuan-Feng Li, Xiao-Ye Xu, Guang-Can Guo, Erika Andersson, Rosario Lo Franco, and Giuseppe Compagno. Experimental recovery of quantum correlations in absence of system-environment back-action. *Nature communications*, 4(1):2851, 2013. (cited on pages 154 and 162)

[626] Daniel M Reich, Nadav Katz, and Christiane P Koch. Exploiting non-markovianity for quantum control. *Scientific reports*, 5(1):12430, 2015. (cited on pages 154 and 162)

[627] Sebastian Deffner and Eric Lutz. Quantum speed limit for non-markovian dynamics. *Phys. Rev. Lett.*, 111:010402, Jul 2013. (cited on pages 154 and 162)

[628] Bogna Bylicka, D Chruściński, and Sci Maniscalco. Non-markovianity and reservoir memory of quantum channels: a quantum information theory perspective. *Scientific reports*, 4(1):5720, 2014. (cited on pages 154 and 162)

[629] Valentin Kasper, Daniel González-Cuadra, Apoorva Hegde, Andy Xia, Alexandre Dauphin, Felix Huber, Eberhard Tiemann, Maciej Lewenstein, Fred Jendrzejewski, and Philipp Hauke. Universal quantum computation and quantum error correction with ultracold atomic mixtures. *Quantum Science and Technology*, 7(1):015008, 2021. (cited on page 155)

[630] M. S. Blok, V. V. Ramasesh, T. Schuster, K. O'Brien, J. M. Kreikebaum, D. Dahlen, A. Morvan, B. Yoshida, N. Y. Yao, and I. Siddiqi. Quantum information scrambling on a superconducting qutrit processor. *Phys. Rev. X*, 11:021010, Apr 2021. (cited on page 155)

[631] Martin Ringbauer, Michael Meth, Lukas Postler, Roman Stricker, Rainer Blatt, Philipp Schindler, and Thomas Monz. A universal qudit quantum processor with trapped ions. *Nature Physics*, 18(9):1053–1057, 2022. (cited on page 155)

[632] Yulin Chi, Jieshan Huang, Zhanchuan Zhang, Jun Mao, Zinan Zhou, Xiaojiong Chen, Chonghao Zhai, Jueming Bao, Tianxiang Dai, Huihong Yuan, et al. A programmable qudit-based quantum processor. *Nature communications*, 13(1):1166, 2022. (cited on page 155)

[633] Pavel Hrmo, Benjamin Wilhelm, Lukas Gerster, Martin W van Mourik, Marcus Huber, Rainer Blatt, Philipp Schindler, Thomas Monz, and Martin Ringbauer. Native qudit entanglement in a trapped ion quantum processor. *Nature Communications*, 14(1):2242, 2023. (cited on page 155)

[634] Laurin E. Fischer, Alessandro Chiesa, Francesco Tacchino, Daniel J. Egger, Stefano Carretta, and Ivano Tavernelli. Universal qudit gate synthesis for transmons. *PRX Quantum*, 4:030327, Aug 2023. (cited on page 155)

[635] Giuseppe Calajó, Giuseppe Magnifico, Claire Edmunds, Martin Ringbauer, Simone Montangero, and Pietro Silvi. Digital quantum simulation of a (1+ 1) d su (2) lattice gauge theory with ion qudits. *PRX Quantum*, 5(4):040309, 2024. (cited on page 155)

[636] Daniel González-Cuadra, Torsten V. Zache, Jose Carrasco, Barbara Kraus, and Peter Zoller. Hardware efficient quantum simulation of non-abelian gauge theories with qudits on rydberg platforms. *Phys. Rev. Lett.*, 129:160501, Oct 2022. (cited on page 155)

[637] David G Tempel and Alán Aspuru-Guzik. The Kitaev–Feynman clock for open quantum systems. *New Journal of Physics*, 16(11):113066, 2014. (cited on page 155)

[638] Motohiko Ezawa. Clock-symmetric non-hermitian second-order topological insulator. *The European Physical Journal B*, 95(6):97, 2022. (cited on page 155)

[639] Adrian Hutter and Daniel Loss. Quantum computing with parafermions. *Phys. Rev. B*, 93:125105, Mar 2016. (cited on page 155)

[640] Weitao Chen, Olivier Giraud, Jiangbin Gong, and Gabriel Lemarié. Quantum logarithmic multifractality. *Phys. Rev. Res.*, 6:L032024, Jul 2024. (cited on pages 155 and 164)

[641] Yue Li, Yang Wu, Yuqi Zhou, Mengxiang Zhang, Xingyu Zhao, Yibo Yuan, Xu Cheng, Yi Li, Xi Qin, Xing Rong, et al. Programmable simulation of high-order exceptional point with a trapped ion. *arXiv preprint arXiv:2412.09776*, 2024. (cited on page 155)

[642] Alessandro Sergi and Konstantin G Zloshchastiev. Non-hermitian quantum dynamics of a two-level system and models of dissipative environments. *International Journal of Modern Physics B*, 27(27):1350163, 2013. (cited on page 158)

[643] Habatwa Vincent Mweene. Vectors and operators for spin 1 derived from first principles, 2000. (cited on page 159)

[644] Linus Ekstrom, Hao Wang, and Sebastian Schmitt. Variational quantum multi-objective optimization, 2023. (cited on page 159)

[645] Mahmoud Mahdian and H Davoodi Yeganeh. Incoherent quantum algorithm dynamics of an open system with near-term devices. *Quantum Information Processing*, 19:1–13, 2020. (cited on page 162)

[646] Robert de Keijzer, Jurgen Snijders, André Carvalho, and Servaas Kokkelmans. Pulse family optimization for parametrized quantum gates using spectral clustering, 2024. (cited on page 162)

[647] IV Gornyi and AD Mirlin. From quantum disorder to quantum chaos. *Journal of low temperature physics*, 126:1339–1354, 2002. (cited on page 163)

[648] Manuel Pino, Lev B Ioffe, and Boris L Altshuler. Nonergodic metallic and insulating phases of josephson junction chains. *Proceedings of the National Academy of Sciences*, 113(3):536–541, 2016. (cited on page 163)

[649] Denis M Basko, Igor L Aleiner, and Boris L Altshuler. Metal–insulator transition in a weakly interacting many-electron system with localized single-particle states. *Annals of physics*, 321(5):1126–1205, 2006. (cited on pages 163, 173, and 174)

[650] Daniel Green. Disorder in the early universe. *Journal of Cosmology and Astroparticle Physics*, 2015(03):020, 2015. (cited on page 163)

[651] Dmitry A. Abanin, Ehud Altman, Immanuel Bloch, and Maksym Serbyn. Colloquium: Many-body localization, thermalization, and entanglement. *Rev. Mod. Phys.*, 91:021001, May 2019. (cited on pages 163 and 166)

[652] M. V. Berry. Regular and irregular semiclassical wavefunctions. *J. Phys. A*, 10(12):2083, 1977. (cited on page 163)

[653] O. Bohigas, M. J. Giannoni, and C. Schmit. Characterization of chaotic quantum spectra and universality of level fluctuation laws. *Phys. Rev. Lett.*, 52:1–4, 1984. (cited on page 163)

[654] Fritz Haake. *Quantum signatures of chaos*. Springer, 1991. (cited on page 163)

[655] Vincent Lahoche and Dine Ousmane Samary. Revisited functional renormalization group approach for random matrices in the large-n limit. *Phys. Rev. D*, 101:106015, May 2020. (cited on page 163)

[656] Ferdinand Evers and Alexander D. Mirlin. Anderson transitions. *Reviews of Modern Physics*, 80(4):1355–1417, October 2008. (cited on pages 163, 169, and 176)

[657] Philipp Hauke and Markus Heyl. Many-body localization and quantum ergodicity in disordered long-range ising models. *Phys. Rev. B*, 92:134204, Oct 2015. (cited on page 163)

[658] Ehud Altman and Ronen Vosk. Universal dynamics and renormalization in many-body-localized systems. *Annu. Rev. Condens. Matter Phys.*, 6(1):383–409, 2015. (cited on page 163)

[659] Anna Goremykina, Romain Vasseur, and Maksym Serbyn. Analytically solvable renormalization group for the many-body localization transition. *Phys. Rev. Lett.*, 122:040601, Jan 2019. (cited on page 163)

[660] Joana Fraxanet, Tymoteusz Salamon, and Maciej Lewenstein. *The Coming Decades of Quantum Simulation*, pages 85–125. Springer International Publishing, Cham, 2023. (cited on page 163)

[661] Petar Jurcevic, Ben P Lanyon, Philipp Hauke, Cornelius Hempel, Peter Zoller, Rainer Blatt, and Christian F Roos. Quasiparticle engineering and entanglement propagation in a quantum many-body system. *Nature*, 511(7508):202–205, 2014. (cited on page 163)

[662] Michael Schreiber, Sean S. Hodgman, Pranjal Bordia, Henrik P. Lüschen, Mark H. Fischer, Ronen Vosk, Ehud Altman, Ulrich Schneider, and Immanuel Bloch. Observation of many-body localization of interacting fermions in a quasirandom optical lattice. *Science*, 349(6250):842–845, 2015. (cited on page 163)

[663] Jae yoon Choi, Sebastian Hild, Johannes Zeiher, Peter Schauß, Antonio Rubio-Abadal, Tarik Yefsah, Vedika Khemani, David A. Huse, Immanuel Bloch, and Christian Gross. Exploring the many-body localization transition in two dimensions. *Science*, 352(6293):1547–1552, 2016. (cited on page 163)

[664] J. Smith, A. Lee, P. Richerme, B. Neyenhuis, P. W. Hess, P. Hauke, M. Heyl, D. A. Huse, and C. Monroe. Many-body localization in a quantum simulator with programmable random disorder. *Nature Physics*, 12(10):907–911, Oct 2016. (cited on page 163)

[665] Pranjal Bordia, Henrik Lüschen, Sebastian Scherg, Sarang Gopalakrishnan, Michael Knap, Ulrich Schneider, and Immanuel Bloch. Probing slow relaxation and many-body localization in two-dimensional quasiperiodic systems. *Phys. Rev. X*, 7:041047, Nov 2017. (cited on page 163)

[666] Henrik P. Lüschen, Pranjal Bordia, Sean S. Hodgman, Michael Schreiber, Saubhik Sarkar, Andrew J. Daley, Mark H. Fischer, Ehud Altman, Immanuel Bloch, and Ulrich Schneider. Signatures of many-body localization in a controlled open quantum system. *Phys. Rev. X*, 7:011034, Mar 2017. (cited on page 163)

[667] Matthew Rispoli, Alexander Lukin, Robert Schittko, Sooshin Kim, M. Eric Tai, Julian Léonard, and Markus Greiner. Quantum critical behaviour at the many-body localization transition. *Nature*, 573(7774):385–389, Sep 2019. (cited on page 163)

[668] Nick Sauerwein, Francesca Orsi, Philipp Uhrich, Soumik Bandyopadhyay, Francesco Mattiotti, Tigrane Cantat-Moltrecht, Guido Pupillo, Philipp Hauke, and Jean-Philippe Brantut. Engineering random spin models with atoms in a high-finesse cavity. *Nat. Phys.*, 19(8):1128–1134, Aug 2023. (cited on page 163)

[669] Tobias J Osborne. Hamiltonian complexity. *Reports on Progress in Physics*, 75(2):022001, jan 2012. (cited on page 163)

[670] Stefano Baiguera, Vijay Balasubramanian, Pawel Caputa, Shira Chapman, Jonas Haferkamp, Michal P Heller, and Nicole Yunger Halpern. Quantum complexity in gravity, quantum field theory, and quantum information science. *arXiv preprint arXiv:2503.10753*, 2025. (cited on page 163)

[671] Jiale Huang, Xiangjian Qian, and Mingpu Qin. Non-stabilizerness entanglement entropy: a measure of hardness in the classical simulation of quantum many-body systems. *arXiv:2409.16895*, 2024. (cited on page 163)

[672] Ryszard Horodecki, Paweł Horodecki, Michał Horodecki, and Karol Horodecki. Quantum entanglement. *Rev. Mod. Phys.*, 81:865–942, Jun 2009. (cited on page 163)

[673] Jens Eisert. Entanglement and tensor network states. *arXiv:1308.3318*, 2013. (cited on pages 163, 167, and 189)

[674] Simone Montangero, Evenson Montangero, and Evenson. *Introduction to tensor network methods*. Springer, 2018. (cited on pages 163, 167, and 189)

[675] Caterina E. Mora and Hans J. Briegel. Algorithmic complexity and entanglement of quantum states. *Phys. Rev. Lett.*, 95:200503, Nov 2005. (cited on page 163)

[676] Ivan Chernyshev, Caroline EP Robin, and Martin J Savage. Quantum magic and computational complexity in the neutrino sector. *arXiv:2411.04203*, 2024. (cited on pages 163 and 164)

[677] Florian Brökemeier, S. Momme Hengstenberg, James W. T. Keeble, Caroline E. P. Robin, Federico Rocco, and Martin J. Savage. Quantum magic and multipartite entanglement in the structure of nuclei. *Phys. Rev. C*, 111:034317, Mar 2025. (cited on pages 163 and 164)

[678] Manoj K Joshi, Christian Kokail, Rick van Bijnen, Florian Kranzl, Torsten V Zache, Rainer Blatt, Christian F Roos, and Peter Zoller. Exploring large-scale entanglement in quantum simulation. *Nature*, 624(7992):539–544, 2023. (cited on page 163)

[679] Mark Howard and Earl Campbell. Application of a resource theory for magic states to fault-tolerant quantum computing. *Phys. Rev. Lett.*, 118:090501, Mar 2017. (cited on page 163)

[680] Zi-Wen Liu, Seth Lloyd, Elton Zhu, and Huangjun Zhu. Entanglement, quantum randomness, and complexity beyond scrambling. *Journal of High Energy Physics*, 2018(7):1–62, 2018. (cited on page 163)

[681] Stefano Baiguera, Shira Chapman, Giuseppe Policastro, and Tal Schwartzman. The complexity of being entangled. *Quantum*, 8:1472, 2024. (cited on page 163)

[682] Kaifeng Bu, Roy J Garcia, Arthur Jaffe, Dax Enshan Koh, and Lu Li. Complexity of quantum circuits via sensitivity, magic, and coherence. *Communications in Mathematical Physics*, 405(7):161, 2024. (cited on pages 163 and 164)

[683] Norbert Rosenzweig and Charles E. Porter. "repulsion of energy levels" in complex atomic spectra. *Phys. Rev.*, 120:1698–1714, Dec 1960. (cited on pages 163 and 169)

[684] Alexander Altland, Martin Janssen, and Boris Shapiro. Perturbation theory for the rosenzweig-porter matrix model. *Phys. Rev. E*, 56:1471–1475, Aug 1997. (cited on page 163)

[685] Alexander D Mirlin, Yan V Fyodorov, Frank-Michael Dittes, Javier Quezada, and Thomas H Seligman. Transition from localized to extended eigenstates in the ensemble of power-law random banded matrices. *Phys. Rev. E*, 54(4):3221, 1996. (cited on pages 163, 164, 167, 173, and 176)

[686] Subir Sachdev and Jinwu Ye. Gapless spin-fluid ground state in a random quantum heisenberg magnet. *Phys. Rev. Lett.*, 70(21):3339–3342, 1993. (cited on pages 163 and 178)

[687] Alexei Kitaev. A simple model of quantum holography. *Online Lecture Notes*, 2015. Talks at KITP, April and May 2015. (cited on pages 163 and 178)

[688] F. Evers and A. D. Mirlin. Fluctuations of the inverse participation ratio at the anderson transition. *Phys. Rev. Lett.*, 84:3690–3693, Apr 2000. (cited on pages 163, 166, 167, 173, and 176)

[689] VE Kravtsov, IM Khaymovich, E Cuevas, and M Amini. A random matrix model with localization and ergodic transitions. *New Journal of Physics*, 17(12):122002, 2015. (cited on pages 163, 167, 169, 170, and 188)

[690] A. D. Mirlin and F. Evers. Multifractality and critical fluctuations at the anderson transition. *Phys. Rev. B*, 62:7920–7933, Sep 2000. (cited on pages 163, 166, 173, and 176)

[691] Juan Maldacena, Stephen H Shenker, and Douglas Stanford. A bound on chaos. *Journal of High Energy Physics*, 2016(8):1–17, 2016. (cited on page 163)

[692] Debanjan Chowdhury, Antoine Georges, Olivier Parcollet, and Subir Sachdev. Sachdev-Ye-Kitaev models and beyond: Window into non-Fermi liquids. *Rev. Mod. Phys.*, 94(3):035004, 2022. (cited on page 163)

[693] Subir Sachdev. Bekenstein-hawking entropy and strange metals. *Phys. Rev. X*, 5:041025, Nov 2015. (cited on pages 163 and 178)

[694] Jordan S Cotler, Guy Gur-Ari, Masanori Hanada, Joseph Polchinski, Phil Saad, Stephen H Shenker, Douglas Stanford, Alexandre Streicher, and Masaki Tezuka. Black holes and random matrices. *Journal of High Energy Physics*, 2017(5):1–54, 2017. (cited on pages 163, 178, and 181)

[695] Claudio Castellani and Luca Peliti. Multifractal wavefunction at the localisation threshold. *Journal of physics A: mathematical and general*, 19(8):L429, 1986. (cited on pages 163, 166, and 173)

[696] Thomas C. Halsey, Mogens H. Jensen, Leo P. Kadanoff, Itamar Procaccia, and Boris I. Shraiman. Fractal measures and their singularities: The characterization of strange sets. *Phys. Rev. A*, 33:1141–1151, Feb 1986. (cited on pages 163 and 166)

[697] Hideo Aoki. Fractal dimensionality of wave functions at the mobility edge: Quantum fractal in the landau levels. *Phys. Rev. B*, 33:7310–7313, May 1986. (cited on pages 163 and 166)

[698] Bernhard Kramer and Angus MacKinnon. Localization: theory and experiment. *Reports on Progress in Physics*, 56(12):1469, 1993. (cited on pages 163 and 166)

[699] Tilen Čadež, Dillip Kumar Nandy, Dario Rosa, Alexei Andreanov, and Barbara Dietz. The rosenzweig–porter model revisited for the three wigner–dyson symmetry classes. *New Journal of Physics*, 26(8):083018, aug 2024. (cited on pages 163, 166, and 173)

[700] Gil Refael and Joel E Moore. Criticality and entanglement in random quantum systems. *Journal of physics a: mathematical and theoretical*, 42(50):504010, 2009. (cited on page 164)

[701] Alexander Lukin, Matthew Rispoli, Robert Schittko, M Eric Tai, Adam M Kaufman, Soonwon Choi, Vedika Khemani, Julian Léonard, and Markus Greiner. Probing entanglement in a many-body–localized system. *Science*, 364(6437):256–260, 2019. (cited on page 164)

[702] Piotr Sierant, Maciej Lewenstein, Antonello Scardicchio, Lev Vidmar, and Jakub Zakrzewski. Many-body localization in the age of classical computing*. *Rept. Prog. Phys.*, 88(2):026502, 2025. (cited on page 164)

[703] Christopher Vairogs and Bin Yan. Extracting randomness from quantum'magic'. *arXiv:2402.10181*, 2024. (cited on page 164)

[704] Liyuan Chen, Roy J. Garcia, Kaifeng Bu, and Arthur Jaffe. Magic of random matrix product states. *Phys. Rev. B*, 109:174207, May 2024. (cited on page 164)

[705] Yuzhen Zhang and Yingfei Gu. Quantum magic dynamics in random circuits. *arXiv:2410.21128*, 2024. (cited on page 164)

[706] Xhek Turkeshi, Marco Schirò, and Piotr Sierant. Measuring nonstabilizerness via multifractal flatness. *Phys. Rev. A*, 108:042408, Oct 2023. (cited on pages 164 and 172)

[707] Lorenzo Leone, Salvatore FE Oliviero, You Zhou, and Alioscia Hamma. Quantum chaos is quantum. *Quantum*, 5:453, 2021. (cited on page 164)

[708] Kanato Goto, Tomoki Nosaka, and Masahiro Nozaki. Probing chaos by magic monotones. *Phys. Rev. D*, 106:126009, Dec 2022. (cited on page 164)

[709] Poetri Sonya Tarabunga, Emanuele Tirrito, Titas Chanda, and Marcello Dalmonte. Many-body magic via pauli-markov chains—from criticality to gauge theories. *PRX Quantum*, 4:040317, Oct 2023. (cited on page 164)

[710] Pedro R Nicácio Falcão, Poetri Sonya Tarabunga, Martina Frau, Emanuele Tirrito, Jakub Zakrzewski, and Marcello Dalmonte. Non-stabilizerness in u (1) lattice gauge theory. *arXiv:2409.01789*, 2024. (cited on page 164)

[711] Barbara Jasser, Jovan Odavic, and Alioscia Hamma. Stabilizer entropy and entanglement complexity in the sachdev-ye-kitaev model. *arXiv:2502.03093*, 2025. (cited on pages 164 and 182)

[712] Yi-Ming Ding, Zhe Wang, and Zheng Yan. Evaluating many-body stabilizer r\'enyi entropy by sampling reduced pauli strings: singularities, volume law, and nonlocal magic. *arXiv:2501.12146*, 2025. (cited on page 164)

[713] Zhi-Cheng Yang, Alioscia Hamma, Salvatore M. Giampaolo, Eduardo R. Mucciolo, and Claudio Chamon. Entanglement complexity in quantum many-body dynamics, thermalization, and localization. *Phys. Rev. B*, 96:020408, Jul 2017. (cited on page 164)

[714] Soumik Ghosh, Abhinav Deshpande, Dominik Hangleiter, Alexey V. Gorshkov, and Bill Fefferman. Complexity phase transitions generated by entanglement. *Phys. Rev. Lett.*, 131:030601, Jul 2023. (cited on page 164)

[715] E Rabinovici, A Sánchez-Garrido, R Shir, and J Sonner. Krylov complexity from integrability to chaos. *Journal of High Energy Physics*, 2022(7):1–29, 2022. (cited on page 164)

[716] Ritam Basu, Anirban Ganguly, Souparna Nath, and Onkar Parrikar. Complexity growth and the krylov-wigner function. *Journal of High Energy Physics*, 2024(5):1–32, 2024. (cited on page 164)

[717] Khen Cohen, Yaron Oz, and De-liang Zhong. Complexity measure diagnostics of ergodic to many-body localization transition. *arXiv:2404.15940*, 2024. (cited on page 164)

[718] Himanshu Sahu, Aranya Bhattacharya, and Pingal Pratyush Nath. Quantum complexity and localization in random quantum circuits. *arXiv:2409.03656*, 2024. (cited on page 164)

[719] Budhaditya Bhattacharjee and Pratik Nandy. Krylov fractality and complexity in generic random matrix ensembles. *Phys. Rev. B*, 111:L060202, Feb 2025. (cited on page 164)

[720] Adam Nahum, Sagar Vijay, and Jeongwan Haah. Operator spreading in random unitary circuits. *Phys. Rev. X*, 8:021014, Apr 2018. (cited on page 164)

[721] Mohsen Alishahiha. Holographic complexity. *Phys. Rev. D*, 92:126009, Dec 2015. (cited on page 164)

[722] John Watrous. Quantum computational complexity. *arXiv:0804.3401*, 2008. (cited on page 164)

[723] P. Prelovšek, O. S. Barišić, and M. Mierzejewski. Reduced-basis approach to many-body localization. *Phys. Rev. B*, 97(3), January 2018. (cited on page 166)

[724] Francesca Pietracaprina and Nicolas Laflorencie. Hilbert-space fragmentation, multifractality, and many-body localization. *Annals Phys.*, 435:168502, 2021. (cited on page 166)

[725] Arnd Bäcker, Masudul Haque, and Ivan M Khaymovich. Multifractal dimensions for random matrices, chaotic quantum maps, and many-body systems. *Phys. Rev. E*, 100(3):032117, 2019. (cited on page 166)

[726] Matthew B Hastings. An area law for one-dimensional quantum systems. *Journal of statistical mechanics: theory and experiment*, 2007(08):P08024, 2007. (cited on page 167)

[727] J. Eisert, M. Cramer, and M. B. Plenio. Colloquium: Area laws for the entanglement entropy. *Rev. Mod. Phys.*, 82:277–306, Feb 2010. (cited on page 167)

[728] L.-A. Wu, M. S. Sarandy, and D. A. Lidar. Quantum phase transitions and bipartite entanglement. *Phys. Rev. Lett.*, 93:250404, Dec 2004. (cited on page 167)

[729] Andreas Osterloh, Luigi Amico, Giuseppe Falci, and Rosario Fazio. Scaling of entanglement close to a quantum phase transition. *Nature*, 416(6881):608–610, 2002. (cited on page 167)

[730] Luigi Amico, Rosario Fazio, Andreas Osterloh, and Vlatko Vedral. Entanglement in many-body systems. *Rev. Mod. Phys.*, 80:517–576, May 2008. (cited on page 167)

[731] Pasquale Calabrese and John Cardy. Entanglement entropy and conformal field theory. *Journal of physics a: mathematical and theoretical*, 42(50):504005, 2009. (cited on page 167)

[732] Scott D. Geraedts, Rahul Nandkishore, and Nicolas Regnault. Many-body localization and thermalization: Insights from the entanglement spectrum. *Phys. Rev. B*, 93:174202, May 2016. (cited on page 167)

[733] Don N. Page. Average entropy of a subsystem. *Phys. Rev. Lett.*, 71:1291–1294, Aug 1993. (cited on page 167)

[734] Daniel A Roberts and Beni Yoshida. Chaos and complexity by design. *Journal of High Energy Physics*, 2017(4):1–64, 2017. (cited on page 168)

[735] Madan Lal Mehta. *Random matrices*, volume 142. Elsevier, 2004. (cited on page 168)

[736] Hervé Kunz and Boris Shapiro. Transition from poisson to gaussian unitary statistics:the two-point correlation function. *Phys. Rev. E*, 58(1):400–406, July 1998. (cited on page 169)

[737] Per von Soosten and Simone Warzel. Non-ergodic delocalization in the rosenzweig–porter model. *Letters in Mathematical Physics*, 109:905–922, 2019. (cited on page 169)

[738] E. Bogomolny and M. Sieber. Eigenfunction distribution for the rosenzweig-porter model. *Phys. Rev. E*, 98(3), September 2018. (cited on page 169)

[739] K. Truong and A. Ossipov. Eigenvectors under a generic perturbation: Non-perturbative results from the random matrix approach. *Europhysics Letters*, 116(3):37002, dec 2016. (cited on page 169)

[740] Cécile Monthus. Multifractality of eigenstates in the delocalized non-ergodic phase of some random matrix models: Wigner–weisskopf approach. *Journal of Physics A: Mathematical and Theoretical*, 50(29):295101, jun 2017. (cited on page 170)

[741] M Amini. Spread of wave packets in disordered hierarchical lattices. *Europhysics L*, 117(3):30003, 2017. (cited on page 170)

[742] Soumya Bera, Giuseppe De Tomasi, Ivan M. Khaymovich, and Antonello Scardicchio. Return probability for the anderson model on the random regular graph. *Phys. Rev. B*, 98:134205, Oct 2018. (cited on page 170)

[743] Giuseppe De Tomasi, Mohsen Amini, Soumya Bera, Ivan M. Khaymovich, and Vladimir E. Kravtsov. Survival probability in Generalized Rosenzweig-Porter random matrix ensemble. *SciPost Phys.*, 6:014, 2019. (cited on page 170)

[744] M Pino, J Tabanera, and P Serna. From ergodic to non-ergodic chaos in rosenzweig–porter model. *Journal of Physics A: Mathematical and Theoretical*, 52(47):475101, oct 2019. (cited on page 172)

[745] Sasha Sodin. The spectral edge of some random band matrices. *Annals of mathematics*, pages 2223–2251, 2010. (cited on pages 173 and 174)

[746] Titas Chanda, Piotr Sierant, and Jakub Zakrzewski. Many-body localization transition in large quantum spin chains: The mobility edge. *Phys. Rev. Res.*, 2:032045, Aug 2020. (cited on pages 173 and 174)

[747] Qiujiang Guo, Chen Cheng, Zheng-Hang Sun, Zixuan Song, Hekang Li, Zhen Wang, Wenhui Ren, Hang Dong, Dongning Zheng, Yu-Ran Zhang, et al. Observation of energy-resolved many-body localization. *Nature Physics*, 17(2):234–239, 2021. (cited on pages 173 and 174)

[748] Andreas Geißler and Guido Pupillo. Mobility edge of the two-dimensional bose-hubbard model. *Phys. Rev. Res.*, 2:042037, Dec 2020. (cited on pages 173, 174, and 188)

[749] Xingbo Wei, Rubem Mondaini, and Gao Xianlong. Characterization of many-body mobility edges with random matrices. *arXiv:2001.04105*, 2020. (cited on pages 173 and 174)

[750] Rozhin Yousefjani and Abolfazl Bayat. Mobility edge in long-range interacting many-body localized systems. *Phys. Rev. B*, 107:045108, Jan 2023. (cited on pages 173 and 174)

[751] Wang-Fang Xu and WJ Rao. Non-ergodic extended regime in random matrix ensembles: insights from eigenvalue spectra. *Scientific Reports*, 13(1):634, 2023. (cited on page 176)

[752] E. Bogomolny and M. Sieber. Eigenfunction distribution for the rosenzweig-porter model. *Phys. Rev. E*, 98:032139, Sep 2018. (cited on page 176)

[753] Andrea Legramandi, Soumik Bandyopadhyay, and Philipp Hauke. Many-body spectral transitions through the lens of variable-range syk2 model. *arXiv:2412.14280*, 2024. (cited on page 176)

[754] Imre Varga and Daniel Braun. Critical statistics in a power-law random-banded matrix ensemble. *Phys. Rev. B*, 61:R11859–R11862, May 2000. (cited on page 176)

[755] Wouter Buijsman, Masudul Haque, and Ivan M Khaymovich. Power-law banded random matrix ensemble as a model for quantum many-body hamiltonians. *arXiv:2503.08825*, 2025. (cited on page 178)

[756] Juan Maldacena and Douglas Stanford. Remarks on the Sachdev-Ye-Kitaev model. *Phys. Rev. D*, 94(10):106002, 2016. (cited on page 178)

[757] Alexander Altland, Kun Woo Kim, Tobias Micklitz, Maedeh Rezaei, Julian Sonner, and Jacobus J. M. Verbaarschot. Quantum chaos on edge. *Phys. Rev. Res.*, 6:033286, Sep 2024. (cited on pages 178 and 182)

[758] Juan Martin Maldacena. Wilson loops in large N field theories. *Phys. Rev. Lett.*, 80:4859–4862, 1998. (cited on page 178)

[759] Edward Witten. Anti de Sitter space and holography. *Adv. Theor. Math. Phys.*, 2:253–291, 1998. (cited on page 178)

[760] Juan Maldacena, Douglas Stanford, and Zhenbin Yang. Conformal symmetry and its breaking in two dimensional Nearly Anti-de-Sitter space. *PTEP*, 2016(12):12C104, 2016. (cited on page 178)

[761] L. García-Álvarez, I. L. Egusquiza, L. Lamata, A. del Campo, J. Sonner, and E. Solano. Digital quantum simulation of minimal AdS/CFT. *Phys. Rev. Lett.*, 119:040501, Jul 2017. (cited on page 179)

[762] Tianlin Li, Junyu Liu, Yuan Xin, and Yehao Zhou. Supersymmetric SYK model and random matrix theory. *Journal of High Energy Physics*, 06:111, 2017. (cited on pages 179 and 188)

[763] Takuya Kanazawa and Tilo Wettig. Complete random matrix classification of SYK models with $\mathcal{N} = 0$, 1 and 2 supersymmetry. *Journal of High Energy Physics*, 2017(9):1–42, 2017. (cited on pages 181 and 188)

[764] Andrea Legramandi and Neil Talwar. The moments of the spectral form factor in syk. *arXiv:2412.18737*, 2024. (cited on page 182)

[765] Chiara Capecci, Gopal Chandra Santra, Alberto Bottarelli, Emanuele Tirrito, and Philipp Hauke. Role of nonstabilizerness in quantum optimization. *arXiv:2505.17185*, 2025. (cited on pages 182 and 196)

[766] Michael Beverland, Earl Campbell, Mark Howard, and Vadym Kliuchnikov. Lower bounds on the non-clifford resources for quantum computations. *Quantum Science and Technology*, 5(3):035009, may 2020. (cited on page 186)

[767] Isaías Vallejo-Fabila, Adway Kumar Das, David A. Zarate-Herrada, Apollonas S. Matsoukas-Roubeas, E. Jonathan Torres-Herrera, and Lea F. Santos. Reducing dynamical fluctuations and enforcing self-averaging by opening many-body quantum systems. *Phys. Rev. B*, 110:075138, Aug 2024. (cited on page 187)

[768] A. V. Lunkin, K. S. Tikhonov, and M. V. Feigel'man. Sachdev-ye-kitaev model with quadratic perturbations: The route to a non-fermi liquid. *Phys. Rev. Lett.*, 121:236601, Dec 2018. (cited on page 188)

[769] E. J. Torres-Herrera and Lea F. Santos. Extended nonergodic states in disordered many-body quantum systems. *Annalen der Physik*, 529(7), January 2017. (cited on page 188)

[770] Nicolas Macé, Fabien Alet, and Nicolas Laflorencie. Multifractal scalings across the many-body localization transition. *Phys. Rev. Lett.*, 123(18):180601, 2019. (cited on page 188)

[771] Jakob Lindinger, Andreas Buchleitner, and Alberto Rodríguez. Many-body multifractality throughout bosonic superfluid and mott insulator phases. *Phys. Rev. Lett.*, 122(10):106603, 2019. (cited on page 188)

[772] Chenfeng Cao, Yeqing Zhou, Swamit Tannu, Nic Shannon, and Robert Joynt. Exploiting many-body localization for scalable variational quantum simulation. *arXiv:2404.17560*, 2024. (cited on page 188)

[773] John Preskill. Quantum computing and the entanglement frontier. *arXiv:1203.5813*, 2012. (cited on page 188)

[774] Google Quantum AI. Suppressing quantum errors by scaling a surface code logical qubit. *Nature*, 614(7949):676–681, 2023. (cited on page 189)

[775] Amara Katabarwa, Katerina Gratsea, Athena Caesura, and Peter D. Johnson. Early fault-tolerant quantum computing. *PRX Quantum*, 5:020101, Jun 2024. (cited on page 189)

[776] IBM Quantum Team. Heron r : A 156-qubit heavy-hex processor delivering 5,000-gate circuit depth at utility scale. *Quantum Science and Technology (technical report)*, November 2024. Enhanced fidelity and circuit depth; nearly 50× faster over 2023 utility benchmark. (cited on page 193)

[777] JA Montanez-Barrera, Kristel Michielsen, and David E Bernal Neira. Evaluating the performance of quantum processing units at large width and depth. *arXiv preprint arXiv:2502.06471*, 2025. (cited on page 193)

[778] Dennis Willsch, Madita Willsch, Carlos D Gonzalez Calaza, Fengping Jin, Hans De Raedt, Marika Svensson, and Kristel Michielsen. Benchmarking advantage and d-wave 2000q quantum annealers with exact cover problems. *Quantum Information Processing*, 21(4):141, 2022. (cited on page 193)

[779] Vrinda Mehta, Hans De Raedt, Kristel Michielsen, and Fengping Jin. Understanding the physics of d-wave annealers: From schr\" odinger to lindblad to markovian dynamics. *arXiv preprint arXiv:2503.21565*, 2025. (cited on page 193)

[780] Vrinda Mehta, Hans De Raedt, Kristel Michielsen, and Fengping Jin. Unraveling reverse annealing: A study of d-wave quantum annealers. *Physical Review A*, 112(1):012414, 2025. (cited on page 193)

[781] Anatole Kenfack and Karol Życzkowski. Negativity of the wigner function as an indicator of non-classicality. *Journal of Optics B: Quantum and Semiclassical Optics*, 6(10):396, 2004. (cited on page 193)

[782] M Frau, PS Tarabunga, M Collura, M Dalmonte, and E Tirrito. Nonstabilizerness versus entanglement in matrix product states. *Phys. Rev. B*, 110(4):045101, 2024. (cited on page 193)

[783] Gerald E Fux, Emanuele Tirrito, Marcello Dalmonte, and Rosario Fazio. Entanglement–nonstabilizerness separation in hybrid quantum circuits. *Physical Review Research*, 6(4):L042030, 2024. (cited on page 193)

[784] Yuto Ashida, Zongping Gong, and Masahito Ueda. Non-hermitian physics. *Advances in Physics*, 69(3):249–435, 2020. (cited on page 193)

[785] Daoyi Dong and Ian R Petersen. Quantum control theory and applications: a survey. *IET control theory & applications*, 4(12):2651–2671, 2010. (cited on page 193)

[786] Gopal Chandra Santra and Philipp Hauke. Disorder-averaged qudit dynamics. *arXiv preprint arXiv:2412.17519*, 2024. (cited on page 195)

[787] Ashwath N Madhusudan, Gopal Chandra Santra, Inderpreet Kaur, Weibin Li, and Rejish Nath. Commensurate supersolids and re-entrant transitions in an extended bose-hubbard ladder. *arXiv preprint arXiv:2407.20107*, 2024. (cited on page 196)